

# **Search for the H Dibaryon ( $S = -2$ ) Using Diffraction Dissociation**

Karl M. Ecklund

Ph.D. Thesis, Stanford University, Stanford, CA 94309

---

*Stanford Linear Accelerator Center, Stanford University, Stanford, CA 94309*

Work supported by Department of Energy contract DE-AC03-76SF00515.

---

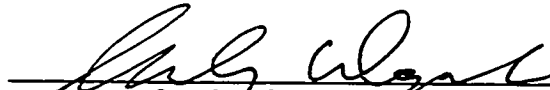
SEARCH FOR THE  $H$  DIBARYON ( $S = -2$ )  
USING DIFFRACTION DISSOCIATION

A DISSERTATION  
SUBMITTED TO THE DEPARTMENT OF PHYSICS  
AND THE COMMITTEE ON GRADUATE STUDIES  
OF STANFORD UNIVERSITY  
IN PARTIAL FULFILLMENT OF THE REQUIREMENTS  
FOR THE DEGREE OF  
DOCTOR OF PHILOSOPHY

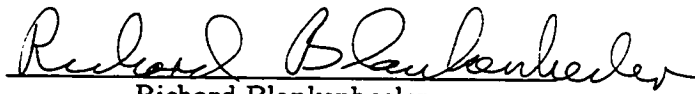
By  
Karl Matthew Ecklund  
March 1996

© Copyright 1996 by Karl Matthew Ecklund  
All Rights Reserved

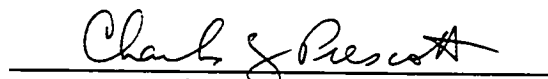
I certify that I have read this dissertation and that in my opinion it is fully adequate, in scope and in quality, as a dissertation for the degree of Doctor of Philosophy.

  
Stanley G. Wojcicki  
(Principal Advisor)


I certify that I have read this dissertation and that in my opinion it is fully adequate, in scope and in quality, as a dissertation for the degree of Doctor of Philosophy.

  
Richard Blankenbecler  
(SLAC)

I certify that I have read this dissertation and that in my opinion it is fully adequate, in scope and in quality, as a dissertation for the degree of Doctor of Philosophy.

  
Charles Prescott  
(SLAC)

Approved for the University Committee on Graduate Studies:

  
\_\_\_\_\_

# Abstract

The observed hadrons are understood as bound states of three quarks (baryons) or of quarks and antiquarks (mesons). To date no six quark bound state other than the loosely bound deuteron has been observed. Quantum Chromodynamics permits other color-singlet bound states of quarks, and a number of phenomenological models extended from the baryon ( $q^3$ ) and meson ( $q\bar{q}$ ) sectors predict bound six quark states ( $q^6$ ). The most probable candidate is the  $H$  dibaryon, composed of two each of the lightest three quarks ( $udsuds$ ), with quantum numbers  $J^P = 0^+$ ,  $I = 0$  and  $S = -2$ . Its mass would likely be between the deuteron mass and twice the  $\Lambda$  ( $uds$ ) mass.

This dissertation describes a search for the  $H$  dibaryon conducted in a neutral beam at the Brookhaven National Laboratory's Alternating Gradient Synchrotron. In the experiment a 24.1 GeV/c proton beam struck a 1.35 interaction length platinum target producing a collimated neutral beam ( $62 \mu\text{sr}$  at 65 mrad from the incident proton direction) which propagated through a 18 m vacuum decay tank before entering a double arm spectrometer. Approximately 20 m from the production target a 10 cm (0.15 interaction length) long active scintillator dissociator was placed in the beam.

The  $H$  is searched for by the diffractive dissociation reaction  $HA \rightarrow \Lambda\Lambda A$  where the  $\Lambda$ 's decay to charged particles measured in the spectrometer. Reconstruction of the  $\Lambda$ 's allows the determination of a primary vertex position, and events are selected consistent with two  $V^0$ 's coming from a space point inside the dissociator. A total of 40  $\Lambda\Lambda$  events are observed with a background of 3.2 events, but they are inconsistent with  $H$  dissociation. There is an identifiable and topologically similar signal of coherent diffractive dissociation of neutrons to  $\Lambda K_S^0$ ,  $n + C \rightarrow \Lambda K_S^0 + C$ , which is used

to estimate the sensitivity achieved in the search. An upper limit on the differential cross section for  $H$  production is set at 0.6 mb/sr. The experiment is sensitive to all  $H$  masses below  $2m_A$ , but is limited to lifetimes greater than approximately  $10^{-8}$  sec.

# Acknowledgments

As is often the case in High Energy Physics experiments, there are many people without whom this work would not be possible, and all of them are due thanks for the part they played in the planning, running and data analysis of BNL E888. I thank Val Fitch, Josh Klein and Morgan May for dreaming up the experiment and bringing it before the E791 and E871 collaborations, and Bob Cousins and Milind Diwan for their encouragement, enthusiasm and hard work during the days leading to the proposal. The members of E791 deserve the credit for most of the detector hardware, and the members of E871 are thanked for making room in an already busy schedule for another experiment. E871 gave up not only precious running time, but also the creative minds and dedicated efforts of more than a few physicists. All of the collaboration members of E888 (Appendix A) contributed time and effort to the running of the experiment. A few deserve special mention for their extraordinary contributions during the run: Bob Cousins for able leadership, unfailing vision and constant vigilance during the run; Alan Schwartz for much hard work with the Level 3 trigger and for tutoring me in the art of maintaining electronics; Milind Diwan for many late nights calibrating the drift chambers, debugging the trigger counters and helping me get started with the offline program; Dayle Hancock for his efforts to hobble together an online computer and keep it running during the experiment; Virgil Highland for bringing up the Čerenkov counter with Freon; George Irwin for expert help in adapting the offline code for a new experiment; Josh Klein and Brent Ware for spending a snowy February at BNL restringing four damaged chambers; Steve Kettell for setting up the trigger; Morgan May and Sebastian White for help with the dissociator and drift chambers; Jim McDonough for lending his expert hand in



keeping the experiment going and being the easiest person to talk to about physics; and Steve Worm for discussions about the magnetic field.

I also owe a debt of thanks to the data analysis team of Bob Cousins and Josh Klein. Bob lead Josh and I through a "high class" data analysis, and taught me much about physics and the tools of the trade. Josh often forged the path ahead, and his efforts and insight defined the direction for the analysis. Bob and Josh also deserve recognition for their patience when other commitments kept me from devoting more time to the analysis, when it might have been easier to leave me behind. While working on the analysis I have also benefited from discussions with Milind Diwan, Val Fitch, George Irwin, Morgan May, Bill Molzon, Brent Ware and Sebastian White. Thanks also to those who took the trouble to lend their expertise at analysis meetings at BNL and Princeton.

My advisor, Stan Wojcicki, has proven the ideal mentor, cutting me loose to learn on my own, yet always ready to listen and point out other avenues of attack when I reached an impasse. His advice and guidance have been invaluable.

It has been a pleasure to work with the members of Group G at SLAC. I have learned from all of them, but best of all they have become friends. Thanks to George, Dale, Milind, Casey, Marize, Mike, and Maxine. Thanks are especially due to our secretaries Judy and Karen who kept track of my travels between Stanford and New York. Thanks also to Marcia Keating of the Physics Department.

I also wish to thank those who provided encouragement, moral support and friendship during my years at Stanford and Brookhaven. I was glad to have the company of Suzanne, Robert, Garth, Sing-Foong and Nancy, fellow graduate students at Stanford, when going through the rigors of classwork and later during the writing of my thesis. The grad students and post-docs of E871 helped me remain sane during the intense runs at BNL.

Finally, I thank my brothers and sister-in-law for encouraging me through the long years of graduate school, and my parents for believing I could do almost anything, providing opportunities for the same and being behind me 100%. The caring and love of my family means more to me than anything else.

# Contents

<b>Abstract</b>	<b>iv</b>
<b>Acknowledgments</b>	<b>vi</b>
<b>1 Introduction</b>	<b>1</b>
1.1 Motivation . . . . .	1
1.2 Organization of Thesis . . . . .	2
<b>2 The <math>H</math> Dibaryon</b>	<b>3</b>
2.1 Quantum Chromodynamics . . . . .	4
2.2 $H$ Predictions . . . . .	6
2.2.1 The Bag Model . . . . .	6
2.2.2 Other Models . . . . .	9
2.2.3 Prospects for the $H$ . . . . .	11
2.3 $H$ Decays and Lifetime . . . . .	13
2.4 $H$ Production . . . . .	15
2.5 Summary . . . . .	16
<b>3 The <math>H</math> Dibaryon in Experiment</b>	<b>17</b>
3.1 Double Weak Decay of Nuclei . . . . .	17
3.2 Heavy Neutral Particle Search . . . . .	18
3.3 $H$ Searches . . . . .	19
3.3.1 Carroll <i>et al.</i> . . . . .	19
3.3.2 $\bar{p}$ Production Experiments . . . . .	20

3.3.3	KEK $K^-$ Experiments . . . . .	20
3.3.4	Shahbazian <i>et al.</i> . . . . .	22
3.3.5	Alekseev <i>et al.</i> . . . . .	25
3.4	Double Hypernucleus Implications . . . . .	27
3.5	Summary . . . . .	30
<b>4</b>	<b>Experimental Method - BNL E888</b>	<b>32</b>
4.1	$H$ Production . . . . .	33
4.1.1	Coalescence . . . . .	33
4.2	$H$ Dissociation . . . . .	45
4.2.1	Diffraction Phenomenology . . . . .	45
4.2.2	Simple Breakup Model . . . . .	49
4.2.3	Glauber Model . . . . .	51
4.2.4	Applied Phenomenology . . . . .	56
4.2.5	The Case of the $H$ . . . . .	58
4.3	Signal and Backgrounds . . . . .	60
4.3.1	Signal . . . . .	60
4.3.2	Backgrounds . . . . .	60
4.4	Detector Design . . . . .	62
4.4.1	Experimental Constraints . . . . .	62
4.4.2	Dissociator . . . . .	63
4.4.3	Magnetic Spectrometer . . . . .	65
4.4.4	Particle Identification . . . . .	68
<b>5</b>	<b>Apparatus</b>	<b>71</b>
5.1	Overview . . . . .	71
5.2	Beam . . . . .	71
5.2.1	Primary Beam and Target . . . . .	73
5.2.2	Neutral Beam Defining elements . . . . .	73
5.2.3	Neutral Beam Content . . . . .	75
5.3	Dissociator (DSC) . . . . .	75
5.4	Spectrometer . . . . .	77

5.4.1	Drift Chambers (DC)	78
5.4.2	Magnetic Field	80
5.5	Trigger Hodoscope (TSC)	81
5.6	Čerenkov (CER)	82
5.7	Other Particle ID	83
5.8	Level 1 Trigger (L1)	83
5.9	Data Acquisition	85
5.10	Level 3 Trigger (L3) Algorithm	88
5.11	Online Monitor	89
<b>6</b>	<b>Data Analysis</b>	<b>90</b>
6.1	Raw Data Set	92
6.2	Drift Chamber Calibration	92
6.3	Pass 1	93
6.3.1	Pattern Recognition	94
6.3.2	Pass 1 Selection Cuts	108
6.3.3	Pass 1 Results	109
6.4	Pass 2	114
6.4.1	Track Grouping	115
6.4.2	Track Fitting	116
6.4.3	Track Reconstruction Summary	121
6.4.4	Vertex Fitting (2tkV)	122
6.4.5	Pass 2 Selection Cuts	124
6.4.6	Pass 2 Results	125
6.5	Pass 3	126
6.5.1	Vertex Fitting (VV)	127
6.5.2	Pass 3 Cuts	128
6.5.3	Pass 3 Results	132
6.6	Pass 4 - Final sample selection	133
6.6.1	Refining VV Cuts	134
6.6.2	Dissociator Information	139

6.6.3	Čerenkov Information . . . . .	141
6.6.4	$\Lambda K_S^0$ sample . . . . .	142
6.6.5	$\Lambda\Lambda$ sample . . . . .	144
6.7	Data Analysis Summary . . . . .	147
<b>7</b>	<b>Interpretation</b>	<b>148</b>
7.1	$\Lambda K_S^0$ Events . . . . .	148
7.1.1	Invariant Mass Distribution . . . . .	151
7.1.2	Momentum Spectrum . . . . .	152
7.1.3	$t'$ Distribution . . . . .	154
7.1.4	Normalization Sample . . . . .	157
7.2	$\Lambda\Lambda$ Events . . . . .	157
7.2.1	$\Lambda\Lambda$ Kinematics . . . . .	159
7.2.2	Empty Veto $\Lambda\Lambda$ Events: A Closer Look . . . . .	164
7.3	Setting a Limit on $H$ Production . . . . .	170
7.3.1	Method . . . . .	170
7.3.2	Result . . . . .	176
7.4	Conclusion and Implications . . . . .	176
<b>A</b>	<b>BNL E888 Collaboration</b>	<b>178</b>
	<b>Bibliography</b>	<b>180</b>

# List of Tables

2.1	<i>H</i> Decay Modes . . . . .	13
3.1	<i>H</i> Dibaryon Candidates Observed by Shahbazian <i>et al.</i> . . . . .	25
3.2	$H \rightarrow \Lambda p \pi^-$ Candidates Observed by Alekseev <i>et al.</i> . . . . .	26
3.3	Double Hypernuclei Candidates . . . . .	30
4.1	Fit Parameters to Inclusive $\Lambda$ Production . . . . .	39
6.1	Pass 1 Pattern Recognition Cuts . . . . .	110
6.2	Pass 1 Summary . . . . .	111
6.3	Pass 2 Event Selection . . . . .	125
6.4	Pass 2 Cut Fraction . . . . .	126
6.5	Pass 3 Selection Cuts . . . . .	128
6.6	Pass 3 Event Types . . . . .	132
6.7	Pass 3 Results . . . . .	133
6.8	Pass 4 VV Cuts . . . . .	135
6.9	Data Analysis Summary . . . . .	147
7.1	Resonances Used to Generate Diffractive $\Lambda K_S^0$ Events . . . . .	151
7.2	Kinematics of Empty Veto $\Lambda\Lambda$ events . . . . .	164
7.3	Monte Carlo $\Lambda K_S^0$ Acceptance . . . . .	172
7.4	Monte Carlo $\Lambda\Lambda$ Acceptance . . . . .	174

# List of Figures

2.1	<i>H</i> Mass Predictions . . . . .	12
2.2	<i>H</i> Lifetime . . . . .	14
4.1	Inclusive $\Lambda$ Production . . . . .	39
4.2	Total Cross Section for <i>H</i> Production . . . . .	41
4.3	Differential Cross Section for <i>H</i> Production at 65 mrad . . . . .	42
4.4	<i>H</i> Coalescence Momentum Spectrum . . . . .	43
4.5	Diffraction Dissociation . . . . .	46
4.6	Triple Pomeron Exchange . . . . .	47
4.7	Breakup Model Dissociation Cross Section . . . . .	50
4.8	Glauber Cross Section . . . . .	56
4.9	<i>H</i> Dissociation Cross Section from Phenomenology . . . . .	59
4.10	<i>H</i> Dissociation Topology . . . . .	60
4.11	The E791 Detector and Beamline. . . . .	64
4.12	Typical Signal Event Topology in Dissociator . . . . .	66
4.13	E791 Spectrometer . . . . .	67
4.14	E888 Spectrometer . . . . .	69
5.1	Plan View of Detector Layout . . . . .	72
5.2	Target Station and Collimators . . . . .	74
5.3	Dissociator Assembly: top and side views. . . . .	76
5.4	Drift Chamber Cell Pattern . . . . .	79
5.5	Čerenkov Counter Schematic . . . . .	82
5.6	Block diagram of the E791 data acquisition system . . . . .	86

6.1	Data Analysis Flow Chart . . . . .	91
6.2	Pattern Recognition Flow Chart . . . . .	95
6.3	Wire Hit Topologies: Single Track . . . . .	96
6.4	Good DOCA Sums and DOCA Difference . . . . .	97
6.5	Wire Hit Topologies: Two or More Tracks . . . . .	98
6.6	DOCA Sum Distribution from Data . . . . .	99
6.7	$x$ -track finding . . . . .	102
6.8	Track Segment Slope Distributions from Data . . . . .	103
6.9	Cuts at TSC for $x$ -track Segments . . . . .	104
6.10	X-Track Segment Matching at Magnet Center . . . . .	104
6.11	Y-Track Recognition for Right Side . . . . .	105
6.12	Y-Track Recognition for Left Side . . . . .	106
6.13	3d-Track Matching at DC2 . . . . .	107
6.14	Beam Strip Charts . . . . .	113
6.15	Pass 1 Reconstruction Fraction . . . . .	114
6.16	Track $\chi^2$ Distributions . . . . .	120
6.17	$FOM_{\text{Track}}$ Distributions . . . . .	122
6.18	$V^0$ $\chi^2$ Distribution . . . . .	128
6.19	VV DOCA and $\chi^2$ Distributions . . . . .	129
6.20	VV FOM Distributions . . . . .	130
6.21	$\Lambda$ and $K_S^0$ Mass Resolution . . . . .	131
6.22	Cut on $(x, y)$ -position of VV . . . . .	136
6.23	$z_{VV}$ Resolution Determined from MC Events . . . . .	136
6.24	Cuts on $z$ -position of VV . . . . .	137
6.25	$y_{VV}$ vs $z_{VV}$ for VV Events . . . . .	138
6.26	Cut on $z$ -position of $V^0$ 's . . . . .	139
6.27	DSC TDC Distributions from $\Lambda K_S^0$ Events. . . . .	141
6.28	Inclusive $\Lambda K_S^0$ : $m(\pi^+\pi^-)$ vs $m(p\pi^-)$ . . . . .	143
6.29	$\Lambda\Lambda$ : $m(p\pi^-)_1$ vs $m(p\pi^-)_2$ . . . . .	145
6.30	$\Lambda\Lambda$ : $m(p\pi^-)_2$ vs $m(p\pi^-)_1$ Lego Plot . . . . .	146



7.1	$M_{\Lambda K_S^0}$ Spectrum Modeled in Monte Carlo . . . . .	152
7.2	Invariant Mass of $\Lambda K_S^0$ Events . . . . .	153
7.3	Neutron Momentum Spectrum . . . . .	155
7.4	Distribution of $p_T^2$ for Empty Veto $\Lambda K_S^0$ Events . . . . .	156
7.5	$t' = t - t_{\min}$ Distribution . . . . .	158
7.6	$M_{\Lambda\Lambda}$ Distribution . . . . .	161
7.7	$p_{\Lambda\Lambda}$ Distribution . . . . .	162
7.8	$M_{\Lambda\Lambda}$ vs $p_{\Lambda\Lambda}$ . . . . .	163
7.9	Distribution of $p_T^2$ for $\Lambda\Lambda$ Events . . . . .	165
7.10	DSC Event Plot for Empty Veto $\Lambda\Lambda$ Event. . . . .	167
7.11	Event Plot $(x, z)$ for Empty Veto $\Lambda\Lambda$ Event. . . . .	168
7.12	Event Plot $(y, z)$ for Empty Veto $\Lambda\Lambda$ Event. . . . .	169

# Chapter 1

## Introduction

This thesis describes an experimental search for the  $H$  dibaryon, a proposed doubly strange six quark bound state. The experiment was undertaken in 1992 at Brookhaven National Laboratory (BNL) by a collaboration (E888) of experimenters from BNL, University of California Irvine, University of California Los Angeles, Princeton University, Stanford University, Temple University, The University of Texas at Austin and The College of William and Mary. A list of the E888 collaboration members may be found in Appendix A.

### 1.1 Motivation

The Standard Model of particle physics has enjoyed increasing success in describing the interactions of particles in the past decades. The fundamental particles of this model, quarks and leptons, interact with each other through four fundamental forces. Quantum Chromodynamics (QCD), the theory of the strong interaction in the Standard Model, describes the interaction of quarks, and as such it must describe the bound states of quarks to be a successful theory. As of this writing most of the observed hadrons (strongly interacting particles) are understood as bound states of three quarks (baryons), or of a quark and an antiquark (mesons). Within QCD, other groupings of quarks, such as six-quark states or dibaryons, are permitted, but so far no state with more than three quarks or one quark and one antiquark has been

observed. (The weakly bound deuteron is truly an exception, which is discussed in Chapter 2.) There remains a fundamental question whether other types of bound states exist. By searching for the  $H$  dibaryon, considered to be the most probable on theoretical grounds, we aim to investigate this question. The observation of a six quark hadron would be the discovery of a completely new form of matter, and its properties would be of great interest for understanding QCD and strong interactions. Definitive evidence that the  $H$  dibaryon is not produced at the level expected in many calculations would also be interesting, but understandably less so.

## 1.2 Organization of Thesis

Following this introductory chapter, the theory of the  $H$  and its properties are discussed in Chapter 2. Chapter 3 gives an overview of other experimental searches for the  $H$  dibaryon, and Chapter 4 describes the experimental method employed for this search. A description of the apparatus employed is found in Chapter 5. Chapter 6 gives a detailed description of the data analysis and the selection of candidate events. Chapter 7 interprets the results of the data analysis and discusses the implications for the existence of the  $H$  dibaryon.

## Chapter 2

### The $H$ Dibaryon

In the Standard Model, the hadrons are described as bound states of quarks ( $q$ ) and antiquarks ( $\bar{q}$ ). The colored quarks are bound by the exchange of gluons, the quantum of the Quantum Chromodynamic (QCD) field, into states which are manifested in Nature as baryons ( $qqq$ ), anti-baryons ( $\bar{q}\bar{q}\bar{q}$ ) and mesons ( $q\bar{q}$ ). In principle other combinations of quarks are allowed by QCD, with the sole prescription that the state be a color singlet, that is having no net color charge, but all observed hadrons to date are understood as either  $q^3$  ( $\bar{q}^3$ ) or  $q\bar{q}$  states.<sup>1</sup> This opens the fundamental question of whether other color singlet states such as  $q^6$ ,  $q^4\bar{q}$  and  $q^2\bar{q}^2$  are predicted by QCD, and if they are predicted, whether they exist.

Unfortunately, although QCD is a theoretically simple description of strong interactions and therefore aesthetically attractive, it has proven to be intractable at the low energies appropriate to answering this question. It is difficult to calculate in QCD at low energy because the strength of the interaction requires that all orders of perturbation theory be included in any calculation. In addition, the quantum of QCD, the gluon, itself carries color requiring interactions between gluons to be considered. This is in contrast to Quantum Electrodynamics (QED) where the strength of the interaction is weak, so perturbation theory gives (relatively) easy answers to

---

<sup>1</sup>QCD also allows bound states of quarks and gluons or just gluons. The identification of a number of meson resonances with these hybrid ( $q\bar{q}g$ ) and glueball ( $gg$ ) states appears increasingly likely.

high precision, and the photon carries no charge, reducing the number of processes which must be considered when carrying out calculations. Despite these difficulties in calculating directly from the pure QCD theory, many have attempted to understand the spectrum of hadrons using phenomenological models inspired by QCD.

One of the most successful calculations, the MIT Bag Model developed by R.L. Jaffe and others at the Massachusetts Institute of Technology, when applied to possible six quark states predicts a stable configuration of two each of the lightest three quarks: up, down and strange. This spin 0, spherically symmetric state  $u^2 d^2 s^2$  was dubbed the  $H$  for hexaquark by Jaffe in 1977 [1]. Choosing parameters of his model to reproduce the masses of the known baryons, he found that the  $H$  should be about  $80 \text{ MeV}/c^2$  lighter than the threshold for strong decay into two lambdas ( $\Lambda = uds$ ) ( $2.23 \text{ GeV}/c^2$ ). If the six quark configuration has energy greater than the mass of two  $\Lambda$ 's, then such a state if formed would decay via the strong interaction to  $\Lambda\Lambda$  with very short lifetime ( $\sim 10^{-20} \text{ s}$ ). Below  $2m_\Lambda$  the  $H$  must decay weakly with a long lifetime of order  $10^{-8}$  seconds. Other models also predict the mass of the  $H$ , with varying estimates from  $1.1$ – $2.8 \text{ GeV}/c^2$ , masses (if correct) implying anything from an absolutely stable  $H$  ( $m_H \leq 1.875 \text{ GeV}/c^2$ ) to a resonance in the  $\Lambda$ - $\Lambda$  system ( $2m_\Lambda < m_H < 2m_\Sigma$ ) to a unbound state ( $m_H > 2m_\Sigma$ ), meaning a repulsive  $\Lambda$ - $\Lambda$  interaction.

The discovery of the  $H$  in experiment would be the observation of a completely new type of matter. By studying the  $H$  and measuring its properties we would gain better understanding of the strong interaction and perhaps help to determine whether QCD is the correct theory of strong interactions at low energy.

## 2.1 Quantum Chromodynamics

Quantum Chromodynamic (QCD) is defined by the Lagrangian density

$$\mathcal{L}_{\text{QCD}} = \bar{q}(i\gamma^\mu \partial_\mu - m)q - \frac{1}{2}g(\bar{q}\gamma^\mu \lambda_a q)A_\mu^a - \frac{1}{4}F_{\mu\nu}^a F_a^{\mu\nu} \quad (2.1)$$

where

$$F_{\mu\nu}^a = \partial_\mu A_\nu^a - \partial_\nu A_\mu^a - gf_{abc}A_\mu^b A_\nu^c \quad (2.2)$$

is the color electromagnetic field tensor with color index,  $a = 1, 2, \dots, 8$ ;  $A_\mu^a$  is the color vector potential;  $g$  is the strong interaction coupling constant;  $q$  is the quark field spinor;  $f_{abc}$  are the structure constants for SU(3) color;  $\lambda_a$  are the matrix generators of SU(3); and  $m$  is the quark mass. The Lagrangian density in Eq. 2.1 is believed to give the correct description of strong interactions. It has been shown to be renormalizable and asymptotically free at short distances where perturbation theory is valid. To date this description agrees well with experiment: quarks indeed appear to behave as free particles at short distances ( $r \sim 1$  fm) and strong interactions are consistently described as the exchange of a single gluon, with small corrections to account for higher order processes. At these small distances (or equivalently, high energies) QCD appears to be the theory of strong interactions. At large distances perturbation theory fails because the coupling constant becomes large, and there are few theoretical predictions from first principles. However, despite the lack of quantitative predictions, there is an increasing qualitative understanding of how QCD could account for the low energy behavior of quarks. It is very likely that QCD confines quarks into color singlet bound states (hadrons) at these distances, a phenomenon referred to as color confinement, although no proof has yet been found. The strong coupling is so great at large distances that when two quarks are separated, it becomes energetically favorable to create a quark-antiquark pair out of the vacuum between the separated quarks to confine the color field to a smaller region of space. Because of the great energy stored in the gluon field between separated quarks, we expect to find quarks only in bound states, as indeed has been the case experimentally.

The same strong coupling which makes the strong force strong and leads to the confinement of quarks makes it impossible to calculate in QCD the nature of bound states using perturbation theory. Other methods have been used to investigate bound states of quarks, and some of them have been quite successful. Beginning with the MIT Bag Model, I discuss some of the models applied to the bound state problem, focusing on what they have to say about the  $H$ .

## 2.2 $H$ Predictions

### 2.2.1 The Bag Model

There are several bag type models of QCD, but the most successful in reproducing the properties of known hadrons is the MIT Bag Model [2]. (Reference [3] gives a review of bag models.) The bag models are inspired by the observation that quarks are confined to finite regions by the strong interaction. In the MIT Bag Model, the quarks are confined to a spherical bag of radius  $R$  by the vacuum which exerts an inward pressure  $B$ . The Lagrangian density is modified to be  $\mathcal{L}_{\text{bag}} = (\mathcal{L}_{\text{QCD}} - B)\theta_V$ , where the step function  $\theta_V$  causes the density to vanish outside of the bag volume  $V$ . Within the bag, the normal modes or eigenstates of the quarks are calculated, and approximations of the quark-quark interactions are used to calculate the energy for a configuration of quarks placed in the eigenstates of the bag.

The particular approximation for the  $q$ - $q$  interaction used in the MIT Bag Model is the lowest order one in QCD: exchange of single gluons between quarks. In the language of perturbation theory, only diagrams of order  $\alpha_s = g^2/\pi$  are considered. This greatly simplifies the calculation and allows results to be obtained. In this limit, QCD is analogous to QED (because  $g$ - $g$  interactions are ignored), except there are eight gluon fields instead of one photon field. The mass of a hadron in the bag model is given by

$$M = E_V + E_0 + E_Q + E_M + E_E. \quad (2.3)$$

Here  $E_V = 4/3\pi BR^3$  is the energy of the bag supported against the vacuum, and  $E_0$  is the zero point energy of the Dirac sea of quarks in the bag. The zero point energy is in principle calculable from the quark states in the bag, but often it is parameterized as  $-Z_0/R$ , where  $Z_0$  is a constant parameter of the model.  $E_Q$  adds the quark energies in the bag eigenstates. The final two terms come from single gluon exchange. In analogy with QED, there are separate color-magnetic ( $E_M$ ) and color-electric ( $E_E$ ) interactions between the colored quarks mediated by the gluon fields.

Of the two, the color-magnetic contribution to the hadron mass is most responsible for the mass spectrum of the states having the same number of quarks.  $E_M$  is

proportional to

$$\Delta = - \sum_{i < j} \vec{\sigma}_i \cdot \vec{\sigma}_j \vec{\lambda}_i \cdot \vec{\lambda}_j M(m_i R, m_j R). \quad (2.4)$$

The sum is over all distinct pairs of quarks in the hadron, and  $\vec{\sigma}_i$  ( $\vec{\lambda}_i$ ) denotes the spin (color) vector of the quarks. Here  $M(m_i R, m_j R)$  measures the strength of the interaction; in the bag model it is a simple function of the quark masses, which introduce small SU(3) flavor violations. The color-magnetic interaction gives rise to the mass difference between hadrons containing the same quarks ( $N - \Delta$  and  $\Lambda - \Sigma$  for example). In QED it is the charge-magnetic interaction that gives rise to the familiar hyperfine splitting in atomic physics. The size of the splitting is large in QCD compared to QED due to the strength of the interaction.  $((m_N - m_\Delta)c^2 \approx 300$  MeV, while the energy of the hyperfine transition in hydrogen is only  $6 \mu\text{eV}$ !)

The bag model has six parameters:  $B$  the bag pressure,  $Z_0$  the zero point energy,  $\alpha_s$  the strong coupling constant and the three quark masses. Often the up and down quarks are taken to be massless. (The size of the bag,  $R$ , is related to the other parameters by the static boundary condition that the bag pressure be balanced by the quark and gluon field pressures.) In [2] DeGrand *et al.* use the observed masses of the  $\Delta$ ,  $p$  and  $\omega$  to fix  $B$ ,  $Z_0$  and  $\alpha_s$ , and the  $\Omega$  mass to fix  $m_s$  (with  $m_d = m_u = 0$ ), completely constraining the model. The predicted masses of the remaining S-wave hadron states may be checked against experiment. The bag model does surprisingly well, with a few exceptions.<sup>2</sup> The baryon decuplet ( $J = 3/2$ ) is well reproduced, and for the octet ( $J = 1/2$ ) the  $\Xi$  mass is about  $30 \text{ MeV}/c^2$  too low and the  $\Lambda$ - $\Sigma$  splitting half of the observed value. The meson sector is not as well reproduced. The  $\pi$ - $K$  splitting is only  $210 \text{ MeV}$  compared to an experimental value of  $350 \text{ MeV}$ , with the  $\pi$  coming out too massive. The bag model also predicts magnetic moments and charge radii. In these areas there is also general agreement with experiment.

Jaffe pointed out that the bag model could be used to investigate the six quark sector [1]. Using the same parameters fixed from the baryon and meson sectors, he found that the model predicts an S-wave flavor-singlet dihyperon ( $S = -2$ ) state with

<sup>2</sup>A notable exception is the  $\eta$ - $\eta'$  mass splitting, believed to be caused by an effect, not included in the bag model, the instanton induced interaction.



$J^P = 0^+$  and mass  $2150 \text{ MeV}/c^2$ .

Jaffe notes that the binding of the  $H$  is due to the symmetry of the  $H$  wave function. In the limit of massless (or equal mass) quarks, the interaction energy of Eq. 2.4 has a simple form. By combining the color ( $SU(3)_c$ ) and spin ( $SU(2)_s$ ) symmetries of the quarks into "colorspin" ( $SU(6)_{cs}$ ), the interaction energy for  $N$  quarks in the ground state wavefunctions of the S-wave hadron becomes

$$\Delta = [8N - \frac{1}{2}C_6 + \frac{4}{3}J(J+1)]\bar{M}. \quad (2.5)$$

In the above equation,  $C_6$  is the quadratic Casimir operator for  $SU(6)$ , and  $J$  is the total angular momentum of the quarks.  $\bar{M} = M(0,0)$  represents the interaction strength assuming  $SU(3)$  flavor symmetry. When Jaffe first wrote the contribution of the color-magnetic interaction this way he noted that for a given  $N$ , the most favorable states will have the largest possible eigenvalue of  $C_6$  and hence the greatest symmetry in color-spin space. When the  $SU(3)_f$  symmetry was broken by putting in quark masses, this still remains true. The  $H$  is the lightest six quark state with the maximal symmetry (color, flavor and spin singlet) and largest  $C_6$  eigenvalue. In the language of group theory it is an  $SU(6)$  490 representation with  $C_6 = 144$ .

Jaffe is also quick to note that the  $H$  of the bag model is a six quark state unlike the deuteron, which more closely resembles a molecule like baryon-baryon bound state, where the neutron and proton retain their identity in a dumbbell-like wavefunction. The bag model confines the six quarks to the same central bag; all six quarks in the  $H$  are placed in the same  $s_{\frac{1}{2}}$  orbitals. In fact, Jaffe finds the lowest lying state with deuteron quantum numbers to be  $\sim 300 \text{ MeV}$  above  $m_n + m_p$ . He notes that weakly bound states like the deuteron may simply escape notice in the bag model. The conclusion one can draw from the unbound  $300 \text{ MeV}$   $n$ - $p$  state, is that the short range nuclear repulsion, well known in nuclear physics, prevents a six quark bag-like deuteron from being bound. The bag model has nothing to say about the long range baryon-baryon force, which would be responsible for the binding energy of the deuteron.

Following Jaffe's initial prediction of the  $H$ , others have used the bag model to

make improved estimates of its mass. Aerts *et al.* find  $m_H = 2.20 \text{ GeV}/c^2$  after optimally picking the bag parameters to reproduce baryon masses [4]. Mulders and Thomas consider the effect of interactions with a surrounding pion field, finding the mass to be close to the  $2m_\Lambda$  threshold [5]. Liu and Wong attempt to correct for the kinetic energy of the center-of-mass motion of the six quark system caused by oscillations of the center-of-mass. Accounting for this effect in their new model causes the  $H$  to become unbound at the 10 MeV level [6]. Calculations in the color dielectric model attempt to account for all of these corrections consistently in a single calculation finding binding energies of about 100 MeV [7, 8]. Recently Golowich and Sotirelis have extended the  $q$ - $q$  interaction to second order in  $\alpha_s$ , deducing a mass in the range 2.12–2.18  $\text{GeV}/c^2$  [9]. These and other bag model results are plotted in Figure 2.1 versus date of publication.

## 2.2.2 Other Models

### Non-relativistic Quark Potential Models

Like the bag models, quark potential models are phenomenologically motivated. Instead of imposing boundary conditions, they use an effective potential to confine the quarks. Another difference is that the treatment of quark motion is taken to be nonrelativistic. The potential and model parameters are chosen to reproduce the hadronic mass spectrum. Such models have had success comparable to the bag models in reproducing the experimentally observed properties of hadrons. These models are also successful in describing the short range nucleon-nucleon interaction and were first developed in nuclear physics to this end. They have also been applied to potential six quark states. The first calculations found the  $H$  to be unbound by 30 MeV [11] and 70 MeV [12]. More recently they find the  $H$  to be less bound than in the bag models. Shimizu gives a review of one potential model, the Quark Cluster Model, in [13], discussing its application to the  $H$  dibaryon. Some mass predictions using potential models are shown in Figure 2.1.

### Skyrme Model

From a completely different perspective, low energy QCD may be considered equivalent to an effective meson field theory. In these theories Skyrme noticed that there are soliton solutions for the fields [14]. The soliton solutions remain localized in space and have an absolutely conserved topological quantum number which Skyrme identified with baryon number, so that the solitons are interpreted as baryons. Skyrme's work in the 1960's was on chiral  $SU(2) \times SU(2)$  fields, which only incorporate QCD for two light flavors of quarks. The soliton solutions then are the nucleons and excited states. More recently interest in these solitons, or skyrmions as they are sometimes called, has increased. Balachandran *et al.* extended the Skyrme model to three light flavors ( $SU(3) \times SU(3)$ ) [15, 16], and Witten showed that the solitons are quantized as fermions for two or three light flavors (and any odd number of light flavors) [17]. The interpretation of the skyrmion solutions as baryons has strengthened.

Balachandran *et al.* considered  $B = 2$  solitons within the chiral Skyrme model, finding a low mass solution identified with the  $H$  by its spin and parity. They calculate a mass of 2.21 GeV, although with an uncertainty of 100–200 MeV [15]. In a longer paper the mass estimate is revised to 2.1 GeV [16]. Two other groups considered the  $H$  in chiral models shortly thereafter. Jaffe and Korpa found a low mass of 1.5 GeV/ $c^2$  [18], and Yost and Nappi find an even lower mass of 1.13 GeV/ $c^2$  [19]. These estimates for extremely deeply bound  $H$ 's are ruled out by the stability of the deuteron, although the uncertainty on the Jaffe estimate is large enough to account for this. Later calculations in Skyrme models find the  $H$  to be less bound, between 40 and 100 MeV [20, 21].

### Lattice QCD Calculations

The model closest to the spirit of QCD is of course lattice gauge theory, which approximates differential equations derived directly from the QCD Lagrangian with finite difference equations defined on a space-time grid or lattice. With current computing technology the precision attained so far is adequate to reproduce hadron mass ratios to better than 6% [22], and significant advances are continually being made. Two

calculations have considered the  $H$  with the far less capable computing resources available in the mid 1980's, where the precision obtainable on the hadron masses was 10–15% [23].<sup>3</sup> In addition, the calculations for the  $H$  take significantly longer for the same lattice size because the wavefunction of six quarks has many more terms than those of baryon and meson states. The first result from a calculation by Mackenzie and Thacker [24] found the  $H$  to be above the  $\Lambda\Lambda$  threshold by some 700 MeV. Iwasaki, Yoshié and Tsuboi carried out a improved calculation using a larger lattice ( $16^3 \times 48$ ) and found the  $H$  to be deeply bound ( $m_H = (1.7 \pm 0.15) \text{ GeV}/c^2$ ) [25]. They attribute the discrepancy between the results to the inadequate lattice spacing of the earlier calculation ( $6^2 \times 12 \times 18$ ). Because of the rapid advance of computing technology, it is clear that new results will be substantially better when they are available. The most recent report of a calculation of the  $H$  mass using Lattice QCD comes from a conference report in 1989, using a yet larger lattice ( $24^3 \times 60$ ) [26]. Yoshié *et al.* find the  $H$  to be bound by about 100 MeV, which is substantially less bound than in their previous calculation. The preliminary result was obtained using a simple formulation of the action instead of the “improved action” used in [25]. They mention that calculations using the improved action on the larger lattice are underway, but no results have been reported.

### 2.2.3 Prospects for the $H$

The phenomenological models of hadrons vary in their estimates for the mass of the  $H$  dibaryon. Even within the same type of model, different calculations may disagree as to the nature of the six quark state  $u^2d^2s^2$ . Lattice gauge theory calculations, which are the closest to the physics of QCD, also differ on their predictions for the  $H$ . Nonetheless Figure 2.1 shows that the majority of the estimates favor an  $H$  below the threshold for strong decay ( $2.231 \text{ GeV}/c^2$ ) and above the threshold for double weak decays ( $1.875 \text{ GeV}/c^2$ ). This bias towards the existence of the  $H$  makes experimental

---

<sup>3</sup>As an additional point of comparison, the 1993 calculations of hadron masses by Butler *et al.* at IBM were made using a massively parallel computer capable of 5–7 Gflops (billion operations per second) and took 1 year to complete, while the  $H$  calculations consumed only weeks of computer time on Mflop class computers.

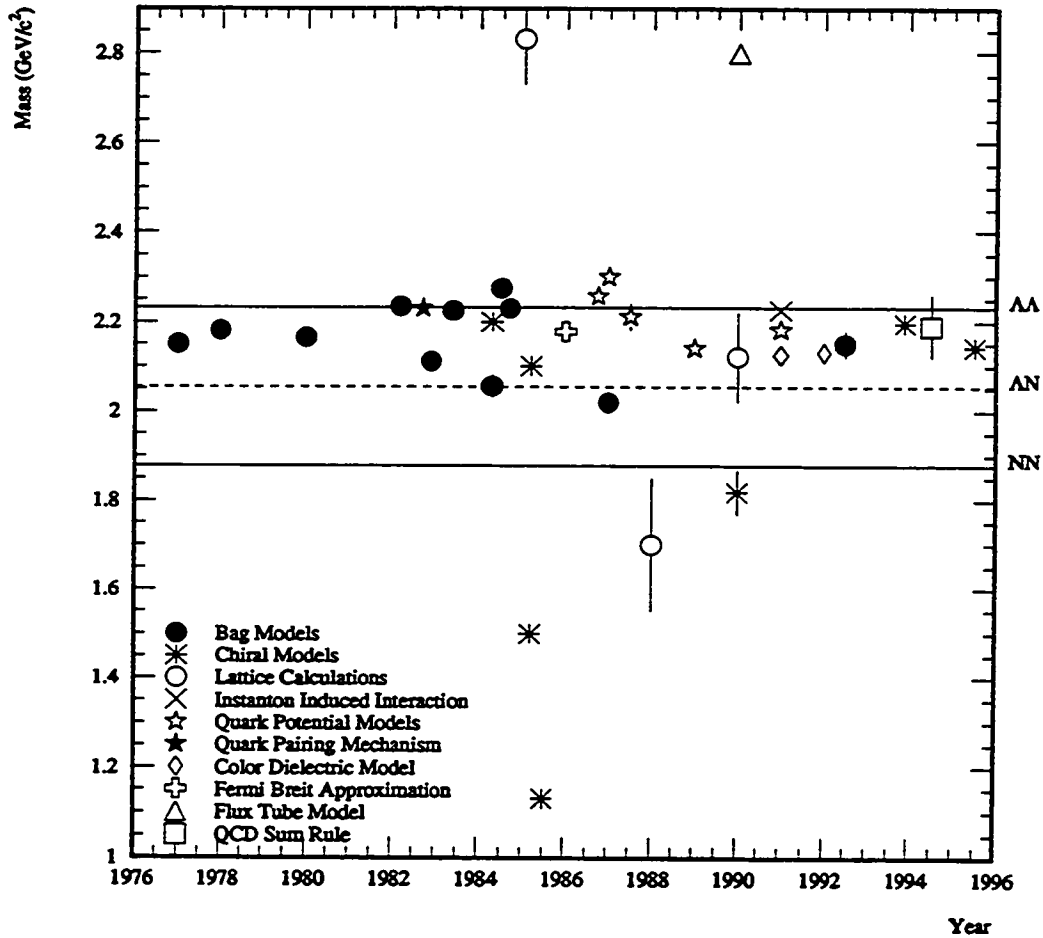


Figure 2.1:  $H$  mass predictions (after Klein [28]). Predicted masses are plotted versus publication date and classified by the model used. Error bars are only plotted if explicitly mentioned in the papers; a mass range is converted to its central value. The thresholds for strong ( $\Lambda\Lambda$ ),  $\Delta S = 1$  ( $\Delta N$ ) and  $\Delta S = 2$  ( $NN$ ) decays are shown as solid and dotted lines. Most predictions fall between the  $\Lambda\Lambda$  and  $\Delta N$  thresholds. From references [1,4–12,15,16,18–21,23–27] and [1,3,5–28] in reference [28].

Mass	Decay	Lifetime	Transition
$2m_\Sigma < m_H$	unbound	—	
$2m_\Lambda < m_H < 2m_\Sigma$	$H \rightarrow \Lambda\Lambda$	$\sim 10^{-20}$ s	Strong
$m_\Lambda + m_n < m_H < 2m_\Lambda$	$H \rightarrow \Lambda n$	$10^{-6}$ – $10^{-8}$ s	Weak
	$H \rightarrow \Sigma N$		$\Delta S = 1$
	$H \rightarrow \Lambda p \pi^-$		
$2m_n < m_H < m_\Lambda + m_n$	$H \rightarrow nn$	$10^6$ – $10^7$ s	$\Delta S = 2$
$m_H < 2m_n$	stable	$\infty$	

Table 2.1:  $H$  Decay Modes

searches promising.

### 2.3 $H$ Decays and Lifetime

The decay channels available to the  $H$  depend on its mass. For  $m_H > 2m_\Lambda$  the strong channel  $H \rightarrow \Lambda\Lambda$  is open, and the lifetime would be typical of strong decays,  $10^{-20}$  s. Below twice the  $\Sigma$  mass ( $2385 \text{ MeV}/c^2$ ), the  $H$  would appear as a  $\Sigma\Sigma$  bound state exhibiting itself as a resonance in the  $\Lambda\Lambda$  or  $\Xi N$  channels. If the  $H$  mass lies above the  $\Sigma\Sigma$  threshold ( $2387 \text{ MeV}$ ), then it is completely unbound. Below the  $\Lambda\Lambda$  threshold, the lightest doubly strange two baryon system, the  $H$  must decay weakly. For masses above the  $\Lambda n$  threshold, the decays are  $\Delta S = 1$  with lifetimes of order  $10^{-7}$  s. There are two body channels:  $\Lambda n$ ,  $\Sigma^0 n$  and  $\Sigma^- p$ . A three body channel  $\Lambda p \pi^-$  is kinematically allowed for the narrow range of mass 38 MeV below the  $\Lambda\Lambda$  threshold. If the mass of the  $H$  is less than  $m_\Lambda + m_n$  ( $2055 \text{ MeV}/c^2$ ), then it must decay by a double weak ( $\Delta S = 2$ ) decay. Reducing two units of strangeness simultaneously is very improbable, resulting in long lifetimes of order  $10^6$  s. Finally if  $m_H < 2m_n$ , then there are no  $B = 2$  final states kinematically allowed; in this case the  $H$  would be absolutely stable. The decay modes for various  $H$  mass possibilities are summarized in Table 2.1.

Donoghue, Golowich and Holstein have calculated the lifetime of the  $H$  assuming the highly symmetric wavefunction implied by the bag model [29]. The result of

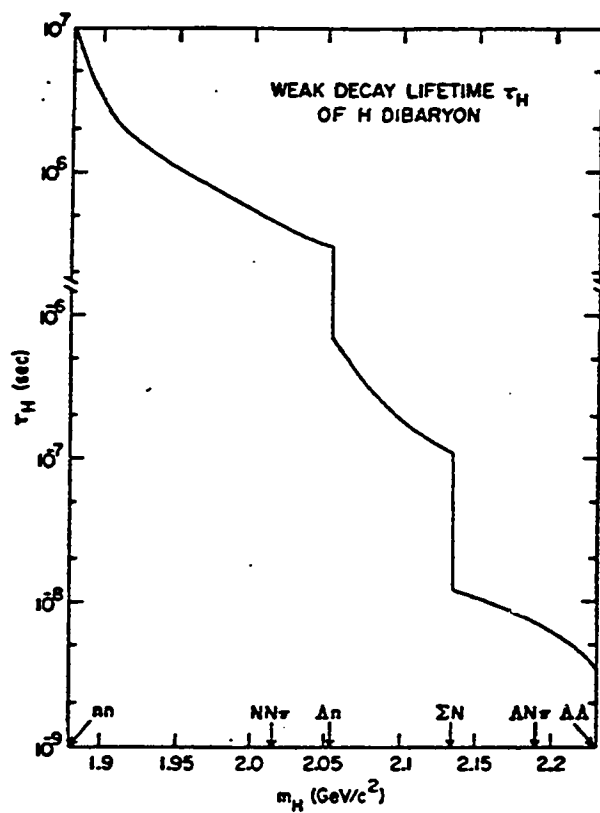


Figure 2.2:  $H$  Lifetime Calculation from Donoghue *et al.* [29].

their calculation is shown in Figure 2.2, showing clearly the effect of new channels becoming available at each threshold. Below the  $\Lambda n$  threshold, the lifetime is quite long since the decay must proceed through a  $\Delta S = 2$  process. For heavier masses, the lifetime is longer than would be expected from considering the  $H$  to be a deuteron-like  $\Lambda$ - $\Lambda$  bound state due to the symmetry of the  $H$  wavefunction. As the mass of the  $H$  approaches the  $\Lambda\Lambda$  threshold, the wavefunction will become more molecule-like, reflecting the small binding energy. The weak decay of an  $H$  near the  $\Lambda\Lambda$  threshold would be expected to be governed by the  $\Lambda$  lifetime ( $\tau_\Lambda = 2.6 \cdot 10^{-10}$  s), with  $\tau_H$  approaching  $\tau_\Lambda/2$  as the binding energy goes to zero. The long lifetime for a highly space symmetric  $H$  wavefunction opens the possibility that significant numbers of  $H$ 's are present in existing neutral beams.

## 2.4 $H$ Production

Production of the  $H$  requires the production of two units of strangeness, such as through double associated production, e.g.  $pp \rightarrow HK^+K^+$ . Beams of hyperons or kaons already carry one unit of strangeness, thus requiring the creation of only one  $s\bar{s}$  pair, but these beams must be produced in a primary interaction so the overall yield is at best the same for a given primary incident flux of nonstrange hadrons. There may be experimental advantages to such beams however, such as better control of background. The reactions  $K^-d \rightarrow HK^0$  or  $\Lambda p \rightarrow HK^+$  could be employed to produce the  $H$ .

A number of phenomenological calculations based on coalescence models predict cross sections for  $H$  production. In these calculations an  $S = -2$  two baryon system produced in an initial reaction is considered to form an  $H$  when the two baryons are "close enough" in phase space. More detail on these coalescence models appears in Section 4.1.



## 2.5 Summary

The question of whether bound six quark states should exist is a difficult one to answer. The  $H$  dibaryon, composed of the three lightest quarks, is perhaps the most promising candidate for a stable six quark state due to the symmetry of the quark wavefunctions. In phenomenological models and numerical calculations of lattice gauge theory the  $H$  appears likely to exist. We stand to learn a great deal about the low energy limit to Quantum Chromodynamics by investigating the question of the existence of the  $H$  dibaryon, both experimentally and through better phenomenological models.

## Chapter 3

# The $H$ Dibaryon in Experiment

Since the  $H$  was first proposed by Jaffe in 1977, there have been a number of experiments to search for it. Because of the wide range of possible masses (and therefore production and decay modes) predicted for the  $H$ , there is no single definitive experiment. Researchers have used very different techniques to attempt to produce and detect this particle, and partly because of this it is difficult to summarize the results of their experiments compactly. However, the searches undertaken so far do admit to categorization as follows.

### 3.1 Double Weak Decay of Nuclei

The prediction of a very light  $H$  ( $m_H < 2m_N$ ) in some calculations opens the possibility that the  $H$  is the ground state of baryonic matter. Such a light  $H$  would be energetically favorable to ordinary nucleon pairs ( $pp, np, nn$ ), which could decay through doubly weak interactions to the  $H$ . A paper by Ejiri *et al.* considers such decays within nuclei [30]. In particular, they consider the processes  $p + p \rightarrow H + 2e^+ + 2\nu$ ,  $n + p \rightarrow H + e^+ + \nu$  and  $n + n \rightarrow H$  inside nuclei and compare the expected lifetimes with those experimentally determined. In the case of stable isotopes, the absence of the decay to the  $H$  establishes a lower limit for the mass of the  $H$ .

The most restrictive limit comes from the observation that the deuteron is stable. Accounting for the binding energy of the  $n$  and  $p$  in the deuteron they conclude

$m_H > 1875 \text{ MeV}/c^2$ , which is  $2.7 \text{ MeV}/c^2$  below  $m_n + m_p$ . The stable nucleus  ${}^6\text{Li}$  similarly excludes masses below  $1873.8 \text{ MeV}/c^2$ .

In addition to these limits from stable nuclei, Ejiri *et al.* also report on experiments undertaken to detect a nuclear decay to the  $H$  by observing the final state positron or  $\gamma$ -ray emitted from an excited nucleus in the final state. One experiment excludes masses below  $1862 \text{ MeV}/c^2$  by looking for the  $\beta^+$  spectrum from  ${}^{127}\text{I} \rightarrow {}^{125}\text{Te} + H + \beta^+ + \nu$  using a NaI crystal as both a source of iodine and a calorimeter. The observed spectrum shows no evidence for this  $\beta$  decay. In addition they looked for  $nn \rightarrow H$  decays inside germanium nuclei of an intrinsic Ge solid state detector:  ${}^{74}\text{Ge} \rightarrow {}^{72}\text{Ge}(2^+) + H$ . This decay would be observed by the detection of a line in the Ge energy spectrum from the  $\gamma$ -ray emitted in the  $2^+ \rightarrow 0^+$  transition of the  ${}^{72}\text{Ge}$  nucleus in the final state. The energy of the line observed in the detector would also include the recoil of the nucleus against the  $H$  emission, so it is possible to obtain  $m_H$  from the exact location of the line. The lines of the measured spectrum are all attributed to known sources, and the expected rate calculated for this process exceeds the background level by many orders of magnitude. They conclude  $m_H > 1861.4 \text{ MeV}/c^2$ . Although these lower limits on  $m_H$  are not as large as the one from deuteron stability (1875.1), they provide additional evidence that a very light  $H$  is excluded by experimental data.

## 3.2 Heavy Neutral Particle Search

Although not carried out as a search for the  $H$ , Gustafson *et al.* [31] undertook a search for long-lived neutral particles which has some sensitivity to the  $H$ . With a neutral beam produced with a 300 GeV proton beam incident on beryllium and tantalum targets, they used time of flight information and a total absorption calorimeter to identify potential candidates for new neutral particles. Using the narrow ( $\sim 1 \text{ ns}$ ) RF structure of the beam at Fermilab as a timing reference, they determine the time of flight for particles interacting in their calorimeter. Particles of a given species are

identified by the relationship between their time of flight and their energy.

$$m \approx \sqrt{2cE^2\Delta t/\ell}, \quad (3.1)$$

where  $\ell$  is the distance between the target and the calorimeter (590 m),  $\Delta t$  is the time of flight relative to photons. In the mass range 2.0–3.0 GeV/ $c^2$ , 14 events consistent with the tail of the neutron distribution are found. They set a limit (90% confidence level) on the invariant cross section:  $E d^3\sigma/dp^3 \leq 1.1 \cdot 10^{-32} \text{cm}^2/\text{GeV}^2/\text{nucleon}$ .

Their result is limited to particles with masses heavier than 2 GeV/ $c^2$  and lifetimes  $\gtrsim 10^{-7}$  s. In addition, the experiment covers a small portion of the available phase space in 300 GeV  $p - A$  collisions:  $-0.05 < x_F < 0.09$  and  $p_T=0.13\text{--}0.32$  GeV/ $c$ . The lower limit in the mass sensitivity is crucial in interpreting the results for the  $H$ . The limit comes about because they are unable to reliably separate the copious production of neutrons from new particles of masses lower than 2.0 GeV/ $c^2$  given their timing and energy resolution. From the published information it is not possible to determine whether their result is valid all the way down to 2.0 GeV/ $c^2$ .

### 3.3 $H$ Searches

#### 3.3.1 Carroll *et al.*

After Jaffe's prediction of the  $H$ , a number of experiments searched for it. Carroll *et al.* searched for  $H$ 's at Brookhaven using a missing mass technique in tagged  $pp \rightarrow K^+K^+X$  interactions [32]. With the two kaons detected in a spectrometer and identified with Čerenkov counters, the remaining particle(s) in the final state,  $X$ , has  $B = 2$  and  $S = -2$ , the quantum numbers of the  $H$ . Using incident proton beams of 5.1, 5.4 and 5.9 GeV/ $c$ , Carroll *et al.* searched for a peak in the missing mass spectrum. Finding no narrow structure in the mass range 2.0–2.5 GeV/ $c^2$ , they set limits (as a function of  $H$  mass and proton momentum) of 30–130 nb for  $H$  production in  $pp$  collisions. Although a theoretical calculations soon gave an estimate an order of magnitude lower [33], their results were the first available, and the limit is comparable to expectations from comparison to deuteron production at threshold.

In their paper they note that near threshold  $\sigma(pp \rightarrow \pi^+\pi^0 d)/\sigma(pp \rightarrow \pi^+\pi^0 np) = 0.2$ . If  $\sigma(pp \rightarrow K^+K^+H)/\sigma(pp \rightarrow K^+K^+\Lambda\Lambda)$  at threshold is comparable, then one might expect the  $H$  production cross section to be of order 100 nb for an incident beam of 5.9 GeV/c. Note that because the  $H$  is detected through its production rather than its decay, their technique is sensitive to  $H$ 's of all masses and lifetimes, even absolutely stable ones.

### 3.3.2 $\bar{p}$ Production Experiments

Speculations about the possibility of production of doubly strange systems of particles in multi-nucleon absorption of slow antiprotons fueled two searches for the  $H$  using  $\bar{p}$  beams. Condo *et al.* placed thin plates in a bubble chamber and irradiated them with 290 MeV/c  $\bar{p}$ 's [34]. The thickness of the plates (C, Ti, Ta and Pb) was chosen to just stop the incident antiproton. An  $H$  may be produced in the annihilation process and detected via its decay to  $\Sigma^- p$  in the bubble chamber. The  $\Sigma^-$  would be identified by its decay  $\Sigma^- \rightarrow \pi^- n$ , which leaves a kink in the negative track, or by the interaction  $\Sigma^- p \rightarrow \Lambda n$ , where the  $\Lambda$  is reconstructed pointing to the terminus of the negative track. Condo *et al.* scanned 80,000  $\bar{p}$  annihilations, and found no candidates. Accounting for probability of  $H$  decay (assuming  $\tau_H \approx \tau_\Lambda$ ) and reconstruction efficiency they set a limit on the probability of  $H$  emission of less than  $9 \cdot 10^{-5}$  per annihilation at the 90% confidence level. In addition they search for  $\Lambda\Lambda$  production setting a limit at  $4 \cdot 10^{-4}$ . A similar experiment was undertaken by the DIANA collaboration [35] using a Xe bubble chamber. They scanned  $10^5$  annihilations, finding no  $H$  candidates and one  $\bar{p}\text{Xe} \rightarrow K^+K_S^0\Lambda\Lambda X$  event. Their upper limit of  $4 \cdot 10^{-5}$  (90% C.L.) is slightly better than the earlier experiment, but still not low enough challenge the theoretical predictions at  $10^{-6}$ – $10^{-7}$  cited in their paper.

### 3.3.3 KEK $K^-$ Experiments

Two experiments undertaken at KEK in Japan have reported negative results in searching for the  $H$ . The experiments (E176 [36] and E224 [37]) both utilize a 1.66 GeV/c  $K^-$  beam incident on a target (emulsion or scintillator) where the reaction

$K^- + (pp) \rightarrow H + K^+$  should be possible [38];  $(pp)$  is a pair of protons in a nucleus of the target. For sufficiently bound  $H$ 's, the momentum of the outgoing  $K^+$  has momentum greater than one from the quasi-free process  $K^- + (p) \rightarrow \Xi^- + K^+$ . The  $H$  would be identified by a peak in the  $K^+$  momentum spectrum above the quasi-free  $\Xi^-$  peak at 1.1 GeV/ $c$ .

Čerenkov counters and a time of flight system identify incident  $K^-$ 's with high efficiency and purity; the  $\pi^-/K^-$  ratio is less than  $10^{-6}$  after Čerenkov veto and time of flight cuts. Another set of Čerenkov counters and time of flight scintillators identify outgoing  $K^+$ 's. A magnetic spectrometer provides a momentum measurement and precision tracking to associate the  $K^+$  track with a vertex in the emulsion (E176) or scintillating fiber (E224) target. In E176 the emulsion target is interspersed with silicon strip detectors (42  $\mu\text{m}$  pitch) to aid in associating spectrometer tracks with emulsion tracks so any candidate events may be examined in detail.

E176 observes about 1700 events attributed to quasi-free  $\Xi^-$  production, with no distinct  $H$  peak above the 1.1 GeV/ $c$  peak. Events above the quasi-free peak are consistent with two sources: real  $K^+$ 's from the tail of the quasi-free peak and misidentified protons. Of the four events above 1.3 GeV/ $c$ , two are rejected by examining the emulsion; all are consistent with misidentified protons. Events closer to the quasi-elastic peak are consistent with the resolution on the  $K^+$  momentum. They set a 90% confidence level limit on the  $H$  production cross section (for  $1.90 \text{ GeV}/c^2 < m_H < 2.16 \text{ GeV}/c^2$ ) at (0.2–0.6)% of the quasi-free  $\Xi^-$  production cross section. (The differential cross section,  $d\sigma/d\Omega(K^-p \rightarrow \Xi^-K^+)$ , is 35  $\mu\text{b}/\text{sr}$  in their acceptance; they obtain a consistent cross section using their beam flux.) The exact value varies as a function of the  $H$  mass due to  $K^+$  detection efficiency, acceptance and mass resolution. This limit is of the same order of magnitude as the predictions by Aerts and Dover [38].

E224, which is the next generation daughter experiment to E176, has reported preliminary results [37]. The emulsion target was replaced with alternating planar arrays of crossed 500  $\mu\text{m}$  scintillating fibers viewed by image intensifier tubes. Using the same analysis technique of examining the  $K^+$  momentum spectrum, they find 4600 quasi-free  $\Xi^-$  events and 13 events above 1.25 GeV/ $c$ , all consistent with misidentified

outgoing  $\pi^+$ 's or  $p$ 's. They reject 7 events by viewing the image intensifier tube images and identifying a  $\Sigma^-$  emission at the interaction vertex. Two more events are rejected by requiring the energy release at the vertex to be consistent with  $H$  production. Taking the remaining four events as background they set a preliminary limit (90% C.L.) at (0.05–0.6)% of the quasi-free  $\Xi^-$  production cross section. The limit applies to  $H$  masses between (1.950–2.200)  $\text{GeV}/c^2$  and is best for light  $H$ 's. For heavier  $H$ 's any  $K^+$  momentum peak from  $H$  production is obscured by the tail from quasi-free  $\Xi^-$  production. They are still able to set a limit above 2.2  $\text{GeV}/c^2$  by using the interaction vertex information in the image intensifier data. For  $2.200 \text{ GeV}/c^2 \leq m_H \leq 2230 \text{ GeV}/c^2$ , they find  $\sigma_H \leq (0.6\text{--}0.7)\% \sigma_{\Xi^-}$  (90% C.L.) by searching for the decays  $H \rightarrow \Sigma^- p$ ,  $\Sigma^- \rightarrow n\pi^-$  inside the scintillating target. The above limit includes the detection efficiency assuming a lifetime for the  $H$  of order the lambda lifetime ( $c\tau_\Lambda = 7.89 \text{ cm}$ ). The preliminary results are below the theoretical estimates for production of lighter  $H$ 's by at most an order of magnitude. For the range of masses above 2.150  $\text{GeV}/c^2$ , the limits are still close to the estimates.

### 3.3.4 Shahbazian *et al.*

A group working at the Joint Institute for Nuclear Research in Dubna, Russia has claimed observation of  $H$  dibaryons. Using a 10  $\text{GeV}/c$  proton beam and a propane bubble chamber, they scan events for signatures of  $H$  production and decay. Charged tracks are identified (when possible) by their ionization, and standard bubble chamber reconstruction programs (such as GRIND from CERN) are used to perform multiver-  
 tex analyses of candidate events. Over the course of the last decade this group has reported on numerous events which they interpret as giving evidence for the existence of  $S = -2$  dibaryons, evidence not for a single dibaryon, but for *four different*  $S = -2$  dibaryon states.

In 1988 Shahbazian *et al.* reported the observation of the weak decay  $H \rightarrow \Sigma^- p$  [39]. They report the observation of a single event which they interpret as the production of an 8  $\text{GeV}/c$   $H$  at a 2-prong star and subsequent weak decay to  $\Sigma^- p$ . They settle on this interpretation after excluding numerous background event types

which could fit this topology using kinematic fits. Despite this attempt to exclude background, the event is still questionable because the  $\Sigma^-$  decay (to  $\pi^-n$ ) is not observed. (They calculate a 10% probability for it to survive at least 40 cm and exit the chamber.) A 2-C fit to the decay vertex gives  $\chi^2 = 0.014$  (C.L. 99.3%) and  $m_H = (2172.7 \pm 15.4) \text{ MeV}/c^2$ . The time of flight of the  $H$  is  $0.668 \cdot 10^{-10} \text{ s}$ .

In 1990 they report on a second candidate event [40] also produced in the bubble chamber by a 10 GeV/c proton beam. The production vertex is a 6-prong star; a  $V^0$  ( $p=1.1 \text{ GeV}/c$ ) pointing to this vertex decays to two charged particles. Again the only hypothesis with reasonable confidence level after the kinematic fit is the weak decay  $H \rightarrow \Sigma^- p$ . The  $\Sigma^-$  candidate track has a kink consistent with the decay  $\Sigma^- \rightarrow n\pi^-$ , with the  $n$  unobserved. The decay length of the  $\Sigma^-$  is too short (2 cm) to allow positive identification using relative ionization, but the final stopping  $\pi^-$  track is clearly identified. The proton track also suffers a kink, which is attributed to rescattering from  $^{12}\text{C}$ , before stopping in the propane. The kinematic fit to the decay chain  $H \rightarrow \Sigma^- p$ ,  $\Sigma^- \rightarrow \pi^- n$  gives  $\chi^2 = 0.07346$  (C.L. 69.43%) and  $m_H = (2218 \pm 12) \text{ MeV}/c^2$ . The time of flight for the  $H$  candidate is  $1.37 \cdot 10^{-10} \text{ s}$ .

In a report presented at Hadron '93 [41] they consider both events as evidence of a single "light" dibaryon  $H^0$ . The masses are consistent within  $2\sigma$  overlap and the observed decays identical. They hypothesize that the production occurred from "dibaryonic fluctuations" within a  $^{12}\text{C}$  nucleus. The first event is consistent with production via  $pD^+ \rightarrow K^0 K^+ p H^0$ , where the  $K^0$  is unobserved and the  $K^+$  and the proton are the two prongs in the production vertex. The  $D^+$  is the piece of the carbon nucleus participating in the interaction. The remainder of the nucleus is postulated to recoil unobserved in the event. They give no hypothesis for the production of the second event, which is associated with a 6-prong star. Taken together the two events have an average mass of  $(2195.4 \pm 9.7) \text{ MeV}/c^2$ , and the production cross section for the  $H$  in 10 GeV/c  $p$ -C collisions is given as  $\approx 60 \text{ nb}$ .

Shahbazian *et al.* report on another event found using the same apparatus in a recent preprint [42]. They observed a  $V^0$  decay, interpreted as  $H \rightarrow \Sigma^- p$ . The slow proton track stops, and the  $\Sigma^- \rightarrow n\pi^-$  decay is observed, the momentum of the  $\pi^-$  track being consistent with  $\Sigma^-$  decay at rest. The ionization of the  $\Sigma^-$  track is also



consistent with expectations. A successful 1C-fit to the  $\Sigma^-$  decay gives a confidence level of 57.4%, and other hypotheses (weak decays of negatively charged particles or strong interactions) are excluded by poor fits. The 1C-fit to the  $V^0$  decay hypothesis  $H \rightarrow \Sigma^- p$  gives  $m(\Sigma^- p) = (2146 \pm 1.0) \text{ MeV}/c^2$  and C.L.=29.8%.

They also performed an exclusive multivertex analysis of the event, but they must hypothesize an elastic scattering of the  $H^0$  candidate from a peripheral neutron in  $^{12}\text{C}$  in order to account for the direction of the  $V^0$  not pointing to the 4-prong/2- $V^0$  star they take as the primary interaction point. The other  $V^0$  in the event is a well identified  $\Lambda$ , and the four prongs are all positively charged. Before settling on the final scenario for the event, they consider numerous strong reactions as possible backgrounds, including all possible primary vertices as a source for the  $H^0$  candidate. The only successful event hypothesis is  $p+^{12}\text{C} \rightarrow H_1^0 + \Lambda + p + K^+ + K^+ + K^+ + ^9\text{Li}$ . The three  $K^+$  tracks are relativistic, and the proton track stops. The hypothetical recoil of the partial nucleus is not observed, which they maintain is consistent with its best fit momentum of  $\sim 280 \text{ MeV}/c$ . The  $H^0$  must undergo a scatter with no observed recoil to fit the primary vertex. They find that the hypothesis of an elastic scatter from a quasi-free neutron has a satisfactory fit (1C, C.L.=88.7%), but scattering coherently from  $^{12}\text{C}$  does not. Finally there is a 42 MeV  $\gamma \rightarrow e^+e^-$  vertex associated with the primary vertex. After failing to associate this photon with possible sources (electromagnetic decays of  $\Sigma^0, \Sigma^+$  or  $K^{*+}$ ;  $\pi^0$  decay with a missed photon and radiative  $\Lambda$  decays) they hypothesize that it comes from the decay of an excited state of the  $H$ ,  $H_1^0 \rightarrow H^0\gamma$ , finding a best fit mass of  $m_{H_1^0} = (2203.0 \pm 5.9) \text{ MeV}/c^2$ .

Based on the three events reported in 1988 [39], 1990 [40] and 1995 [42], Shahbazian *et al.* now claim evidence for an excited state with mass  $(2200.9 \pm 4.1) \text{ MeV}/c^2$  observed in three events. The latest event is claimed as evidence for a ground state  $H$  with  $m_H = (2146.3 \pm 1.0) \text{ MeV}/c^2$ . The effective cross section for  $H$  production in proton  $^{12}\text{C}$  collisions is estimated at 60 nb. The three observations of  $H$  dibaryons by Shahbazian *et al.* are summarized in Table 3.1.

In addition to these three events giving evidence for what they call "light  $H$  dibaryons" ( $H^0, H_1^0$ ), Shahbazian *et al.* have published observation [41, 43] of four other events which they interpret as "heavy neutral ( $\tilde{H}$ ) and charged ( $H^+$ ) dibaryons",

Date	Decay Mode	Mass (MeV/ $c^2$ )	Reference
1988	$H_1^0 \rightarrow \Sigma^- p$	$2172.7 \pm 15.2$	[39]
1990	$H_1^0 \rightarrow \Sigma^- p$	$2218.0 \pm 12.0$	[40]
1995	$H_1^0 \rightarrow H_0 \gamma$	$2203.0 \pm 5.9$	[42]
1995	$H^0 \rightarrow \Sigma^- p$	$2146.3 \pm 1.0$	[42]
1993	$H \rightarrow \Sigma^- p$	$2408.9 \pm 11.2$	[43]
1993	$\tilde{H} \rightarrow \Sigma^- p$	$2384.9 \pm 31.0$	[43]
1993	$H^+ \rightarrow \pi^0 p \Lambda$	$2375.8 \pm 9.3$	[43]
1993	$H^+ \rightarrow \Lambda p$	$2409.3 \pm 13.0$	[43]

Table 3.1:  $H$  Dibaryon Candidates Observed by Shahbazian *et al.*

where heavy means  $m_H > 2m_\Lambda$ . These states have  $S = -2$ , but are claimed to be flavor  $10^*$  representations rather than flavor singlets like Jaffe's  $H$ . Although the two states are found above the threshold for strong decay to  $\Lambda\Lambda$ , the four events are observed through their weak decay modes. The two  $\tilde{H}$  candidates are observed in the decay chain  $\tilde{H} \rightarrow \Sigma^- p$ ,  $\Sigma^- \rightarrow n\pi^-$ . The two  $H^+$  candidates are observed in the decay modes  $H^+ \rightarrow \pi^0 p \Lambda$  and  $H^+ \rightarrow p \Lambda$ , although in the first event the  $\pi^0$  is not observed. The masses of these candidates are summarized in Table 3.1.

### 3.3.5 Alekseev *et al.*

In 1990 Alekseev *et al.* reported two weakly decaying  $H$  candidates,  $H \rightarrow \Lambda p \pi^-$  [44]. Using a neutral beam produced at  $3.5^\circ$  from an internal target in a 10 GeV proton synchrotron, interactions at a 4 cm carbon and 6 cm copper targets placed in the neutral beam were observed with a magnetic spectrometer. Events were recorded only in anticoincidence with a scintillation counter immediately after the target, to ensure only neutral particles exited the target in the direction of the spectrometer. The 40 cm decay volume between the target and the spectrometer was filled with helium to minimize interactions of the neutral beam.

The candidates for  $H \rightarrow \Lambda p \pi^-$  were identified in a  $2 V^0$  topology, where the downstream ( $\Lambda$ ) vertex points to the upstream vertex ( $H$  decay vertex) located downstream

	$m_H$ (MeV/c <sup>2</sup> )	C.L. $H$	C.L. $\Lambda K_S^0$
Event 1	$2217.1 \pm 7.1$	59.5%	$10^{-5}$
Event 2	$2224.3 \pm 8.4$	73.8%	0.38%

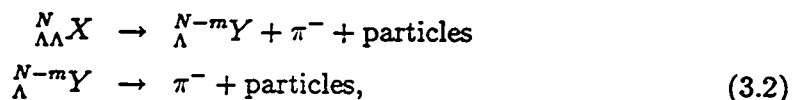
Table 3.2:  $H \rightarrow \Lambda p \pi^-$  Candidates Observed by Alekseev *et al.*

of the target where the  $H$  would be produced. To reject events caused by interactions of primary neutrons in the helium of the decay volume, the distance between the two  $V^0$ 's must be at least 4 cm. In addition to the  $H$  candidates, events with the  $V^0$  pairs  $\Lambda\Lambda$  and  $\Lambda K_S^0$  were identified and used to check the kinematic reconstruction. They require candidates for  $H \rightarrow \Lambda p \pi^-$  to have  $m(p\pi^-) = m_\Lambda \pm 11.5$  MeV/c<sup>2</sup> for the downstream vertex and  $m(p\pi^-) < m_\Lambda$  for the  $p\pi^-$  vertex, in accordance with the requirement  $m_H < 2m_\Lambda$ . It is necessary to reject  $\Lambda K_S^0$  events which satisfy the geometrical and mass cuts accidentally, because without particle identification  $K_S^0 \rightarrow \pi^+\pi^-$  can fake  $p\pi^-$  pairs with  $m(p\pi^-) < m_\Lambda$ . The events remaining after the topological and mass cuts are fit to both the  $\Lambda K_S^0$  and  $H \rightarrow \Lambda p \pi^-$  hypotheses. Two events from the carbon target were found with  $m(\Lambda p \pi^-) < 2m_\Lambda$  and confidence level for the  $H$  hypothesis  $> 1\%$ . One is inconsistent with the  $\Lambda K_S^0$  hypothesis, and the other has C.L.=0.38%. The fit results for the two events are given Table 3.2. These events may be suspected as background from neutron interactions in the target or scintillator veto counter because the coordinates of the  $H$  decay vertex are at the boundary of the target (Event 1) or inside the target (Event 2), but within  $1\sigma$  of the boundary. Using the observed  $\Lambda K_S^0$  events to normalize the flux of neutrons on the target, Alekseev *et al.* estimate the cross section for  $H$  production using the observed product  $\sigma_H \text{Br}_H P_H = 18$  nb/nucleus. Here  $\text{Br}_H$  is the branching ratio for  $H \rightarrow \Lambda p \pi^-$ , and  $P_H$  is the probability for the  $H$  to leave the target and be detected. To extract the cross section, they take  $\text{Br}_H = 25\%$  from [45], and compute  $P_H = 0.53$  using  $\tau_H = 6 \cdot 10^{-11}$  s, giving  $\sigma_H = 138$  nb for  $H$  production from Carbon nuclei. In addition they observe 67  $\Lambda\Lambda$  events; from the  $\Lambda\Lambda$  invariant mass distribution they see no evidence of a resonance above  $2m_\Lambda$ .

### 3.4 Double Hypernucleus Implications

A serious contender to rule out light  $H$ 's are double hypernucleus candidates. The existence of any double hypernucleus places a lower limit on the mass of the  $H$ , because a double hypernucleus, which has two  $\Lambda$ 's bound in the nucleus, can decay strongly to an ordinary nucleus and an  $H$ :  ${}^N_{\Lambda\Lambda}X \rightarrow {}^{N-2}X + H$ . Because it is a strong decay, any opportunity to detect the hypernucleus by its weak decay (pionic lambda decay in the nucleus) is excluded. The unambiguous observation of the weak decay of a double hypernucleus would exclude  $H$ 's lighter than  $2m_\Lambda - B_{\Lambda\Lambda}$ , where  $B_{\Lambda\Lambda}$  is the net binding energy of the  $\Lambda$ 's in the hypernucleus.

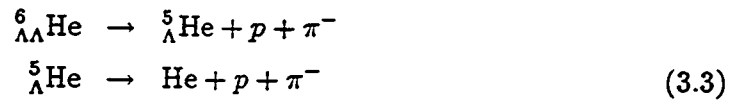
There have been two candidates for sequential weak decay of a double hypernucleus in the literature since 1963 [46, 47] and 1966 [48]; a new one was added in 1990 [49]. All three candidates are presumed to be produced by the capture of a  $\Xi^-$  onto a nucleus in an emulsion target exposed to  $K^-$  beams. The  $\Xi^-$  is produced in the emulsion by a  $K^-$  interaction, and comes to a stop in the emulsion before being captured by a nucleus of the emulsion. The reaction  $\Xi^- + p \rightarrow \Lambda + \Lambda$  produces only 28.5 MeV, and the resulting  $\Lambda$ 's can be captured onto a single nucleus producing a double hypernucleus. The sequential weak decay of the lambdas in the hypernucleus through pionic emission (also allowing for emission of other particles of net baryon number  $m$ ),



is observed by examining the emulsion for tracks and hypothesizing a decay chain. (In the 1990 event, the daughter hypernucleus,  $Y$ , undergoes a nonmesonic decay, where the pion from the decay of the  $\Lambda$  is reabsorbed in the nucleus.) The range of the particles provides an energy measurement, from which the consistency of the decay chain hypothesis may be verified and a binding energy for the double hypernucleus determined.

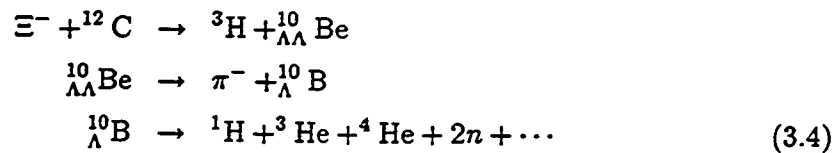
Danysz *et al.* reported the first event in an emulsion exposed at CERN [47]. After rejecting conventional explanations for the event they established the following hypothesis for the event. A  $\Xi^-$  is emitted from a  $K^-$  interaction star(A) coming to rest and being absorbed on  $^{12}\text{C}$  or  $^{14}\text{N}$  at another star(B), producing the double hypernucleus  $^{10}_{\Lambda\Lambda}\text{Be}$ . The  $^{10}_{\Lambda\Lambda}\text{Be}$  decays at a third star(C):  $^{10}_{\Lambda\Lambda}\text{Be} \rightarrow ^9_{\Lambda}\text{Be} + p + \pi^-$ . Finally the  $^9_{\Lambda}\text{Be}$  hypernucleus decays at a fourth star(D) to  $^4\text{He} + ^4\text{He} + p + \pi^-$ . They determine the binding energy of the double hypernucleus  $B_{\Lambda\Lambda} = (17.5 \pm 0.4)$  MeV. Dalitz *et al.* reported on a reexamination of the emulsion [50], confirming the interpretation advanced by Danysz *et al.* and finding  $B_{\Lambda\Lambda} = (17.7 \pm 0.4)$  MeV using an improved measurement of  $B_{\Lambda}$  for  $^9_{\Lambda}\text{Be}$  of  $(6.71 \pm 0.04)$  MeV instead of  $(6.50 \pm 0.16)$  MeV used in the original analysis.

In 1966 Prowse reported the second event found in an emulsion stack placed in a 4–5 GeV  $K^-$  beam at Brookhaven [48]. In this event a  $\Xi^-$  produced outside of the stack is captured on  $^{12}\text{C}$  producing  $^6_{\Lambda\Lambda}\text{He}$  and  $^7\text{Li}$ . The decay chain

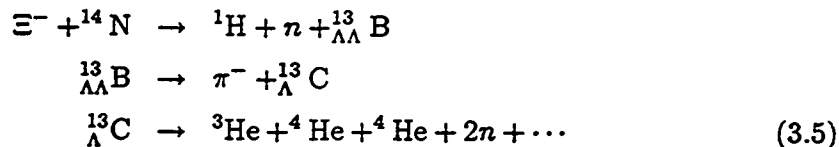


is established as the interpretation of the event. Prowse finds  $B_{\Lambda\Lambda} = (10.9 \pm 0.8)$  MeV.

The third event was found in 1990 [49] using the hybrid emulsion-counter detector of KEK-E176 (see Section 3.3.3). Out of 497  $\Xi^-$  candidates produced in the emulsion by the reaction  $K^- + p \rightarrow \Xi^- K^+$  and identified by tagging the out going  $K^+$ , Aoki *et al.* observe one candidate event consistent with the production and weak decay of a double hypernucleus. Their analysis excludes conventional interpretations, settling on two scenarios for the event, each consistent with the observed tracks in the emulsion. Scenario A,



and scenario B,



differ in the identification of the species of the hypernucleus. Note that in the second hypernucleus decay there is no pion emission. This complicates the analysis and Aoki *et al.* must rely on kinematic arguments to rule out a single hypernucleus decay followed by scattering at the second star. The  $B_{\Lambda\Lambda}$  of  ${}^{10}_{\Lambda\Lambda}\text{Be}$  and  ${}^{13}_{\Lambda\Lambda}\text{B}$  is  $(8.5 \pm 0.7)$  MeV and  $(27.6 \pm 0.7)$  MeV respectively. Scenario B is favored on theoretical grounds by Dover *et al.* [51], who also point out that the  ${}^{10}_{\Lambda\Lambda}\text{Be}$  hypothesis gives a binding energy for the same hypernucleus in disagreement with the Danysz *et al.* event.

The three events taken together could comprise convincing evidence that an  $H$  lighter than  $2m_{\Lambda} - B_{\Lambda\Lambda} \approx 2120$  MeV/ $c^2$  is excluded, but further consideration casts considerable doubt on the interpretation of these events. Dalitz *et al.* reviewed the two events extant in 1989 [50] to see if they were genuine double hypernuclear candidates and to assess their impact on the existence of the  $H$ . The review published an independent examination of the 1963 event undertaken by members of the original collaboration, which confirmed the original interpretation of the event as a  $S = -2$  hypernucleus. However, they found the observation of a double hypernucleus to be improbable in a Monte Carlo estimate. The emulsion was exposed to a total of 31,000 interactions of  $K^-$  mesons. From a MC estimate of  $10^5$  interactions producing 380  $\Xi^-$ , Dalitz *et al.* expect only 1% to stop inside the emulsion. For the exposure received, only one or two  $\Xi^-$  would be expected to be stopped. Accounting for the probability of capture onto a light emulsion nucleus ( $\sim 40\%$ ) and the branching ratio for pionic decay of a bound lambda ( $\sim 20\%$ ), they find the observation of a single event to be remarkable. They also report that in a later scanning of 40,000 interactions the collaboration found no other stopped  $\Xi^-$  tracks, consistent with expectations from the calculation. The experiment of Prowse is even less likely to have produced a stopped  $\Xi^-$  in the emulsion due to the higher beam energy ( $\sim 4.5$  GeV compared

Event	Year	Species	$B_{\Lambda\Lambda}$	$m_H$ (MeV/ $c^2$ )
Danysz	1963	$^{10}_{\Lambda\Lambda}\text{Be}$	$17.7 \pm 0.4$	$\geq 2213.7$
Prowse	1966	$^6_{\Lambda\Lambda}\text{He}$	$10.9 \pm 0.8$	$\geq 2220.5$
Aoki:A	1990	$^{10}_{\Lambda\Lambda}\text{Be}$	$8.5 \pm 0.7$	$\geq 2222.9$
Aoki:B	1990	$^{13}_{\Lambda\Lambda}\text{B}$	$27.6 \pm 0.7$	$\geq 2203.8$

Table 3.3: Three double hypernuclei candidates from [47, 48, 49]. The binding energy of the lambdas in the nucleus is given along with the lower limit implied for  $m_H$ . Both scenarios for the Aoki 1990 event are shown.

to 1.5 GeV). Given that Aoki *et al.* have recorded only one candidate with three orders of magnitude more  $K^-$  interactions ( $10^8$ ), the two earlier events are called into question. They calculate a probability of  $10^{-3}$  for the Danysz *et al.* event to be genuine by extrapolating from their single observed event from their 497  $\Xi^-$  tags and 80 stopping  $\Xi^-$  tracks; they assign a probability less than  $10^{-3}$  for the Prowse event [49].

The event reported by Aoki *et al.* has a  $K^+$  tag making the interpretation of the stopped track more certain than the earlier events, but the nonmesonic decay of the second lambda makes the interpretation of the decay chain less certain. As Klein points out [28], the decay topology of this event allows for the interpretation of the event as production and weak decay of an  $H$  bound in the nucleus.

If the events are taken at face value, they restrict  $m_H$  to be greater than limits shown in Table 3.3. However as there are only a few events and their interpretation is in question, to definitively rule out a lighter  $H$  seems premature.

### 3.5 Summary

With the exception of the lower limit on the mass of the  $H$  ( $m_H \geq 1875$  MeV/ $c^2$ ) from the absence of weak decays of nuclei, experimental results do not definitively rule out the existence of the  $H$  in their respective regions of parameter space, nor do they convincingly demonstrate its existence. The experiment of Carroll *et al.* set limits an order of magnitude above the expectations from phenomenology, and the

stopped antiproton experiments are beginning to probe on the level of the predictions. The KEK  $K^-$  beam experiments also are at the level of the theoretical predictions, and may continue to make progress in future runs. The candidates of Shahbazian *et al.* are unconvincing without a better understanding of background from less exotic reactions. Unconfirmed (and to many, unexpected) observations of multiple ( $S = -2$ ) dibaryon states do not add to the credibility of the candidate events. The two events of Alekseev *et al.* are consistent with background. The double hypernucleus candidates are on tenuous ground. An  $H$  heavier than  $2m_N$  is still within the realm of possibility.



## Chapter 4

### Experimental Method - BNL E888

This chapter describes one experiment designed to search for the  $H$ . An exhaustive search is difficult due to the unknown parameters of the  $H$ , particularly the varying lifetime and mass estimates. The E888 collaboration at Brookhaven National Laboratory (BNL) undertook two complimentary searches for the  $H$  dibaryon. For the first search we used a detector built to study rare  $K_L^0$  decays to search for decays of an  $H$  in the mass range  $\sim 2.09$  to  $2.21$   $\text{GeV}/c^2$  via the channel  $H \rightarrow \Lambda n$ , where the  $\Lambda$  is detected at high transverse momentum, and many  $\Lambda$  lifetimes away from the primary target. We then undertook a second search by inserting an active target of scintillator in the neutral beam and reconfiguring the detector to optimize for detection of a long-lived  $H$  via diffractive dissociation of  $H$ 's in the neutral beam at the active target:  $HA \rightarrow H^*A \rightarrow \Lambda\Lambda A$ . The dissociation search is sensitive to lighter  $H$ 's than the decay search, since the diffraction process allows the  $H$  to be excited to a higher mass state  $H^*$  which may lie above the  $2\Lambda$  threshold. The mass of the  $H$  itself may lie below the  $\Lambda N$  threshold. This second search is the subject of this dissertation. The first search is described in detail in reference [52].

The remainder of this chapter describes the experimental method used to undertake the dissociation search for the  $H$ . It was necessary to develop a plausible mechanism for  $H$  production which could be used to calculate the expected flux and momentum spectrum of  $H$  particles should they exist in our neutral beam. Also necessary is an estimate of the cross section for the diffractive dissociation process and

an understanding of the expected kinematic characteristics of the diffractively produced  $\Lambda\Lambda$ 's in order to define a signal. Of course, an identification and understanding of possible backgrounds is required. Finally, armed with these estimates, a detector design and experimental strategy can be developed and refined using Monte Carlo simulation.

## 4.1 $H$ Production

In both the decay and dissociation searches of E888 the  $H$  must be produced at the primary target of the neutral beam-line in the process  $p + A \rightarrow HX$ . In the decay search the target material was copper ( $A = \text{Cu}$ ), and the dissociation search used platinum ( $A = \text{Pt}$ ). In both cases the proton momentum was 24.1 GeV/ $c$  and the spectrometer viewed the target at a small nonzero angle ( $2.75^\circ$  decay,  $3.75^\circ$  dissociation).

Production of a complex state like the  $H$  is not easily calculated from first principles. Although QCD gives reasonably good predictions in agreement with experiment for high energy processes where single quark and gluon interactions dominate, calculations at low energy involving multiple quarks and exchange of many gluons have proven intractable and exceedingly difficult. Nonetheless progress has been made in hadronic physics using phenomenological models (often inspired by QCD) to calculate in approximation to the complete QCD theory. In the area of  $H$  production, estimates have been made using coalescence models in which a two baryon system (with the quantum numbers of the  $H$ ) produced in hadron-hadron collisions may coalesce into a bound state. This entails the approximation of the  $H$  as a baryon-baryon bound state.

### 4.1.1 Coalescence

Calculations of  $H$  production use the coalescence prescription, used to great effect in estimating deuteron production in hadron collisions [53, 54],  $\pi$ - $\mu$  atom formation in  $K_{\mu 3}$  decays [55, 56] and even anti-deuteron production in  $e^+e^-$  collisions [57]. In

coalescence models, two constituent particles fuse or coalesce to produce a bound state when the coalescence criteria are met. In a classical coalescence model the criterion is simply that the relative momentum of the two constituents be less than the scale momentum of the bound state,  $p_0$ , which is related to the binding energy. Quantum mechanical and field theoretical models employ more sophisticated criteria, but all models have a dependence on detailed nature of the bound state.

### *H* Coalescence Models

Badalyan and Simonov have used a coalescence type calculation to estimate the total *H* production cross section near threshold in  $p$ - $p$  collisions ( $p_p \approx 5$  GeV/ $c$ ) [33]. They consider production of two lambdas in the process  $pp \rightarrow \Lambda\Lambda K^+ K^+$  followed by coalescence of the two lambdas. They check their calculation by using it to compute the cross section ratio of  $\sigma(pp \rightarrow \pi^+ \pi^0 d)$  and  $\sigma(pp \rightarrow \pi^+ \pi^0 np)$  at threshold. They find good agreement with experiment and apply the calculation to the *H*. They calculate  $\sigma_H \approx 2 \cdot 10^{-3} \sigma_{\Lambda\Lambda} = 2$  nb, where they take  $\sigma_{\Lambda\Lambda}$  from an early *H* experiment [32].

Rotondo has computed a cross section for *H* production by coalescence of  $\Xi^0 n$  systems produced in  $p$ +Be collisions at Fermilab energies [58]. He parameterizes  $\Xi^0$  production data at 400 GeV as a function of rapidity and  $p_T^2$ . He then computes a "penalty factor" for the coalescence of a neutron onto another baryon, using deuteron production at similar energies as a guide. The calculation then assumes that *H* production is comparable to the formation of a  $\Xi^0 n$  nucleus:  $\sigma_H = F_1 F_2 \sigma_{\Xi^0 n}$ .  $F_1$  accounts for the possibility of other channels for *H* production other than  $\Xi^0 n$ . If each of the baryon baryon channels ( $\Lambda\Lambda, \Sigma^0 \Sigma^0, \Sigma^+ \Sigma^-, \Xi^- p$ ) contributes equally,  $F_1 \sim 4$ . The factor  $F_2$  represents the difference between a  $\Xi^0 n$  nucleus and the *H*. Rotondo estimates the effect of a smaller *H* radius compared to a deuteron like  $\Xi^0 n$  nucleus to be  $\sim \frac{1}{8}$ . Because the factors  $F_1$  and  $F_2$  can not be calculated with great precision and the simple arguments above indicate that  $F_1 F_2 \sim 1$ , he assumes results for the  $\Xi^0 n$  nucleus apply to the *H*, finding  $\sigma_H = 1.2 \mu\text{b}$ .

Neither calculation is directly applicable to the situation in our experiment ( $p_p = 24.1$  GeV/ $c$ ), so two members of this collaboration undertook a calculation [59, 60]

where inclusive lambda production data is used to estimate  $H$  production rates in three similar coalescence models. After establishing a common framework for these coalescence models in the next section, we give the details of the calculation and discuss the results in comparison to the other predictions.

### General coalescence considerations

A coalescence model relates the two particle density for producing unbound states,  $d^6 N_{12}/d\mathbf{p}_1 d\mathbf{p}_2$ , to the density of bound states,  $d^3 N_b/d\mathbf{P}$ , by including the probability that the two particles coalesce into a bound state and integrating over all configurations of the two particle system. The physics of a coalescence model is simply phase space and statistics. In a simple classical coalescence model, the particles may be taken to coalesce if their relative momentum has magnitude less than some critical value  $p_0$ . The integral over phase space reduces to the volume of a sphere in relative momentum space with radius  $p_0$ . It is reasonable to treat the motion of the two particles non-relativistically given the small momentum scale  $p_0$ , with the addition of the Lorentz factor  $\gamma = \sqrt{1 + P^2/m^2}$  to account for phase space contraction due to relativistic boost of the bound state system.

$$\frac{dN_b^3}{d^3\mathbf{P}} = f_s \gamma \frac{4\pi}{3} p_0^3 \frac{d^6 N_{12}}{d^3\mathbf{P} d^3\mathbf{p}} \Big|_{\mathbf{p}=0} \quad (4.1)$$

Here  $\mathbf{P} = (\mathbf{p}_1 + \mathbf{p}_2)$  is the momentum of the bound state, and  $\mathbf{p} = (\mathbf{p}_1 - \mathbf{p}_2)/2$  is the relative momentum of the two coalescing particles. Also included is a spin factor  $f_s$  to account for the correct spin alignment. The two particle density may be evaluated at  $p = 0$ , or in an extension to this model it may be integrated over relative momenta up to  $p = p_0$ . Cousins and Klein treat both the simple model and the classical integration model in [59].

Quantum mechanically, the coalescence probability may be taken as the overlap of the bound state wavefunction with the two particle state. It is easy to show that this reduces to the value of the coordinate space wavefunction at the origin times  $(2\pi)^3$  if one uses the momentum space representation for the overlap matrix element in the approximation that the unbound density is constant for small relative momentum  $p$ ,

and may be evaluated at  $p=0$ .

$$\frac{d^3 N_b}{d^3 \mathbf{P}} = f_s \gamma (2\pi)^3 |\psi_b(\mathbf{r} = 0)|^2 \frac{d^6 N_{12}}{d^3 \mathbf{P} d^3 \mathbf{p}} \Big|_{\mathbf{p}=0} \quad (4.2)$$

The classical model gives the same result as the quantum mechanical model when  $p_0$  replaced by  $3.9|\psi_b(\mathbf{r} = 0)|^{2/3}$ . The difference is only in the name of the bound state parameter, either a scale momentum or a wavefunction value at the origin. For convenience, Cousins and Klein give results in terms of the parameter  $p_{rms}$  which is the average ( $\sqrt{\langle p^2 \rangle}$ ) of the relative momentum of the particles in the bound state. For the classical model with a  $p$ -space wavefunction vanishing for  $p > p_0$  and constant for  $p \leq p_0$ ,  $p_{rms} = p_0/1.80$ . For a gaussian wavefunction for the bound state,  $p_{rms} = 2.17|\psi(0)|^{2/3}$ .

In addition to information about the bound state, coalescence models also rely on information about the unbound two particle distributions ( $d^6 N/d^3 \mathbf{p}_1 d^3 \mathbf{p}_2$ ). In the case of  $\pi$ - $\mu$  atoms from  $K_L^0$  decay, the particle distributions are measured in the Dalitz plot for the decay  $K_L^0 \rightarrow \pi\mu\nu$ . The bound state is assumed to be well modeled by quantum mechanics and the Coulomb forces between the "nucleus" and "electron". For the deuteron, the force arises from the strong interaction, but the wavefunction of the deuteron essentially contains all the information needed about the bound state, and this is well measured despite the difficulty of deriving this information from first principles. The two particle densities are approximated as the product of single particle (neutron and proton) densities, or even as the square of the proton density. For the deuteron this approximation that

$$\frac{d^6 N}{d^3 \mathbf{p}_1 d^3 \mathbf{p}_2} = \frac{d^3 N_1}{d^3 \mathbf{p}_1} \frac{d^3 N_2}{d^3 \mathbf{p}_2} \quad (4.3)$$

assumes that there is no correlation between the neutron and proton densities, an approximation justified by the agreement of the coalescence prediction and experiment. In the case of the  $H$  we are left with no information about the wavefunction, and no experimental data on the two particle density. We choose to parameterize our ignorance about the  $H$  wavefunction by treating the scale momentum  $p_{rms}$  as a parameter

of the model, varying it through reasonable values. For the two particle density we are forced to approximate this from single lambda production data because there is no experimental data on the production of baryon-baryon systems with the quantum numbers of the  $H$ . As for the deuteron, the two particle density is taken from Eq. 4.3, but it is not clear that inclusive lambda production data can be used (effectively twice in each interaction) because of the difficulty of producing two strange baryons.

### Calculational details

Due to the lack of experimental measurements of the two particle density, Cousins and Klein use inclusive lambda production data from a bubble chamber experiment for the single particle densities. Blobel *et al.* [61] measure the differential cross section for  $\Lambda$  production in  $pp$  collisions at 24 GeV/c, but to make use of this data, some reduction of the bubble chamber data is necessary.

First the  $pp$  data must be scaled to correct for the  $A$  dependence in the cross sections. To go from  $p+p$  to  $p+Pt$  collisions, they scale by the ratio of total inelastic cross sections. Although crude, this is a better scaling than one based on fits to a power law for the  $A$  dependence because of the well known problem extrapolating to or from  $A = 1$  using a power law. For example, the Particle Data Group's compilation [62] of high-energy total inelastic cross sections for  $p$ -nucleus collisions are well fit by  $\sigma_I = 0.0425 \times A^{0.70}$  b. But this formula overestimates the actual  $pp$  inelastic cross section (0.033 b) by 29% for  $A = 1$ . The correction factor for platinum from the ratio of the PDG values for high-energy total inelastic cross sections is  $1.708/0.033 = 51.8$ . Although the 24.1 GeV/c beam momentum is below the range of validity for the PDG data (60-375 GeV/c), the total inelastic cross section is energy independent to a good approximation for momenta between 10 and  $\sim 300$  GeV/c.

To use the inclusive *single* lambda production data to estimate *double* lambda production, Cousins and Klein consider the inclusive production of two lambdas,

$$p_1 + p_2 \rightarrow \Lambda_1 \Lambda_2 X, \quad (4.4)$$

where  $p_1$  and  $p_2$  are the beam and target protons, and where  $\Lambda_1$  and  $\Lambda_2$  are predominantly associated with beam fragmentation at  $x > 0$  and target fragmentation at  $x < 0$  respectively. In so doing they neglect problems of quantum mechanical indistinguishability of identical particles and assume that it is meaningful semiclassically to have separate cross sections for  $\Lambda_1$  and  $\Lambda_2$ , which are reflected in  $x$  about  $x = 0$  with respect to one another. So that,

$$E_1 \frac{d^3\sigma_{\Lambda_1}}{d^3p_1}(x_1, p_{T_1}) = f(x_1, p_{T_1}) \quad (-1 \leq x \leq 1), \quad (4.5)$$

and using the same function  $f$ ,

$$E_2 \frac{d^3\sigma_{\Lambda_2}}{d^3p_2}(x_2, p_{T_2}) = f(-x_2, p_{T_2}). \quad (4.6)$$

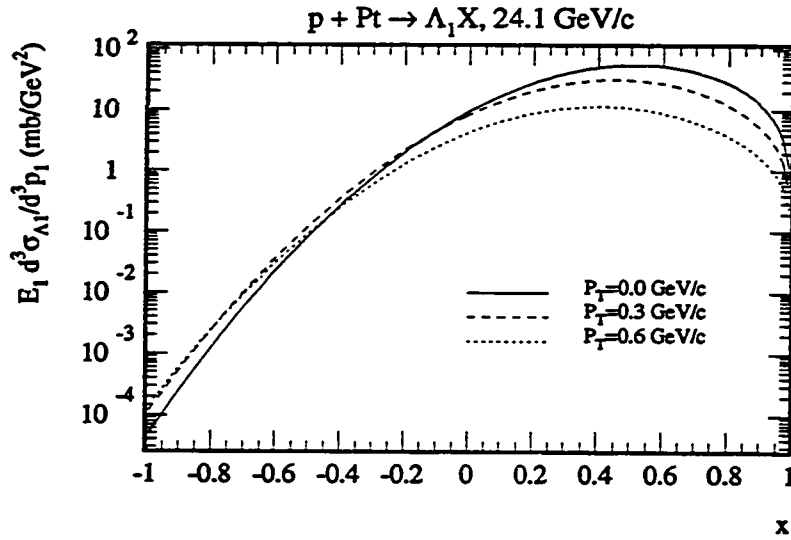
$\Lambda_1$  production includes the leading particle effect in the direction of  $p_1$ , where  $\Lambda_1$  may carry two of the three quarks of the beam proton. The model extends the association of  $\Lambda_1$  with  $p_1$  to small and even negative  $x$ , and at  $x = 0$  half of the inclusive  $\Lambda$  production is assigned to  $\Lambda_1$ . Although the separation of leading target particles breaks down at small  $x$ , it is reasonable to assign non-zero values for  $\Lambda_1$  production at negative  $x$  as long as the production smoothly decreases as  $x$  becomes more negative. The function  $f$  is determined from the data for inclusive lambda production, which is the sum of  $\Lambda_1$  and  $\Lambda_2$  production:

$$E \frac{d^3\sigma_{\Lambda}}{d^3p}(x, p_T) = f(x, p_T) + f(-x, p_T). \quad (4.7)$$

In their model  $pp \rightarrow \Lambda X$  data at 24 GeV/c are fit to the physically inspired form for the differential cross section used by Skubic *et al.* [63] to fit inclusive spectra in 300 GeV/c  $pp$ -interactions (for  $-0.2 \leq x \leq 1$ ). The use of the following form constrains the shape of  $f(x, p_T)$  and ensures a smooth decrease for  $x < 0$ :

$$E \frac{d^3\sigma}{d^3p} = f(x, p_T) = \exp(c_1 + c_2 x^2 + c_3 x + c_4 x p_T + c_5 p_T^2 + c_6 p_T^4 + c_7 p_T^6) (1 - x)^{(c_8 + c_9 p_T^2)}. \quad (4.8)$$

$c_1$	$c_2$	$c_3$	$c_4$	$c_5$	$c_6$	$c_7$	$c_8$	$c_9$
-1.71	-5.42	7.51	-3.40	-0.88	-4.83	3.12	0.91	-0.76

Table 4.1: Best Fit Parameters for Inclusive  $\Lambda$  Production to Eq. 4.8Figure 4.1:  $f(x, p_T)$  plotted as a function of  $x$  for  $p_T = 0.0, 0.3, 0.6$  GeV/c

The resulting fit parameters ( $c_1 \dots c_9$ ) are given in Table 4.1, and  $f(x, p_T)$  is plotted versus  $x$  for representative values of  $p_T$  in Figure 4.1.

With  $f(x, p_T)$  determined from  $pp \rightarrow \Lambda X$  data, they proceed to calculate spectra. In converting from lab momenta to  $x_F = p_z^*/p_{z\max}^*$  they use the value  $p_{z\max}^* = 3.04$  GeV/c to be consistent with production of the  $H$  with additional particles as required by strangeness and 4-momentum conservation.

The overlap of the flavor wave function of the  $H$  with  $\Lambda\Lambda$  must be taken into account. Equation 4.9 gives the  $H$  flavor wavefunction in the baryon-baryon basis,



following Donoghue *et al.* [29].

$$H = \frac{1}{\sqrt{8}}(\Lambda\Lambda + \Sigma^0\Sigma^0 + \Sigma^+\Sigma^- + \Sigma^-\Sigma^+ + p\Xi^- + \Xi^-p + \Xi^0n + n\Xi^0) \quad (4.9)$$

Including a factor of 1/8 for the flavor wave function of the  $H$  and dividing by a factor of  $\sigma_{\text{abs}}$ , the beam-target absorption cross section, to avoid double counting the probability of the beam particle hitting the target particle, the cross section for  $H$  production is

$$\frac{d^3\sigma_H}{d^3\mathbf{P}_H} = \frac{1}{4} \frac{1}{8} \gamma (2\pi)^3 |\psi(\mathbf{r} = 0)|^2 \frac{d^3\sigma_{\Lambda 1}}{d^3\mathbf{P}_1} \Big|_{\mathbf{p}_1 = \mathbf{P}_H/2} \frac{1}{\sigma_{\text{abs}}} \frac{d^3\sigma_{\Lambda 2}}{d^3\mathbf{P}_2} \Big|_{\mathbf{p}_2 = \mathbf{P}_H/2}. \quad (4.10)$$

The equation above gives the QM estimate and the simplest classical estimate for  $p_0 = 3.9|\psi(0)|^{2/3}$ . Both of these are obtained by evaluating the two particle density at  $p = 0$ , which assumes the density does not change for  $p < p_0$ . The classical integration estimate avoids this assumption at the expense of using an unrealistic wavefunction by integrating the two particle density from  $p = 0$  to  $p = p_0$ , instead of multiplying the density at  $p = 0$  by  $(4/3)\pi p_0^3$ .

## Results

Given a value for  $p_{\text{rms}}$  one can then find invariant cross section estimates for  $H$  production. The cross section goes as  $p_{\text{rms}}^3$ , and the total cross section is plotted vs  $p_{\text{rms}}$  in Fig. 4.2. The cubic rise of the total cross section with  $p_{\text{rms}}$  is clearly visible for the QM model. The Classical Integration model shows a reduction for larger values of  $p_{\text{rms}}$ , as the assumption of constant density of states for  $p < p_{\text{rms}}$  breaks down. For reasonable values of the scale momentum, the cross section is well below 0.1 mb.

Besides the total cross section for  $H$  production, the differential cross section and the momentum spectrum at a particular angle in the lab frame is useful in the design and interpretation of our experiment. The differential cross section at 65 mrad (the targeting angle used in the dissociation search) is given as a function of  $p_{\text{rms}}$  in Figure 4.3. Figure 4.4 gives the momentum spectrum at 65 mrad in both models for a typical scale momentum:  $p_{\text{rms}} = 150 \text{ MeV}/c$ . Typical of the distributions is a

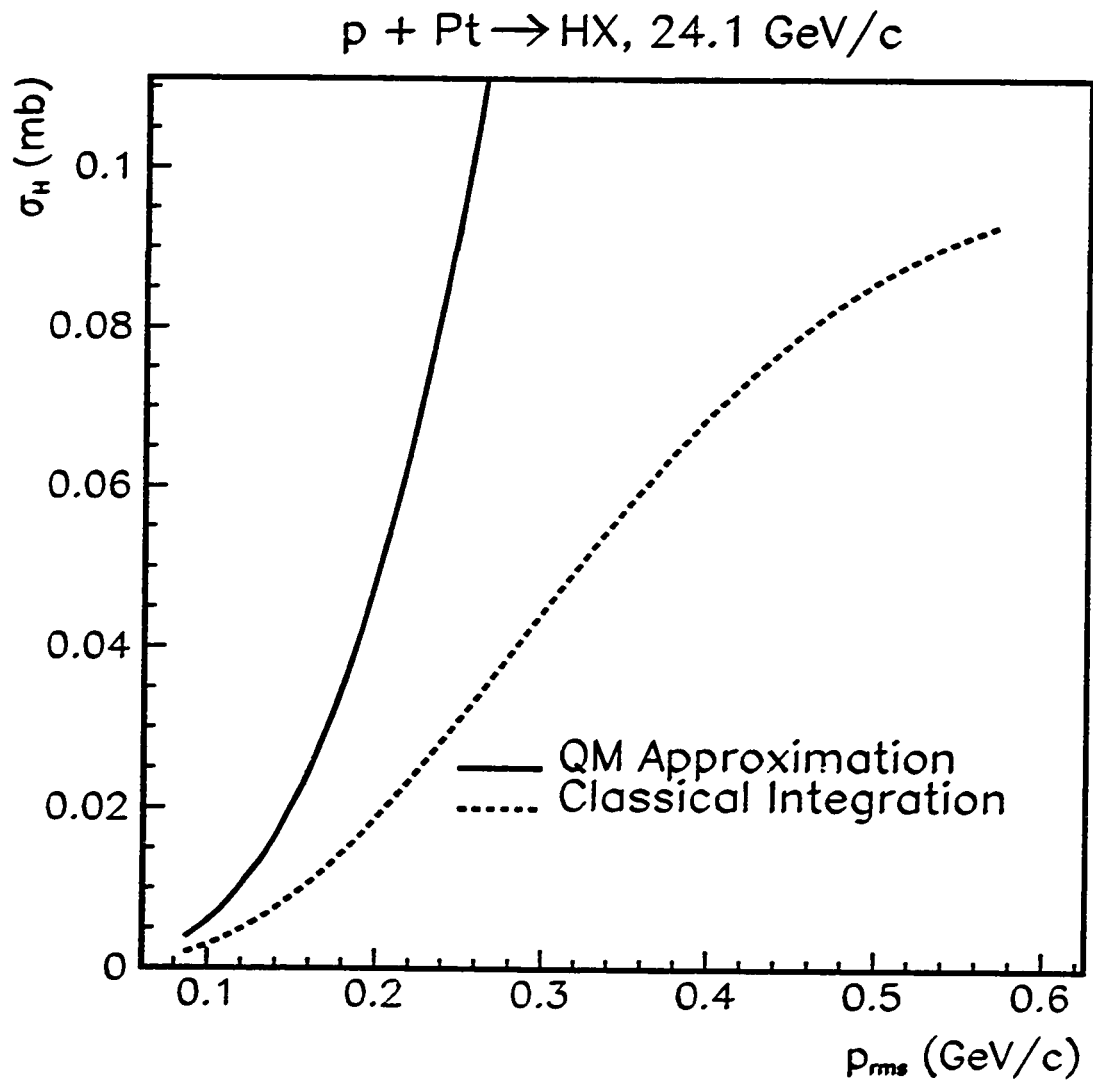
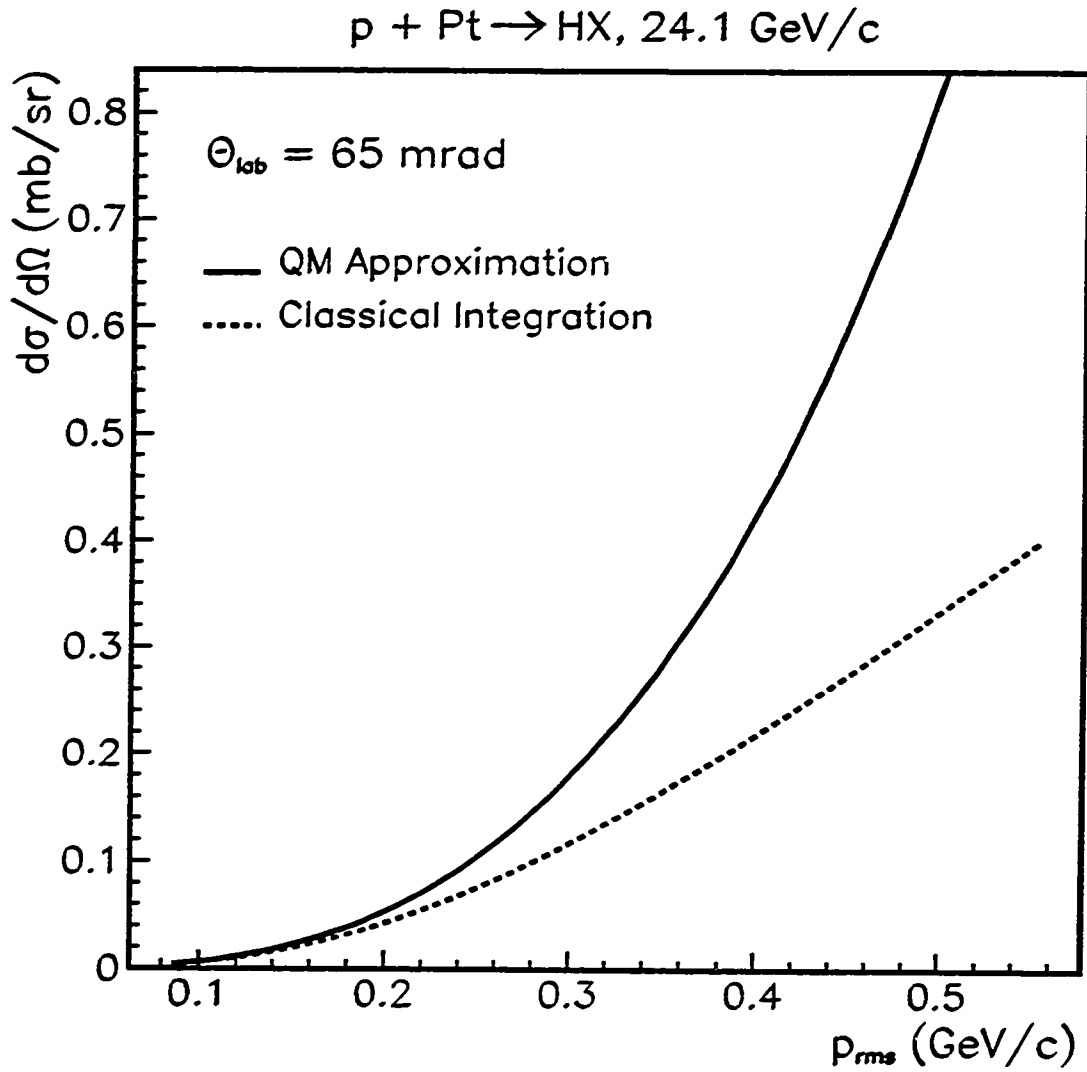


Figure 4.2: Total cross section for  $H$  production versus  $p_{rms}$ .

Figure 4.3: Differential Cross Section for  $H$  Production at 65 mrad

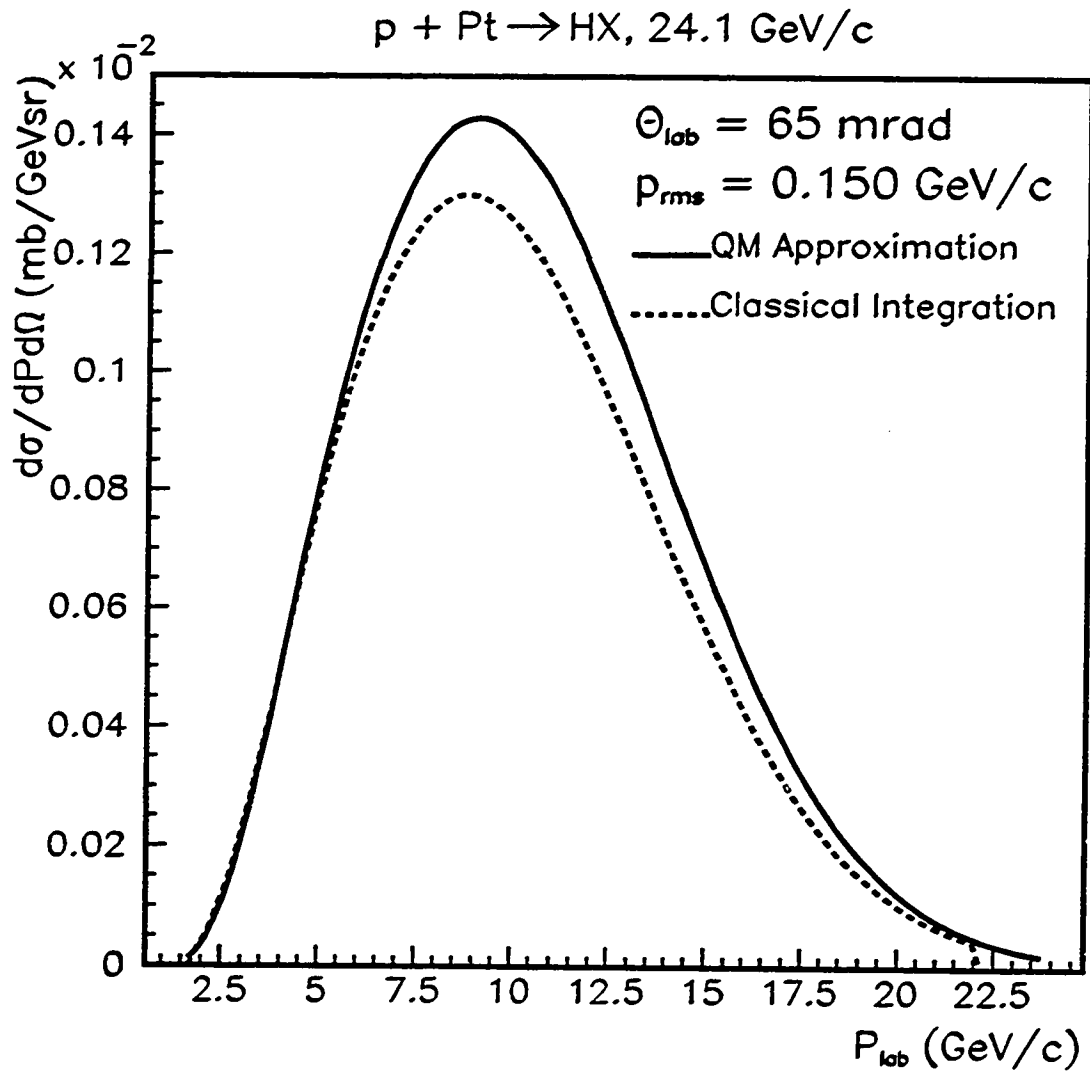


Figure 4.4:  $d\sigma_H/dp_H d\Omega$  at 65 mrad. Quantum Mechanical and Classical Integration models with  $p_{rms} = 150 \text{ MeV}/c$ .

peak near the central momentum of  $\sim 8$  GeV/c, with tails extending forward and backward in the center of momentum frame.

### Comparison

Our estimates for  $H$  production may be compared with the calculation of Rotondo [58] and the calculation of Badalyan and Simonov [33]. Because Badalyan and Simonov's estimate was made close to threshold and Rotondo's estimate was made at high-energy, it is easier to compare if we factor out the cross section for production of  $\Lambda\Lambda$  states:  $\sigma_H = P_{\text{coal.}}\sigma_{\Lambda\Lambda}$ . The low energy calculation gives  $P_{\text{coal.}} = 4 \cdot 10^{-3}$ , and Rotondo's calculation uses a coalescence probability of  $1/1350 = 0.74 \cdot 10^{-3}$ . The Cousins Klein model has a coalescence probability of  $1-10 \cdot 10^{-3}$  depending on the choice of  $p_{\text{rms}}$ . Put in this way all three estimates are comparable.

There is also a recent coalescence calculation from Cole *et al.* [64] which uses a nuclear cascade model (RQMD) to predict the two particle density for  $\Lambda\Lambda$  and  $\Xi N$  in  $p$ -A collisions at 28.4 GeV/c. On an event by event basis they apply a particular coalescence criterion which works for deuteron production ( $p_{\text{max}} = 110$  MeV/c and  $\Delta r < 3$  fm) to space and momentum four vectors generated by the RQMD Monte Carlo.  $\Lambda\Lambda$  and  $\Xi N$  pairs which pass the coalescence cuts are used to predict  $H$  production. Their results for  $p$ -Au collisions are the most applicable to our Pt target. They find  $P_{\text{coal.}} = 1.2 \pm 0.4 \cdot 10^{-3}$  for  $\Lambda\Lambda$ . They also include  $\Xi^0 n$  ( $P_{\text{coal.}} = 0.6 \pm 0.2 \cdot 10^{-3}$ ) and  $\Xi^- p$  ( $P_{\text{coal.}} = 0.4 \pm 0.18 \cdot 10^{-3}$ ) pairs in the estimate for  $H$  production giving a net cross section of  $8.5 \cdot 10^{-5} \sigma_{\text{inelas.}} = 0.15$  mb.

### Summary

The results of the coalescence calculation demonstrate a feasible mechanism for the production of the  $H$  dibaryon in  $p$ -A collisions, although there are a number of uncertainties due to our lack of knowledge about the precise nature of the  $H$  (should it exist) and due to the absence of experimental data on the production of doubly strange, baryon number equal two systems. The model also provides a momentum spectrum and angular distribution which are helpful in designing an experiment and

interpreting the results.

## 4.2 $H$ Dissociation

We now have some assurance that there may be  $H$ 's in our neutral beam, but that is not enough. We must also be able to detect them. Our plan was to do so by detecting their diffraction dissociation to two lambdas when they interact in a target placed in the neutral beam.

Estimating the cross section for diffractive dissociation of a completely new type of particle is clearly a non-trivial exercise. The possibility that the  $H$  is totally unlike other hadrons makes any estimate subject to a high degree of uncertainty, but some expectations from phenomenology of hadronic interactions in the diffractive regime can still be useful. Based on an understanding of hadronic interactions from phenomenology, we estimate the cross section for  $H$  diffraction dissociation in three different ways. An added uncertainty is the binding energy/mass of the  $H$ . In the three calculations the cross section varies through similar ranges as a function of the  $H$  mass.

### 4.2.1 Diffraction Phenomenology

Goulios gives a review of diffractive interactions in [65]. Although the phenomenological theories are more appropriate to high energy interactions, diffraction dissociation phenomenology can be meaningful when applied to low energy reactions.

In a diffractive dissociation interaction (illustrated schematically in Fig. 4.5) two hadrons undergo a glancing, low momentum transfer interaction in which one particle is left intact by the process, and the other is excited to a higher mass virtual state which then decays strongly. An example would be  $np \rightarrow p\pi^-p$ , where the first proton and the  $\pi$  are associated with fragmentation of the beam neutron, and the recoiling target proton carries little kinetic energy from the low momentum transfer interaction.

Such reactions are observed in hadron hadron collisions from low energy on out to the highest energies yet attained in the laboratory. The characteristics of diffraction

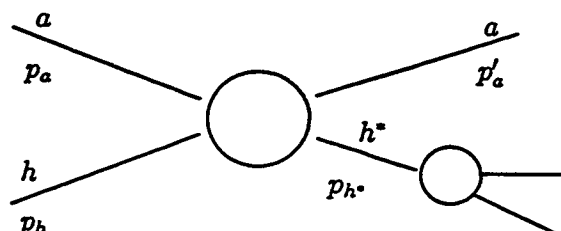


Figure 4.5: Diffraction Dissociation:  $ha \rightarrow h^*a$ . Two hadrons scatter. One ( $h$ ) is excited to a higher mass state ( $h^*$ ) which subsequently decays strongly.

dissociation observed in experiment are small momentum transfer, distribution in invariant mass of the excited hadron which falls as  $1/M_{\text{diff}}^2$  and weak dependence on beam energy and type of hadron dissociating.

#### $t$ distribution

Diffraction Dissociation is characterized by a small momentum transfer interaction, followed by breakup of one or the other particle. The square four-momentum transfer,  $t = (p_h - p_{h^*})^2$ , is typified by an exponential falloff,

$$d\sigma/dt \sim \exp(-b|t|), \quad b \sim 9 \text{ GeV}^{-2}. \quad (4.11)$$

The slope,  $b$ , is independent of beam particle [66], slightly dependent on energy, and mainly determined by the effective size of the target particle. For nucleon targets and beam momenta of order  $10 \text{ GeV}/c$ ,  $b \sim 10 \text{ GeV}^{-2}$ . Nuclear targets give a much steeper falloff with momentum transfer. It is this exponential falloff with momentum transfer resulting in forward scattering of the beam which gives diffraction dissociation its characteristic *diffractive* character in analogy with optics.

#### Invariant mass spectrum

The dissociation part of diffractive *dissociation* describes the fragmentation of one of the hadrons. For high mass diffractive states, the spectrum of invariant mass for the

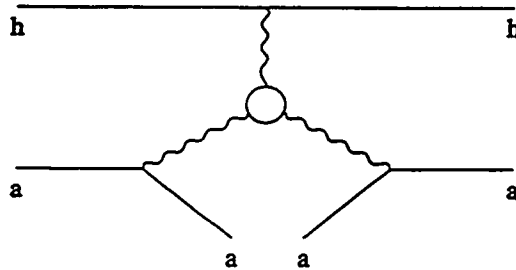


Figure 4.6: Triple Pomeron Exchange Picture of Diffraction Dissociation

fragmentation system falls as  $1/M_{\text{diff}}^2$ . Near threshold there are phase space effects (which reduce the low mass peak) and often resonant diffractive excitation events. As an example of the latter consider  $np \rightarrow N^*p \rightarrow p\pi^-p$ , where the dissociating neutron is excited to a resonance  $N^*$  which then decays to  $p\pi^-$ . Despite these separate regimes in diffraction dissociation (excitation and non-resonant dissociation), a result from phenomenology unifies the two behaviors.

The phenomenological model of elastic scattering and diffractive interactions of hadrons treats the interactions as the exchange of Pomerons, which are Regge trajectories with the quantum numbers of the vacuum. In this model diffraction dissociation is understood as a triple pomeron diagram (c.f. Fig. 4.6), and elastic scattering is understood as a single Pomeron exchange. Within the context of this model, there is a Finite Mass Sum Rule (FMSR), which states that the average behavior of  $d\sigma/dM_{\text{diff}}^2$  is exactly what would be expected by extrapolating from high  $M_{\text{diff}}^2$ . The resonances and elastic scattering at small  $M^2$  are completely equivalent to the triple Pomeron exchange when “averaged” out. This triple Pomeron exchange gives a  $1/M^2$  dependence for the cross section. The departure from the expected  $1/M^2$  behavior at low mass is understood as the resonant production of higher mass states (diffractive excitation), e.g.  $N^*$  for p diffraction etc. At very low invariant mass there is a threshold effect due to shrinking phase space. The FMSR shows that the sum of elastic scattering and the resonant behavior is equivalent to the treatment in terms of triple Pomeron



exchange.

The precise statement of the FMSR is given in terms of the kinematic variable  $\nu = M_{\text{diff}}^2 - M_h^2 - t$  instead of  $M^2$  directly.

$$|t| \frac{d\sigma_{\text{el}}}{dt} + \int_0^{\nu_0} \nu \frac{d^2\sigma}{dt d\nu} d\nu = \int_0^{\nu_0} \nu \left( \frac{d^2\sigma}{dt d\nu} \right)_{\text{fit}} d\nu \quad (4.12)$$

Here the subscript "fit" denotes a fit to high  $\nu$  ( $\nu > \nu_0$ ) behavior for the cross section, and  $\nu_0$  must be large enough to lie beyond the resonance region. According to Regge phenomenology and experiment,  $\nu d^2\sigma/dt d\nu$  becomes a constant for  $\nu > \nu_0$ .

### Kinematics

Consider the diffraction dissociation of an  $H$  on a nuclear target  $A$ :  $HA \rightarrow H^*A' \rightarrow \Lambda\Lambda A'$ . Here  $A'$  denotes the recoiling but still intact nucleus. The square four-momentum transfer is taken between incoming and outgoing particles:

$$t = (p_H - p_{H^*})^2 = (p_A - p_{A'})^2. \quad (4.13)$$

If the right hand side is evaluated in the lab frame where the target is at rest,  $t$  has a particularly simple form:

$$t = -2m_A(E_{A'} - m_A) = -2m_A K_{A'}. \quad (4.14)$$

Thus by measuring the kinetic energy,  $K_{A'}$ , of the recoiling target,  $t$  is easily obtained. Like  $t$ ,  $K_{A'}$  also has an exponentially falling distribution. For a proton target with  $b = 9 \text{ GeV}^{-2}$  the scale recoil energy is 60 MeV.

By combining a measurement of  $t$  (from the recoil kinetic energy) with spectrometer measurements of the  $\Lambda\Lambda$  system, it is possible to deduce the mass of the  $H$ . Beginning with the definition of  $t$  we have

$$t = (p_H - p_{H^*})^2 = m_H^2 + m_{H^*}^2 - 2E_H E_{H^*} + 2\mathbf{p}_H \cdot \mathbf{p}_{H^*}. \quad (4.15)$$

The right hand side may be evaluated by using the reconstructed  $\Lambda\Lambda$  vertex and the

primary target to define a direction for the incoming  $H$  (taken to be the  $z$ -axis). Four momentum conservation gives the energy and momentum of the  $H$  in terms of the  $\Lambda\Lambda$  and the recoil quantities. Solving Eq. 4.15 for  $m_H^2$  and replacing  $t$  with  $-2m_A K_{A'}$  we have,

$$m_H^2 = -2m_A K_{A'} + m_{\Lambda\Lambda}^2 + 2E_{\Lambda\Lambda} K_{A'} - 2\mathbf{p}_{\Lambda\Lambda} \cdot \mathbf{p}_{A'}. \quad (4.16)$$

Even without measuring the angle of recoil, the last term may be evaluated by imposing the constraint of transverse momentum conservation:  $\mathbf{p}_{\Lambda\Lambda} \cdot \mathbf{p}_{A'} = -p_T^2 + p_{\Lambda\Lambda}^z p_{A'}^z$ . The  $z$ -components are easily obtained by removing  $p_T$ .

$$p_{\Lambda\Lambda}^z = \sqrt{p_{\Lambda\Lambda}^2 - p_T^2}; \quad p_{A'}^z = \sqrt{K_{A'}^2 + 2m_A K_{A'} - p_T^2} \quad (4.17)$$

With these substitutions we are left with

$$m_H^2 = m_{\Lambda\Lambda}^2 + 2p_T^2 - 2\sqrt{p_{\Lambda\Lambda}^2 - p_T^2} \sqrt{K_{A'}^2 + 2m_A K_{A'} - p_T^2} + 2K_{A'}(E_{\Lambda\Lambda} - m_A). \quad (4.18)$$

### 4.2.2 Simple Breakup Model

A simple estimate of the  $H$  dissociation cross section is based on elastic scattering of constituent  $\Lambda$ 's. In this model, the  $H$  is considered a baryon-baryon bound state which dissociates when one of the lambdas undergoes a scatter with sufficient momentum transfer to unbind the state. The minimum momentum transfer for dissociation is a function of binding energy and incident momentum. The minimum four-momentum transfer magnitude is

$$t_{\min} \approx - \left( \frac{M_{\Lambda\Lambda}^2 - M_H^2}{2p_{\text{lab}}} \right)^2. \quad (4.19)$$

The above approximation is valid when the energy transfer is negligible. When one of the two lambdas in the  $H$  undergoes a scatter with a four momentum magnitude larger than  $|t_{\min}|$  for  $M_{\Lambda\Lambda} = 2m_\Lambda$ , the  $H$  dissociates.

The elastic scattering cross section for  $\Lambda p$  is parameterized as  $d\sigma/dt = A \exp(bt)$  and fit to data at  $p = 6-17$  GeV/c by Anderson *et al.* [67]. They find  $b = 7.2$  GeV<sup>-2</sup> and  $A = 29.5$  mb/GeV<sup>2</sup>. To get the dissociation cross section, we integrate over  $t$  up to  $t_{\min}$  multiplying by 2 to allow either lambda to scatter and an overall factor of 1/8

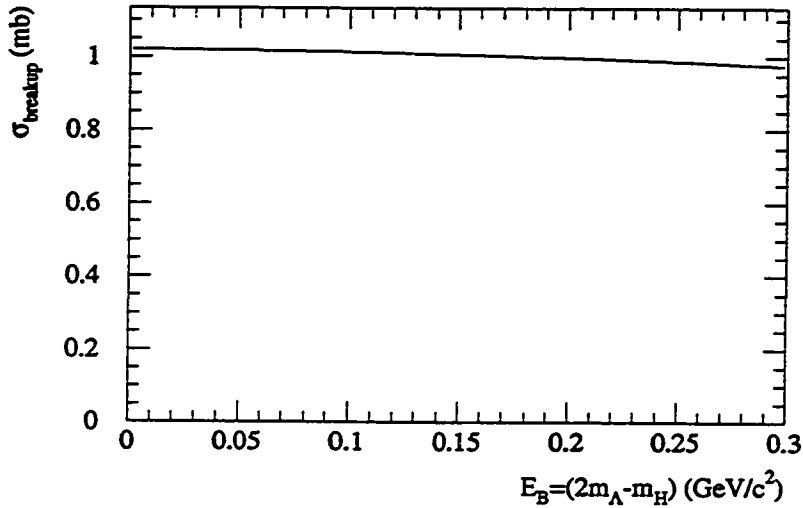


Figure 4.7: Breakup Model Dissociation Cross Section

from the overlap of the  $H$  baryon-baryon wavefunction with  $\Lambda\Lambda$  (*c.f.* Eq. 4.9).

$$\sigma_H = \frac{2}{8} \int_{-\infty}^{t_{\min}} A \exp(bt) dt = \frac{1}{4} \frac{A}{b} \exp(bt_{\min}). \quad (4.20)$$

Figure 4.7 plots the result as a function of binding energy of the  $H$ ,  $E_B = 2m_\Lambda - m_H$ . It remains nearly constant at 1 mb for the range of binding energy applicable to the  $H$ . In determining  $t_{\min}$ ,  $p_{\text{lab}}$  is taken to be 8.0 GeV/ $c$ , which is the peak momentum from our coalescence calculation and the momentum of a centrally produced  $H$  in the lab frame. The breakup model calculation is an upper bound because it does not consider the possibility that the  $H$  remains bound after the lambda scatters. It also considers the scattering of the two lambdas independently without accounting for screening of one by the other. This last defect is corrected in the next model, based on a model developed for deuteron scattering.

### 4.2.3 Glauber Model

An improvement to the simplistic picture of the breakup model takes advantage of a calculation by Franco and Glauber [68, 69]. They considered deuteron scattering in a high-energy approximation for small scattering angles which allowed scattering in the two-particle system to be calculated in a reasonably simple and accurate way. The definition of high-energy in this context is that the wavelength of the incident particle be small compared to its range of interaction with the nucleons in the deuteron. The optical analogue is Fraunhofer Diffraction. Under this condition a semi-classical treatment of the scattering is valid.

An incoming plane wave,  $\psi = \exp(i\mathbf{k} \cdot \mathbf{r})$ , is scattered by a small angle with negligible energy transfer to the deuteron. The outgoing particle state has wave-vector  $\mathbf{k}'$ , with the same energy as the incident wave. The amplitude for scattering from a single nucleon is given by

$$f(\mathbf{k}', \mathbf{k}) = \frac{ik}{2\pi} \int \exp [i(\mathbf{k} - \mathbf{k}') \cdot \mathbf{b}] \{1 - \exp[i\chi(\mathbf{b})]\} d^2\mathbf{b}, \quad (4.21)$$

where the integral is over impact parameters,  $\mathbf{b}$ , and  $\chi(\mathbf{b})$  is a complex-valued phase shift of the scattered wave,  $\psi_{sc} = \exp(i\mathbf{k}' \cdot \mathbf{r} + i\chi(\mathbf{b}))$ . In what follows it is convenient to introduce the profile function  $\Gamma(\mathbf{b}) = 1 - \exp[i\chi(\mathbf{b})]$ .

To consider scattering from a system with internal degrees of freedom, they introduce the Glauber approximation [68] which considers the nucleons to be frozen in their positions during the passage of the relativistic beam particle. The profile function then will depend on the configuration of nucleons in the bound state (with positions denoted by  $\mathbf{r}_j$ ), and the amplitude for scattering becomes

$$F_{fi}(\mathbf{k}', \mathbf{k}) = \frac{ik}{2\pi} \int \exp [i(\mathbf{k} - \mathbf{k}') \cdot \mathbf{b}] \langle f | \Gamma_{tot}(\mathbf{b}, \mathbf{r}_1, \dots, \mathbf{r}_N) | i \rangle d^2\mathbf{b} \quad (4.22)$$

which includes a matrix element of  $\Gamma_{tot}$  between the final ( $f$ ) and initial ( $i$ ) states of the nucleus, including the possibility of an unbound final state. This matrix element includes an average over the possible instantaneous internal configurations of the nucleons in the nucleus.

If the nucleons interact with the incident particle through two-body interactions, the total phase shift is the sum of the phase shifts produced by the individual nucleons:

$$\chi_{\text{tot}}(\mathbf{b}, \mathbf{r}_1, \dots, \mathbf{r}_N) = \sum_{i=1}^N \chi_j(\mathbf{b} - \mathbf{s}_j). \quad (4.23)$$

Here the  $\mathbf{s}_j$  are components of the coordinates  $\mathbf{r}_j$  in the plane of the impact parameter  $\mathbf{b}$ . The total profile function is then

$$\Gamma_{\text{tot}}(\mathbf{b}, \mathbf{r}_1, \dots, \mathbf{r}_N) = 1 - \exp \left[ i \sum_{j=1}^N \chi_j(\mathbf{b} - \mathbf{s}_j) \right]. \quad (4.24)$$

This treatment of scattering implicitly includes all significant ways an incident particle may be multiply scattered by summing phase shifts rather than scattering amplitudes.

Franco and Glauber apply this analysis to the deuteron as a  $n$ - $p$  bound state, and we may apply it to the  $H$  as a  $\Lambda$ - $\Lambda$  bound state. Let the subscripts 1 and 2 denote the individual nucleons,  $n, p$  for the deuteron and  $\Lambda_1, \Lambda_2$  for the  $H$ . The separation of the two particles  $\mathbf{r} = \mathbf{r}_1 - \mathbf{r}_2$  in the bound state describes the internal configuration. Let  $\phi_i(\mathbf{r})$  and  $\phi_f(\mathbf{r})$  be the initial and final state wavefunctions for the  $d$  or  $H$ . The amplitude for a process transferring momentum  $\hbar\mathbf{q} = \hbar(\mathbf{k}' - \mathbf{k})$  to the two particle state and leaving it in the final state  $\phi_f$  is

$$F_{fi}(\mathbf{q}) = \frac{ik}{2\pi} \int e^{i\mathbf{q}\cdot\mathbf{b}} d^2\mathbf{b} \int \phi_f^*(\mathbf{r}) \left\{ 1 - \exp \left[ i\chi_1(\mathbf{b} - \frac{1}{2}\mathbf{s}) + i\chi_2(\mathbf{b} + \frac{1}{2}\mathbf{s}) \right] \right\} \phi_i(\mathbf{r}) d^3\mathbf{r}. \quad (4.25)$$

In this equation,  $\mathbf{s}$  is the projection of  $\mathbf{r}$  onto the plane perpendicular to the direction of the incident beam, and we have evaluated the matrix element  $\langle f | \Gamma_{\text{tot}} | i \rangle$  using the coordinate space wavefunctions. Franco and Glauber show that this amplitude may be expressed in terms of the amplitudes for scattering from a single nucleon (or  $\Lambda$  in our case) by expanding the profile function as follows.

$$\begin{aligned} \Gamma_{\text{tot}} &= 1 - \exp \left[ i\chi_1(\mathbf{b} - \frac{1}{2}\mathbf{s}) + i\chi_2(\mathbf{b} + \frac{1}{2}\mathbf{s}) \right] \\ &= \Gamma_1(\mathbf{b} - \frac{1}{2}\mathbf{s}) + \Gamma_2(\mathbf{b} + \frac{1}{2}\mathbf{s}) - \Gamma_1(\mathbf{b} - \frac{1}{2}\mathbf{s})\Gamma_2(\mathbf{b} + \frac{1}{2}\mathbf{s}) \end{aligned} \quad (4.26)$$

With the aid of this expression for  $\Gamma_{\text{tot}}$  they find the scattering amplitude to be

$$F_{fi}(\mathbf{q}) = \langle f | F(\mathbf{q}, \mathbf{s}) | i \rangle \quad (4.27)$$

where

$$F(\mathbf{q}, \mathbf{s}) = \exp(\frac{1}{2}i\mathbf{q} \cdot \mathbf{s})f_1(\mathbf{q}) \exp(-\frac{1}{2}i\mathbf{q} \cdot \mathbf{s})f_2(\mathbf{q}) \\ + \frac{i}{2\pi k} \int \exp(i\mathbf{q}' \cdot \mathbf{s})f_1(\mathbf{q}' + \frac{1}{2}\mathbf{q})f_2(-\mathbf{q}' + \frac{1}{2}\mathbf{q})d^2\mathbf{q}' \quad (4.28)$$

The first two terms are single scattering amplitudes from each of the lambdas, and the final term is the double scattering amplitude.

Using Eq. 4.28 they give the elastic scattering amplitude by inserting the final state  $f = i$ .

$$F_{ii}(\mathbf{q}) = S(\frac{1}{2}\mathbf{q})f_1(\mathbf{q}) + S(-\frac{1}{2}\mathbf{q})f_2(\mathbf{q}) + \frac{i}{2\pi k} \int S(\mathbf{q}')f_1(\frac{1}{2}\mathbf{q} + \mathbf{q}')f_2(\frac{1}{2}\mathbf{q} - \mathbf{q}')d^2\mathbf{q}'. \quad (4.29)$$

Here  $S(\mathbf{q})$  is the form factor of the bound state  $\phi_i(\mathbf{r})$ :

$$S(\mathbf{q}) = \int e^{i\mathbf{q} \cdot \mathbf{r}} |\phi(\mathbf{r})|^2 d^3\mathbf{r} \quad (4.30)$$

The differential cross section for elastic scattering is just  $|F_{ii}|^2$ , which becomes

$$\frac{d\sigma_{el}}{d\Omega} \approx S^2(\frac{1}{2}\mathbf{q}) \{ |f_1(\mathbf{q})|^2 + |f_2(\mathbf{q})|^2 + 2\text{Re}[f_1(\mathbf{q})f_2^*(\mathbf{q})] \}, \quad (4.31)$$

if we ignore the double scattering amplitude. Applying this to the  $H$ , we insert  $f_\Lambda$ , the elastic scattering amplitude for lambdas, in place of  $f_1$  and  $f_2$  to get

$$\frac{d\sigma_{el}}{d\Omega} = 4S^2(\frac{1}{2}\mathbf{q})|f_\Lambda(\mathbf{q})|^2. \quad (4.32)$$

It is also possible to use Eq. 4.28 to extract the differential cross section for all

scattering processes by summing over all final states  $f$ .

$$\frac{d\sigma_{sc}}{d\Omega} = \sum_f |F_{fi}|^2 \quad (4.33)$$

Inserting the completeness relation for the states  $\phi_j$ , Franco and Glauber find

$$\begin{aligned} \frac{d\sigma_{sc}}{d\Omega} &= \langle i | |F(\mathbf{q}, \mathbf{s})|^2 | f \rangle \\ &= |f_1(\mathbf{q})|^2 + |f_2(\mathbf{q})|^2 + 2S(\mathbf{q})\text{Re}[f_1(\mathbf{q})f_2^*(\mathbf{q})] \\ &\quad - \frac{1}{\pi k} \text{Im} f_1^*(\mathbf{q}) \int S(\mathbf{q}' - \frac{1}{2}\mathbf{q}) f_1(\frac{1}{2}\mathbf{q} + \mathbf{q}') f_2(\frac{1}{2}\mathbf{q} - \mathbf{q}') d^2\mathbf{q}' \\ &\quad - \frac{1}{\pi k} \text{Im} f_2^*(\mathbf{q}) \int S(\mathbf{q}' - \frac{1}{2}\mathbf{q}) f_1(\frac{1}{2}\mathbf{q} + \mathbf{q}') f_2(\frac{1}{2}\mathbf{q} - \mathbf{q}') d^2\mathbf{q}' \\ &\quad + \frac{1}{(2\pi k)^2} \int d^3\mathbf{r} |\phi(\mathbf{r})|^2 \left| \int d^2\mathbf{q}' e^{i\mathbf{q}' \cdot \mathbf{s}} f_1(\frac{1}{2}\mathbf{q} + \mathbf{q}') f_2(\frac{1}{2}\mathbf{q} - \mathbf{q}') \right|^2. \end{aligned} \quad (4.34)$$

The first and second terms are the intensities for scattering from a free nucleon. The third term is the interference of these amplitudes. The fourth and fifth terms come from interference of the double scattering amplitude with the free nucleon amplitudes, and the final term is just the intensity for double scattering. If we ignore the terms from double scattering, we have something that is easy to evaluate given the form factor  $S(\mathbf{q})$  and the free particle intensities.

$$\frac{d\sigma_{sc}}{d\Omega} \approx |f_1(\mathbf{q})|^2 + |f_2(\mathbf{q})|^2 + 2S(\mathbf{q})\text{Re}[f_1(\mathbf{q})f_2^*(\mathbf{q})] \quad (4.35)$$

$$= 2(1 + S(\mathbf{q})) |f_\Lambda(\mathbf{q})|^2 \quad (4.36)$$

Where in the final step we have explicitly inserted  $f_\Lambda$  for both  $f_1$  and  $f_2$  in application to the  $H$ .

The difference of the summed scattering cross section and the elastic scattering cross section gives the inelastic contribution to the scattering cross section:  $d\sigma_{inel}/d\Omega = d\sigma_{sc}/d\Omega - d\sigma_{el}/d\Omega$ . Here inelastic means the bound  $\Lambda\Lambda$  state is excited to a final state

$\phi_f \neq \phi_i$ , and in absence of any stable resonances this state dissociates into two lambdas. So from Eq. 4.36 and Eq. 4.32 the dissociation cross section is given by

$$\frac{d\sigma_{H \rightarrow \Lambda\Lambda}}{d\Omega} = \frac{1}{4}(1 + S(\mathbf{q}))|f_\Lambda(\mathbf{q})|^2 - \frac{1}{2}S^2(\frac{1}{2}\mathbf{q})|f_\Lambda(\mathbf{q})|^2. \quad (4.37)$$

The above includes a factor of 1/8 to account for the overlap of the  $H$  state vector with  $\Lambda\Lambda$  in baryon-baryon basis (c.f. Eq. 4.9). This may be evaluated using the cross section for elastic lambda scattering since  $d\sigma_\Lambda/d\Omega = |f_\Lambda(\mathbf{q})|^2$ . It is convenient to change variables to  $t \approx -q^2$  from  $\Omega$  and use the form of the scattering cross-section from Anderson *et al.* ( $d\sigma/dt = Ae^{bt}$ ). To complete the estimate for the dissociation cross section, it is necessary to evaluate the form factor  $S(\mathbf{q})$ . As an approximation consider the gaussian wave-function introduced in the coalescence estimate.

$$\phi_H(\mathbf{r}) = \left(\frac{2\sigma_q^2}{\pi}\right)^{\frac{3}{4}} e^{-\sigma_q^2 r^2} \quad (4.38)$$

The form factor has the simple form

$$S(\mathbf{q}) = \exp\left(\frac{-q^2}{8\sigma_q^2}\right). \quad (4.39)$$

Using the above approximate wave-function Eq. 4.37 becomes

$$\frac{d\sigma_{H \rightarrow \Lambda\Lambda}}{dt} = \left[\frac{1}{4}(1 + S(\mathbf{q})) - \frac{1}{2}S^2(\frac{1}{2}\mathbf{q})\right] A \exp(bt) \quad (4.40)$$

$$= \frac{A}{4} \exp(bt) \left[1 - \exp\left(\frac{t}{16\sigma_q^2}\right)\right]^2. \quad (4.41)$$

Integration over the allowed range of  $t$  gives the cross section for  $H$  dissociation to  $\Lambda\Lambda$ .

$$\begin{aligned} \sigma_{H \rightarrow \Lambda\Lambda} &= \int_{-\infty}^0 \frac{d\sigma}{dt} dt \\ &= \frac{A}{4} \left[ \frac{1}{b} + \frac{1}{b + \frac{1}{8\sigma_q^2}} - \frac{2}{b + \frac{1}{16\sigma_q^2}} \right] \end{aligned}$$



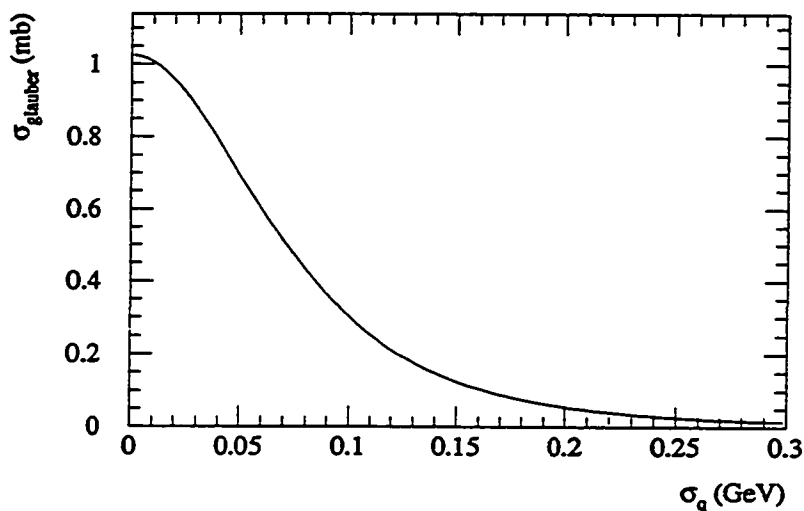


Figure 4.8: The  $H$  Dissociation cross section computed using the Glauber Approximation. The cross section (Eq. 4.42) is given as a function of  $\sigma_q$ , which parameterizes the  $H$  wavefunction (Eq. 4.38).

$$= \frac{A}{4b(8\sigma_q^2 b + 1)(16\sigma_q^2 b + 1)} \quad (4.42)$$

Anderson *et al.* found  $A/b=29.5$  mb and  $b = 7.2$   $\text{GeV}^{-2}$  in their  $\Lambda$ - $p$  elastic scattering experiment [67]. We use these values to plot  $\sigma_{H \rightarrow \Lambda\Lambda}$  in Fig. 4.8 versus  $\sigma_q$ , the momentum scale factor in the gaussian  $H$  wave-function. The cross section falls quickly from its 1 mb value for barely bound  $H$  at  $\sigma_q = 0$ .

#### 4.2.4 Applied Phenomenology

As an alternative to the breakup model calculation and the Glauber approximation calculation of the  $H$  dissociation cross section, we can treat the  $H$  like any other hadron and take advantage of the universality of diffraction dissociation to estimate

the dissociation cross section. In the Regge theory of diffraction dissociation, the factorization of the scattering diagrams in diffraction (triple pomeron) and total hadronic cross section implies that the ratio of total and diffractive cross sections is *independent* of the hadron dissociating. The Rockefeller group has tested this factorization in experiments with  $p, \bar{p}, \pi^\pm$  and  $K^\pm$  beams at 100 and 200 GeV/c [66], and found that the dissociation cross section ( $hp \rightarrow Xp$ , with  $h$  the hadron beam) is well described by

$$\frac{d^2\sigma_{hp \rightarrow Xp}}{dxdt} = 0.1 \text{ GeV}^{-2} \frac{\sigma_T}{1-x} \exp(b(t + 0.05 \text{ GeV}^2)). \quad (4.43)$$

The exponential slope  $b$  ranges from 6 to 12  $\text{GeV}^{-2}$  depending on the hadron and (weakly) on the center of mass energy  $\sqrt{s}$ , and  $\sigma_T$  is the total hadronic cross section for  $hp$  collisions.

To apply this result to  $H$  dissociation at low energies, we rely on the Finite Mass Sum Rule (see Sec. 4.2.1) to correctly extrapolate the high energy behavior to the threshold region. The triple pomeron model of diffraction dissociation suggests the scale independent variable is  $\nu = M_X^2 - M_h^2 - t$ . At high energy  $\nu \approx s(1-x)$ , so the formula of the Rockefeller group can be written,

$$\frac{d^2\sigma_{hp \rightarrow Xp}}{dt d\nu} = \frac{0.1 \text{ GeV}^{-2} \sigma_T}{\nu} e^{b(t+0.05 \text{ GeV}^2)}. \quad (4.44)$$

Or in terms of  $M_X^2$  as

$$\frac{d^2\sigma_{hp \rightarrow Xp}}{dt dM_X^2} = \frac{0.1 \text{ GeV}^{-2} \sigma_T}{M_X^2 - M_h^2 - t} e^{b(t+0.05 \text{ GeV}^2)}. \quad (4.45)$$

Since we are interested in dissociation to  $\Lambda\Lambda$  states, we consider diffractive masses ( $M_X$ ) from threshold  $M_{X1} = 2m_\Lambda$  to  $M_{X2} = m_{\Xi^0} + m_n$ , since below  $m_{\Xi^0} + m_n$ , no diffractive channels other than  $\Lambda\Lambda$  are available. Integrating over  $M_X^2$  we find

$$\frac{d\sigma}{dt} = 0.1 \text{ GeV}^{-2} \sigma_T e^{b(t+0.05 \text{ GeV}^2)} \log \left[ \frac{M_{X2}^2 - m_H^2}{M_{X1}^2 - m_H^2} \right], \quad (4.46)$$

where we have ignored  $t$  compared to the difference of the square of the masses. (Not a good approximation for barely bound  $H$ 's.) We integrate over the allowed region

of  $t$ , taking  $t_{\min}$  from Eq. 4.19 for a 8 GeV/ $c$  momentum incident  $H$  and a diffractive mass of  $(M_{X1} + M_{X2})/2$  to find

$$\begin{aligned}\sigma_{Hp \rightarrow \Lambda\Lambda X} &= \int_{-\infty}^{t_{\min}} 0.1 \text{ GeV}^{-2} \sigma_T \log \left[ \frac{M_{X2}^2 - M_H^2}{M_{X1}^2 - M_H^2} \right] e^{b(t+0.05 \text{ GeV}^2)} \\ &= 0.46 \log \left[ \frac{M_{X2}^2 - M_H^2}{M_{X1}^2 - M_H^2} \right] \text{ mb.}\end{aligned}\quad (4.47)$$

In the last line we take  $b = 9 \text{ GeV}^{-2}$  and  $\sigma_T = 40 \text{ mb}$ , a cross section conservatively equal to the  $pp$  cross section, although for the  $H$  one a factor of two larger would also be believable.

The resulting cross section is plotted versus  $H$  binding energy in Figure 4.9. The actual cross section would not be so sharply peaked at threshold; the infinite slope is an artifact of ignoring  $t$  in the expression for  $\nu$ . In addition, the FMSR ensures that the low diffractive mass region is on average what one would expect from the high mass limit, but in reality resonances would dominate the threshold region. This is somewhat problematic since we integrate over diffractive masses where  $\Lambda\Lambda$  is the only kinematically allowed channel, and this narrow 29 MeV/ $c^2$  region is clearly at threshold. Lacking information about the  $H$  mass let alone any resonances, we take the simplest estimate as a first approximation.

#### 4.2.5 The Case of the $H$

In all of the above models for  $H$  dissociation, the cross section varies from 0.1 mb to 1.0 mb as the binding energy of the  $H$  varies. More deeply bound  $H$ 's are harder to dissociate in all of the models. The relatively good agreement among the different models gives us some hope that the cross section is accurate (if indeed the  $H$  exists) to within an order of magnitude.

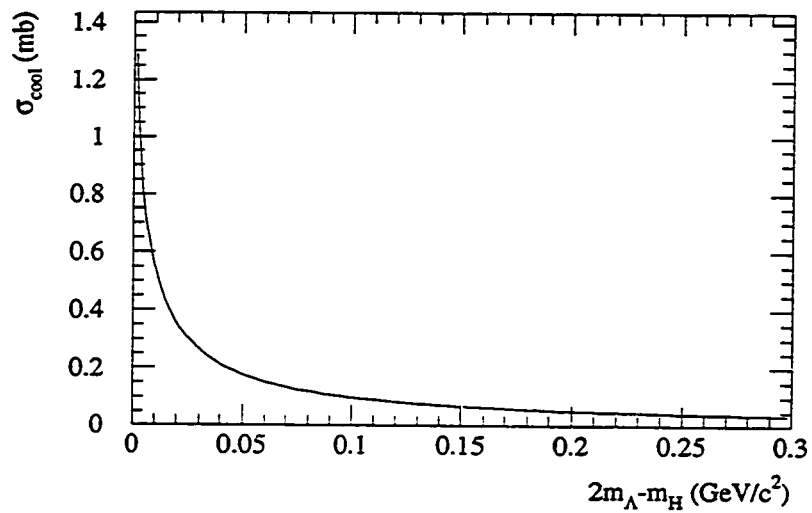
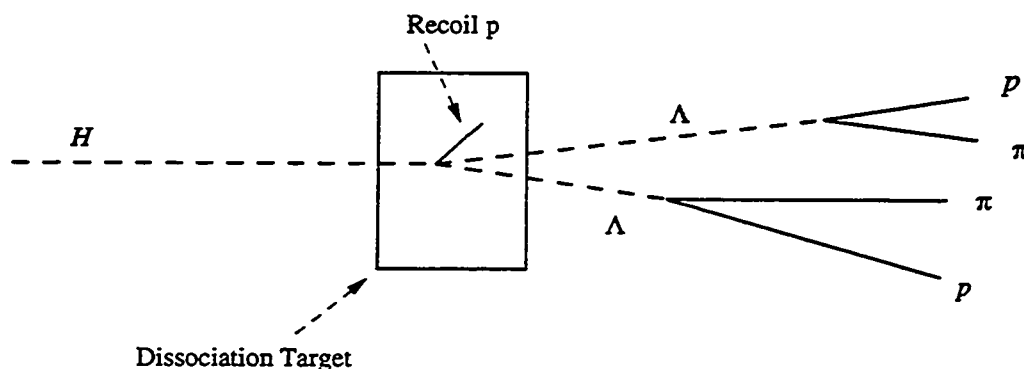


Figure 4.9:  $H$  dissociation cross section calculated using phenomenological fits to high energy data for hadron dissociation. The cross section is given as a function of  $H$  binding energy.

Figure 4.10:  $H$  Dissociation Topology

## 4.3 Signal and Backgrounds

### 4.3.1 Signal

Diffractive dissociation of a bound  $H$  is characterized by two  $\Lambda$ 's originating from the decay vertex of the excited  $H^*$  accompanied by a recoiling nucleus or proton of at most few hundred MeV. The experimental signature of such events would be events with two reconstructed lambdas which point back to a common vertex within the dissociation target. (See Figure 4.10.) The small recoil energy associated with diffractive events can serve as an additional signature which is useful in separating the  $H$  dissociation signal from backgrounds from neutron interactions where larger recoils and possibly additional charged particles are expected. The addition of a veto counter downstream of the dissociator allows further discrimination against background production of two lambdas with additional charged particles.

### 4.3.2 Backgrounds

To discriminate any potential  $\Lambda\Lambda$  signal from  $H$  dissociation from backgrounds due to interactions of other neutral beam particles it is necessary to identify the possible

sources of background and plan the experiment to provide discriminating information.

### Neutron Interactions

A major source of background comes from neutron interactions in the dissociator which produce two lambdas:  $n + A \rightarrow \Lambda\Lambda X$ . Although the cross section for double associated production of strangeness is small, this background is potentially troubling, particularly as we rely on the same interaction at the primary target to produce the  $H$ 's in the neutral beam. Typically however,  $X$  will contain other charged particles which can be detected in a strategically placed piece of scintillator downstream of the target. In addition, the additional strange particles in  $X$  required by conservation of strangeness in strong interactions can cause the transverse momentum of the  $\Lambda\Lambda$  system to be incompatible with the characteristically small  $p_t$  of diffractive events. Finally the invariant mass of the  $\Lambda\Lambda$  system in such events will be broadly distributed while diffractive events are likely to be close to threshold.

### Neutron Diffraction

Another potential background comes from diffractive dissociation of neutrons at the dissociator:  $n + A \rightarrow \Lambda K_S^0 A$ . Without the ability to distinguish  $\pi^+$ 's from protons, it is possible for  $K_S^0 \rightarrow \pi\pi$  to mimic  $\Lambda \rightarrow p\pi$ . This kinematic ambiguity occurs when assigning tracks to a particle hypothesis solely by their charge. For some regions of phase space, both  $m(\pi^+\pi^-) \approx m_{K^0}$  and  $m(p\pi^-) \approx m_\Lambda$ . Fortunately requiring the  $\pi$ - $\pi$  invariant mass to be incompatible with the  $K_S^0$  mass removes this source of background at the expense of a small amount of the signal. In fact this "background" becomes a valuable calibration of the experiment if it is understood because of its identical topology (two  $V^0$ 's coming from a vertex in the dissociator) and production mechanism (diffractive dissociation of a neutral beam particle). By reconstructing these  $\Lambda K_S^0$  events, we are able to check our reconstruction software and in principle normalize our  $H$  experiment to the number of observed  $\Lambda K_S^0$  events.

## 4.4 Detector Design

Given the characteristics expected for signal and background events it is possible to design a detector to efficiently identify  $H$  candidates while at the same time discriminating against the expected backgrounds. The main features of our detector design are an instrumented dissociation target for a recoil energy measurement, a magnetic spectrometer with planar drift chambers for charged track and vertex reconstruction, and a gas threshold Čerenkov counter for particle identification and background discrimination.

### 4.4.1 Experimental Constraints

The design task was constrained by available time and resources. The experiment was conceived by Val Fitch and Josh Klein of Princeton along with Morgan May of Brookhaven National Lab (BNL). In June of 1991 they proposed to join with members of the E791/E871 collaboration at BNL and undertake a search for the  $H$  using the E791 beam line and detectors during the spring of 1992. Interested parties from both E791 and E871 joined the three instigators from Princeton and BNL to form the E888 collaboration, making an official proposal to BNL in January 1992 for the run beginning in April of the same year.

In addition to the two phases of E888, beam and detector tests for E871 were scheduled for the 1992 run cycle. Since the E888 collaboration shared not only the beam line but also experimenters and detectors with E871, these logistical realities imposed nontrivial constraints on the ability to prepare for and undertake an experiment. Clearly it was important to use as much of the existing detector as practical and avoid construction of any new detectors.

Figure 4.11 shows our raw material: the layout of the E791 spectrometer, designed to detect two body  $K_L^0$  decays. The neutral beam is produced at a primary target with the aid of sweeping magnets and collimators. A conical vacuum tank extends to the double arm spectrometer which begins about 17 m from the target. In E791 a  $K_L^0$  decaying inside the vacuum decay tank may be detected by the resulting charged tracks, one on each side of the detector. The neutral beam passes through the center

of a double arm spectrometer which features planar drift chambers and two dipole magnets. Particle identification counters, including a gas threshold Čerenkov, a lead glass calorimeter and a muon range-finder complete the detector.

For the dissociation search, the plan was to insert a instrumented target into the neutral beam to dissociate any  $H$ 's in the beam to two lambdas. We detect the lambdas through their charged decay mode  $\Lambda \rightarrow p\pi^-$  in the spectrometer. The only completely new detector required was the dissociation target (dissociator). The rest of the detector could be assembled from existing E791 components. The design of the experiment conveniently divides into two relatively decoupled tasks: the design of the dissociator and the arrangement of the E791 detector to optimally detect diffractively produced lambdas.

#### 4.4.2 Dissociator

Besides serving as a target for the neutral beam, the dissociator needs to provide an energy measurement of the recoiling nucleus in our signal diffraction dissociation events. Additionally it must be simple to construct and interface to existing electronics. Ideally it would be constructed out of a material with a high fraction of hydrogen since a typical energy for a recoiling proton (hydrogen nucleus) in a diffractive events is of order 60 MeV. Anything heavier reduces the recoil energy (by virtue of  $t = -2m_{\text{targ}}K_{\text{targ}}$  and a larger  $b$  in  $d\sigma/dt \sim \exp(bt)$  due to the larger size of the diffractive target) making its measurement more difficult.

A simple solution was considered: make the dissociator out of a block of scintillator with transverse dimension determined by the beam and longitudinal dimension big enough to contain a recoiling proton and viewed from the side by phototubes. The neutral beam has a cross section of approximately 10 cm wide by 40 cm tall at the spectrometer, and a 50 MeV kinetic energy proton has a range of  $2 \pm 0.3$  cm in polystyrene. The phototubes would be easily connected to existing ADCs, and only a few channels would be necessary. With a few modifications, this is the design we settled on for the dissociator.



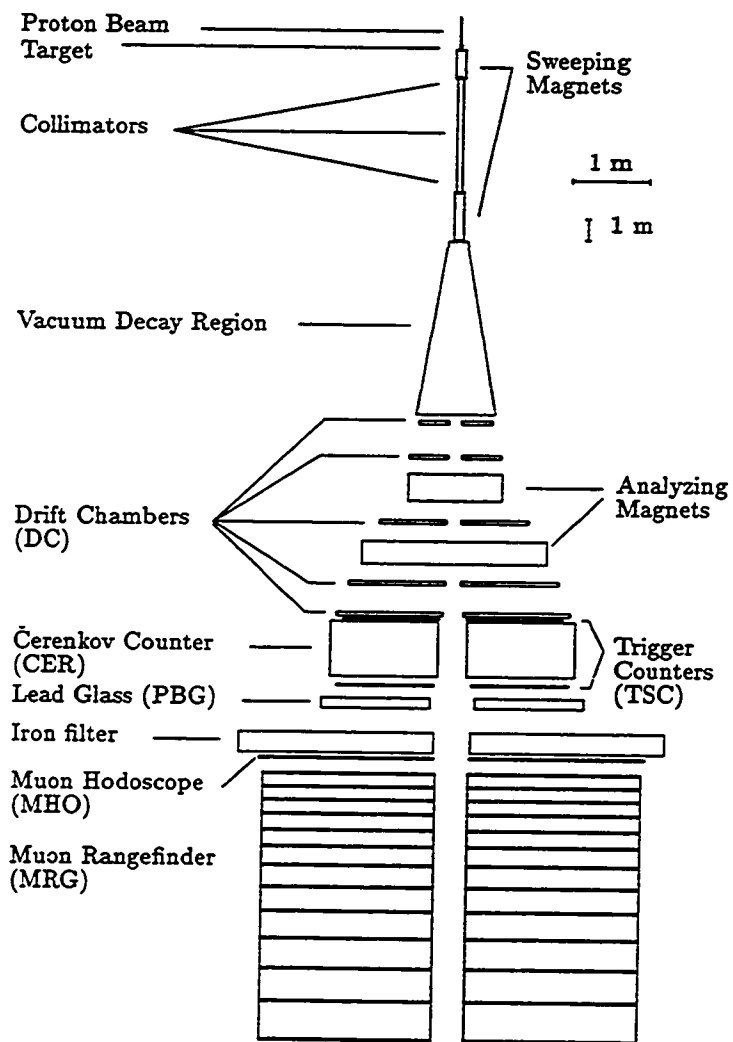


Figure 4.11: The E791 Detector and Beamline.

To aid in discrimination between through-going particles or inelastic neutron interactions (typically with additional charged particles produced) and fully contained diffractive recoil events, we chose to make the dissociator out of eight 0.5 inch thick planes (5 inches square) of scintillator stacked perpendicular to the beam direction followed by a single thin (0.125 inch) veto counter with a larger cross section (12 inches square). The beam itself extends above and below the dissociator in  $y$ , but is narrower (10 cm) than the width of the counters (12.7 cm). A contained diffraction dissociation event will be identifiable by a block consecutive counters with energy deposited, followed by one or more empty counters, and no energy in the veto counter. An inelastic neutron interaction will leave energy in every counter downstream of the interaction point, including the veto counter if any energetic charged particles are produced. The segmentation can also be used to match a vertex reconstructed using the spectrometer to the interaction point as determined from the first counter of the dissociator with energy deposited. The expected topology for a signal event is shown in Figure 4.12.

### 4.4.3 Magnetic Spectrometer

Given the existing detectors and some physical constraints for their placement inside the experimental area, the design task became one of optimally the placing the dissociation target (dissociator) and the spectrometer drift chambers around the fixed magnet and vacuum tank positions. It was not possible to move the magnets, nor was it practical to move the trigger counters. The only degrees of freedom left were the positions of the dissociator and drift chambers.

Figure 4.13 gives an overhead view of the spectrometer as it was configured for E791. Drift chamber modules are placed in five  $z$ -positions on both sides of the neutral beam, two modules upstream of the first magnet, one between the magnets, and two more downstream of the second magnet.

In a dissociation event, we expect four charged tracks, two from each lambda. All four of these tracks will be very close together due to the small  $Q$  in both the  $H^*$  and the  $\Lambda$  decays. The magnetic field will separate the positively and negatively

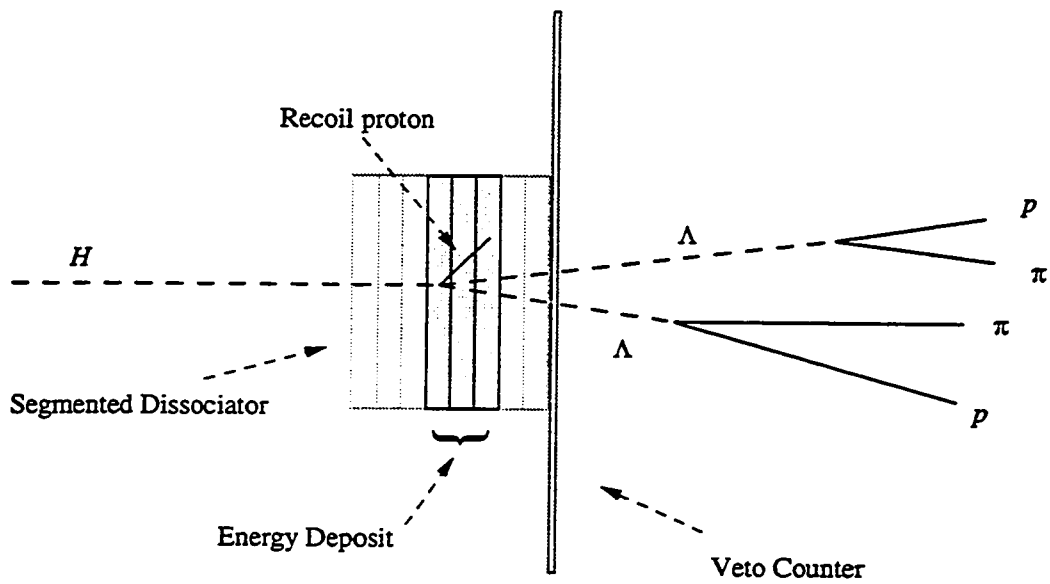


Figure 4.12:  $H$  diffraction dissociation event topology showing isolated energy deposit in dissociator.

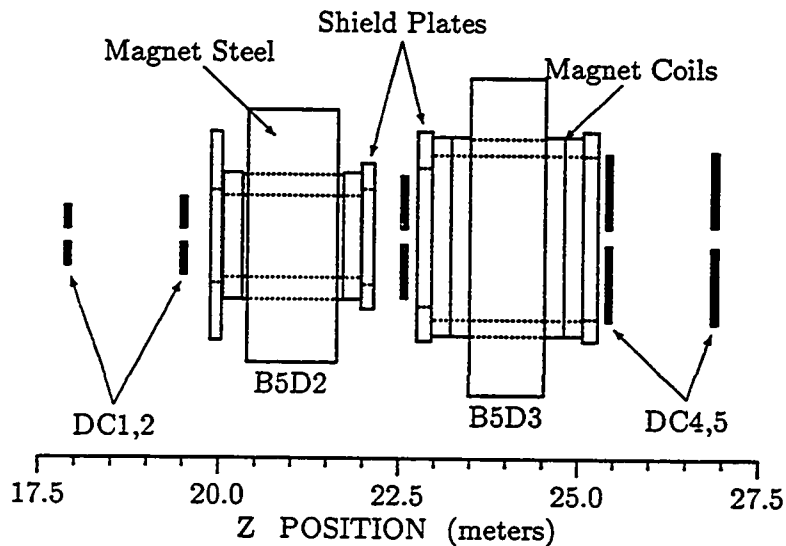


Figure 4.13: E791 spectrometer as seen from above. The shaded areas represent the drift chamber modules.

charged tracks, but upstream of the magnet, these tracks will remain close together in the neutral beam. We therefore considered placing chambers along the beam axis between the magnet and the dissociator. We need at least two chambers upstream of the magnet to define a direction for the track. The E791 chamber modules have vertical and horizontal planes (2 each) of sense wires. To aid in untangling hits on the perpendicular planes of wires into candidate tracks, we also wanted a stereo view upstream of the magnet. Four tracks will leave as many as four hit wires in each plane, leaving 16 possible  $(x, y)$  pairs, only four of which are true. To provide an additional constraint in front of the magnet we added a third chamber module rotated by  $20^\circ$  about the beam direction to give two a stereo planes  $(u, v)$ .

We used Monte Carlo simulation of diffractive  $H$  and  $n \rightarrow \Lambda K_S^0$  events as an aid in the optimization of the detector. We wrote a new event generator for the E791 custom detector Monte Carlo program, which produced  $H$  diffraction dissociation events. The program generated events according to an exponential distribution in square four-momentum transfer  $t$ , with a slope of  $9 \text{ GeV}^{-2}$  and a diffractive mass distribution

$d\sigma/dM_{H^*}^2 \sim 1/(M_{H^*}^2 - M_H^2)$ , according to diffraction dissociation phenomenology. The  $H^*$  decays immediately to two lambdas, which are passed to the standard E791 Monte Carlo to be propagated and decayed in the detector. The trajectory of the charged decay products is obtained by swimming the charged tracks in the measured magnetic field of the spectrometer dipole. In this way we calculated the geometrical acceptance for various trial configurations of the drift chambers.

We considered both two magnet and one magnet geometries. The final arrangement which did the best job within the physical constraints uses only one of the two magnets for a momentum measurement (See Fig. 4.14). The dissociator is placed inside the first magnet (with field off) and three planes of drift chambers barely fit in the space between the two magnets. (In fact, we removed the downstream mirror plate from 48D48 to make enough room for the chambers.) Downstream of the magnet, drift chamber modules are placed on each side of the beam gap at two different locations. The chambers on beam left accept protons from the lambda decay; those on beam right accept the  $\pi^-$  from the  $\Lambda$  decay. The acceptance is optimized when the proton side chambers are moved transversely in towards the beam gap, because protons from lambda decays carry most of the momentum of the lambda, and are not bent very much by the magnetic field. Conversely the pions are very soft and are bent through a large angle. Therefore the chambers on the beam right side are translated away from beam gap to optimize acceptance.

#### 4.4.4 Particle Identification

Particle identification can help in background suppression by discriminating between charged pions and protons. A two pion  $K_S^0$  decay can look like a  $\Lambda$  decay if the  $\pi^+$  is assigned the proton mass. The mass requirement  $|m_{\pi\pi} - m_{K^0}| > \delta$  will remove events without reconstruction errors, but will not affect events where a reconstruction error or large multiple scatter causes the invariant mass to move away from the kaon mass. Some of these events can still reconstruct as lambdas. So additional background suppression is possible if a particle identification cut can be made.

With this in mind, we changed the gas in the Čerenkov detector on the beam

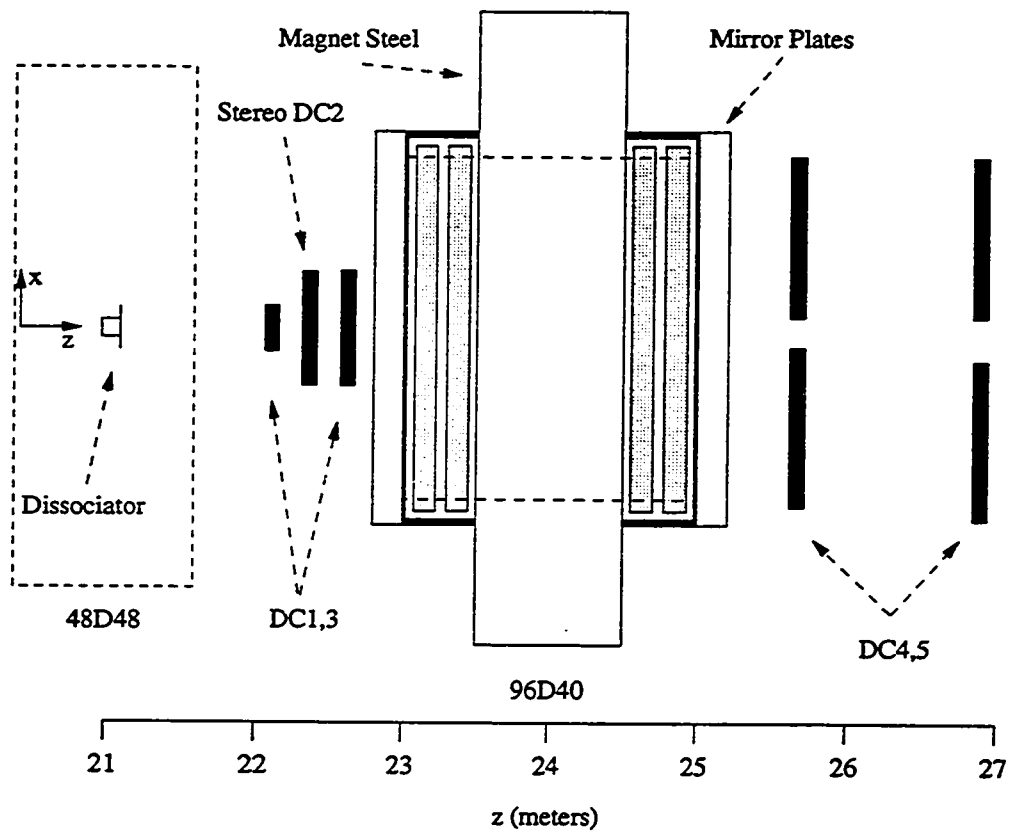


Figure 4.14: Plan view of E888 spectrometer showing placement of drift chambers and dissociator within the E791 detector.

left side, where we expect protons only in lambda decays. We picked freon as a gas because its index of refraction ( $n = 1.001065$ ) gives a momentum threshold of 3 GeV/ $c$  for pions. While this will not provide complete coverage for the momentum range of pions from  $K_S^0 \rightarrow \pi\pi$ , it adds some rejection power for this background channel.

# Chapter 5

## Apparatus

### 5.1 Overview

Our experiment to search for the  $H$  was conducted at Brookhaven National Laboratory's (BNL) Alternating Gradient Synchrotron (AGS) in neutral beam line B5. The detector consists of a neutral beam line, an active dissociator, a magnetic spectrometer, a gas threshold Čerenkov and a trigger hodoscope. The layout of the experiment is shown in Figure 5.1. The detector elements are instrumented and read out with custom and commercial electronics. Fast signals from the trigger hodoscope are processed by a hardware trigger denoted Level 1 (L1). The L1 decision enables digitization of all detector signals. Custom data acquisition hardware presents the data to custom Level 3 Trigger processors (L3) which execute a software filter. Events passing one or more streams of the software filter are uploaded to a DAQ host computer, which writes events to 9-track (6250 bpi) tape. An online system performs low level detector and beam quality monitoring during running.

### 5.2 Beam

E888 was conducted at the AGS at Brookhaven, in a neutral beam line constructed to study very rare  $K_L^0$  decays in Experiment 791 [70, 71].



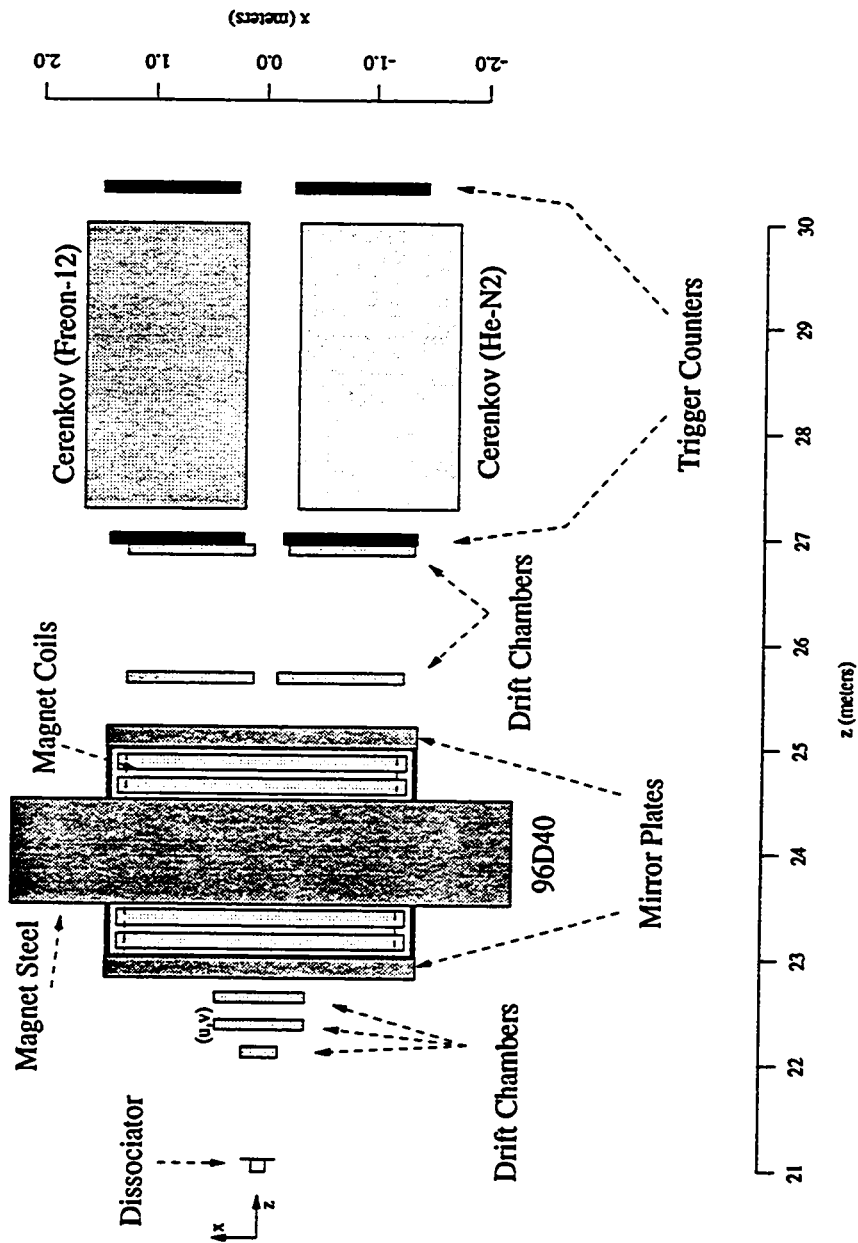


Figure 5.1: Plan View of Detector Layout

### 5.2.1 Primary Beam and Target

Protons of momentum  $24.1 \text{ GeV}/c$  are de-bunched and slowly extracted from the AGS over a 1 to 1.4 second spill every 3.8 seconds. The extracted beam is transported to our primary target, a  $4.7''$  by  $1/10''$  by  $1/8''$  platinum rod. The target is  $1.33$  hadronic interaction lengths long in the beam direction. The target station is mounted on an assembly which can be adjusted in vertical angle with respect to the neutral beam defining collimating system. For this experiment we ran with an angle of  $3.75^\circ$  ( $65 \text{ mrad}$ ).

### 5.2.2 Neutral Beam Defining elements

After the target station two pitching magnets are operated in opposite polarities to deflect charged particles from the beam. The first magnet (B5P4) deflects positively charged secondaries and non-interacting protons down with a field of  $27 \text{ kG}$ , for a total momentum kick of  $1.6 \text{ GeV}/c$ . About  $3 \text{ m}$  downstream there is a beam dump consisting of tungsten plates. The second magnet (B5P5) is operated at  $16 \text{ kG}$  which gives a transverse kick of  $1.2 \text{ GeV}/c$ . Three brass collimators define a cone with  $5 \text{ mrad}$  horizontal by  $20 \text{ mrad}$  vertical angular divergence. The apex of the cone formed by the precision collimators (defining the origin of the coordinate system  $(x, y, z) = (0, 0, 0)$ ) lies approximately  $10 \text{ cm}$  downstream of the target. This alignment insures none of the collimator faces "sees" the target directly, thus reducing beam halo caused by singly scattered particles from a collimator face. It also reduces the effective solid angle of the beam to  $62 \mu\text{sr}$ . Figure 5.2 shows the target station, sweeping magnet and collimator installation.

Photons produced in the target are converted by a series of lead "foils" in the neutral beam. A total of  $18$  foils of thickness  $0.53 \text{ cm}$  are placed every  $5 \text{ cm}$  within the first sweeping magnet to ensure that photons are converted and the conversion electrons are swept from the beam. The neutral beam propagates in vacuum beginning inside the second collimator to the detector area beginning at  $z=18 \text{ m}$ , where it passes through a mylar vacuum window made from two mylar sheets of thickness  $0.010''$ . The upstream vacuum window is made from a single sheet of  $0.010''$  mylar.

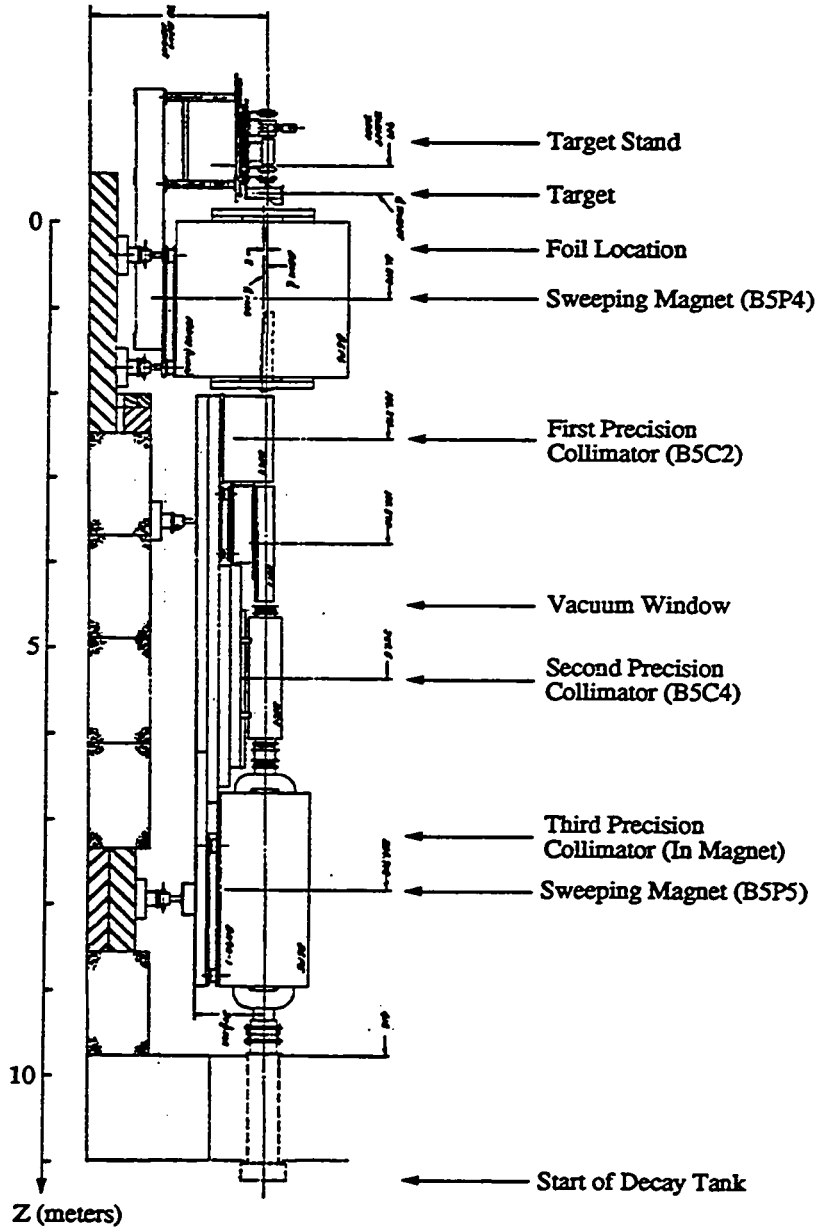


Figure 5.2: Target Station and Collimators

The vacuum was maintained at better than  $1 \mu\text{m}$  during the run.

In the spectrometer, the detector elements are arranged to allow passage of the neutral beam through the detector with minimum material in the neutral beam to minimize interactions. The beam gap is filled with helium bags where possible to further minimize interactions of the neutral beam.

### 5.2.3 Neutral Beam Content

The neutral beam consists mainly of neutral kaons, lambdas and neutrons. At the detector the short-lived  $\Lambda$ 's and  $K_S^0$ 's have been greatly attenuated by the long flight path, leaving neutrons and  $K_L^0$ 's. In the detector area the  $n/K_L$  ratio has been estimated at  $18 \pm 6$  in the same beam line with a copper target at  $2.75^\circ$  [72]. For the larger targeting angle the ratio is expected to be smaller. Target studies for E871 [73] show the switch to Pt from Cu and the larger targeting angle reduces the background rate from neutron interactions by a factor of two relative to the signal rate from  $K_L^0$  decays. Assuming the relative acceptances are unchanged, this would predict  $n/K_L^0 \sim 10$ .

## 5.3 Dissociator (DSC)

The dissociator is a secondary target placed within the neutral beam. The dissociator is made from eight 5" by 5" by 0.5" slabs of scintillator placed one after another on the beam axis. (Figure 5.3) Each counter is wrapped to be individually light tight and coupled to a phototube (outside the neutral beam) by an adiabatically curved light pipe. Due to the thickness of the wrapping, the total length of the eight 1/2" counters is roughly 4.625". The counters are numbered from 1 to 8, the even and odd counters' phototubes mounted on opposite sides of the beam. This instrumentation provides segmentation in  $z$  (along the beam direction).

At downstream end of the eight counters of the dissociator is a 12" by 12" by 0.125" veto counter. The veto counter is coupled to two phototubes, one on each side of the beam. Its size (wider and taller than the neutral beam) and redundant

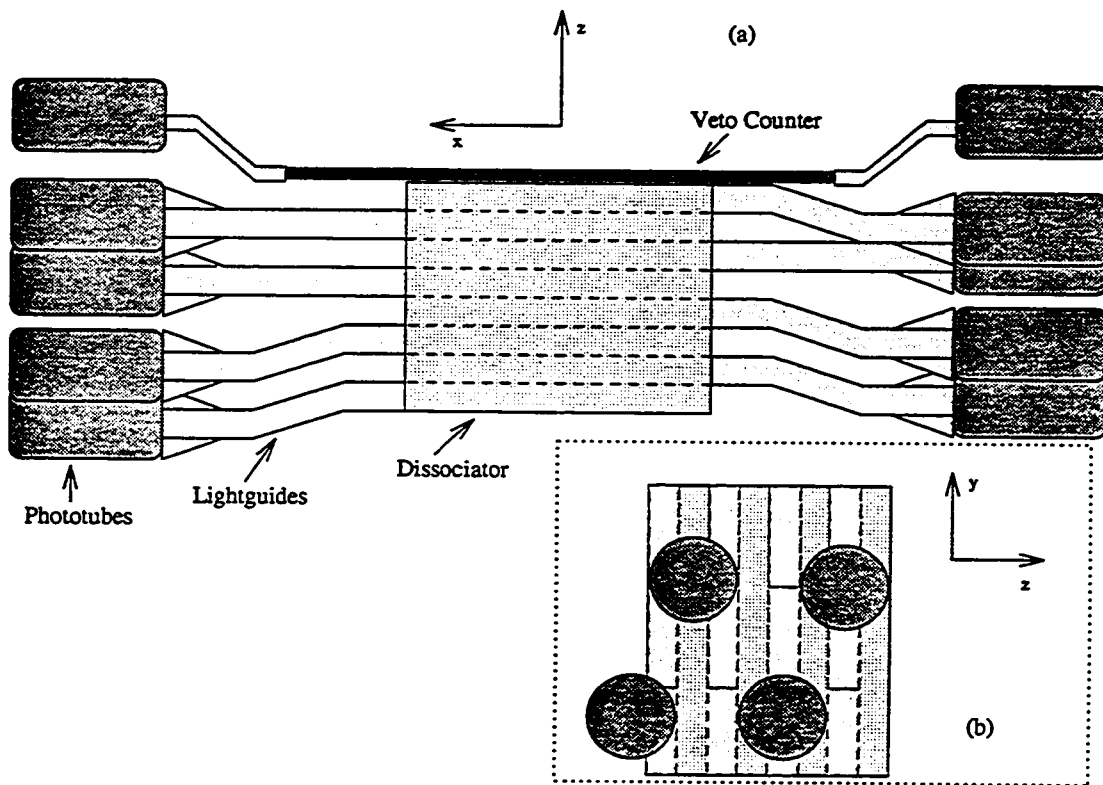


Figure 5.3: Dissociator Assembly: top view (a) and side view (b inset). The arrangement of the phototubes (dark cylinders) is shown relative to the eight slabs of scintillator. The phototubes are mounted on alternate sides of the beam axis, connected the scintillator by curved light guides.

phototubes give adequate coverage to efficiently detect charged particles produced by interactions within the eight counters of the dissociator proper, providing the option for a charged particle veto.

Each phototube is connected via 150 ns of RG-8 cable to a  $50 \Omega$  splitter which couples the signal to an eight-bit bilinear ADC [74] and a LeCroy 4416 discriminator. The discriminator output is available in the L1 trigger and also goes to a 220 ps least count TDC [75]. Additional information regarding the dissociator construction and calibration may be found in [28].

## 5.4 Spectrometer

The primary means of identification of particles in the experiment is through kinematic reconstruction of particle decays. Lambdas and kaons are both identified by tracking charged decay products to a common three dimensional vertex. Coupled with a momentum determination from the spectrometer, a mass may be computed based on track-particle hypotheses. The spectrometer provides the important three dimensional tracking and momentum information used in event reconstruction.

The spectrometer consists of five drift chamber stations located at different  $z$  positions along the beam and one spectrometer magnet with vertical field such that positively charged particles are deflected to the left side of the beam ( $x > 0$ ). Each of the drift chamber stations is composed of two orthogonal views ( $x, y$ ). Two staggered planes of wires provide two measurements of the track in each view. The first three stations are located upstream of the magnet and are centered on the beam line. The second station is rotated by  $20^\circ$  to provide a stereo view ( $u, v$ ). The last two stations are located downstream of the magnet, with separate left and right side chambers. The change in direction of tracks between up and downstream sections of the spectrometer allows a determination of the track momentum and charge.

### 5.4.1 Drift Chambers (DC)

The drift chambers are constructed with aluminum frames and precision manufactured printed circuit boards to which the sense and field wires are soldered. Thin aluminized mylar windows (0.0005 " mylar and 0.00035 " aluminum) are fixed to the front and rear of the drift chamber box to form a gas volume. A gas mixture of 49% Argon, 49% Ethane and 2% ethanol is flowed continuously through the chambers. High voltage is applied to the field wires while the sense wires are kept at ground. The chambers are operated at -2.5 kV. The drift velocity for these operating conditions is measured to be 51  $\mu\text{m}/\text{ns}$ . The sense wires are 0.0043" diameter gold plated tungsten, tensioned to 40 gm to be stable against electrostatic forces. Each sense wire is surrounded by six Aluminum field wires of diameter 0.001". Grounded guard wires are placed outside the cells to extend the symmetry of the cell structure. A schematic showing the cell geometry is given in figure 5.4. The field and ground wires are tensioned to 140 gm, so that the gravitational sag on horizontal wires matches that of the sense wires. The hexagonal cell is shortened slightly in the beam direction. The amount of material in the chambers is kept small to minimize multiple scattering which limits the tracking resolution. The thickness in radiation lengths of a chamber (both views) is 0.00176.

Eight-channel preamplifiers are mounted directly on the PC board. Coaxial cable connects the preamp output to front end electronic modules (ADM boards) in racks adjacent to the chambers. The ADM boards further amplify and discriminate the chamber signals. They also provide meantimer output to the Level 1 trigger electronics. The staggered sub-plane geometry of the drift chamber views ensures one valid meantimer output per track apart from pathologies, since the sum of drift times is constant apart from smearing by chamber resolution and varying track direction.

ECL signals from the ADM boards arrive at 6-bit 2.5 ns least count TDCs [76] after propagating through 500 ns delay cables. For chambers 1 and 3 the ECL signals were daisy chained into two TDC channels per wire. Here the tracks are expected to be very close together and possibly within the same drift chamber cell. The TDC normally latches the first hit to arrive, giving the drift time for the closest track to the wire. The second TDC channel connected to these chambers' wires was modified

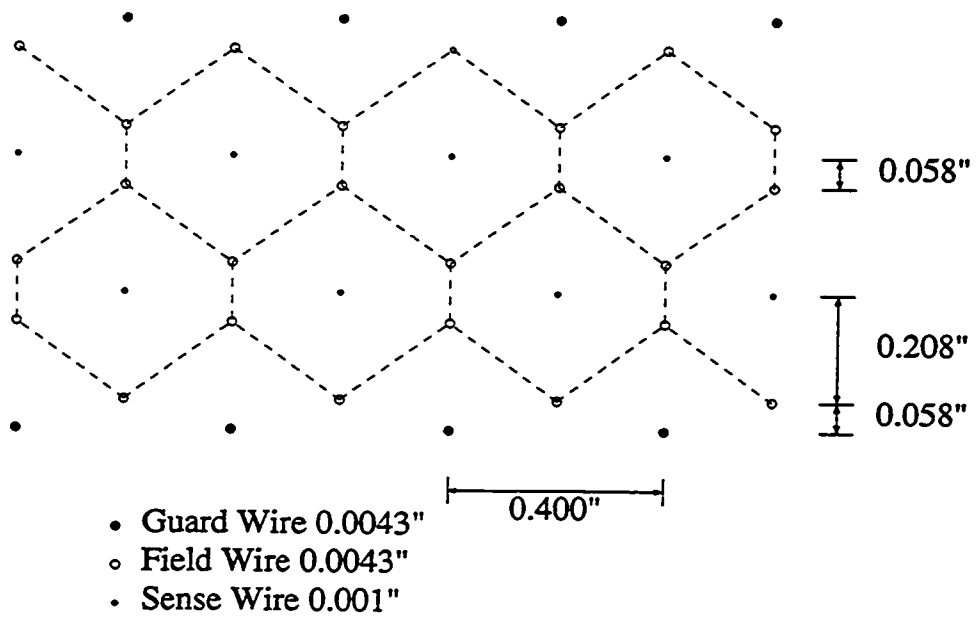


Figure 5.4: Drift Chamber Cell Pattern



to latch the last hit to arrive. Using both first and last hits on a wire allows a good determination of drift times for up to two tracks per cell. The remaining chambers were instrumented with one (first hit) TDC channel per wire. Chamber 2 was too large to allow the addition of last hit TDCs, while chambers 4 and 5 are far enough downstream that even close tracks will be sufficiently separated. The last hit TDCs were a precautionary effort which proved unnecessary. Only first hit TDC information is used in track reconstruction.

The chambers as operated in the experiment give single wire resolutions of 150  $\mu\text{m}$  and efficiencies of 99% or higher. Fewer than 0.5% of all wires were nonfunctional due to dead electronics or broken wires removed during the run.

#### 5.4.2 Magnetic Field

The vertical magnetic field is provided by a large gap spectrometer magnet with mirror plates. The field was set to 6.3 kG in the center of the magnet for a momentum kick of roughly 300 MeV/c for energetic particles. The actual field components ( $y$  and  $x$ ) were measured using two Hall probes mounted on a cart pulled along a rail in the  $z$  direction. The alignment of the probes was monitored and the data was reduced to a three component magnetic field vector on a 2"  $\times$  2"  $\times$  2" grid. The third component ( $z$ ) is obtained from a Poisson model tuned to match the measured data in the other two components.

These field components were measured for E791, where there were two spectrometer magnets. For E888, the upstream dipole (48D48) was turned off and its mirror plate was removed to provide more room for drift chambers between the magnets, and the downstream magnet (96D40) was run in reverse polarity. To obtain a new field map, new field measurements were taken in the E888 configuration [77]. Because the downstream magnet was not altered, we rely on the E791 field measurements for  $z > 24$  m, where the effect of the upstream magnet is negligible, and reflect these measurements about the magnet center ( $z = 24$  m) to give a first approximation of the actual field for the upstream half of the magnet. This estimate is corrected using the measurement scans taken in the E888 configuration. Ref. [77] describes the

correction and final field map.

## 5.5 Trigger Hodoscope (TSC)

The trigger hodoscope has four banks of scintillation counters, two on each side of the beam in two  $z$  positions. The upstream bank is located 15 cm downstream of the last drift chamber station and is separated from the downstream bank by 3.3 m. The Čerenkov counter sits in between the two banks. A gap between banks at the same  $z$  position allows passage of the neutral beam. Each bank has both vertical and horizontal counters, individually wrapped to be optically isolated. There are 62 vertical counters of width 2.01 cm and length 180 cm. The 64 horizontal counters have width 2.81 cm and length 128 cm. The counters are 5 mm and 10 mm thick, the thinner counters chosen for the upstream bank in order to reduce interactions and multiple scattering. The attenuation length in the counter is measured to be 1.8 m, and the overall efficiency for a single bank is greater than 99.8% [78]. (In E791 the single counter efficiency was determined to be greater than 99.9% for all but a few counters and greater than 99% for all counters.)

Both horizontal and vertical counters are coupled to 1" Hamamatsu R1398 phototubes by translucent silicon "cookies" which are sandwiched between the scintillator and the phototube. The horizontal counters each have one phototube mounted on the outer end of the counter. The vertical counters are viewed on both ends by phototubes. Each phototube views two adjacent slats, with the pairs of counters viewed from the top offset by one counter compared to the bottom so that a hit counter causes a signal on a unique pair of phototubes. In this way only one phototube per counter is required, but signals are obtained from both ends of the counter. This allows meantiming in the trigger, and the time difference allows a determination of the length along the counter of the hit (in addition to the hit on the horizontal counter).

The phototube signals are brought to LeCroy 4416 Camac discriminator modules via lengths 150 ns RG-8 50  $\Omega$  cable. The discriminator output is used in the Level 1 trigger and sent to individual TDC channels. The  $x$ -measuring channels are put into 8-bit 200 ps least count fast TDCs [75], so that time sums and differences may be

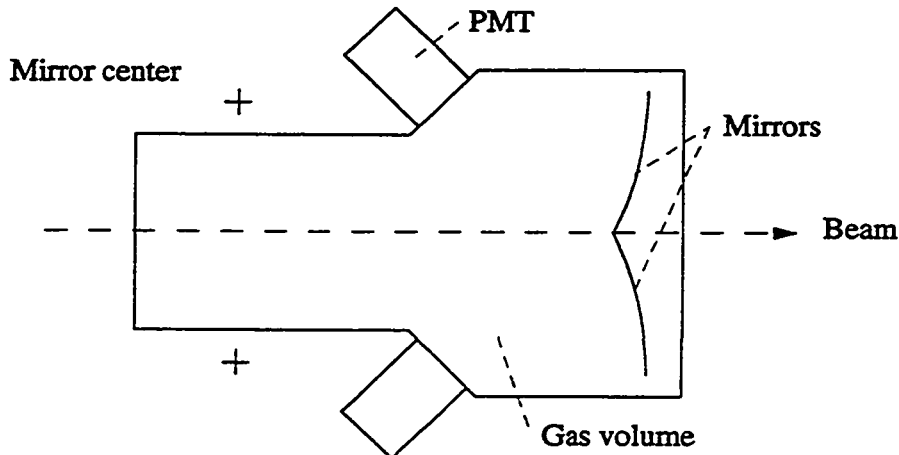


Figure 5.5: Čerenkov Counter Schematic

formed offline. The  $y$ -measuring channels are sent to 6-bit 2.5 ns least count TDCs [76], as only coincidence with other detectors is required for these channels. As the fast TDC is edge triggered, the discriminated TDC signals are also sent to strobed latch modules to eliminate inefficiencies caused by early hits.

## 5.6 Čerenkov (CER)

The Čerenkov counter consists of two identical (apart from gas) aluminum boxes which are placed on each side of the beam. The beam left counter is filled with freon-12 ( $n_I = 1.001065$ ). The beam right box is filled with a 50-50 mixture of helium and nitrogen ( $n_I = 1.00140$ ). The index of the mixture is monitored with an interferometer. The gas on the left side was chosen to provide identification of pions above 3 GeV/ $c$ . In lambda decays we expect only protons on this side of the detector.

Each counter has an entrance window of thin aluminum. Eight mirrors are mounted on the downstream wall facing upstream to collect Čerenkov photons and focus them through quartz windows onto phototubes mounted on the upstream box wall (Figure 5.5). The mirrors were aligned in a previous experiment to optimally

focus photons emitted from an apparent source point calculated in Monte Carlo. No further alignment of the mirrors was necessary for this experiment, although the position of the detector was adjusted to give good coverage of tracks as calculated in Monte Carlo for dissociation events.

Phototube signals are carried to the counting house by 150 ns long RG-8 cables where they are split to 8-bit fast ADCs and a LeCroy discriminator. Discriminator output is available for the Level 1 trigger and is sent to a 200 ps fast TDC [75]. The timing resolution is roughly 1.5 ns.

## 5.7 Other Particle ID

Although not used in this experiment the detector includes other particle identification counters including a lead glass calorimeter optimized to identify electrons from  $K_{e3}$  decays, a muon hodoscope following an iron filter and a muon range finder with coverage to  $E_\mu = 6$  GeV. These detectors would have been valuable in verifying the consistency of any  $H$  signal found in the experiment, but are not essential to establishing a limit.

## 5.8 Level 1 Trigger (L1)

Signals from the detector are used to determine whether to perform a complete read-out of the detector. The hardware trigger forms this decision in stages. First discriminated signals from the trigger hodoscope are required to be consistent with at least one track in each arm of the spectrometer. This coincidence is termed Level 0 (L0). Flexibility in the custom trigger electronics allowed other signals to be required for the Level 1 trigger. These other signals include a drift chamber hit requirement, trigger counter multiplicity, a Cerenkov veto, a DSC/Veto Counter veto or coincidence, and various combinations of the signals. When setting up the experiment we settled on a trigger hodoscope multiplicity requirement for the Level 1 trigger. The other options were provided should they be required to reduce the data rate, however they proved to be unnecessary (and potentially harmful to the experiment without a

thorough understanding of their effect) when we turned on the experiment and got a look at the data.

Output from the TSC discriminators form the input to the Level 0 determination. ECL signals from the two phototubes of a  $x$ -measuring TSC counter are fed into mean timing circuits. The output of the mean timers for an entire module are OR'ed to form a single mean timer signal for each bank. (*e.g.*  $RTFx$  is the mean timer output for the right front  $x$  bank of TSC counters.) These signals are required to be in coincidence for the 2 upstream TSC banks and the left side downstream TSC bank. A coincidence is also required with the OR of the discriminator outputs of the downstream left side TSC  $y$  bank ( $LTBy$ ). The right side downstream TSC bank is not included in the trigger because negatively charged pions from lambda decay can bend too far in the magnetic field to remain within the aperture of the TSC this far downstream. The Level 0 determination may be expressed compactly:

$$L0 = RTFx \cdot LTFx \cdot LTBx \cdot LTBy,$$

and this trigger is consistent with having one track on each side of the detector, allowing the right side track to miss the downstream trigger counters.

To form the L1 trigger decision, discriminator output from other detectors is compared with the L0 signal. For this experiment we defined two L1 trigger streams, a minimum bias stream denoted [mb] and a "physics" stream, [hj]. The L1 trigger provides multiple streams, with the bit set in the trigger word indicating which stream(s) caused the trigger.

The minimum bias stream, denoted [mb], is identical to the L0 signal. The physics stream [hj] is formed by a coincidence of the hodoscope multiplicity signal (Mult) with L0. The multiplicity requirement is intended to select events having at least 2 tracks on each side of the detector. The Mult signal is formed from a coincidence of  $n$ -fold coincidences of four TSC banks. In the two upstream TSC  $x$  banks a three fold coincidence is required from the discriminator output. The requirement that 3 or more phototubes be hit insures at least two counters be hit, but allows events with two adjacent  $x$  counters hit to cause a trigger. In the latter case only three phototubes

would be hit since the two slats share one phototube. Finally at least two phototube hits are required from each of TSC  $L\overline{T}B\overline{y}$  and  $R\overline{T}F\overline{y}$ .  $R\overline{T}B\overline{y}$  is omitted because of low acceptance for slow pions, and  $L\overline{T}F\overline{x}/\overline{y}$  are omitted to allow one of the two tracks on the left side to miss the inner edge of the upstream counter. This is to be expected for some hard proton tracks from lambda decay. The Level 1 physics stream [hj] then is

$$[hj] = L0 \cdot \text{Mult},$$

where

$$\text{Mult} = [n(L\overline{T}B\overline{x}) \geq 3] \cdot [n(L\overline{T}B\overline{y}) \geq 2] \cdot [n(R\overline{T}F\overline{x}) \geq 3] \cdot [n(R\overline{T}F\overline{y}) \geq 2].$$

## 5.9 Data Acquisition

A schematic of the data acquisition system is shown in Figure 5.6. The main sections of the system are the Readout Supervisor (RS), the 32 front end crates and data modules, the eight Level 3 processors, and the data acquisition host computer with its two tape drives. A short description of the system follows. A more complete description of the system can be found in reference [79].

The Readout Supervisor is a Camac crate of custom modules which interface the Level 1 trigger, the front end crates, the trigger processors and the host computer. The RS directs the acquisition and transfer of data from (in turn) the front end modules (TDCs [76, 75] and ADCs [74]) to the 3081E trigger processors [81] and finally to the host computer. Upon receiving a signal from L1, the RS sends signals for all crates to enable data inputs on their modules.

Each front end crate contains a crate scanner module which communicates with the front end modules via the crate backplane and with the RS via several twisted pair cables. It also is connected to each of the eight dual port memories of the Level 3 processors by a 17 pair cable. When instructed by the RS it enables the modules to receive data. Within 150 ns all signals received at the front end modules have been digitized and shifted into a two stage pipeline buffer on the front end modules, so that the front end is ready for another event even before the readout has been

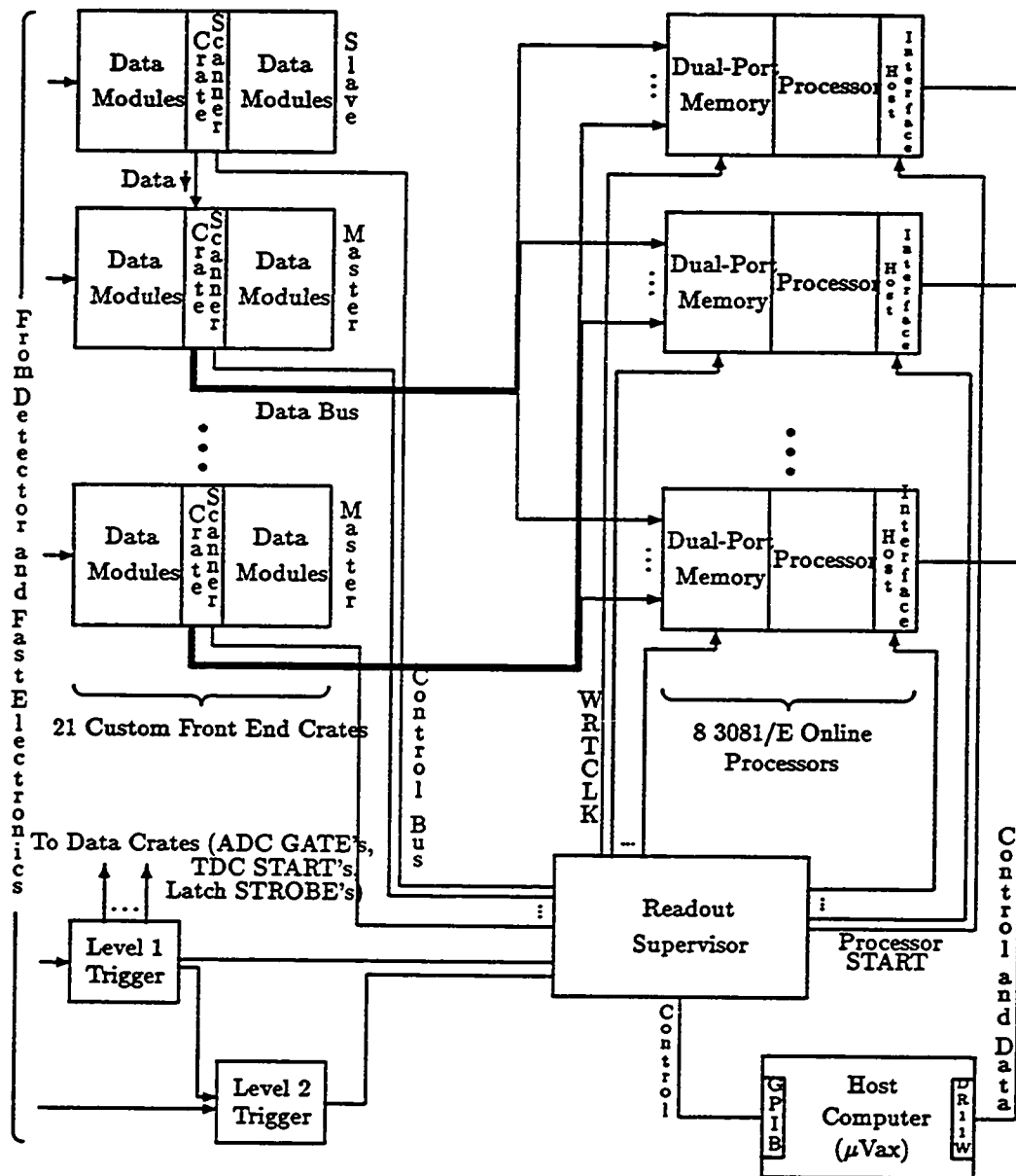


Figure 5.6: Block diagram of the E791 data acquisition system. Figure from [80]

completed. A *second* event will cause the experiment to deadtime until readout of the first event is completed, but the extra register greatly reduces the deadtime that would result without the two stage pipeline. If the stage 2 registers are empty an event only deadtimes the experiment until digitization is complete — about 200 ns. Data moves from the stage 1 register to the stage 2 register during the actual readout of the crate.

The readout proceeds by a shift of hit channel's data into a stage two register. The readout supervisor receives a status line from each front end crate and selects each crate in turn to clock data to the processor dual port memory with a cycle time of 100ns. The RS enables one processor to receive data from the event. The selected crate writes 16 bit data words from its modules containing channel address bits so that only hit channels need be readout. The crate ends its data transmission with an identifying crate word containing a crate identifier and a word count. The RS then selects the next crate with data to be readout, continuing until all crates have been cleared. The sparse data stream greatly reduces the readout time from a large number of channels, only a few of which are hit on any one event. Subsequent events are transferred to the selected processor's memory until it is full.

The readout supervisor then selects a new processor to receive data and starts the full processor executing the software filter. When a processor has completed execution of the L3 trigger program, the RS selects it to upload data to the host computer. Based on the L3 software trigger decision, an event is either uploaded, or discarded during the upload process. After uploading, the processor is returned to the queue of available processors.

The host computer receives data from the L3 processors as directed by the RS via a DR11W interface. The raw data records and Level 3 trigger data is buffered on disk and written to the active tape drive. When a tape is full a new run is begun automatically and tape writing begins on the other drive.



## 5.10 Level 3 Trigger (L3) Algorithm

The Level 3 trigger program runs on the eight 3081 emulators to select events for uploading. The software filter employed in the experiment was very simple due to time constraints during the running of the experiment. In principle partial reconstruction of the event may be performed to select promising events. The simplest thing to do is to require that data received from the drift chambers be consistent with at least two tracks on each side of the downstream chambers, and at least four tracks upstream. This is easily done in stages.

The first stage simply counts hits coming from each of the drift chamber planes. The front end TDCs for a DC plane are located in a single crate for exactly this reason. The number of hits in the plane is easily obtained from the crate word count inserted in the data stream by the crate scanner. Each hit gives one 16 bit data word. The crate adds a known number of words (usually two), one of which contains the word count from the crate. One track will pass through two drift chamber cells leaving two hit wires. Occasionally a third hit will be recorded on an adjacent wire for large drift distances. Requiring four hits in the plane corresponds to two tracks. For the front chambers we expect 4 tracks to be very close together. The requirement was set at 10 hits per plane, for DC 1 and DC 3 which have first and last hit TDCs (four separated tracks would produce hits on eight wires or 16 TDC channels), and five hits per plane for DC 2 which has only first hit TDCs. In chambers 4 and 5 where only two tracks are expected on each side the requirement was set at two or more hits per plane.

The second stage exploits the chamber geometry. The sum of drift times on adjacent wires will be approximately constant. The differing angles of the tracks and the resolution of the chamber will cause a broadening, but cuts are made to select good time sum wire pairs. A minimum number of good time sums in each DC plane is required in the L3 algorithm. The reduction in rate achieved by the software filter was more than a factor of eight.

The trigger is not 100% efficient due to inefficient wires. Also two tracks may pass through the same cells if they are very close together. This loss is not as bad

as it might seem since these events will prove difficult to reconstruct offline for the same reasons they fail the trigger. Of course noise hits in the chamber or hits from unassociated tracks from an early or late event, can cause a positive decision on an event we don't want. This is unavoidable, nonetheless, the ratio of useful events to junk is greatly reduced by the trigger process.

Events passing the software filter and a prescaled fraction of raw events, plus prescaled fraction of minimum bias events are uploaded and written to tape.

## 5.11 Online Monitor

The data acquisition host computer also runs a program to monitor the data integrity, beam quality and detector performance. The analyzer program does this by filling histograms which are viewed by shift personnel to quickly detect any number of problems with the detector subsystems, beam and the data acquisition system. In addition to the diagnostic histograms, a number of scalers in Camac crates are read-out by the online computer each spill. The scaler channels give quick feedback on the beam quality from target instrumentation, including secondary emission counters (SEC) and threefold coincidence scintillation counter telescopes (B5T1 and B5T2) viewing the primary target. The scalers also monitor trigger rates and signals from the L1 trigger. The scaler data is written to tape along with the event data for further analysis offline. Monitoring of the beam quality with the scalers and detector performance with the online histograms allowed shift personnel to ensure the experiment was running as optimally as possible. This was particularly important due to the minimal running time available to this experiment.

# Chapter 6

## Data Analysis

With the detector described in the previous chapter we undertook a search for  $H$  dissociation. Data were accumulated over a two week period. Initial attempts were made during the running to reconstruct lambdas and kaons to assess detector performance and choose beam intensity. Following the data taking, analysis began with the development of pattern recognition and fitting software. We chose to make a multi-pass analysis of the data set, applying more restrictive cuts to select interesting events at each pass and discarding those that fail to meet the selection criteria. The multi-pass approach has the advantage of minimizing computation time, since events are removed from the analysis at each pass. More practically it allows development of analysis tools in parallel with production analysis, allowing appropriate reconstruction programs to be developed in stages based on the result of the previous pass. This is an important advantage given limited manpower. The goal of the multi-pass analysis is to identify a final sample of  $\Lambda\Lambda$  events (from which we will select  $H$  candidates) and a calibration sample of  $\Lambda K_S^0$  events. Figure 6.1 is a flow chart of the data analysis, showing the four passes. In each pass, information from the offline reconstruction program is used to select events for further processing in the next pass. In the first pass we select events which fulfill minimal requirements on our ability to reconstruct track candidates from the tracking detectors. In Pass 2, we fit these track candidates to deduce the track parameters (momentum, direction), and we make more stringent track quality requirements to select events with at least

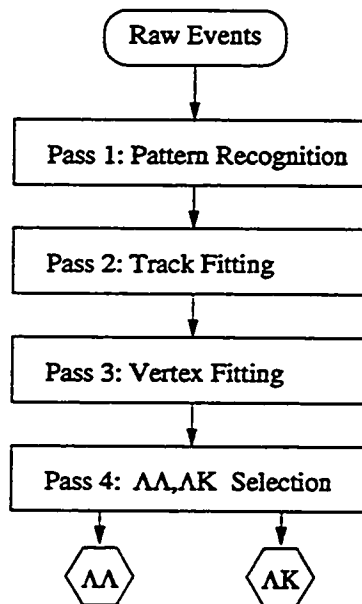


Figure 6.1: Data Analysis Flow Chart

four charged tracks. We refine the reconstruction in Pass 3 by fitting events with two neutral vertices to our expected topology of a  $VV$ . Finally in Pass 4 we select the  $VV$  events which satisfy invariant mass cuts for  $\Lambda\Lambda$  and  $\Lambda K_S^0$ . The remainder of this chapter describes each pass of the data analysis in more detail.

## 6.1 Raw Data Set

After an initial checkout of the detector, we recorded events with the dissociator in two positions. The first position placed the DSC approximately one meter from the first chambers. The DSC was moved 50 cm further upstream of the chambers about half way through the run. The two positions were a compromise between acceptance and concerns about our ability to reconstruct all four tracks from dissociation events in the front chambers where they are expected to be very close together. In the end reconstruction of close tracks was not an obstacle in the analysis, and the two dissociator positions enabled some cross checks on experimental results.

The data taking was broken up into separate runs. Each run is taken with a well defined trigger, and typically the beam conditions are similar through a run. Runs were routinely ended by shift personnel when beam conditions or detector problems warranted. A single run does not exceed one 6250 bpi data tape (approximately 140,000 events) and typically lasts 20-30 minutes. A total of 365 raw data tapes for physics runs were written, containing a grand total of 40,866,016 events. In addition various calibration runs were recorded with special triggers to aid in calibration of the detectors, including magnet off data for drift chamber alignment, dissociator coincidence triggers with background muons passing through the detector for energy calibration of the DSC and electron triggers for calibration of the lead glass calorimeter.

## 6.2 Drift Chamber Calibration

Before any tracking information can be used to understand the detector and beam during the beginning of the experiment, the drift chamber calibration constants must

be determined to some accuracy. Each chamber module must be located with respect to other detectors and the beam line. In addition, time offsets for each TDC channel must be determined to make accurate drift time measurements. For the final analysis these constants are refined to as high a degree as possible, but initial values are determined during the run to provide the trigger algorithm with the time offsets required to make time sum cuts on drift chamber hits. The initial values are also used to reconstruct kaon and lambda decays providing some reassurance that the experiment is working.

The time to distance relationship for the drift chambers was calibrated by a previous experiment [71]. For the operating conditions of the chambers, the drift velocity was found to be well approximated by a constant  $51 \mu\text{m}/\text{ns}$ . The time offsets for each wire channel and alignment constants for each drift chamber module are obtained by observing straight tracks taken with the magnet off. Loose pattern recognition cuts are made to identify wire hits in each chamber that appear to lie on the track candidate. A three dimensional fit to the track position (including the correlations from multiple scattering) is used to identify well measured tracks. From residuals in these fits the calibration constants are determined in an iterative process. Individual time offsets are determined using time sums of all wire pairs in a particular chamber module view for well measured tracks.

### 6.3 Pass 1

Events from the raw data set are expected to have a high multiplicity of charged tracks. However the Level 1 and Level 3 triggers are unable to discriminate between noisy events, where the multiple drift chamber and trigger hodoscope hits are caused by only partially contained tracks and events, and well contained tracks which may be reconstructed as vertices. In the first pass of the data our goal was to cut the noise events without removing too many interesting events. A preliminary track reconstruction is applied to the events and we simply require that it be able to identify at least one track candidate on each side of the detector for an event to pass. Most of the "noise" events are removed by this requirement, and the interesting classes of

events,  $V^0$ 's and double  $V^0$  vertices (VVs), may be selected from the remaining events. In this section the software used to identify track candidates (Pattern Recognition) and the event selection criteria applied in the first pass of data reduction are described.

### 6.3.1 Pattern Recognition

The goal of pattern recognition is to identify the collection of DC and TSC hits which are likely to be caused by a single charged particle. Each collection of hits consistent with a track is stored in a list of track candidates for further analysis. As the name implies this is done by exploiting the patterns of hits to be expected from a track passing through the spectrometer. The pattern recognition software was written in stages as illustrated in Figure 6.2. Following a brief description of the algorithm, each stage is discussed in detail.

After placing simple counting requirements on the number of hits in each detector element consistent with at least a single track on each side (PAHPRE), we next search the drift chamber hits for clusters of adjacent wires with valid hits (PAHCLS). The wire clusters are converted to hit positions by classifying hits using the sum of distances of closest approach on all adjacent wires (PAHSUM). Trigger counter hits are also checked for consistency by using cuts on hit times and cuts on time sums of top and bottom tubes. Good TSC hits are converted to  $(x, z)$  or  $(y, z)$  coordinates to be used in tracking (PAHSUT). From the list of  $(x, z)$  and  $(y, z)$  coordinate pairs, two dimensional track segments are formed by connecting the hits in the  $x$  or  $y$  view chambers (PAHGMX/Y). Next a full three dimensional track candidate is formed by performing an  $x, y$  match using the rotated chamber hits on all possible 2d track combinations. The list of all 3d track candidates is compiled by PAH3DM. Given the approximate track parameters, the hit positions may now be refined. From the  $(x, y)$  position at the magnet PAHADJ adjusts the track direction cosines before and after the magnet to correct for fringe fields and gives a better estimate of the track momentum. A special routine checks DC hit time sums given the track angle information and flags unusual topologies, such as tracks at extreme angles which pass by the same side of adjacent wires rather than between them (PAHSFL). The final stage of pattern recognition (PAHXPB) expands the

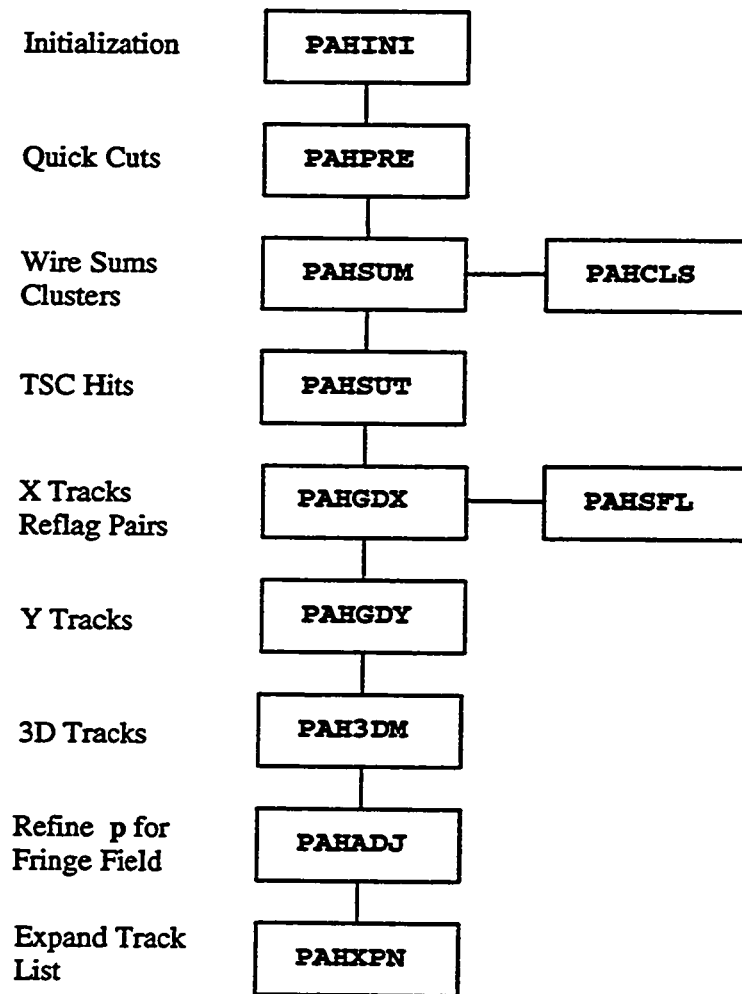


Figure 6.2: Pattern Recognition Flow Chart



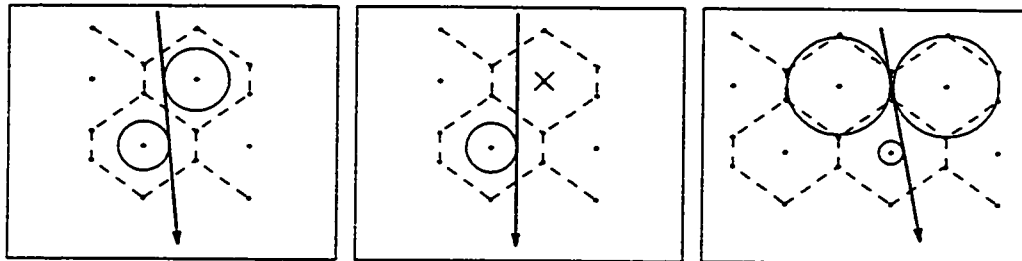


Figure 6.3: Wire Hit Topologies: Single Track

list of wire hit clusters to include the new topologies identified by PAHSFL. Any new ambiguity is added to the track list.

#### Clustering and Wire DOCA Sums

To form track candidates, the wire hit information from the drift chambers must be converted to coordinate points,  $(x, z)$  or  $(y, z)$ , through which it is likely that a track has passed. For each chamber view, a list of coordinate pairs is made by examining the drift time and wire position information, with account taken of the hit topology. For each cluster of adjacent hit wires, one or more coordinate pair is added to the list of points as described below.

A single track passing through a drift chamber will usually leave hits on a pair of adjacent wires, one in each staggered sub plane. Due to an inefficiency or a dead wire, occasionally only a single wire will be hit. An inclined track may also cause hits on three adjacent wires when it passes near the edge of two cells in one sub-plane. (Figure 6.3 shows these three common topologies.) When wire hits are caused by the passage of a single track on opposite sides of adjacent wires, the sum of the distances of closet approach (DOCA) is approximately equal to the wire pitch. Given the angle of the track, the expected DOCA sum may be calculated as

$$\Sigma_{\text{DOCA}} = b \cos(\alpha) \pm a \sin(\alpha), \quad (6.1)$$

where the sign of the second term is determined by comparing the track direction to

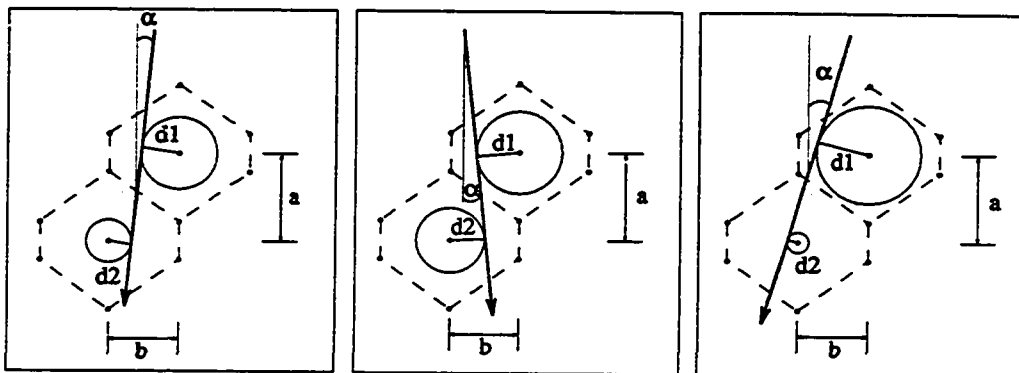


Figure 6.4: Good DOCA Sums and DOCA Difference

the vector between the two wires. Here  $a$  and  $b$  are the wire separations, and  $\alpha$  is the track angle as shown in Figure 6.4.

Likewise, when the track passes the same side of two adjacent wires, possible for even slightly inclined tracks, the DOCA *difference* is approximately equal to the wire pitch. In these cases the expected DOCA difference given by

$$\Delta_{\text{DOCA}} = b \cos(\alpha) - a \sin(\alpha). \quad (6.2)$$

DC hit pairs caused by real tracks of a given angle will have either a good DOCA sum or a good DOCA difference. Given a distribution of track angles at a particular chamber, good wire hits will fall into an expected range of  $\Sigma_{\text{DOCA}}$  or  $\Delta_{\text{DOCA}}$ . Pattern recognition uses this characteristic to identify good hits in the DCs. Once a track candidate is found, the angle is known, and the corrected sum or difference aids in determining where the track passed relative to the wires.

These single track topologies are adequate to identify most of the DC hits, however there are a significant number of events in which there are two or more tracks passing through the same cell or adjacent cells. (See Figure 6.5.) This occurs often in the front chambers, where the track separation is very small, as expected for signal events. (In Monte Carlo, simulated  $H$  dissociation events are typified by four very close tracks

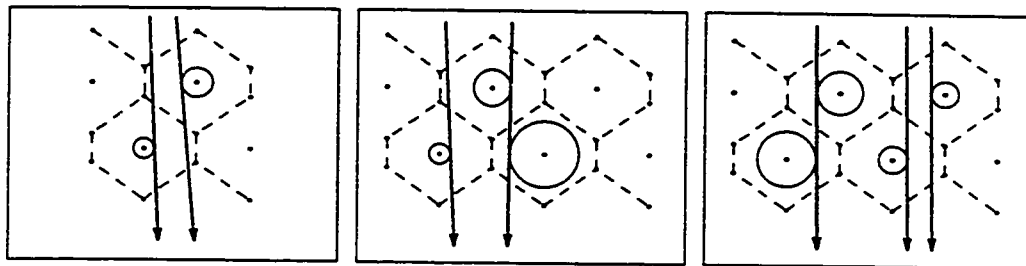


Figure 6.5: Wire Hit Topologies: Two or More Tracks

in the front chambers. In addition, the protons often remain very close together even after the bend in the magnet.) A second track within the same cell disrupts the usual DOCA sum and DOCA difference relationships used to identify good wire hits. Two or more tracks close together can cause more than 2 or 3 adjacent hit wires. In addition, delta rays may leave large groups of adjacent hits.

The pattern recognition strategy which efficiently identifies drift chamber hits accounts for the close tracks by first grouping the DC hits into clusters, which are defined as groups of  $n$  consecutive hit wires, which may be caused by one or more tracks. The clusters are then scanned for good wire pairs to identify cells consistent with a single track. Cells which fail good DOCA sum cuts are considered to result from multiple tracks.

The clusters are converted to hit positions for the track finder by requiring good DOCA sums between the  $x(y)$  and  $x'(y')$  subplanes. The expected DOCA sum depends on the track angle, so these cuts are set by looking at DOCA sum distributions from real data and Monte Carlo, which reflect the distribution of track angles from actual tracks. Figure 6.6 shows the uncorrected DOCA sum distribution at chambers 3x and 4Ry in actual data, with the cuts indicated on the figure. (The cuts at DC4X and DC5X are set very wide, to allow the low momentum pions from  $\Lambda$  decays to be accepted. In Monte Carlo, the DOCA distribution in 4Rx and 5Rx is very wide due to the varied distribution of angles for the low momentum pions after they are bent in the magnetic field; once the track angle is determined the corrected DOCA sum is

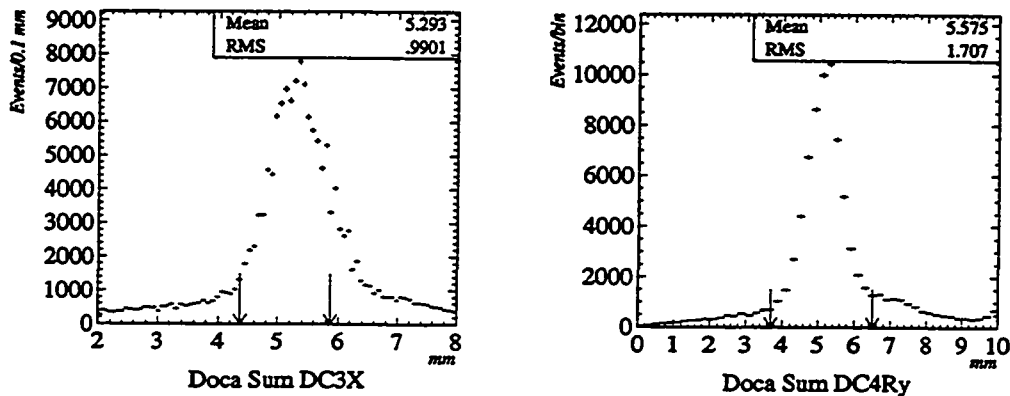


Figure 6.6: DOCA sum distribution from data events at chambers 3x and 4Ry. The cuts shown select good pairs consistent with a single track passing through the cell.

cut at  $5.1 \pm 1.0$  mm in PAHSFL.)

To avoid massive multiplicity of track candidates two assumptions are made to reduce the number of hits entered for clusters. First, wires are assumed to be 100% efficient to the extent that no hit is entered on the outside edge of a cluster, since only rarely will the adjacent (unhit) wire be dead or inefficient. The second principle applied assumes that occasionally two tracks will pass within the same cell, causing time sums to fail the single track cut. Hits are entered to allow both tracks to be identified. No attempt is made to account for more than two tracks passing within the same cell.

Applying these principles to various cluster topologies gives the following hit assignments: Isolated single hits ( $n = 1$ ) are entered as two coordinate pair points, one on each side of the wire assuming normal incidence for the track. Ambiguities like this are always entered separately into the hit list for forming track candidates. A two wire cluster ( $n = 2$ ) is identified either as a good time sum double or as two single wire clusters. In the case of a double, one point is entered into the list. This position is given by a center of mass like weighting of the drift distances. When the DOCA

sum fails the cut, each wire is entered separately, with the points on the inside of the pair. This strategy assumes the bad DOCA sum is caused by the passage of two tracks through the same cell.

The special case of a triple ( $n = 3$ ) allows for the single track causing a triple cluster. If the DOCA for the outside wires is greater than 80% of the cell radius, and the DOCA from the center wire of the triple is less than 35% of the cell radius, the cluster of three wires is identified as a good triple. In this case a single point is entered in the list. If the cluster fails the triple cuts then the two pairs of adjacent wires are considered. If there is one good DOCA sum, the good pair is treated as a double, and the remaining wire adds one point on the side closest to the other hit wires. If neither pair is good, four points are entered, again omitting the outer ambiguity solutions for the edge wires of the cluster.

Within a cluster of 4 or more hits, DOCA sums of all adjacent pairs are checked. A good DOCA sum puts a single point on the list. A wire with no good DOCA sum with either neighbor is treated as an isolated single hit, putting two points on the list. End wires of the cluster enter points only on the inner edge, in keeping with the high efficiency assumption. All pairs in the cluster are checked, and multiple points are entered for the cluster.

### TSC Hit Conversion

It is desirable to make full use of the trigger hodoscope information in identifying tracks. PAHSUT does this by selecting TSC hits which are in time with the event. In time hits are converted to hit positions  $(x, z)$  or  $(y, z)$ . For X counters both top and bottom tubes must be hit, or one tube may be hit if there is also a latch hit for that counter. A cut is placed on the hit times and the mean time for X tubes without a latch hit to ensure good timing. For Y counters the timing cut requires a good time or a latch hit for an early time. (The TDCs digitize the first hit to arrive within the gate.) Hits passing the timing cuts are converted to coordinate pairs by using the center of the counter. (In principle there is  $y$  hit location information available in the time difference from X counters with top and bottom tube hits, but this is not used in pattern recognition.)

## 2d Track Forming

The next stage in pattern recognition forms track candidates from the DC and TSC hits. Given the spectrometer geometry and vertical field of the spectrometer magnet, tracks are expected to be straight lines in the  $(y, z)$  plane. Tracks in the  $(x, z)$  plane may be approximated as piecewise linear, with a kink at the magnet position, which amounts to approximating the magnet as a  $p_T$  kick or a thin lens. Positively (negatively) charged tracks are bent to the left (right) side of the spectrometer by the magnet. In principle tracks may cross from one side to the other between DC4 and DC5, however the acceptance for these tracks is extremely small. The trigger is also not designed with this in mind. For these reasons tracks candidates are required to lie on a single side (left/right) of the spectrometer. This applies only to DC4, DC5 and the TSC.

The strategy for identifying tracks in the horizontal plane is to find a straight segment downstream of the magnet which meets a segment from upstream at the center of the magnet ( $z = 24$  m). Downstream segments are found using DC4, DC5 and the TSC, and upstream segments use only DC1 and DC2. As illustrated in Figure 6.7, these segments are projected to the center of the magnet, and a cut is made on the difference,  $\Delta = x_{\text{Front}} - x_{\text{Back}}$ . In the approximation of a small change in direction for the track, or equivalently for an infinitely thin magnet,  $\Delta$  will be zero within resolution for actual tracks. Because the magnet is not infinitely thin (particularly for low momentum tracks), the difference between projected positions at the magnet center will have an asymmetric distribution. This is illustrated for the exaggerated case in the figure. To set the cut on  $\Delta$ , we use distributions from Monte Carlo and actual data.

The  $(x, z)$  track forming begins by considering all track segments between DC4 and DC5, and placing a cut on the slope of the line segment, because only certain slopes have a chance of intersecting a track segment from the front of the spectrometer. Figure 6.8 shows the slope distribution from sample data events. At this point the segment is projected to the trigger counters. All good TSC hits are compared to the expected position for the segment. A cut requiring the difference of the projected position and the TSC hit position to be less than some tolerance is made. (See

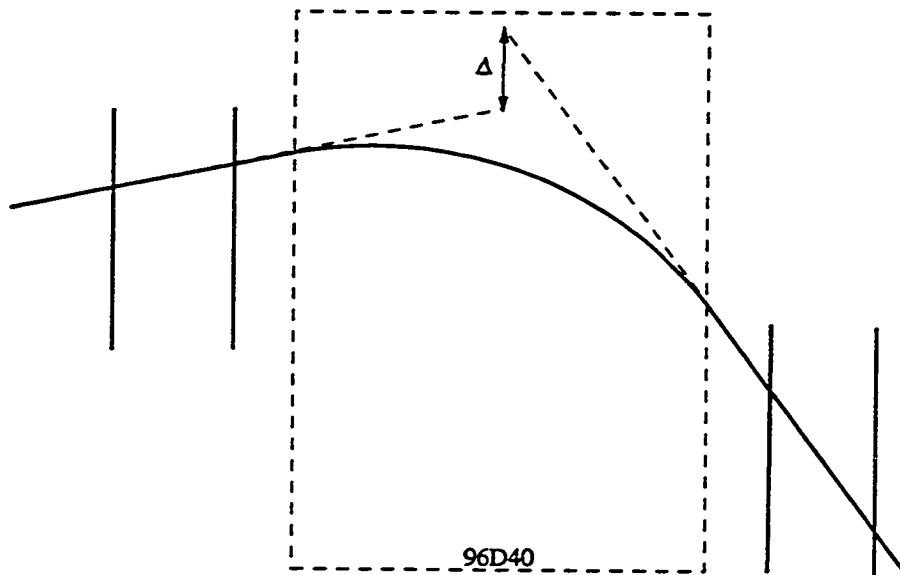


Figure 6.7:  $x$ -track finding by projecting segments from front and back chambers to the center of the magnet. A cut is made on the difference,  $\Delta$ , of the projected positions. As shown in the figure, the distribution in  $\Delta$  for actual tracks is asymmetric, since the point of inflection for the low momentum tracks is not at the center of the magnet. The figure is exaggerated for clarity.

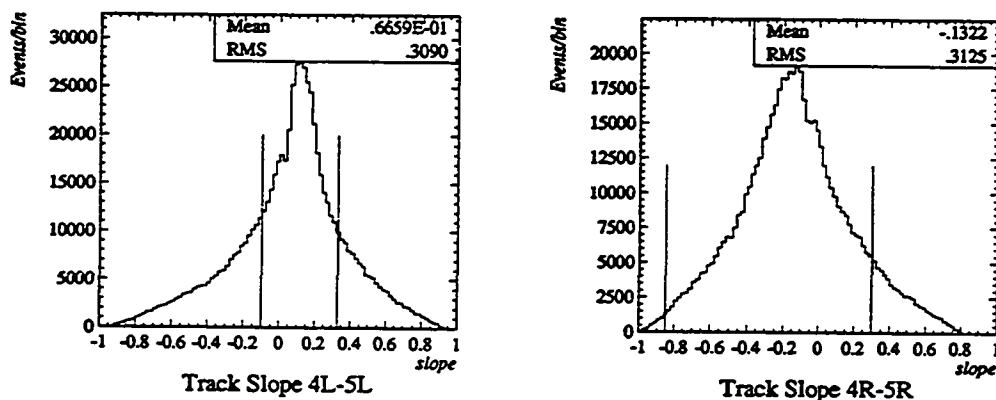


Figure 6.8: Track Segment Slope Distributions from Data

Figure 6.9.) To be consistent with the Level 1 trigger, left side tracks must have a good match in either TSC1x or TSC2x, while for right side tracks only TSC1x is required. Those segments with a TSC match are projected to the magnet center. Segments are formed using DC1 and DC3, which are projected to the magnet center, and a cut is placed on the difference between the front and back projections. The cuts placed on track slopes, TSC match, magnet match and the effective magnet position are chosen using actual data, by locating peaks in the relevant distributions. Monte Carlo simulation was also used to check the algorithm and cuts. Figures 6.8, 6.9 and 6.10 show distributions and cuts used to select  $x$  tracks from an actual data run.

In the  $(y, z)$  plane tracks are typically straight, however there is a substantial vertical focusing effect for low momentum tracks on the right side of the spectrometer (the  $\pi^-$  side in  $\Lambda$  decay). This is understood since the track angle changes appreciatively due to the small momentum of these tracks, and the small  $z$ -component of the magnetic field causes a focusing of tracks in the vertical plane. To account for this,  $y$  tracks on the right side were treated the same as  $x$ -tracks. The distributions and cuts are shown in Figure 6.11. As in the  $x$ -track case, the magnet match cut is



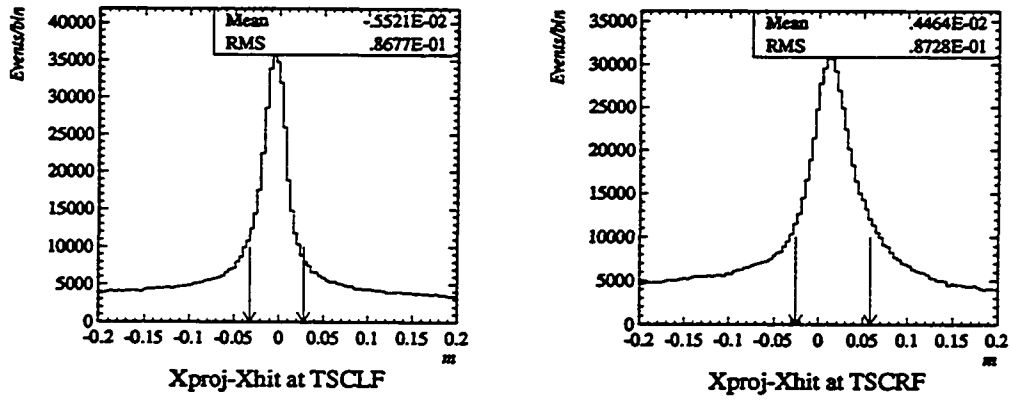


Figure 6.9:  $x_{hit} - x_{project}$  at TSC for  $x$ -track segments

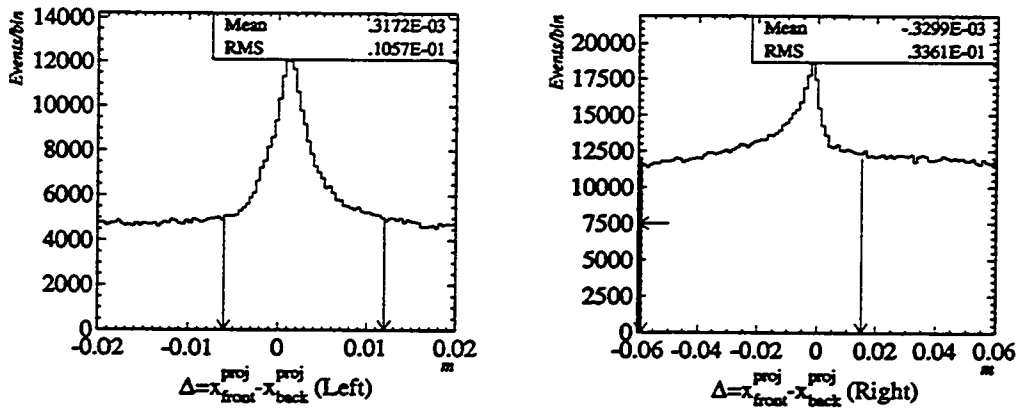


Figure 6.10: X-Track Segment Matching at Magnet Center

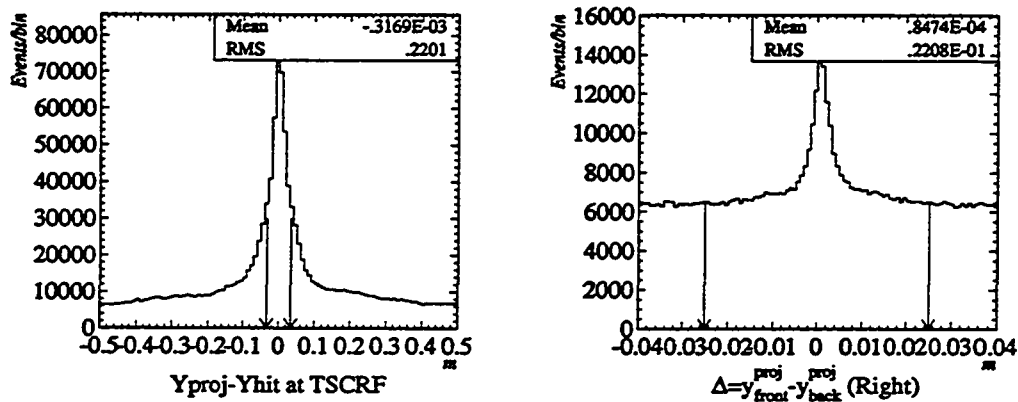


Figure 6.11: Y-Track Recognition for Right Side

made very loose to efficiently accept low momentum tracks. On the left side, where there is very little focusing, tracks are formed by extrapolating all segments between the downstream chambers (DC4&5) to the the upstream chambers DC1 and DC2. The downstream segments are required to have a hit in the either TSC1y or TSC2y. (Right side tracks must match at TSC1y.) A cut is placed on the missed distance at chamber 3. Surviving segments are refined by adding the new hit and extrapolating to DC1 where a final cut is made. As can be seen from Fig. 6.12, these cuts were chosen as tight as practical without reducing the efficiency for identifying real tracks. (The TSC cuts are too restrictive. This is a small loss of efficiency. Unfortunately this was not noticed until too late.)

### 3d track Forming

From the two 2d track lists a preliminary list of 3d tracks is made by pairing all  $x$  tracks with  $y$  tracks, and interpolating at the rotated chamber position. A match on both  $u$  and  $v$  coordinates at this chamber is required. For each  $x$  track  $y$  track combination, all hits in DC2 are checked for a  $u, v$  match. This cut can be made very

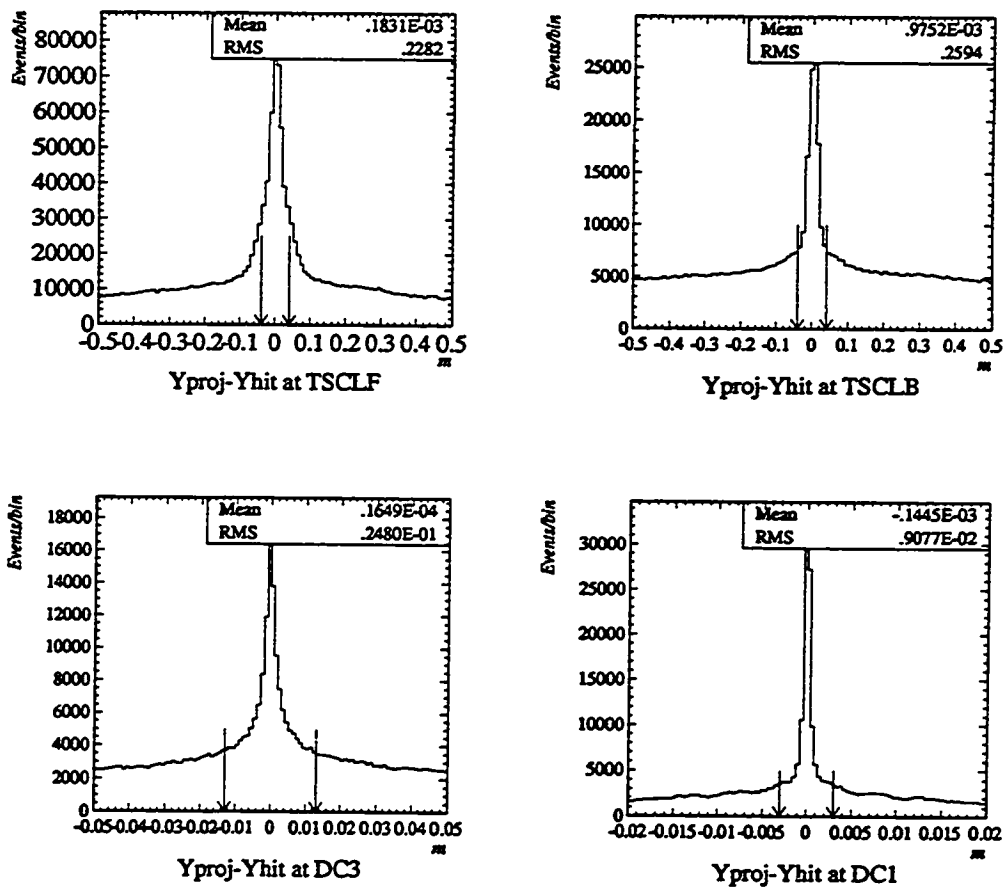


Figure 6.12: Y-Track Recognition for Left Side

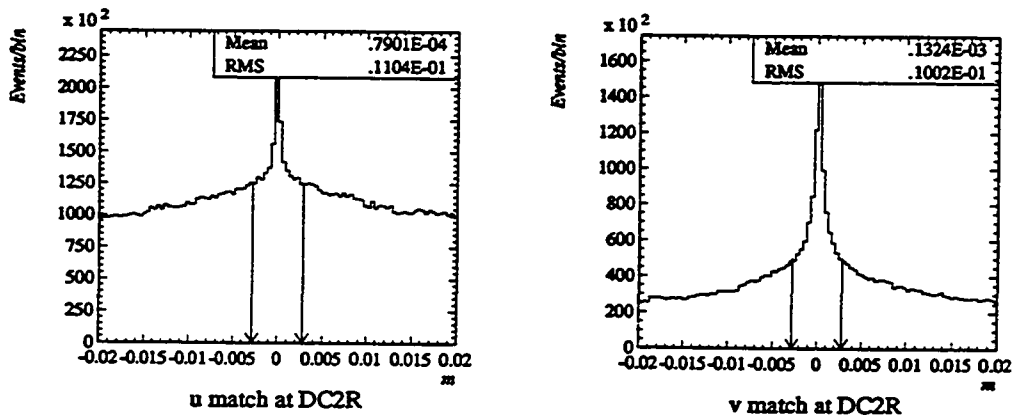


Figure 6.13: 3d-Track Matching at DC2

narrow without loss in efficiency (see Figure 6.13), substantially reducing combinatoric ghost tracks, particularly in the upstream track segments. All  $x, y$  track pairs that pass the  $u, v$  match are considered as 3d track candidates. From the change in track slope in the magnet an estimate of the track momentum is made.

At this point the list of 3d-track candidates includes all possible combination of wire hits from each chamber, provided the track candidate passes the track selection cuts. In the case of ambiguities, such as a single wire hit where the actual hit position may be on either side of the wire, each ambiguity solution appears separately in the track list, and indeed may appear in more than two tracks. All ambiguities are resolved at a later stage in the event reconstruction.

### Hit Position Adjustment

Given a candidate track, the track angle is known allowing a refined DOCA sum or difference cut to be made on adjacent wires using Eqs. 6.1 and 6.2. It was found that there were a significant number hits in DC4 and DC5 where tracks go by the same side of the wires in a pair. In part these are due to extremely high angle tracks on the right

side, where the acceptance and trigger allows this. To account for these types of hits, the hits used in the downstream track segments are recategorized using the expected DOCA sum and DOCA differences. Refined cuts on  $\Delta_{\text{DOCA}}$  and  $\Sigma_{\text{DOCA}}$  are made by subtracting the expected sum or difference from Eqs. 6.1 and 6.2 and dividing by the expected resolution on these quantities ( $\approx 200\text{--}300\mu\text{m}$ ). The resolution is determined from data separately for each chamber. For the downstream chambers on the right side where the angles are large, the resolution set conservatively at  $400\mu\text{m}$ . The cut is placed at  $3.5\sigma$ . Pairs which are consistent with good DOCA differences but not good DOCA sums are tagged as same side hits for the fitter. Pairs with both good sums and good differences cause a copy of the track to be placed at the end of the list with the new assignment. Finally if both sums and differences fail, the pair is split into two single hits; the old track is flagged as having a single instead of a good time sum, and a new track using the other wire is added to the end of the list of 3d tracks.

### Final Track List

A track entry in the final track list contains hit assignments at each chamber, including  $(x, z)$  and  $(y, z)$  at chambers 1, 3, 4 and 5 and  $(u, z)$  and  $(v, z)$  at chamber 2. The two dimensional tracks in  $x$  and  $y$  and the slopes of the upstream and downstream segments are also referenced in the list. From the change in direction of the track in the magnet, an estimate of the momentum of the track is made and a charge is assigned to the track. These parameters are used by the track fitter as an initial solution.

### 6.3.2 Pass 1 Selection Cuts

During Pass 1 events are processed by the offline analysis program to select events worthy of further reconstruction. Pass 1 includes three streams of events which are written to the output tapes. In the raw stream, a prescaled sample (1/5000) of all events are written to tape. The minimum bias stream and the physics stream are classified based on the Level 1 trigger bits. All streams are processed by pattern recognition, but physics and min. bias events are written to tape only if they satisfy

the cuts placed on the result of pattern recognition. In addition to the physics and min. bias triggers processed in Pass 1, calibration events are also present in data. Pedestal triggers for the ADCs are written to the Pass 1 output tape for use in deriving charge from the ADC counts. Scalar "events" are processed into run summaries and histograms, but not written to the output tape. Other calibration events are not written out.

All three streams must satisfy data quality requirements intended to remove events with incomplete detector information due to data acquisition errors. These cuts are essentially consistency checks on the raw data buffer for the event, including Level 1 and Level 3 trigger output. Specifically, events are removed if they have any of the following problems: an illegal 3081/E identification word, no Level 1 trigger bits set, both physics and calibration trigger bits set, missing or illegal crate identification words, or a discrepancy between bits 7 and 8 of the Level 1 trigger word.

The pattern recognition cuts require the event to have at least one 3d track on each side of the spectrometer, each having hits in all five drift chamber stations. Cuts are made as soon as the relevant information is available, so that no further processing of failing events is performed to avoid needless CPU time. In addition, a special version of pattern recognition software was used to shorten the processing time. The special version stops processing an event as soon as one good track is found on each side of the detector. The full pattern recognition is run on the surviving events in Pass 2. The Pass 1 pattern recognition cuts are listed in Table 6.1.

### 6.3.3 Pass 1 Results

A total of 365 raw data tapes (each representing a single run) were analyzed in Pass 1. All but 20 of these runs were taken with the standard Level 1 trigger ([hj]), the remainder representing runs taken with preliminary attempts at a standard trigger before the final trigger was setup. The 345 [hj] runs contain 40,866,016 events with physics or minimum bias triggers in roughly equal amounts. The fraction of physics events surviving the Pass 1 cuts is 0.425, that of the minimum bias events, 0.126. Table 6.2 gives a summary of the first pass of analysis.

<b>Hit Identification</b>	
Wire DOCA	$-0.0005 \text{ m} \leq \text{DOCA} \leq 0.006 \text{ m}$
Wire DOCA Sum DC1-3	$0.00510 \pm 0.00077 \text{ m}$
Wire DOCA Sum DC4-5	various
TSC hit time	$-5.0 \text{ ns} \leq t \leq 21.0 \text{ ns}$
TSC mean time	$-3.0 \text{ ns} \leq \bar{t} \leq 18.0 \text{ ns}$
<b>x Track Finding</b>	
$\frac{dx}{dz}$ DC4-5 Left	$-0.1 \leq \frac{dx}{dz} \leq 0.33$
$(x_{\text{Proj}} - x_{\text{Hit}})_{\text{TSC}}$ Left	$-0.002 \pm 0.030 \text{ m}$
$(x_{13} - x_{45})_{\text{MAG}}$ Left	$0.003 \pm 0.009 \text{ m}$
$\frac{dx}{dz}$ DC4-5 Right	$-0.85 \leq \frac{dx}{dz} \leq 0.30$
$(x_{\text{Proj}} - x_{\text{Hit}})$ Right	$0.017 \pm 0.042 \text{ m}$
$(x_{13} - x_{45})_{\text{MAG}}$ Right	$-0.0225 \pm 0.0375 \text{ m}$
Number of 2d x tracks	$\leq 150$
<b>y Track Finding</b>	
$(y_{\text{Proj}} - y_{\text{Hit}})_{\text{TSC}}$ Left	$0.000 \pm 0.040 \text{ m}$
$(y_{\text{Proj}} - y_{\text{Hit}})_{\text{DC3}}$ Left	$0.000 \pm 0.013 \text{ m}$
$(y_{\text{Proj}} - y_{\text{Hit}})_{\text{DC1}}$ Left	$0.000 \pm 0.003 \text{ m}$
$(y_{\text{Proj}} - y_{\text{Hit}})_{\text{TSC}}$ Right	$0.000 \pm 0.034 \text{ m}$
$(y_{13} - y_{45})_{\text{MAG}}$ Right	$0.000 \pm 0.025 \text{ m}$
Number of 2d y tracks	$\leq 150$
<b>3d Track Finding</b>	
$(u_{\text{Proj}} - u_{\text{Hit}})_{\text{DC2}}$	$0.000 \pm 0.0028 \text{ m}$
$(v_{\text{Proj}} - v_{\text{Hit}})_{\text{DC2}}$	$0.000 \pm 0.0028 \text{ m}$
Number of 3d left tracks	$\geq 1$
Number of 3d right tracks	$\geq 1$

Table 6.1: Pass 1 Pattern Recognition Cuts

<b>All Runs</b>	
Number of tapes read	365
Number of tapes written	131
Number of [hj] trigger tapes	345
<b>[hj] Runs Only</b>	
Total number of events	40866016
Total number of events reconstructed	11660444
Total number of events written	11665773
Total number of L1 physics read	21547888
Total number of L1 physics reconstructed	9147799
Total number of L1 minimum bias read	21449168
Total number of L1 minimum bias reconstructed	2695032
<b>Readout Problems</b>	
Total number of Unpacking errors	2080
Total number of bad L1 triggers	32
Total number of L1 bit 7 $\neq$ bit 8	18607
Total number of bad or missing DAQ crate	1810401

Table 6.2: Pass 1 Summary



A number of anomalies in the data were noted during Pass 1. Notably there was a data acquisition bug that affected a single Level 3 processor. Events processed by Emulator 7 were missing data from a one data acquisition crate (likely due to a cabling problem). Fortunately only 4.4% of the data was affected instead of  $\frac{1}{8}$  since Emulator 7 was the last in the queue and therefore only fully utilized at the highest intensities. This problem was not fixed during the run, and these events must be discarded. There was a period of several runs in which trigger information from the Level 1 trigger was inconsistent in some events. Bits 7 and 8 of the trigger word should be equal. The anomaly was detected during the experiment using the online monitor, and the emulator programs were reloaded, curing the problem before the next run. There were relatively few other data acquisition problems in the data.

Each of the Pass 1 data analysis jobs kept a record of the number of input events, the number passing and the beam conditions as recorded in the raw data file scalar events. Strip charts of these variables as a function of run number provide a check on the running conditions for the experiment.

The main beam intensity indicators are a secondary ionization counter placed upstream of the primary target (B5SEC) and the dissociator itself. As mentioned earlier the counts from the final segment of the DSC was input to a scalar channel, and this scalar was read out and the data written to the raw tapes. The aperture of the ionization counter was larger than the target itself, so the SEC counts do not track the actual beam delivered on target as the steering changes. The DSC counts are a better measure of the actual beam hitting the target. During Pass 1 these scalar records were summed for each run, and a strip chart of DSC and SEC counts normalized to the number of beam spills were produced as a measure of the beam conditions. As can be seen from the B5SEC and DSC8 strip charts (Figure 6.14), the beam conditions fluctuated during the experiment. Prior to Run 820, we were still tuning the experiment and finding optimal primary beam steering. Another obvious feature is visible at Run 961 when the dissociator was moved 50 cm further away from the front chambers. The smaller solid angle subtended by the chambers allowed us to raise the beam intensity to match our self-imposed chamber rate limit. The other variations appear to be consistent with changing conditions in the primary

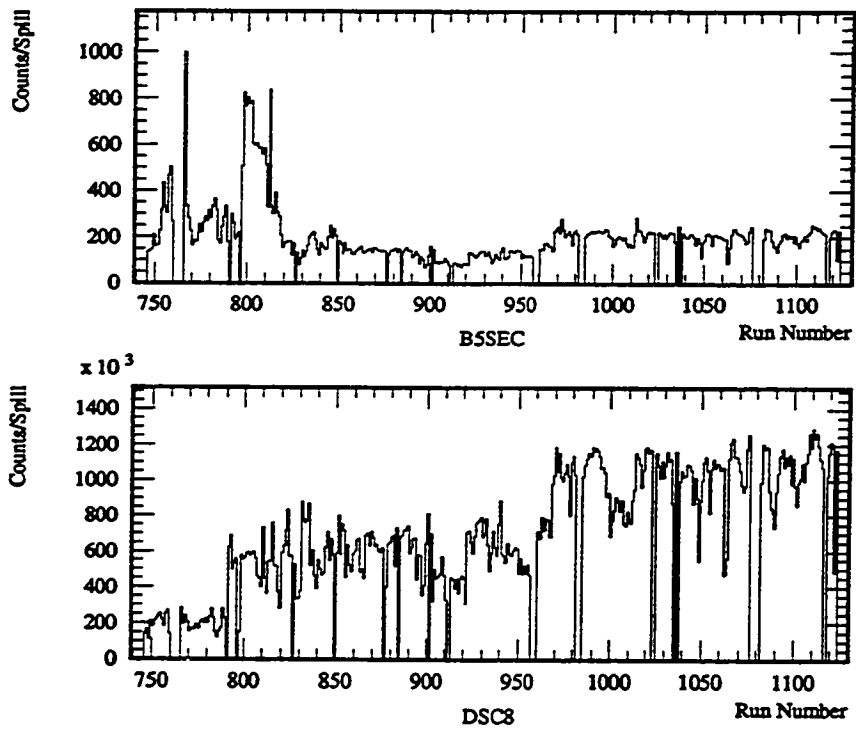


Figure 6.14: Beam Strip Charts

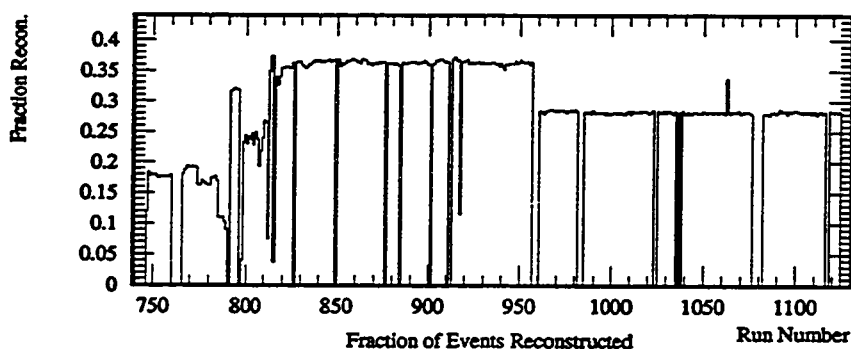


Figure 6.15: Pass 1 Reconstruction Fraction

beam steering and intensity associated with controlling the uncharacteristically low intensity beam. The beam diagnostics used by the operators were calibrated for a different target and targeting angle and intensity. The experiment ran at 25–50 times lower intensity than the previous experiment on the same beam line.

A strip chart of the fraction of events passing pattern recognition plotted against run number provided a check that the Pass 1 analysis was working consistently for all runs. (Figure 6.15) The fraction of physics triggers (including minimum bias events) with at least one left side and one right side 3d track found is greater for the downstream dissociator position at the beginning of the run. The fraction appears to be stable within the periods defined by the DSC position, with the exception of a single run. In Run 1062 the fraction of reconstructed events increases. It was found that this was isolated to the first 3 emulators, but remains unexplained.

## 6.4 Pass 2

Having selected events with at least two recognizable tracks (including ghost tracks from ambiguities) in Pass 1, we then applied further software filters to narrow down the sample to events with at least four well-reconstructed independent tracks (i.e. likely to be associated with the passage of 4 distinct particles), two on each side

of the spectrometer. In addition, a preliminary reconstruction of vertices of charged tracks (2tkV's) was made to flag events with at least two independent vertices. These flagged events are selected for further reconstruction in Pass 3, while any event with at least four good tracks is retained to aid in the study of backgrounds to our double vertex signal. This section describes the software used to identify and fit independent tracks from the various ambiguity solutions found by pattern recognition, the vertex fitting software, and the application of these programs to the data.

### 6.4.1 Track Grouping

The pattern recognition software efficiently identifies track candidates from the drift chamber hits, however the price paid for efficiency here is a multiplicity of tracks. All ambiguities in drift chamber hits are considered separately, and this can lead to a single charged particle being reconstructed as two (or more) software track candidates. For example, a single isolated wire hit is converted into two hit positions, allowing for the possibility of a track passing either side of the wire. Tracks are formed from the available hits at each chamber, so there may be two tracks, identical except for the choice of which software hit position is used at the ambiguity, in the final list of good track candidates. So we see how a single charged particle traversing the spectrometer may be identified by pattern recognition as many track candidates. The problem of correctly reconstructing events requires distinguishing between software tracks which actually represent a single track in the spectrometer and software tracks which represent separate tracks in the spectrometer. It is also necessary to select the best ambiguity solution from the set of software tracks associated with an actual track in the spectrometer.

A scheme for untangling the necessarily complicated collection of tracks produced by pattern recognition separates the tracks into distinct groups, where each group is composed of tracks representing different ambiguity solutions to a single real track in the spectrometer. Each group then is considered to represent a single track in the spectrometer, and within each group the best solution under some criterion is considered to be the correct ambiguity solution. Of course at some point it is impossible

to distinguish two extremely close real tracks from two software tracks formed from finite resolution hits (and noise) in the drift chambers.

The problem may be expressed as the grouping of elements of a list (software tracks) based on an equivalence criterion. If two elements are equivalent then they are placed in the same group. When the equivalence criterion is reflexive, symmetric and transitive, algorithms exist for grouping the list into equivalence classes in a minimum number of passes [82].

This is the approach taken by Josh Klein when writing the track grouping algorithm. Although not transitive, a sensible criterion for equivalence is for tracks to share more than some number of hits from the drift chambers in order to be considered equivalent. As a trial criterion we took 6 out of 8 possible hits in the downstream drift chambers (DC4,5). Since this includes both  $x$  and  $y$  wires, the tracks are really quite close together. However, in  $H$  Monte Carlo events it was found that this criterion found too few groups (less than four) in about 2% of the events. Adding the requirement that tracks share at least one out of two possible hits in DC1x corrected this problem. Out of several hundred Monte Carlo events none were found to have less than four groups. The criterion of 6/8 hits shared in DC4 and DC5 plus 1/2 hits shared in DC1x proved to be functionally transitive for our Monte Carlo. A test of the equivalence class algorithm (which assumes a transitive criterion) was undertaken by comparing with a more computation intensive method of determining two tracks to be independent of each other if they share less than some number of hits. No significant differences were found in a sample of several hundred Monte Carlo events, and the faster method was chosen.

### 6.4.2 Track Fitting

Given a track hypothesis from pattern recognition, an accurate measurement of its momentum and direction cosines may be obtained by fitting the trajectory using the magnetic field measurements. For the purposes of the experiment we found two separate fitters useful. The first one fit to the measurements at the front chambers, without including the effect of multiple scattering (since the chambers are close).

This fit is important because it includes the rotated chamber to constrain tracks in three dimensions. The second fit includes multiple scattering and the downstream chambers, but excludes the rotated chamber (due to the increased complexity in the covariance matrix). The front and full fitters were written by Robert Cousins and are based on the same technique which was developed for E791 by Cousins and Philip Mélése [83, 84].

### Fitting Formalism

An abstract fitting problem may be viewed as the determination of the set of parameters,  $\vec{\alpha}$ , which in some sense best reproduce a set of  $N$  measurements  $d_i$  by the predictions  $y_i = y_i(\vec{\alpha})$ . If there are  $N$  measurements and  $M < N$  parameters, it is possible to determine  $\vec{\alpha}$  so that  $\chi^2$ , a weighted average of the deviations ( $d_i - y_i$ ), is minimized. (See equation 6.3)

$$\chi^2(\vec{\alpha}) = \sum_{i=1}^N (d_i - y_i(\vec{\alpha})) W_{ij} (d_j - y_j(\vec{\alpha})) \quad (6.3)$$

$$(W^{-1})_{ij} = E_{ij} = \langle \sigma_i \sigma_j \rangle \quad (6.4)$$

When the weights  $W_{ij}$  are defined as the inverse of the covariance matrix of the data ( $E_{ij}$  in Equation 6.4), the  $\chi^2$ -function has a well defined meaning in terms of likelihood of the data points being consistent with the parameters  $\vec{\alpha}$  and the predictor  $y_i(\vec{\alpha})$ .

The Newton Step method is one method of iteratively determining the best solution  $\vec{\alpha}$  from the data points [82]. The method relies on a Taylor series expansion of the  $\chi^2$ -function in the parameters  $\vec{\alpha}$ :

$$\chi^2(\vec{\alpha}) \approx \chi^2(\vec{\alpha}_0) + \left. \frac{\partial \chi^2}{\partial \alpha_k} \right|_{\vec{\alpha}_0} \cdot \Delta \alpha_k + \frac{1}{2} \left. \frac{\partial^2 \chi^2}{\partial \alpha_k \partial \alpha_l} \right|_{\vec{\alpha}_0} \Delta \alpha_k \Delta \alpha_l \quad (6.5)$$

$$\approx \chi_0^2 - 2\Delta \vec{\alpha} \cdot \vec{g} + \Delta \vec{\alpha} \cdot \mathbf{A} \cdot \Delta \vec{\alpha} \quad (6.6)$$

Here

$$g_k = (d_i - y_i) W_{ij} \left. \frac{\partial y_j}{\partial \alpha_k} \right|_{\vec{\alpha}_0}, \quad (6.7)$$

and the curvature matrix,

$$A_{kl} = \frac{\partial y_i}{\partial \alpha_l} \Big|_{\vec{\alpha}_0} W_{ij} \frac{\partial y_j}{\partial \alpha_k} \Big|_{\vec{\alpha}_0}. \quad (6.8)$$

To minimize  $\chi^2$  the parameters  $\vec{\alpha}$  are varied, and it is found that a new approximate solution is given by

$$\Delta \vec{\alpha} = \vec{\alpha} - \vec{\alpha}_0 = A^{-1} \cdot \vec{g}. \quad (6.9)$$

The  $\chi^2$  of the new approximate solution  $\vec{\alpha}$  is also predicted via

$$\chi_{\text{new}}^2 = \chi_0^2 - \Delta \vec{\alpha} \cdot \vec{g}. \quad (6.10)$$

Successive applications of the method allow iteration to a final solution. The inverse of  $A$  is the error matrix for the fit parameters, so the fit gives an error estimate in addition to the best fit values for  $\vec{\alpha}$ . In cases where the Taylor series is an exact expression for  $\chi^2$ , a single iteration is all that is necessary. In most situations, the derivatives in the curvature matrix  $A$  and  $\vec{g}$  are only known approximately or are determined using finite differences, and iteration is necessary to obtain a final solution. The degree of non-linearity in the problem determines the number of iterations necessary to converge, and it is possible for some poor initial guesses or poor approximations to not converge at all.

### Front Fitter

The first of the four applications of the Newton Step fitting method in this analysis is the front track fitter. Measurements at the first three drift chambers comprise the data points  $d_i$ , where  $i$  runs from 1 to the number of wire hits assigned to a pattern recognition track hypothesis, in this case as many as 12 hits, or as few as 6 in the rare case of single wire hits in every wire plane. The parameters of the fit are the position and slope at the first chamber's  $z$ -position.

$$\vec{\alpha}_F = (x, x', y, y')$$

The weight matrix  $W_{ij}$  is computed from the theoretical error matrix of the data points assuming chamber resolutions of  $150 \mu\text{m}$  for the diagonal elements, and no off-diagonal elements due to multiple scattering. The rotated chamber does introduce off diagonal elements to the error matrix.

The predictions  $y_i(\vec{\alpha})$  at each wire hit  $z$ -position are obtained from a charged particle swimmer developed for the E791 experiment by Virgil Highland and Robert Cousins [85]. The track momentum is fixed at the pattern recognition value for the fit. The particle swimmer integrates the equations of motion for a charged particle in a magnetic field, using the field measurements taken for this experiment. Although the field is small except inside the spectrometer dipole, fringe fields noticeably affect the trajectories. However, the effect is small enough that the partial derivatives used in the Newton Step may be calculated analytically assuming no magnetic field to speed the calculation. The implementation of the method converges nicely in less than 4 iterations. The  $\chi^2$  distributions from a representative data tape are shown in Figure 6.16. The distribution differs markedly from the expected distribution for 8 degrees of freedom, particularly at large  $\chi^2$ . The cause of the tail is not understood, but is believed to be caused by imperfect magnetic field measurements and/or delta rays. We place cuts conservatively at  $\chi_{\text{Front}}^2 \leq 175$ .

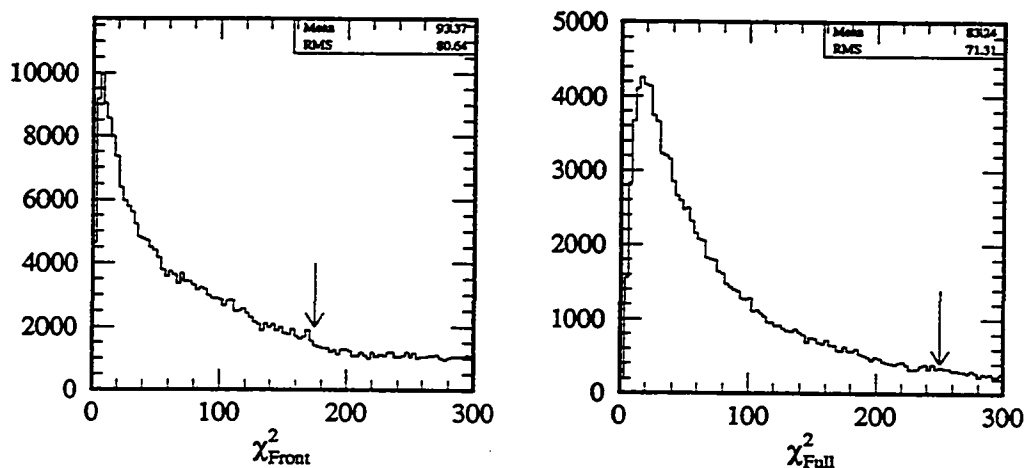
### Full Fitter

The second track fitter proceeds in a similar way to the specialized front fitter. The full fitter uses the wire hits from DC1, 3, 4 and 5, omitting the rotated chamber. This gives as many as 16 wire hits on each track. With the information from the chambers downstream of the magnet, the momentum of the track can be included as a parameter of the fit.

$$\vec{\alpha}_T = (x, x', y, y', q/p) \quad (6.11)$$

The parameters of Equation 6.11 are chosen because they make the Taylor expansion a very good approximation to the  $\chi^2$ -function, allowing quick convergence. In particular the choice of the reciprocal momentum as the fifth parameter is so motivated. The initial guess for the parameters is taken from the front fit solution for the positions and



Figure 6.16: Track  $\chi^2$  Distributions

slopes; the momentum is taken from pattern recognition and refined in a initialization stage based on the missed distance at DC3.

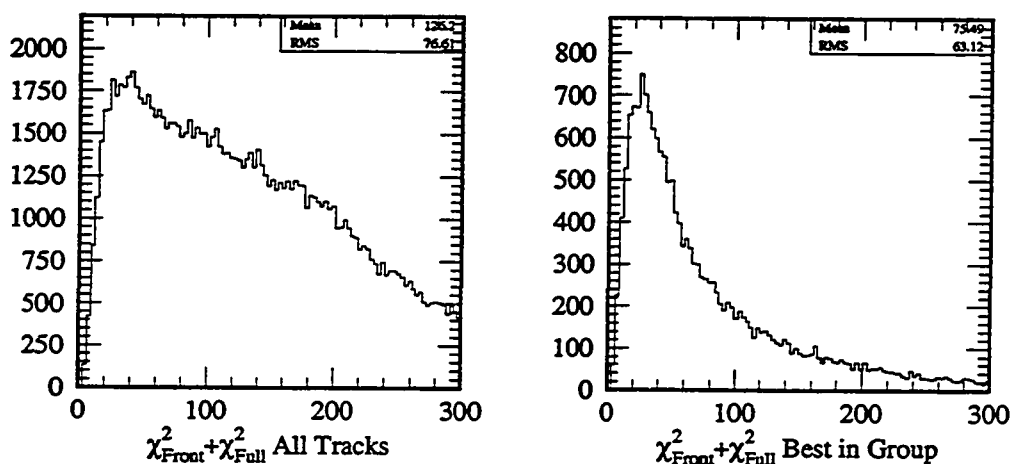
Again the data covariance matrix contains diagonal elements from the intrinsic chamber resolution. For the full fitter, multiple scattering introduces off-diagonal elements to this error matrix. A scattered track introduces correlations between all downstream measurements due to the deflection of the track away from the ideal trajectory. The off-diagonal elements are determined from Monte Carlo using the aforementioned track swimmer including multiple scattering for a large number of simulated tracks. The off-diagonal elements are parameterized as a function of  $p^{-2}$ , as expected for multiple scattering, and the error matrix for the measurements is determined on a track by track basis using the pattern recognition momentum estimate. It is then inverted to give  $W_{ij}$  for use in the iterative solution.

The  $y_i(\vec{\alpha})$  are again computed by swimming the parameterized track to the  $z$ -positions of the wire hits. No multiple scattering is included in the determination of the ideal trajectory. The magnetic field used for the fit is taken from the field map, but is adjusted to account for the deviation of the measured hits from the ideal trajectory.

Essentially this amounts to sampling the field map along the actual trajectory rather than along the ideal trajectory, and this is required to correctly include the effects of multiple scattering. As in the front fitter, the derivatives appearing in the curvature matrix are computed analytically from a simple model of the magnetic field to speed computation. This approximation does not hurt the convergence of the method. Again the fit must converge in four or less iterations or the track is rejected. The fit returns the best values of the five parameters and the  $\chi^2$  for the track (Figure 6.16). When a track is fit to fewer than 16 possible hits, the  $\chi^2$  is scaled by the relative number of degrees of freedom before the cut of  $\chi_{\text{Full}}^2 \leq 250$  is placed. As is the case for the front fitter, the distribution shows a tail at large  $\chi^2$ , which is attributed to inadequate measurement of the magnetic field and/or the effects of delta rays [86]. Inverting  $A$  also gives the error matrix for the five parameters.

### 6.4.3 Track Reconstruction Summary

The multiple track hypotheses found by pattern recognition are first grouped using the equivalence class method. The groups of tracks are then checked for consistency with an actual charged track in the magnetic field of the spectrometer using the two fitters. The front fitter gives the best information on the direction of the track, important for vertexing later in the analysis. The full fitter gives the track momentum, also important in obtaining invariant masses of vertex assignments. Two separate fitters were chosen partly out of convenience, but difficulty with low momentum tracks and uncertainties in the non-vertical magnetic field components made this choice wise. For some low momentum tracks the change in direction away from the  $z$ -axis makes the effect of the unmeasured  $B_z$  field component significant. Because of this it was found that the  $y$  hit positions in the downstream chambers had little correlation with the  $y$  direction cosines at the first chamber. The swum positions and the actual hits often differed significantly in the  $y$  coordinate after the magnet. Using the front fit to determine track direction and the full fit to determine momentum avoids the problem of the uncertainty in field measurements.

Figure 6.17:  $FOM_{\text{Track}}$  Distributions

Both fitters are used to determine the consistency of the track hypotheses. Inconsistent tracks will have a large  $\chi^2$  in either or both track fitters, and many solutions are ruled out by cuts on  $\chi_{\text{Front}}^2$  and  $\chi_{\text{Full}}^2$ . Within each track group, the tracks (various ambiguity solutions for hit assignments) are sorted in increasing order of the sum of the  $\chi^2$ -functions. The best track solution is determined by the goodness of fit criterion  $FOM_{\text{Track}} = \chi_{\text{Front}}^2 + \chi_{\text{Full}}^2$  (See Figure 6.17). This combined figure of merit unrigorously adds two  $\chi^2$ 's from separate fits using some of the same information, but in practice the ranking of ambiguity solutions in order of this figure of merit appears to be justified. In the subsequent analysis all tracks passing the  $\chi^2$  cuts are considered, and the ranking is not considered.

#### 6.4.4 Vertex Fitting (2tkV)

Given a set of well-reconstructed tracks from the fitters, pairs of tracks which appear to originate in a common vertex may be found. Two track vertex candidates (2tkV's) are found by using the distance of closest approach between all pairs of tracks. Using

the two trajectories obtained by the front track fitter, the distance of closest approach for tangents taken at the front chamber is computed. For pairs with a DOCA less than some threshold (5 cm), a detailed fit is carried out to determine the best vertex parameters given the measured track parameters.

The vertex fitter was written by Robert Cousins based on the fitting package used by E791 [83, 84]. Following the formalism given in section 6.4.2, the nine vertex parameters are defined in equation 6.12.

$$\vec{\alpha}_V = (x, y, z, x'_1, y'_1, q_1/p_1, x'_2, y'_2, q_2/p_2) \quad (6.12)$$

The vertex position is given by  $(x, y, z)$ . The track directions at the vertex are  $(x'_i, y'_i)$ , and  $q_i/p_i$  parameterizes the track momenta. The experimental measurements are taken to be the ten track parameters found by the track fitters.

$$\vec{d}_V = ((x, y, x', y', q/p)_1, (x, y, x', y', q/p)_2) \quad (6.13)$$

The initial guess for the vertex position is taken as the midpoint of the segment of minimum length between the two tangents to the tracks defined at the first drift chamber. The initial guess for track slopes and momenta are obtained directly from the track fit. The covariance matrix for the track parameters is also obtained from the track fitters. The two inverted  $5 \times 5$  matrices from the track fit are used to make the  $10 \times 10$  block diagonal weight matrix for the vertex fit.

These parameters and measurement variables are chosen because the  $\chi^2$ -function is exactly linear in the parameters in the absence of a magnetic field. The predicted measurements,  $y_i(\vec{\alpha})$ , are obtained by swimming the parameterized tracks from the vertex position to the first chamber. This includes the magnetic field, although it is small in this region. The derivatives in  $\vec{g}$  and  $A_{lk}$  are computed analytically in the limit of zero magnetic field. Because of the nearly linear  $\chi^2$ -function, a solution is obtained in a single iteration. As in the track fits, an error matrix for the 2tkV parameters is obtained from the fit by inverting  $A$ .

### 6.4.5 Pass 2 Selection Cuts

Pass 2 of the data analysis used the track fitters and vertex fitter to select events with at least four good track groups and to flag events with at least two vertices for further processing in Pass 3. The set of events with two vertices includes our signal channels  $\Lambda\Lambda$  and  $\Lambda K_S^0$ , and we keep four track events to study backgrounds to the double vertex sample.

In Pass 2, all track possibilities are pattern recognized, and the tracks are fit using both the front and full fitter. The pattern recognition cuts remain as described in Section 6.3 (*c.f.* Table 6.1), except the number of tracks found on each side of the spectrometer must be greater than two. Cuts are placed on the fitting results to require at least two well-reconstructed independent tracks on each side of the spectrometer. Cuts on  $\chi^2$  from both fitters and the combined track figure of merit,  $FOM_{\text{Track}} = \chi_{\text{Front}}^2 + \chi_{\text{Full}}^2$ , ensure good reconstruction for the track. If a track has missing wire hits, the  $\chi^2$ 's are rescaled by the relative number of degrees of freedom.  $\chi_{\text{Front}}^2$  is scaled by  $8/(n_{\text{front hits}} - 4)$  if the track has less than 12 hits in the front chambers.  $\chi_{\text{Full}}^2$  was scaled by  $15/(n_{\text{hits}} - 5)$  due to an error in converting fitting code from E791. Here  $n_{\text{hits}}$  is the number of hits in all 5 chamber stations, for a maximum of 20 possible hit wires. Actually only the 4 unrotated stations are used in the full fit so the correct scaling is by  $11/(n_{\text{full hits}} - 5)$ , where  $n_{\text{full hits}}$  is the number of hits in chambers 1, 3, 4 and 5. The error was discovered during the Pass 2 data analysis, and investigation of the effect of the incorrect scaling showed it to have a negligible effect. Out of 90,000 events fit in the study, only one event failed the incorrect cut and passed the correctly scaled cut. In addition the Pass 2 cuts were deliberately chosen to be very loose, and we decided not to rerun Pass 2. The  $\chi_{\text{Full}}^2$  scaling was corrected in the remaining stages of the analysis.

Track independence is enforced by treating each track group as a logical track with the group members being different ambiguity solutions for the track hit assignments. A cut is placed on the number of track groups passing the track cuts. The track quality cuts are given in Table 6.3. The track fitter results, including covariance matrices for all tracks, are written to the output tape for use in subsequent analysis.

Given tracks passing the track cuts, the Pass 2 code searches for good vertices

<b>Track Selection:</b>		
$\chi_{\text{Front}}^2$	$\leq$	175
$\chi_{\text{Full}}^2$	$\leq$	250
$FOM_{\text{Track}}$	$\leq$	375
<b>Vertex Selection:</b>		
number of shared wires	$\leq$	3
$\chi_V^2$	$\leq$	50
<b>Event Selection:</b>		
number of good groups	$\geq$	4
<i>OR</i>		
number of unique 2tkV's	$\geq$	2

Table 6.3: Pass 2 Event Selection

upstream of the first drift chamber position. All pairs of tracks are considered. To eliminate vertexing of two software tracks which are different ambiguity solutions of the same real track, a cut is made on the number of shared wires between the two tracks. A fit is made and we cut on the 2tkV  $\chi^2$ . To limit the reconstruction time, the vertex fitting was terminated if two unique vertices were found without fitting all track pairs for vertices. To ensure two unique vertices are found, we require the second vertex to use tracks from groups not used in the first vertex. At this stage no mass or charge cuts are made on the two track vertices. Table 6.3 shows the cuts placed on vertex reconstruction.

#### 6.4.6 Pass 2 Results

We applied the track and vertex fitters to 11,848,895 events remaining after Pass 1. After placing the cuts described above, we find 939,922 events remaining. 44% of these events have two or more unique vees; the remaining events have four or more good track groups and are kept for background studies.

Table 6.4 summarizes the effect of various cuts on the events selected in Pass 1 for a sample data tape ( $\approx 1\%$  of the data). It shows the fraction of events cut at each stage of reconstruction. The cuts are applied sequentially, so an event failing the DC

Stage: Cut	Fraction Cut
PatRec: DC Hit Counting	0.56
PatRec: Less than 2 x tracks left side	0.065
PatRec: Less than 2 y tracks left side	0.0707
PatRec: Too many 3d tracks	0.0173
PatRec: Too few 3d tracks	0.0081
PatRec: ...	...
PatRec: Total	<b>0.7816</b>
Group: Less than 4 groups	0.0907
Group: Too few groups with good front fit	0.0234
Group: Too few groups with good fits	0.0256
Group: Total	<b>0.1397</b>
Vertex: No Vees found	0.0056
Vertex: Only One Vee found	0.0374
Vertex: Total	<b>0.0430</b>

Table 6.4: Fraction of events (out of total) failing Pass 2 cuts for a representative data tape.

hit counting cut is not subjected to further analysis. Pattern recognition cuts (now requiring at least 2 tracks on each side of the detector), reduce the data by almost a factor of five. Simple hit counting in the drift chambers cuts more than half of the events. Many of these events are minimum bias triggers, where hit counting is not applied in the trigger. Track grouping reduces the remaining events by about 10%, and track fitting quality cuts drop another 5%.

## 6.5 Pass 3

In the third pass of the data, we aim to select events which match the topology of the signal  $\Lambda\Lambda$  and  $\Lambda K_S^0$  events, that is events having two  $v$ -zeros which reconstruct to a common vertex inside the dissociator. We wrote a vertex finder and fitter to identify and fit the vertex of  $v$ -zeros (VV). In the analysis we select the VV hypothesis (if any) with the best figure of merit (described below) and categorize the event based on the  $V^0$  masses and VV  $z$ -positions. We retain events satisfying the  $\Lambda\Lambda$  or  $\Lambda K_S^0$

hypothesis with loose cuts for further analysis. In addition, we keep events in a broad mass range near the  $\Lambda\Lambda$  and  $\Lambda K_S^0$  signal boxes for background studies.

### 6.5.1 Vertex Fitting (VV)

Starting with the v-zero parameters determined from the two-track vertex fit (2tkV), we make a one constraint fit of a pair of  $V^0$ s to a common vertex by extrapolating the 2tkV directions upstream and minimizing the  $\chi^2$ -function defined in section 6.4.2. Following the formalism of that section, we take the “measurements” to be the position, slope, momenta of the  $V^0$ s at their decay points:

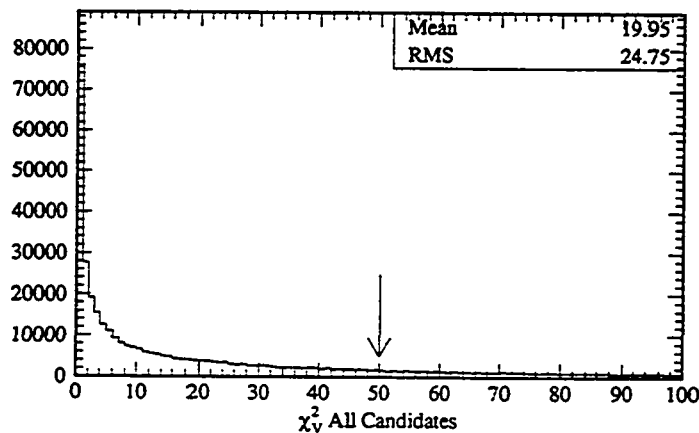
$$\vec{d}_{VV} = (x_1, y_1, z_1, x'_1, y'_1, p_1, x_2, y_2, z_2, x'_2, y'_2, p_2). \quad (6.14)$$

The 11 “parameters” of the VV fit are the VV vertex  $(x, y, z)$ , the direction of each  $V^0$   $(x'_i, y'_i)$ , the  $z$ -position of each  $V^0$  decay  $(z_i)$  and the momentum of each  $V^0$   $(p_{v_i})$ .

$$\vec{\alpha}_{VV} = (x, y, z, x'_1, y'_1, z_1, p_{v_1}, x'_2, y'_2, z_2, p_{v_2}) \quad (6.15)$$

We obtain the  $d_i$  and the data covariance matrix from the five 2tkV fit parameters and their covariance matrix which is a result of the 2tkV fit, making a change of variables from the 2tkV parameters ( $\vec{\alpha}_V$  in Equation 6.11) to those of  $\vec{d}_{VV}$  above. The predicted measurements are easily calculated analytically given  $\vec{\alpha}_{VV}$  by projecting the  $V^0$ s downstream from the VV position. The derivatives in the curvature matrix are also computed analytically. Working with neutral particles there is no need to include the effects of the magnetic field or multiple scattering. As in the 2tkV case we make an initial estimate for the VV as the midpoint of the segment of minimum length between the lines defined by the 2tkV solutions. A single iteration is sufficient to obtain the solution; in this case the  $\chi^2$ -function is exactly linear in the parameters. The fit gives the best value for the 11 parameters, along with error estimates.



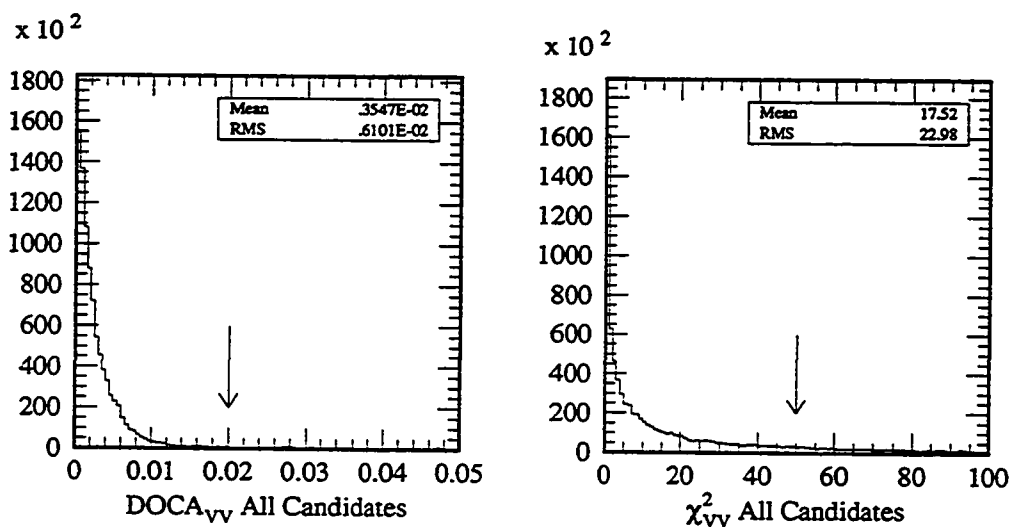
Figure 6.18:  $V^0$   $\chi^2$  Distribution

<b><math>V^0</math> Cuts</b>		
Number of shared wires	$\leq$	3
$\chi^2_V$	$\leq$	50
Number of $V^0$ s	$\geq$	2
<b>VV Cuts</b>		
Number of shared wires	$\leq$	3
DOCA	$\leq$	0.02 m
$\chi^2_{VV}$	$\leq$	50
$FOM_{VV}$	$\leq$	450

Table 6.5: Pass 3 Selection Cuts

### 6.5.2 Pass 3 Cuts

The Pass 3 data analysis program begins with events surviving Pass 2 with two or more two track vertices. We look for 2tkV's from all tracks passing (now correctly scaled)  $\chi^2$  cuts for both front and full fitters. For Pass 3 we consider all track pairs not sharing more than 3 wires and of opposite charge. We keep the  $V^0$ s passing a cut requiring  $\chi^2_V \leq 50$  (*c.f.* Figure 6.18).

Figure 6.19: VV DOCA and  $\chi^2$  Distributions

From the resulting list of  $V^0$ s, we form VV candidates from all pairs which have no tracks in common. To ensure four unique tracks are used we exclude any VV in which any two tracks share more than 3 wires. We make a loose cut requiring the distance of closest approach for the two  $V$ 's to be less than 2 cm before fitting the VV (*c.f.* Figure 6.19). We form a list of all good VV candidates defined by a quality cuts  $\chi^2_{VV} \leq 50$  (Figure 6.19) and  $\mathcal{FOM}_{VV} \leq 450$  (Figure 6.20). We assign this VV figure of merit by summing the full and front  $\chi^2$ 's for all tracks, the 2tkV  $\chi^2$ 's and the VV  $\chi^2$ . This figure of merit is approximately an event hypothesis  $\chi^2$ , and measures the overall consistency of the event with the VV topology. We rank all VV hypotheses in an event by this figure of merit, assigning the candidate with minimum  $\mathcal{FOM}_{VV}$  to be the best solution out of all possible track combinations forming VVs. In a sense this event figure of merit resolves all ambiguities in DC hit assignments to tracks, track assignments to  $V^0$ s and  $V^0$  assignments to VV candidates.

Once the best VV candidate (if any) is determined, we then categorize the event based on  $V^0$  invariant masses and whether the  $V^0$ s decay within the dissociator. We keep events of 9 types. The first six are  $\Lambda\Lambda$  and  $\Lambda K_S^0$  candidates with zero, one or

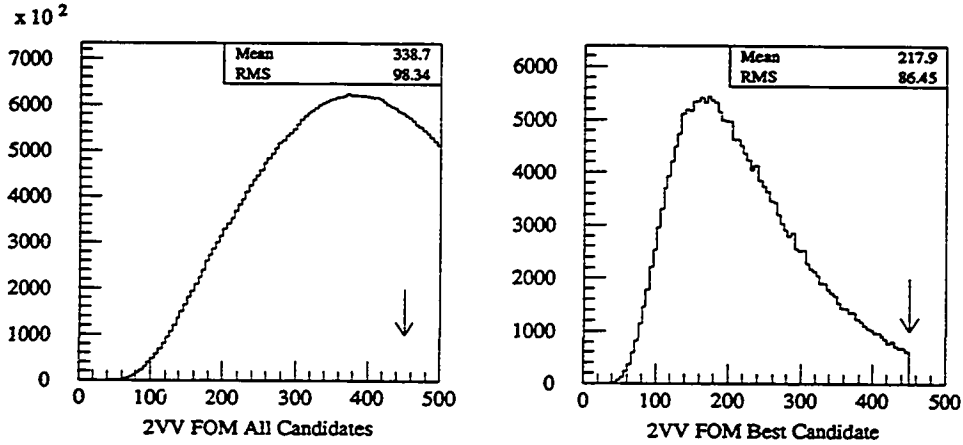


Figure 6.20: VV FOM Distributions

both  $V^0$ s inside the DSC; we also identify two background types in the mass sidebands for  $\Lambda\Lambda$  and  $\Lambda K_S^0$ , and a final background type for any VV failing the above mass cuts and having both  $V^0$ s outside the DSC. The event types are summarized in Table 6.6.

We determine the  $V^0$  masses using the best fit track parameters for the four tracks in the VV. (Vertex constrained masses from the  $V^0$  fits are also available, but are not used at this stage of the analysis due to oversight.) We compute  $m_{\pi^+\pi^-}$  and  $m_{p\pi}$  for each  $V^0$ , by assigning the appropriate mass to the positively charged track. Figure 6.21 shows invariant mass distributions for  $V^0$ s in VV's at the  $\Lambda$  and  $K^0$  mass. From the Gaussian fits shown, we set conservatively loose cuts of  $5 \text{ MeV}/c^2$  ( $10 \text{ MeV}/c^2$ ) to provisionally identify  $\Lambda$ 's ( $K_S^0$ 's). Events with one vertex satisfying the  $\Lambda$  cut and the other vertex the  $K_S^0$  cut are assigned to  $\Lambda K_S^0$  type. Likewise events with two  $\Lambda$ 's are categorized as  $\Lambda\Lambda$ . In the case of an event with a kinematic ambiguity (a  $V^0$  satisfying both mass cuts) we assign it to the  $\Lambda K_S^0$  type, to avoid contaminating the  $\Lambda\Lambda$  sample with background from  $\Lambda K_S^0$ . In addition, we reassign any  $\Lambda\Lambda$  candidate in which any neutral combination of the four tracks passes the  $K_S^0$  cut to  $\Lambda\Lambda$  background. The broad mass sidebands for the  $\Lambda\Lambda$  background type are defined as  $1.1 < m_{p\pi} < 1.2 \text{ GeV}/c^2$  with the signal region removed. The  $\Lambda K_S^0$

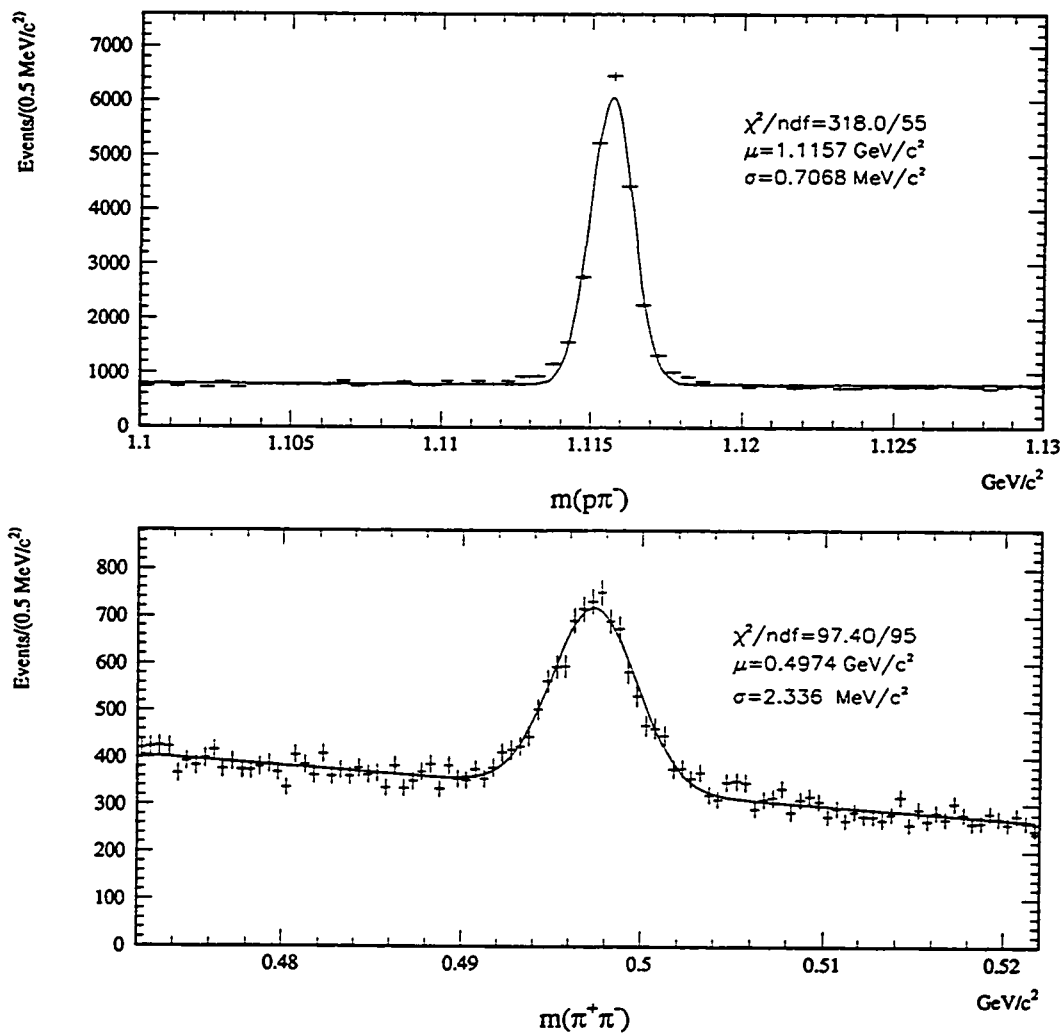


Figure 6.21: Maximum Likelihood fit (gaussian + linear background) to  $m_{p\pi}$  and  $m_{\pi\pi}$  from best  $V^0$ .

Type	Invariant Mass Cuts ( $\text{GeV}/c^2$ )		$V^0$ 's in DSC
1			0
2 $\Lambda\Lambda$	$ m_{p\pi} - m_\Lambda _1 < 0.005$	$ m_{p\pi} - m_\Lambda _2 < 0.005$	1
3			2
4			0
5 $\Lambda K_S^0$	$ m_{p\pi} - m_\Lambda _1 < 0.005$	$ m_{\pi\pi} - m_{K^0} _2 < 0.010$	1
6			2
7 $\Lambda K_S^0$ Bkgd	$1.1 < (m_{p\pi})_1 < 1.2$	$0.45 < (m_{\pi\pi})_2 < 0.55$	0,1,2
8 $\Lambda\Lambda$ Bkgd	$1.1 < (m_{p\pi})_1 < 1.2$	$1.1 < (m_{p\pi})_2 < 1.2$	0,1,2
9 $V^0V^0$ Bkgd	<i>none</i>		0

Table 6.6: Pass 3 Event Types

background sidebands extend from 0.450 to 0.550  $\text{GeV}/c^2$  in  $m_{\pi\pi}$  and from 1.1 to 1.2  $\text{GeV}/c^2$  in  $m_{p\pi}$ .

To complete the event classification, we use the 2tkV fit results for vertex position to identify  $V^0$ 's which decay inside the dissociator. Using Monte Carlo we verified that the error estimate from the fit,  $\sigma_{zV}$  (typically 1 cm), is an accurate measure of the true error, so we use the deviation of the  $z$ -coordinate of the  $V^0$  from the downstream face of the DSC in units of  $\sigma_{zV}$  to make a  $3\text{-}\sigma$  cut.

$$V^0\text{deviation} = \frac{z_V - z_{\text{DSC}}}{\sigma_{zV}} \quad (6.16)$$

A  $V^0$  is considered to decay inside the dissociator if the normalized deviation from the DSC is less than 3. Within each of the two signal types  $\Lambda\Lambda$  and  $\Lambda K_S^0$  we separate events into three sub-types: zero, one and two  $V^0$ 's inside the DSC.

### 6.5.3 Pass 3 Results

We keep events categorized in one of the nine types for additional analysis. Of the 415,212 events selected by Pass 2, 56,746 survive the cuts in Pass 3 (13.7%). Table 6.7 gives the breakdown by event type. Minimum bias events entering Pass 3 are about as likely as physics events to pass the selection cuts (11%), a measure of the effectiveness

Type	Number	Fraction
1	102	$0.18 \cdot 10^{-2}$
2 $\Lambda\Lambda$	520	$0.92 \cdot 10^{-2}$
3	281	$0.49 \cdot 10^{-2}$
4	3723	$6.56 \cdot 10^{-2}$
5 $\Lambda K_S^0$	1713	$3.02 \cdot 10^{-2}$
6	542	$0.96 \cdot 10^{-2}$
7 $\Lambda K_S^0$ Bkgd	25441	$4.48 \cdot 10^{-1}$
8 $\Lambda\Lambda$ Bkgd	20104	$3.54 \cdot 10^{-1}$
9 $V^0V^0$	4320	$7.61 \cdot 10^{-2}$
<b>Total</b>	<b>56746</b>	<b>1.00</b>

Table 6.7: Pass 3 Results

of the Pass 1 and Pass 2 selection cuts. We find a few thousand  $VV$  events in the  $\Lambda\Lambda$  and  $\Lambda K_S^0$  categories, along with a healthy sample of background events in the mass sidebands.

## 6.6 Pass 4 - Final sample selection

From the  $VV$  events selected in Pass 3 we select two subsets ( $\Lambda\Lambda$  and  $\Lambda K_S^0$ ) of events using refined  $VV$  cuts. Each subset is further divided into smaller subsets based on additional detector information from the dissociator and Čerenkov. The dissociator and veto counter information is used to select events consistent with diffraction dissociation of either an incident  $H$  dissociating to  $\Lambda\Lambda$  or an incident  $n$  dissociating to  $\Lambda K_S^0$ . Such events will have a small energy deposit in contiguous counters of the DSC and no signal in the veto counter. We require  $\Lambda\Lambda$  events to have no tracks pointing to hit phototubes in the beam left Čerenkov counter, consistent with protons from lambda decay, but not with pions. From these final samples of  $\Lambda\Lambda$  and  $\Lambda K_S^0$  events we select  $H$  candidates and a subset of  $\Lambda K_S^0$  events for a normalization signal.

### 6.6.1 Refining VV Cuts

Both  $\Lambda\Lambda$  and  $\Lambda K_S^0$  events are required to pass the same reconstruction quality cuts. They must also satisfy the VV topology of a 2  $V^0$ -vertex reconstructed inside the eight counters of the dissociator with both  $V^0$ 's decaying downstream of the veto counter. We also make a final invariant mass cut for lambdas and  $K_S^0$ 's.

These selection criteria (with the exception of the mass cuts) were chosen and optimized by using events within the Pass 3  $\Lambda K_S^0$  signal box (types 4-6), the Pass 3  $\Lambda K_S^0$  mass sidebands (type 7), the Pass 3  $\Lambda\Lambda$  mass sidebands (type 8), and 10% of events within the  $\Lambda\Lambda$  signal box. The optimization was carried out by maximizing the signal to background ratio for both  $\Lambda\Lambda$  and  $\Lambda K_S^0$  simultaneously while varying the cuts. The efficiency of the cuts was calculated using Monte Carlo  $H$  and  $\Lambda K_S^0$  events, to ensure we had a reasonable reconstruction efficiency for simulated signal events.

#### Tracking and vertexing quality

The cuts on track and vertex fitting  $\chi^2$ 's in Pass 3 were deliberately chosen to be generous. For a final sample selection we required a better  $\chi^2$  for all of the fits as shown in Table 6.8. The final cuts may be compared to those in Pass 3 and the  $\chi^2$  distributions in Figures 6.16, 6.18 and 6.19.

#### VV Topology

We require the  $\Lambda\Lambda$  and  $\Lambda K_S^0$  events to satisfy the VV topology, with a reconstructed vertex inside the dissociator (in all three dimensions) and both  $V^0$  vertices downstream of the veto counter. This last requirement reduces background from neutron interactions in the dissociator (e.g.  $\geq 4$  track stars, which have a good VV solution with VV and  $V^0$  vertices at the same point inside the DSC, or 2 charged tracks plus a real  $V^0$ ) and also ensures charged tracks from the  $V^0$  decay do not traverse the veto counter.

The cut on vertex position is made consistent with the size of the dissociator and resolution of the reconstruction. In  $x$  we require  $|x| < 0.06$  m, but we allow  $|y| <$

Track and Vertex Quality		
$\chi_{\text{Front}}^2$	$\leq$	125
$\chi_{\text{Full}}^2$	$\leq$	125
$\chi_V^2$	$\leq$	20
$\chi_{VV}^2$	$\leq$	30
VV Topology		
$(z_{VV} - z_{\text{DSC}}^{\text{up}})/\sigma_{z_{VV}}$	$>$	-3
$(z_{VV} - z_{\text{DSC}}^{\text{down}})/\sigma_{z_{VV}}$	$<$	4
$(z_V - z_{\text{veto}})/\sigma_{z_V}$	$>$	4.5
Mass Cuts		
$ m(p\pi^-) - m_{\Lambda} $	$\leq$	2.5 MeV/c <sup>2</sup>
$ m(\pi^+\pi^-) - m_{K^0} $	$\leq$	7.5 MeV/c <sup>2</sup>
$ m(\pi^+\pi^-) - m_{K^0} $	$\geq$	10.0 MeV/c <sup>2</sup>

Table 6.8: Pass 4 VV Cuts

0.07 m. The cut on  $x$  is smaller because the beam is narrower than the dissociator. The  $y$  cut allows for the full height of the dissociator (5 inches) as the beam is taller than the counters. These cuts are shown superimposed on the distributions of  $x_{VV}$  and  $y_{VV}$  for events surviving Pass 3 cuts of  $\Lambda\Lambda$  or  $\Lambda K_S^0$  type. (Figure 6.22)

In the  $z$  coordinate the resolution is not as good ( $\sim 1$  cm) because the small opening angle of the two  $V^0$  trajectories amplifies the uncertainty on the VV position. To make matters worse, our signal events are likely to have very small opening angles because of their expected low invariant mass. To avoid biasing ourselves against these events we chose to place the cut on the significance of the deviation of  $z_{VV}$  from the upstream and downstream faces of the dissociator. In doing this we rely on the event by event uncertainty estimate from the VV fitter for the vertex position. Before blindly proceeding, we checked that this uncertainty estimate is correlated with the true error in Monte Carlo. Figure 6.23 shows a scatter plot of the true error,  $\Delta z = (z_{VV}^{\text{gen}} - z_{VV}^{\text{fit}})$ , against the VV fit uncertainty,  $\sigma_{z_{VV}}$ , for Monte Carlo events. The figure shows that the uncertainty estimate from the VV fitter is well correlated with the true error, but  $\sigma_{z_{VV}}$  underestimates the actual error. We find that the width of the true error distribution is given by  $1.7 \sigma_{z_{VV}}$  where the linear scale factor was



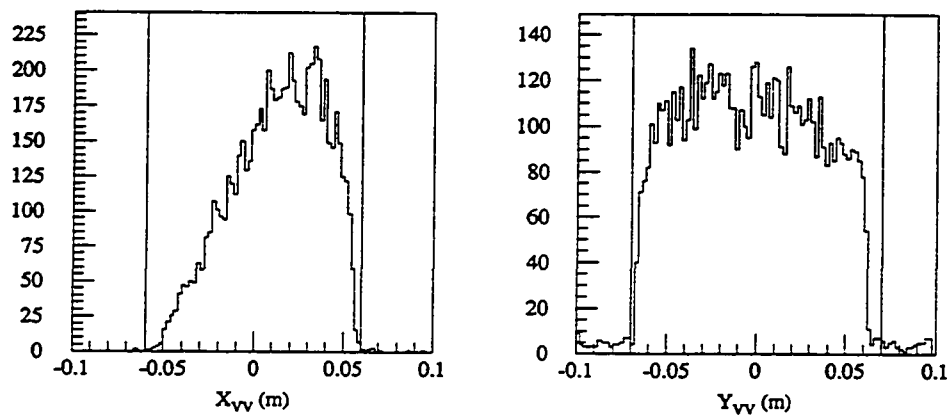


Figure 6.22:  $x_{VV}$  and  $y_{VV}$  for Pass 3 events of type <7.

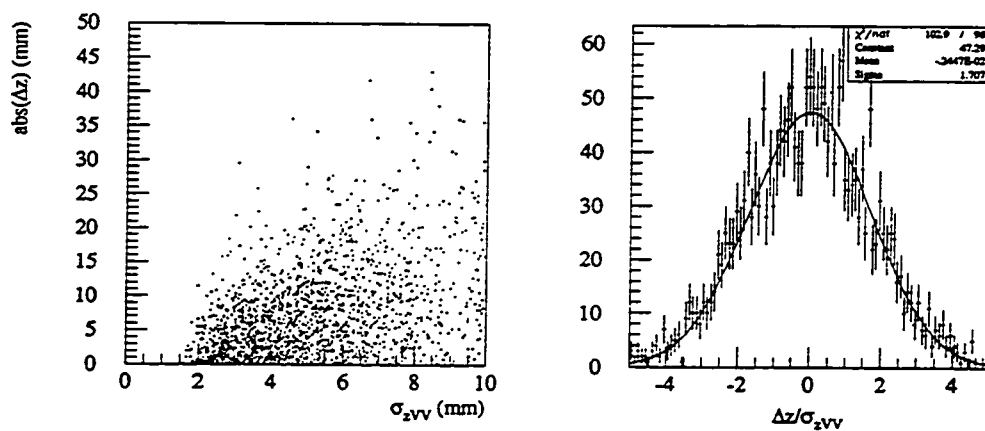
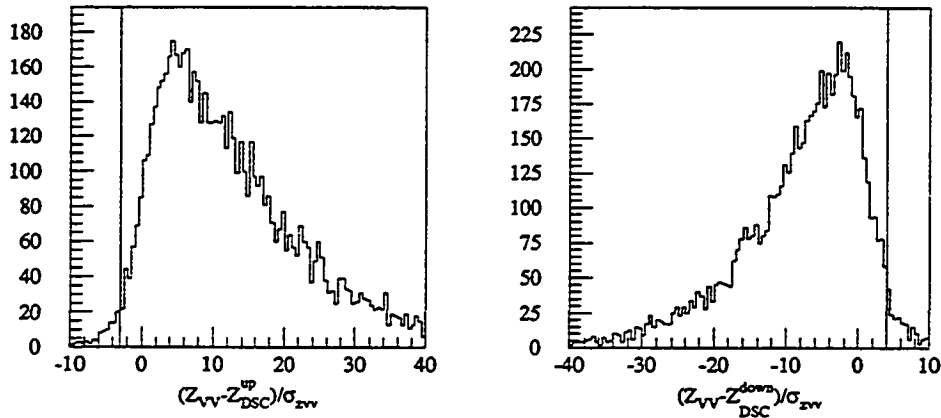


Figure 6.23: Comparison of true error ( $\Delta z$ ) in Monte Carlo events to estimated uncertainty from VV fitter ( $\sigma_{z_{VV}}$ ).

Figure 6.24: Cuts on  $z$ -position of VV

determined by fitting  $\Delta z / \sigma_{zVV}$  to a gaussian and finding a width of 1.7. With  $\sigma_{zVV}$  established as a good measure of the true error, we cut on

$$(z_{VV} - z_{DSC}^{up}) / \sigma_{zVV} > -3.0, \text{ and} \quad (6.17)$$

$$(z_{VV} - z_{DSC}^{down}) / \sigma_{zVV} < 4.0, \quad (6.18)$$

which requires the vertex to be within  $3\sigma$  of the upstream face and within  $4\sigma$  of the downstream face. Because of the factor of 1.7 mentioned above, this does not represent a 99.7% confidence level cut as would normally be implied by a  $3\sigma$  cut. We were able to make a tighter cut at the upstream end because we found that there were fewer  $\Lambda K_S^0$  events appearing to come from far upstream of the dissociator; presumably the same would be true for diffractive  $\Lambda\Lambda$  events. The distribution of the normalized distances from the dissociator faces is shown in Figure 6.24 along with the cuts used.

The profile of the dissociator is easily identified in Figure 6.25 where  $y_{VV}$  is plotted against  $z_{VV}$  for VV events passing the  $z$ -position cut only. The scatter of events at  $z = 20.6$  m and  $|y| > 0.07$  is consistent with events coming from interactions in

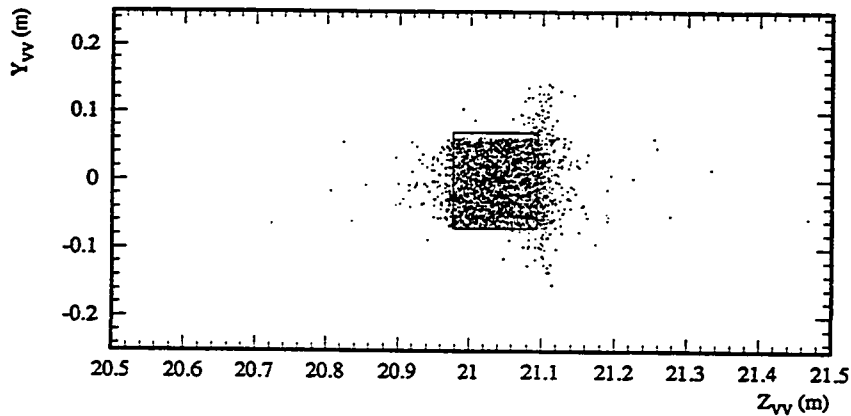
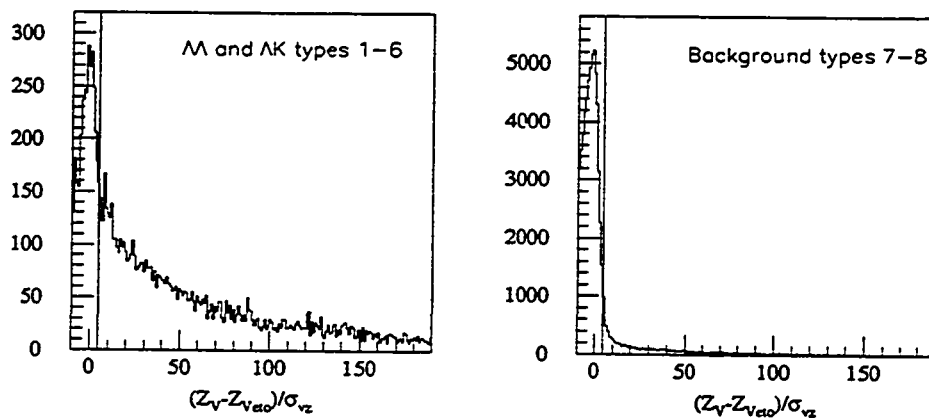


Figure 6.25:  $y_{VV}$  vs  $z_{VV}$  for VV events passing  $z_{VV}$  cuts. The box shows the dimensions of the dissociator.

the veto counter. (Recall the beam is taller than the dissociator. These events are removed by the  $y_{VV}$  cut.)

We also must require the  $z$ -position of the  $V^0$  decay vertex to be downstream of the veto counter. As for the VV vertex, the resolution on this position is affected by the small opening angle of the two tracks, so we make a cut on the normalized difference from the  $z$ -position of the veto counter:  $(z_V - z_{\text{veto}})/\sigma_{z_V} \geq 4.5$ . Again, we must check whether  $\sigma_{z_V}$  is a good estimate of the true error using Monte Carlo, and find that it works well but underestimates the true error by a factor of 1.4. Figure 6.26 shows the normalized deviation of  $V^0$  vertices from the veto counter for both  $\Lambda\Lambda$  and  $\Lambda K_S^0$  event types from Pass 3 on the left and for background event types on the right. The cut at  $4.5 \sigma$  is effective in reducing events from the mass sideband regions (assigned to types 7 or 8 in Pass 3), while there is still a substantial tail of  $\Lambda\Lambda$  and  $\Lambda K_S^0$  types with  $V^0$  vertices many  $\sigma$  away from the dissociator.

Figure 6.26: Cut on  $z$ -position of  $V^0$ 's

### Mass cuts

The mass cuts in Pass 3 were set conservatively. In the final selection we tightened the cuts to about  $3\sigma$ , where  $\sigma$  is the mass resolution for  $\Lambda$ 's or  $K_S^0$ 's, as determined from  $\Lambda K_S^0$  events. In  $\Lambda\Lambda$  events we additionally require  $m(\pi^+\pi^-)$  to be at least  $4\sigma$  away from the  $K^0$  mass. The final mass cuts are given in Table 6.8.

### 6.6.2 Dissociator Information

To identify diffractive events we also make use of the dissociator and veto counter information. As described in Section 4.3, for diffractive events we expect a small energy deposit in the dissociator from the recoiling proton or nucleus. (In the case of a coherent diffraction from a carbon nucleus, the recoil energy is too small to be measured in the DSC.) If the  $V^0$ 's decay outside of the dissociator, then the veto counter should have no energy. So we expect diffractive events to have little or no energy deposit in the eight counters of the DSC, and an empty veto counter. Our primary background to diffraction dissociation comes from neutron interactions which will typically produce charged particles in addition to the  $\Lambda\Lambda$  or  $\Lambda K_S^0$  system.

Inelastic neutron interactions can also leave a large energy deposit in the DSC from the breakup of the target nucleus. Therefore, we can require a small energy deposit in the DSC and no signal in the veto counter to discriminate against neutron interactions. There will still be some background present from neutron interactions which produce only neutral particles and cases where the charged particles escape detection due to inefficiency.

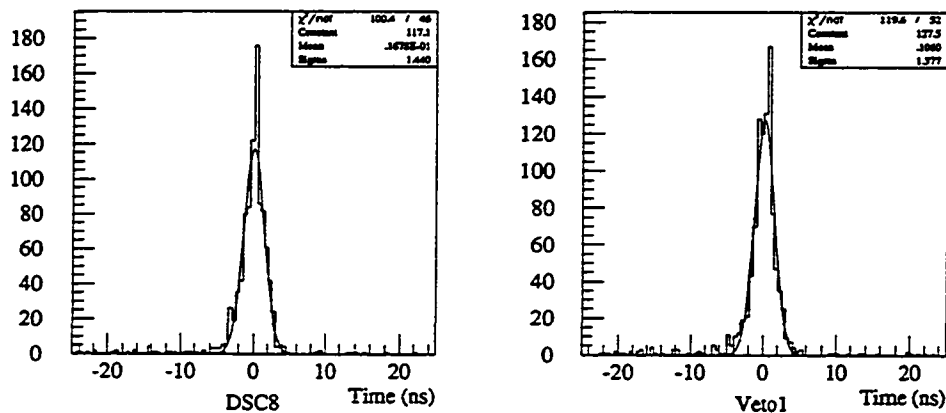
### Calibration

The dissociator and veto system were calibrated using special runs taken for that purpose. We took advantage of the rich environment of the AGS experimental area to take runs with no beam on our target, but with muons (from other beam lines) present. A trigger selected events with at least two adjacent counters above threshold in the DSC for these runs. These high energy muons are good minimum ionizing particles (MIP) and should deposit 2.6 MeV each as they pass through the 1/2" counters of the DSC (less for the 1/8" veto counter). Using the MIP peaks each counter and ADC channel was calibrated by extracting a MIP/charge calibration constant. The positions of these peaks were checked throughout the run to check for gain changes and were found to remain stable to within 15%.

The TDC time offsets relative to the trigger ( $t_0$ ) for the counters were determined from the  $\Lambda K_S^0$  data sample because we required a kinematically similar data set to extract the  $t_0$ 's. The slow protons from diffractive  $\Lambda K_S^0$  events arrive at the trigger counters later than minimum bias events. (For a 2 GeV/c proton the arrival time is as much as 3 ns later.) Compared to our timing resolution of  $\sim 5$  ns this effect could not be ignored. The time distribution for DSC/veto hits in  $\Lambda K_S^0$  events was used to determine the  $t_0$  offset for each channel. Representative distributions from the DSC and Veto TDC channels are shown in Figure 6.27.

### Empty veto

With the DSC ADCs and TDCs calibrated to give pulse heights in MIPS and time relative to the trigger in nanoseconds, we then can define a veto requirement. The

Figure 6.27: DSC TDC Distributions from  $\Lambda K_S^0$  Events.

veto counter is viewed by two phototubes (for redundancy and increased efficiency in this thin counter), so we define an empty veto counter to have no in time hit (i.e.  $|t| > 5$  ns) in either phototube and at least one ADC with less than 1/4 MIP. The ADC requirement is added because the TDCs are edge triggered, and pile-up from an earlier event can cause one or both TDCs to miss a hit.

### 6.6.3 Čerenkov Information

For  $\Lambda\Lambda$  events we require that tracks passing through the left Čerenkov not be associated with any hits in the counter. For  $\Lambda \rightarrow p\pi^-$  decays, these tracks are protons, which are below the Čerenkov threshold. Any background from  $\pi^+$  tracks in this counter will be reduced by this cut. The threshold is 3 GeV/c for pions. Background from muons and electrons is also reduced by this requirement.

#### Track association

Tracks are associated with a hit phototube and its mirror by extrapolating the track trajectory from the spectrometer to Čerenkov box, forming the Čerenkov cone and

projecting it to the mirror surfaces. If the phototube viewing a mirror struck by the cone has a TDC hit or pulse height above pedestal in the ADC, the track is considered to have an associated hit in the Čerenkov counter.

#### 6.6.4 $\Lambda K_S^0$ sample

With the VV cuts in Table 6.8 we select events satisfying the  $\Lambda K_S^0$  mass cuts. Figure 6.28 shows events passing all cuts except the mass cuts. The signal box is shown as a box 5 MeV/c wide on the lambda axis by 15 MeV/c<sup>2</sup> wide on the kaon axis. We find 2607 events inside the signal box, and these events comprise our inclusive  $\Lambda K_S^0$  sample. The band at the  $\Lambda (K_S^0)$  mass corresponds to events where one real  $\Lambda (K_S^0)$  is combined with a background  $V^0$ , possibly from accidental overlap of tracks (combinatoric) or real physics events other than  $\Lambda K_S^0$ . There are no DSC, Veto or CER requirements for the inclusive sample. From the population of events outside the signal box, we can estimate the number of background events which fall inside the signal box. Using the density of events in the lambda and kaon bands and in a box away from the signal box, we estimate a background of 14 events out of the 2607 events by linearly extrapolating into the signal box.

#### Empty Veto and Empty DSC samples

If we make the empty veto requirement (Section 6.6.2), there are 819 events remaining. These events include diffraction dissociation events ( $nA \rightarrow \Lambda K_S^0 A$ ), and inclusive  $\Lambda K_S^0$  events from inelastic neutron interactions where the other particles produced are neutral, or range out in the DSC, or escape the DSC without hitting the veto counter.

If we require also that there be no energy (above 1/3 MIP) in any of the 8 DSCs counters (we define this to be the Empty DSC requirement), there are 292 events remaining. The stricter requirement on energy deposit in the dissociator selects diffraction dissociation events with recoil energy below the detection threshold (a fraction of a MeV in each counter). Diffraction dissociation events which scatter coherently from a Carbon nucleus in the plastic scintillator, will have undetectably small recoil

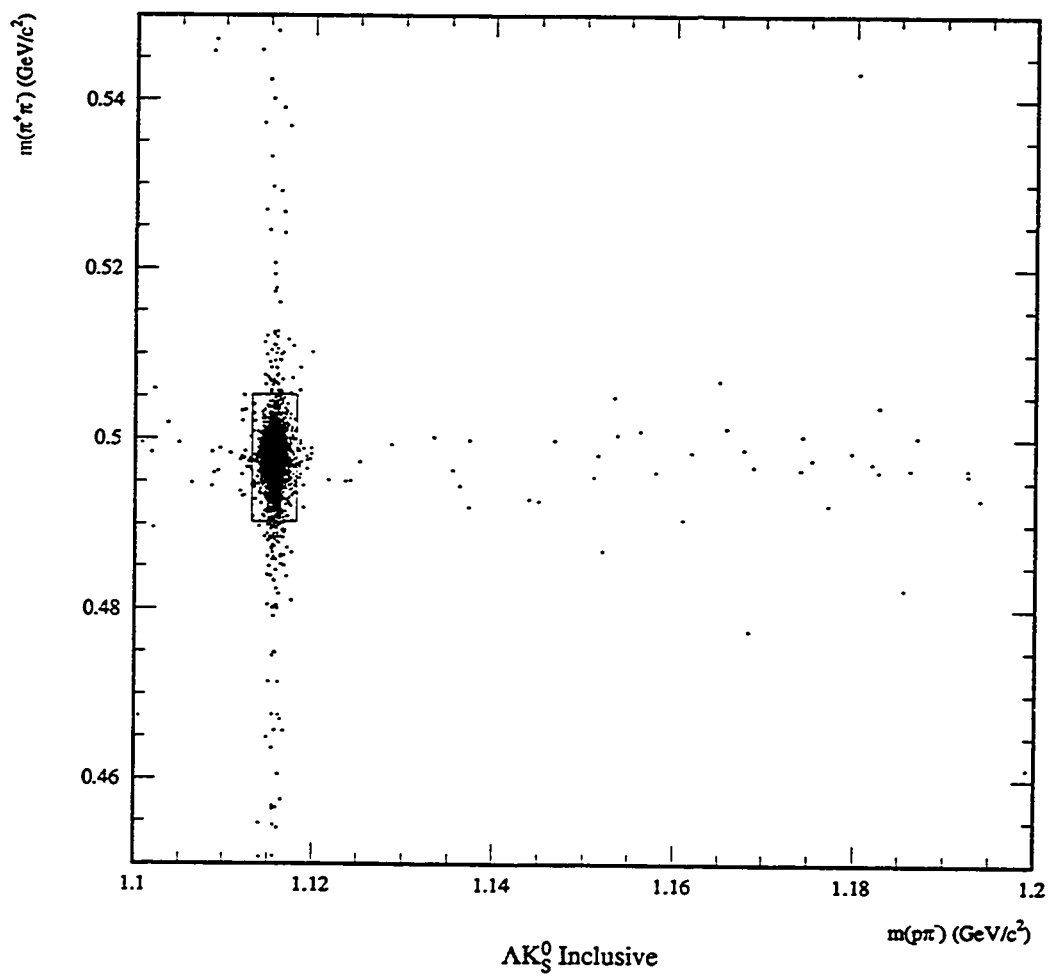


Figure 6.28: Scatter plot of  $m(\pi^+\pi^-)$  vs  $m(p\pi^-)$  for events passing all Inclusive  $\Lambda K_S^0$  cuts except mass. There are 2607 events inside the signal box shown at the intersection of the  $\Lambda$  and  $K^0$  masses.



energies. It is also possible that some diffraction events from neutrons in the Carbon nucleus could fit this sample as the recoiling target neutron would leave no energy unless it interacts.

### 6.6.5 $\Lambda\Lambda$ sample

We also select  $\Lambda\Lambda$  events by applying the VV cuts of Table 6.8 and  $\Lambda\Lambda$  mass cuts to the events from Pass 3. We also require that neither of the 2 positively charged tracks in  $\Lambda\Lambda$  events be associated with a hit Čerenkov mirror, so that the tracks are consistent with being a proton. Figure 6.29 is a scatter plot of  $m(p\pi^-)_1$  versus  $m(p\pi^-)_2$  for Pass 3 events passing the refined VV and Čerenkov cuts. There are 40 events in the signal box and two bands at the lambda masses, one horizontal and one vertical. There are also events in which neither invariant mass reconstructs to the lambda mass, which is indicative of the larger amount of background relative to the  $\Lambda K_S^0$  events.

To assess the significance of the events in the signal box, we estimate the amount of background using the density of events on the two lambda bands and in a box away from the lambda mass bands. In the approximation that the background density is uniform over this plot, we calculate an expected background of 3.2 events inside the signal box ( $5 \text{ MeV}/c^2$  by  $5 \text{ MeV}/c^2$ ). The probability of a fluctuation causing us to observe 40 events is very small. Figure 6.30 shows the significance graphically; it is clear that the overlap of the two lambda bands is not sufficient to explain our peak.

Of the 40 events, only two satisfy the empty veto requirement. Their interpretation is discussed in the next chapter.

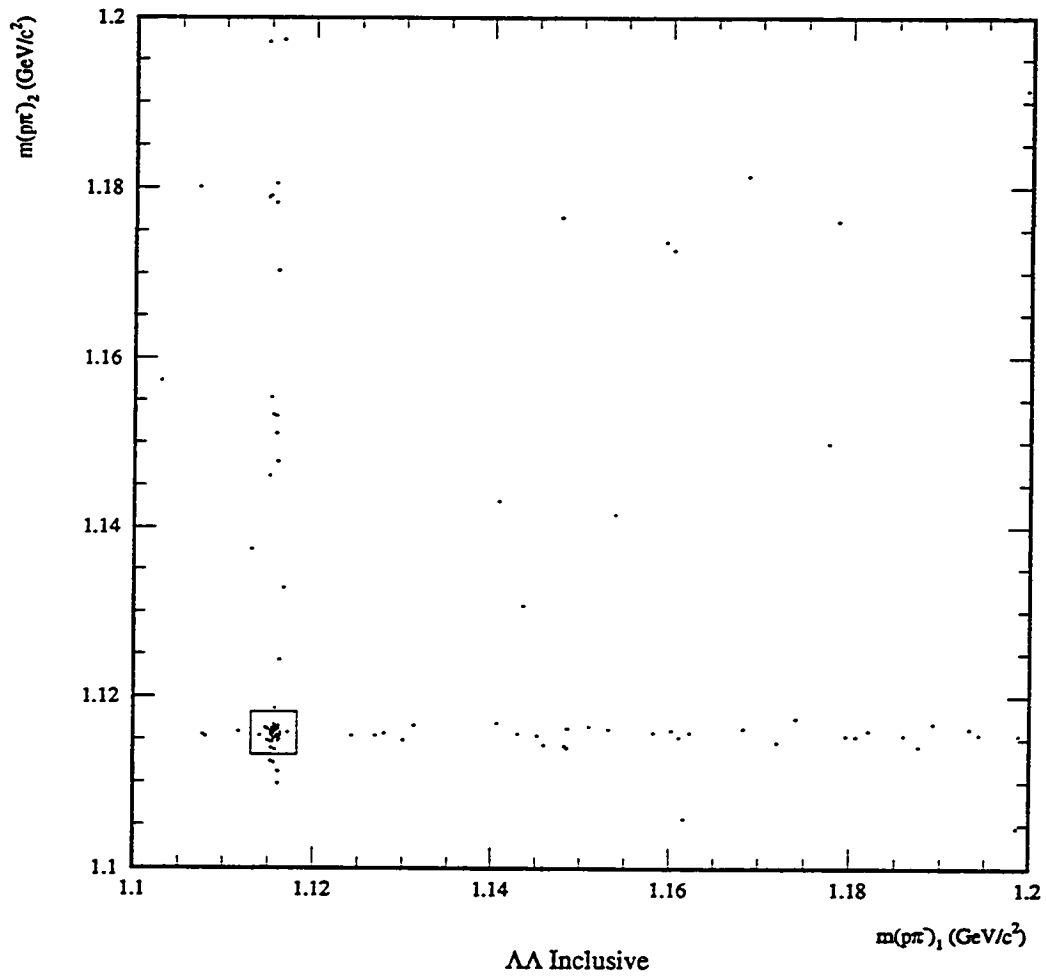


Figure 6.29: Scatter plot of  $m(p\pi^-)_1$  vs  $m(p\pi^-)_2$  for Pass 3 events passing the final VV cuts and the empty Cerenkov requirement. There are 40 events in the signal box with an estimated background of 3.2 events.

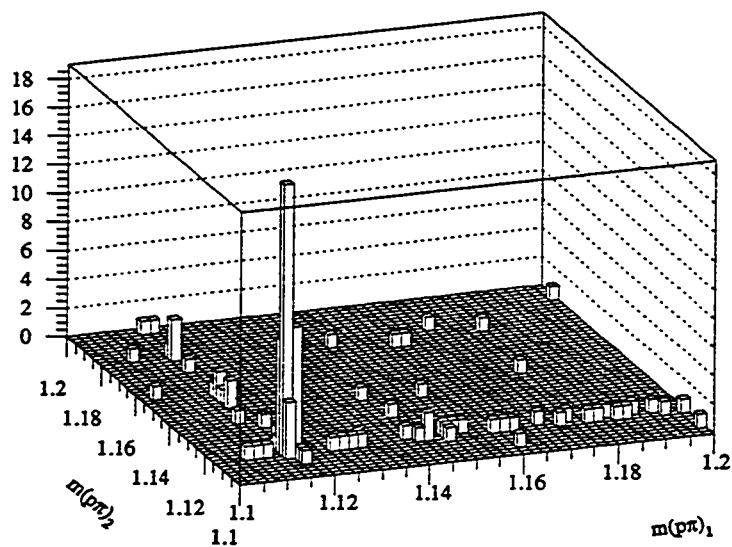


Figure 6.30:  $\Lambda\Lambda$ :  $m(p\pi^-)_2$  vs  $m(p\pi^-)_1$  Lego Plot

Pass	Events	Reduction Factor
Raw Data	40 866 016	1.00
Pass 1	11 665 773	0.28
Pass 2	415 212	0.01
Pass 3	56 746	$0.14 \cdot 10^{-2}$
Pass 4 $\Lambda K_S^0$	2 607	$0.64 \cdot 10^{-4}$
Pass 4 $\Lambda\Lambda$	40	$0.98 \cdot 10^{-6}$

Table 6.9: Data Analysis Summary

## 6.7 Data Analysis Summary

Beginning with the raw data, we have selected two samples of events using a multi-pass analysis. At each pass increasingly restrictive requirements were made to select events satisfying our VV topology while rejecting known sources of background. The final samples,  $\Lambda\Lambda$  and  $\Lambda K_S^0$ , represent a significant reduction of the raw data. Table 6.9 summarizes the events surviving each pass in the analysis. In the next chapter the 40  $\Lambda\Lambda$  events are examined for any sign of the  $H$ , and the  $\Lambda K_S^0$  events are used to normalize the sensitivity of the experiment.

# Chapter 7

## Interpretation

In the data analysis described in the previous chapter,  $\Lambda\Lambda$  and  $\Lambda K_S^0$  events were identified. With only 40  $\Lambda\Lambda$  events, only two of which have an empty veto counter, the most we can hope to do is to set a limit on the cross section for  $H$  production. To do so we must have a way of determining the flux of particles in our beam, and the  $\Lambda K_S^0$  events provide a convenient way to accomplish this—convenient because they have the same topology (VV, four tracks) as our expected signal events and they are produced in the same physical process (diffraction dissociation). After examining the  $\Lambda K_S^0$  and  $\Lambda\Lambda$  event samples in the following sections of this chapter, we establish a limit on  $H$  production and discuss the significance of the result.

### 7.1 $\Lambda K_S^0$ Events

The 2607  $\Lambda K_S^0$  events selected during data analysis may be attributed to a number of sources. Within the forward acceptance of the spectrometer the prominent source is diffraction dissociation of neutrons from either quasi-free protons (hydrogen nuclei) or carbon nuclei in the scintillator.



In 7.2 above, the carbon nucleus remains intact in the so called coherent process where the incoming particle wavefunction scatters coherently from the individual nucleons of the nuclear target. Incoherent processes also occur, where the incoming particle scatters from a single nucleon (or cluster of nucleons) in the carbon nucleus. Such interactions could leave the nucleus in an excited state, resulting in the emission of pions, or the break up the nucleus into constituent fragments.

$$n + C \rightarrow \Lambda K^0 + C^* \rightarrow \Lambda K^0 + p + \alpha + \dots \quad (7.3)$$

$$\rightarrow \Lambda K^0 + C + \pi + \dots \quad (7.4)$$

Other processes besides diffraction dissociation also contribute

$$n + A \rightarrow \Lambda + K^0 + X, \quad (7.5)$$

where an incoming neutron interacts with a nucleus  $A$ , and the final state  $\Lambda$  and  $K^0$  are not necessarily associated with the same initial hadron. An example of such a process is a cascade reaction where reaction products from an initial interaction reinteract (or scatter) with other nucleons in the same nucleus, *e.g.*

$$n + n \rightarrow \Sigma^- + K^0 + p,$$

followed by reinteraction of the  $\Sigma^-$  with a proton in the same nucleus:

$$\Sigma^- + p \rightarrow \Lambda + n.$$

Typically such non-diffractive processes contain charged particles in  $X$ . Such events are less likely to be accepted within the experimental apparatus compared to diffractive events with their characteristic forward production. This difference in physical process is also seen in the invariant mass of  $\Lambda K^0$  pairs, which will typically be much larger for non-diffractive events when the  $\Lambda$  and  $K^0$  do not necessarily come from the dissociation of a single hadron.

Note that in any of the above reactions  $\Sigma^0 K^0$  may replace  $\Lambda K^0$ , because the

subsequent electromagnetic decay  $\Sigma^0 \rightarrow \Lambda \gamma$  also leads to a  $\Lambda$  associated with the event. In the above interactions  $K^0$ , the eigenstate of the strong interaction, appears instead of  $K_S^0$  which is observed through the weak decay  $K_S^0 \rightarrow \pi^+ \pi^-$ . The  $K_S^0$  is a mixture (almost equal) of  $K^0$  and its antiparticle  $\bar{K}^0$ . An initially produced  $\bar{K}^0$  can decay as a  $K_S^0$ , but final states with a  $\bar{K}^0$  are less likely because the  $\bar{K}^0$  carries  $S = -1$ , like the  $\Lambda$ , and would require production of an additional  $S = 1$  particle in the final state, *e.g.*  $nA \rightarrow \Lambda K^+ K^+ \bar{K}^0 \pi^- \pi^- A'$ .

For the purpose of normalizing the sensitivity of the experiment, it is necessary to isolate a subset of the  $\Lambda K_S^0$  events which can be attributed to a single source with a measured cross section. Because non-diffractive interactions often produce additional charged particles, we can enrich the event sample with diffraction dissociation events by requiring an empty veto counter. When we do this there are indications that the 819 vetoless events are fully consistent with diffraction dissociation, with little or no background. Both diffraction from protons and carbon nuclei are included in this sample. To separate the two contributions, a cut requiring no energy above threshold in any of the dissociator counters is made, yielding a sample of 292 events rich in coherent diffraction from carbon. A typical recoiling proton has 80 MeV of kinetic energy; a recoiling intact carbon nucleus will leave no observable energy in the dissociator.

By comparing the observed events with events generated in Monte Carlo with the expected distributions from diffraction dissociation, we can lend support to the diffraction dissociation interpretation of the vetoless  $\Lambda K_S^0$  events. Diffraction dissociation is specified by a four momentum transfer  $t$  and an invariant mass for the dissociated state. The four momentum transfer follows an exponential distribution  $dN/dt \sim \exp(-b|t|)$ , with the slope  $b$  typically  $9 \text{ GeV}^{-2}$  for nucleon targets and the energies in consideration. The invariant mass distribution and the incident neutron momentum spectrum are described in the following sections.

Resonance	Mass MeV/c <sup>2</sup>	Width MeV/c <sup>2</sup>	Reference
$N^*(1650)$	1650	200	PDG [62]
$N^*(1710)$	1710	130	PDG
$S_1(1775)$	1775	300	Cleland <i>et al.</i> [87]
$D_3(1950)$	1953	200	Cleland <i>et al.</i>

Table 7.1: Resonances Used to Generate Diffractive  $\Lambda K_S^0$  Events

### 7.1.1 Invariant Mass Distribution

As described in Section 4.2.1 the invariant mass distribution in diffraction dissociation near threshold is dominated by the production of resonances. With a simple model of diffraction dissociation through 4  $s$ -channel resonances (see Table 7.1), the data are reproduced remarkably well. Two are known  $N^*$  resonances; two are enhancements reported by Cleland *et al.* for  $\Lambda K^+$  diffractive production in  $pp$  scattering [87]. In our simple model each resonance contributes equally to  $\Lambda K_S^0$  production. To account for the reduction in phase space near threshold, events are chosen from one of four Breit-Wigner distributions weighted by the invariant phase space factor for two body decays,  $p^*/M^2$ , where  $M$  is the invariant mass of the resonance. The momentum of the daughters in the resonance rest frame is given in terms of their masses and the mass of the resonance as

$$p^* = \frac{\sqrt{[M^2 - (m_\Lambda + m_{K_S^0})^2][M^2 - (m_\Lambda - m_{K_S^0})^2]}}{2M}. \quad (7.6)$$

With the Breit-Wigner distribution given by

$$\frac{dN}{dM} = \frac{\Gamma_R^2}{4(M - m_R)^2 + \Gamma_R^2}, \quad (7.7)$$

the invariant mass distribution is then

$$\frac{dN}{dM} \approx \sum_i \frac{\Gamma_i^2}{[4(M - m_i)^2 + \Gamma_i^2]} \frac{p^*}{M^2}. \quad (7.8)$$



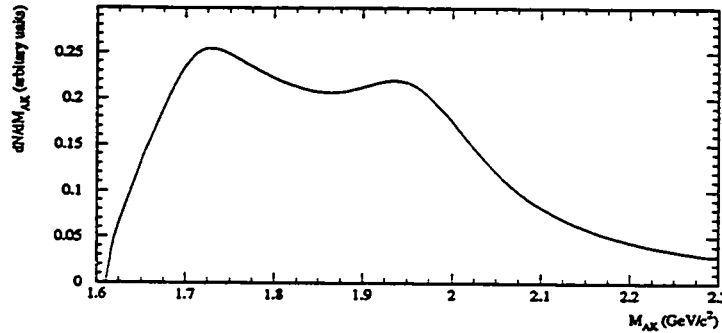


Figure 7.1:  $M_{AK^0}$  Spectrum Modeled in Monte Carlo

Figure 7.1 shows the invariant mass spectrum from Equation 7.8 using the four resonances in Table 7.1.

Events generated in Monte Carlo according to this distribution reproduce the observed events well, despite the simplicity of the model. Figure 7.2 shows the data events overlayed on the Monte Carlo distribution of accepted events for the downstream DSC position. A more complete treatment would replace the phase space factor with a mass dependent width for the resonances and adjust the relative contributions from the different resonances. At the level shown here however this fine tuning is unnecessary. The simple model gives adequate reproduction of the data.

### 7.1.2 Momentum Spectrum

Not mentioned in the above, but necessary for a Monte Carlo simulation, is a neutron momentum spectrum. Unfortunately there are few neutron momentum spectra measured in the medium energy range (24.1 GeV) and angle of the beam line (65 mrad) used in this experiment. We use the observed events to calculate the neutron momentum spectrum, taking advantage of the small momentum transfer implicit in diffraction dissociation. In the approximation that there is no energy transfer between target and beam particles in diffraction dissociation (equivalent to setting the recoil

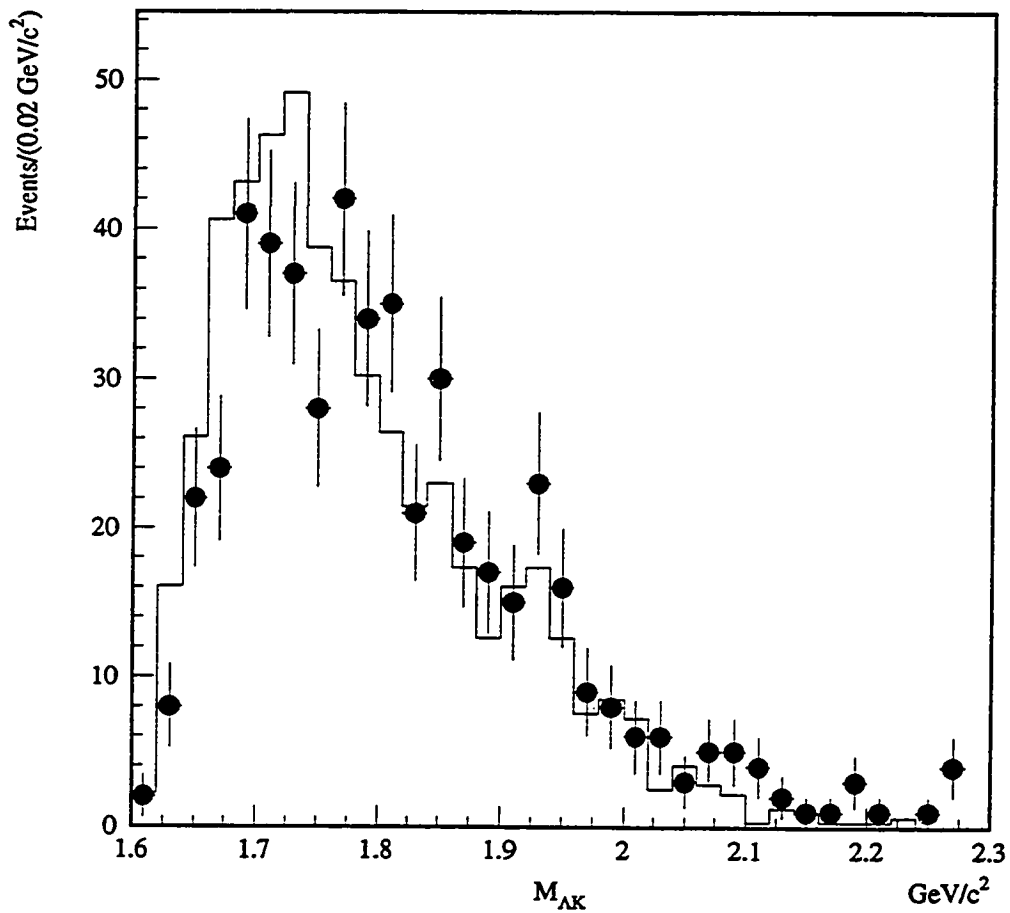


Figure 7.2: Invariant mass of empty veto  $\Lambda K_S^0$  events for data (points) and Monte Carlo (histogram). The comparison is for events from runs with the downstream position of the DSC. The Monte Carlo histogram is normalized to have the same number of events.

kinetic energy to zero), the neutron momentum is given by

$$p_n^2 \approx p_{\Lambda K_S^0}^2 + m_{\Lambda K_S^0}^2 - m_n^2 \quad (7.9)$$

Applying the above to reconstructed events gives an estimate of the observed neutron spectrum for accepted events. From Monte Carlo the acceptance correction is calculated allowing the incident spectrum to be determined from the accepted spectrum.

This spectrum is calculated using runs from one position of the dissociator. Using the derived spectrum in Monte Carlo simulation of the other dissociator position allows an independent check of the spectrum. We compare the spectrum to a measured neutron spectrum at 24 GeV/c in a bubble chamber experiment [61] and to a parameterized proton spectrum obtained from measurements of  $p$ -Be collisions [88]. The proton spectrum is only marginally appropriate to our situation (a light target nucleus, Be, compared to Pt), but one expects the proton and neutron spectra to be similar away from  $0^\circ$ , and we use it as a guide for comparison. Above 8 GeV/c, where we have acceptance, the agreement between all three is reasonable. Figure 7.3 shows the three spectra overlaid with acceptance corrected data.

### 7.1.3 $t'$ Distribution

The four momentum transfer ( $t$ ) distribution in diffraction dissociation events is characterized by an exponential distribution,  $\exp(-b|t - t_{\min}|)$ , where  $b$  is determined mainly by the size of the target particle and  $t_{\min}$  is the minimum kinematically allowed four momentum transfer. (See Section 4.2.1) For a nucleon target  $b \sim 9 \text{ GeV}^{-2}$ , and for carbon, scaling with  $A^{2/3}$ ,  $b \sim 70 \text{ GeV}^{-2}$ . Scattering from a larger object gives a steeper distribution in  $t$ . In this experiment,  $t' = t - t_{\min}$  is very nearly given by  $p_T^2$ , the square of the momentum transverse to the incident neutron direction. Thus by examining the  $p_T^2$  distribution (Figure 7.4) for the empty veto  $\Lambda K_S^0$  event sample, we can see that the events are consistent with diffraction dissociation from single nucleons with a contribution at small  $p_T^2$  from coherent diffraction from a larger nuclear target. The empty DSC requirement reduces the contribution from nucleon targets, allowing the coherent peak to be seen clearly.

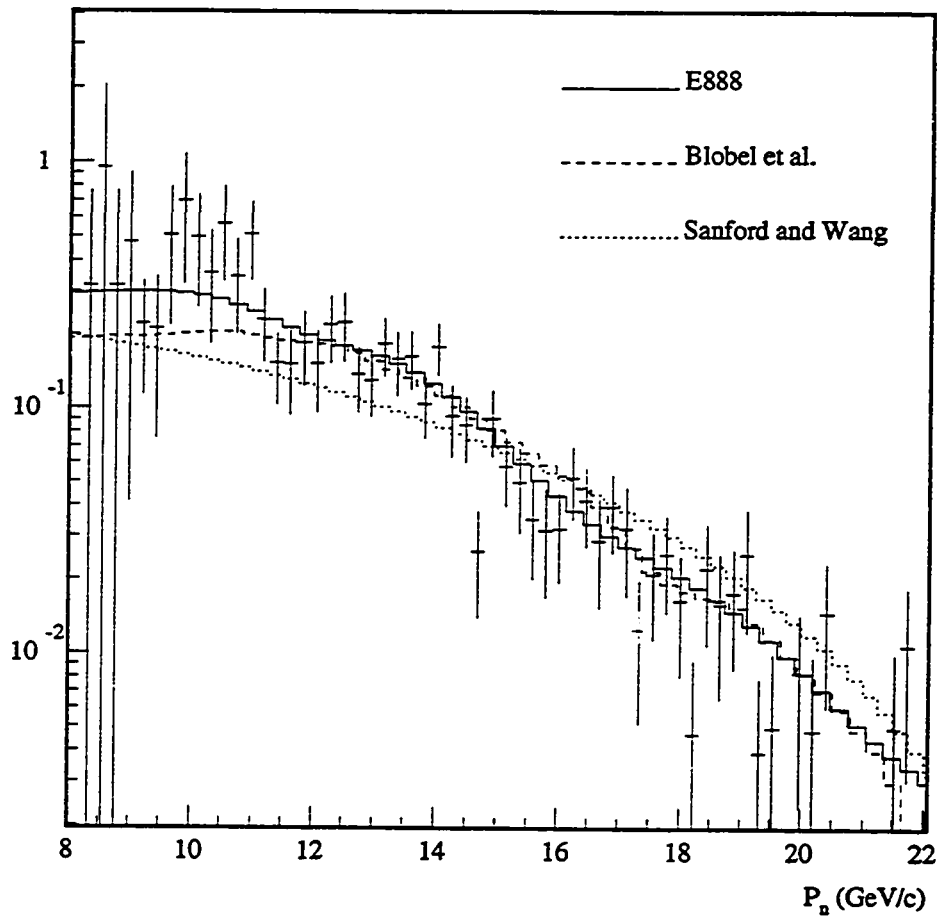


Figure 7.3: Incident neutron momentum spectrum derived from data (points) compared to a measured neutron spectrum (Blobel *et al.* ) and a parameterized proton spectrum (Sanford and Wang). The data points are corrected for acceptance, and the shape of the spectrum derived from the data is shown as a solid histogram.

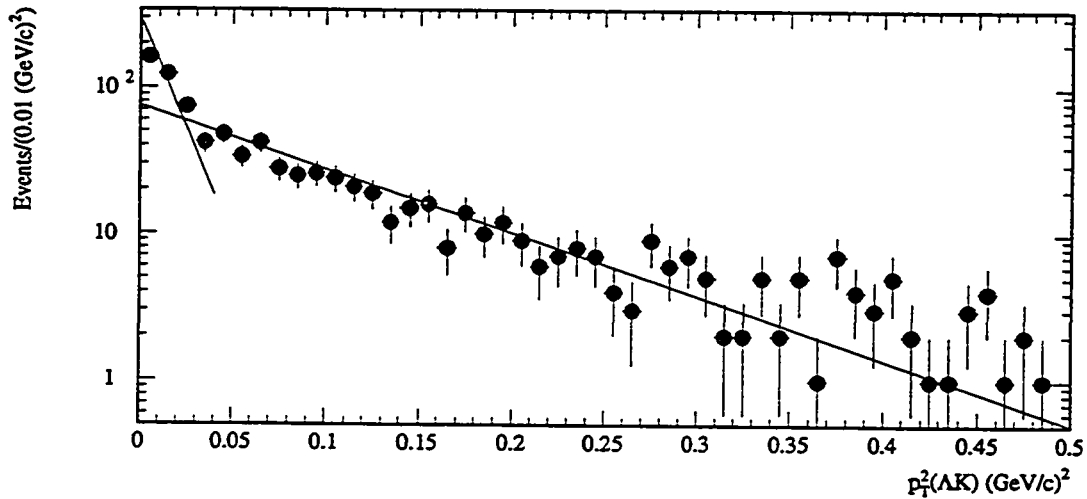


Figure 7.4: Distribution of  $p_T^2$  for empty veto  $\Lambda K_S^0$  events. The two lines are drawn with slopes  $70 \text{ GeV}^{-2}$  and  $10 \text{ GeV}^{-2}$  to guide the eye.

Examining the empty DSC sample in more detail allows the relative contributions to be separated. These events have no energy deposited in any of the dissociator counters, including the veto counters. They therefore come from coherent diffraction, where the recoil energy is too small to result in any deposited energy, or from incoherent diffraction from single nucleons or other processes, where the recoiling particle(s) are neutral and leave no energy in the DSC or veto counters.

It is possible to improve the determination of  $t$  by using complete spectrometer measurements for the event and assuming the diffraction target to be a particular particle. Recall Equation 4.18 written for  $H$  diffraction to two lambdas, now rewritten to apply to the process  $nA \rightarrow \Lambda K^0 A$ :

$$m_n^2 = m_{\Lambda K^0}^2 + 2p_T^2 - 2\sqrt{p_{\Lambda K^0}^2 - p_T^2} \sqrt{K_A^2 + 2m_A K_A - p_T^2} + 2K_A(E_{\Lambda K^0} - m_A). \quad (7.10)$$

The kinetic energy of the recoiling target,  $K_A = -t/(2m_A)$ , is the only unknown, and the equation may be solved for  $t$  numerically on an event by event basis. Taking

the target nucleus ( $A$ ) to be carbon, we obtain the four momentum transfer for the empty DSC events. To extract the exponential slope parameter, we fit the  $t' = t - t_{\min}$  distribution to the sum of two exponentials,

$$\frac{dN}{dt'} = A_C \exp(-b_C t') + A_i \exp(-b_i t'). \quad (7.11)$$

The distribution of  $t'$  for the empty DSC events is shown in Figure 7.5. The coherent contribution has a slope  $b_C = 68 \pm 11 \text{ GeV}^{-2}$ , consistent with expectations that  $b$  should scale with the radius of the target squared or  $A^{2/3}$ . This slope is also consistent with the slope of  $60 \text{ GeV}^{-2}$  observed by O'Brien *et al.* for  $n + C \rightarrow p\pi^- + C$  coherent diffraction dissociation [89]. The background contribution has  $b_i = 11 \pm 2 \text{ GeV}^{-2}$ , consistent with diffraction from single nucleons.

### 7.1.4 Normalization Sample

The empty DSC  $\Lambda K_S^0$  events are the cleanest subset of the  $\Lambda K_S^0$  events. We choose to normalize to the coherent  $\Lambda K_S^0$  events, determining the number contributing to the empty DSC sample by integrating the coherent piece of Eq. 7.11. The fit to the  $t'$  distribution gives  $A_C = 105 \pm 13$ , which implies a total of  $187 \pm 39$  events coming from the coherent process. Choosing to normalize to the coherent diffractive process introduces a theoretical error, because we must rely on a calculation for this specific cross section rather than on a measurement. However, this uncertainty is preferable to the experimental problems associated with obtaining a clean sample of any other process.

## 7.2 $\Lambda\Lambda$ Events

The 40  $\Lambda\Lambda$  events selected in the data analysis are a significant signal (37 events above background) of double lambda production. Before considering possible physics sources of these events, we consider the possibility that they arise from accidental overlap of two separate neutron interactions (say diffraction dissociation) each producing one  $\Lambda$ . Such events would need to overlap both in time and space to fake a

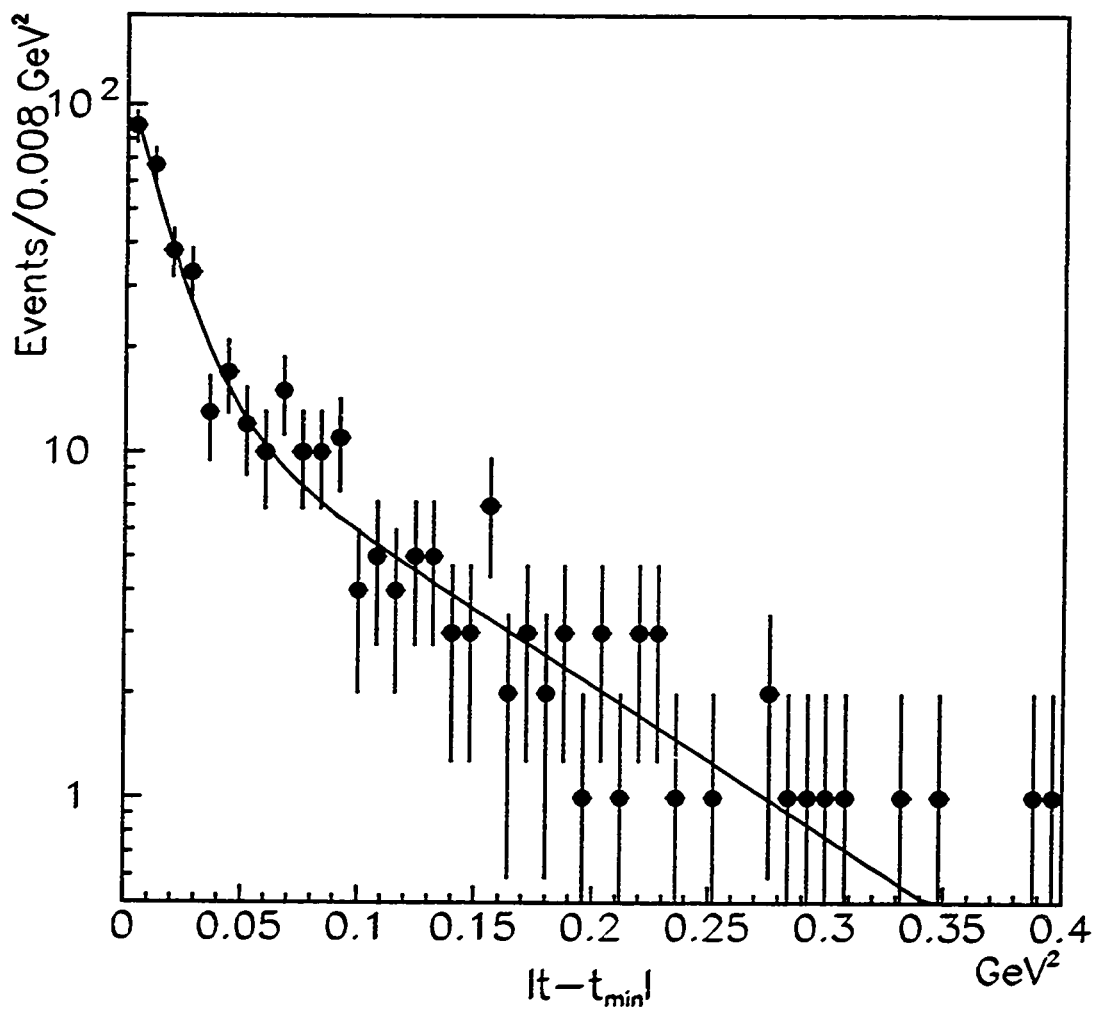


Figure 7.5:  $t' = t - t_{\min}$  distribution for empty DSC  $\Lambda K_S^0$  events. The fit shown is the sum of two exponentials. The peak at small  $t'$  is primarily due to diffraction from carbon nuclei, and the tail extending to larger values comes from diffraction scattering from nucleon targets.

VV topology and be detected in the spectrometer. Although from a crude calculation of the rate of interactions in the detector such an overlap appears impossible, we can not exclude this mechanism as a source of the  $\Lambda\Lambda$  events based on average rate arguments because the beam intensity varies during each spill. Instead we reanalyzed 40% of the data eliminating the VV fits and cut requirements. Based on the number of additional  $\Lambda\Lambda$  events observed (i.e. the ones failing the topology cuts of the original analysis) and a Monte Carlo calculation of the rejection power of the VV cuts on  $\Lambda$ 's produced at different positions in the dissociator, we estimate a contribution of at most 0.08 events to the  $\Lambda\Lambda$  signal from accidental overlap of two neutron interactions. With this systematic source of  $\Lambda\Lambda$  events eliminated we now consider possible physics sources.

Some possible physics processes for  $\Lambda\Lambda$  production are diffraction dissociation of  $H$ 's (our signal)

$$H + A \rightarrow \Lambda\Lambda + A \quad (7.12)$$

and neutron interactions with double associated production of strangeness

$$n + A \rightarrow \Lambda + \Lambda + X, \quad (7.13)$$

where  $X$  must contain particles carrying a net strangeness of  $S = 2$ . An example of the latter would be  $X = K^0 K^+ \dots$ .

We do not expect interactions of  $K_L^0$ 's in the neutral beam to contribute to  $\Lambda\Lambda$  production. Although beginning with one unit of strangeness (the  $K_L^0$  will interact strongly as a  $\bar{K}^0$  half of the time), an additional antibaryon must be produced in association with the second  $\Lambda$ . The difficulty of producing a baryon-antibaryon pair at low energies combined with the reduced flux of  $K_L^0$  relative to neutrons makes this production mechanism unlikely.

### 7.2.1 $\Lambda\Lambda$ Kinematics

In addition to the VV topology and dissociator/veto information of the 40  $\Lambda\Lambda$  events, the distribution of kinematic variables can be used to assess the likelihood that they



signal  $H$  dissociation. Most important (as already mentioned) is the requirement that the veto counter be empty for  $H$  dissociation candidates. Only two of the 40  $\Lambda\Lambda$  events pass the empty veto requirement. To aid in understanding possible backgrounds to the  $H$  dissociation signal, all 40 events are examined in invariant mass, momentum and transverse momentum. The likelihood of the two empty veto events arising from the background process(es) responsible for the other 38 events can thereby be assessed.

### Invariant mass

As argued in section 4.2.1, diffraction dissociation favors low invariant mass. For the  $H$  in particular there is only one decay channel available to an excited  $H^*$  if the excited state mass is below  $m_n + m_{\Xi^0} = 2255 \text{ MeV}/c^2$ . How this situation affects the spectrum of  $\Lambda\Lambda$  invariant mass in  $H$  dissociation is, of course, unknown, but it might be expected that  $H$  dissociation favors low mass states, just as the finite mass sum rule predicts in Regge phenomenology. Other interactions will produce  $\Lambda\Lambda$  pairs with typically large invariant masses. Figure 7.6 shows the invariant mass of the 40  $\Lambda\Lambda$  events. At this point we may also note that no evidence of a  $\Lambda\Lambda$  resonance above  $2m_\Lambda$  is seen.

### Momentum distribution

The momentum of the  $\Lambda\Lambda$  system for the 40 events is plotted in Figure 7.7. In Figure 7.8 a scatter plot of  $\Lambda\Lambda$  invariant mass versus momentum shows no obvious grouping of high momentum-low mass events which we could identify with a dissociation signal.

### $p_T^2$ distribution

The clearest evidence that the two empty veto  $\Lambda\Lambda$  events are not due to  $H$  dissociation is the transverse momentum distribution. For diffraction dissociation we expect the  $p_T^2 \approx t'$  distribution to be peaked at small values; according to diffraction dissociation phenomenology  $dN/dp_T^2 \sim \exp(-bp_T^2)$ . Although we do not know *a priori* what slope

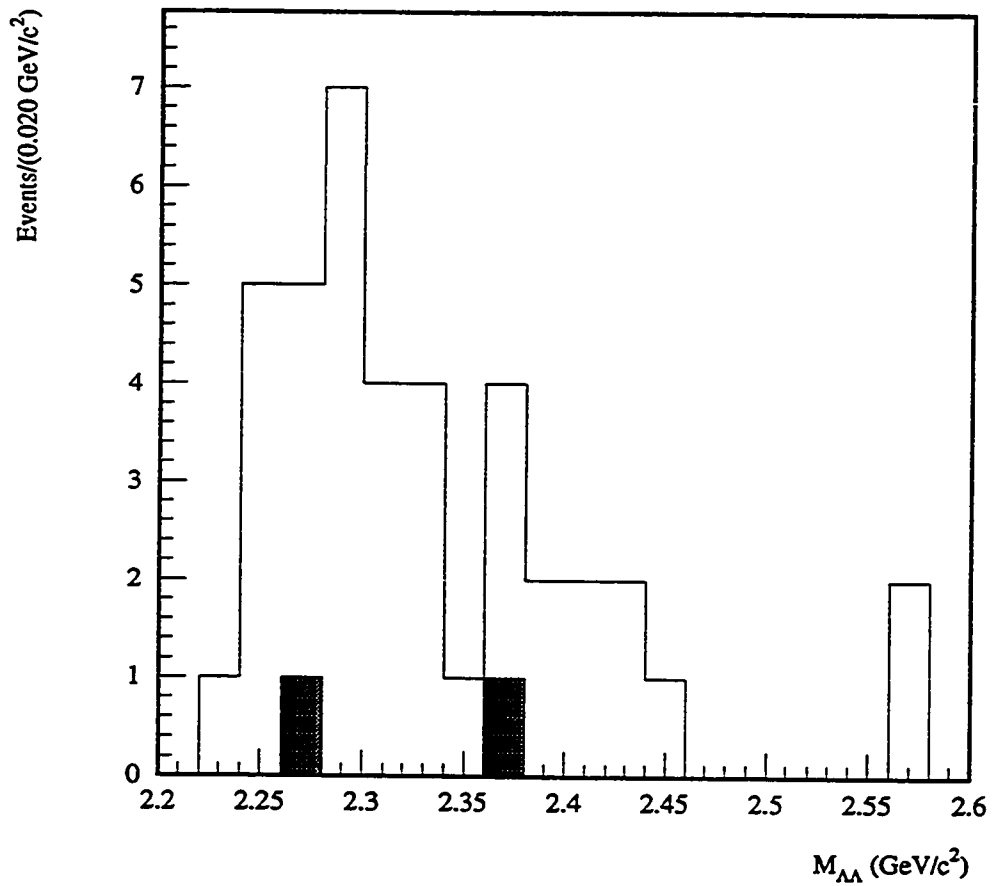


Figure 7.6:  $M_{\Lambda\Lambda}$  distribution. The two empty veto events are shown as solid boxes. The distribution is not acceptance corrected.

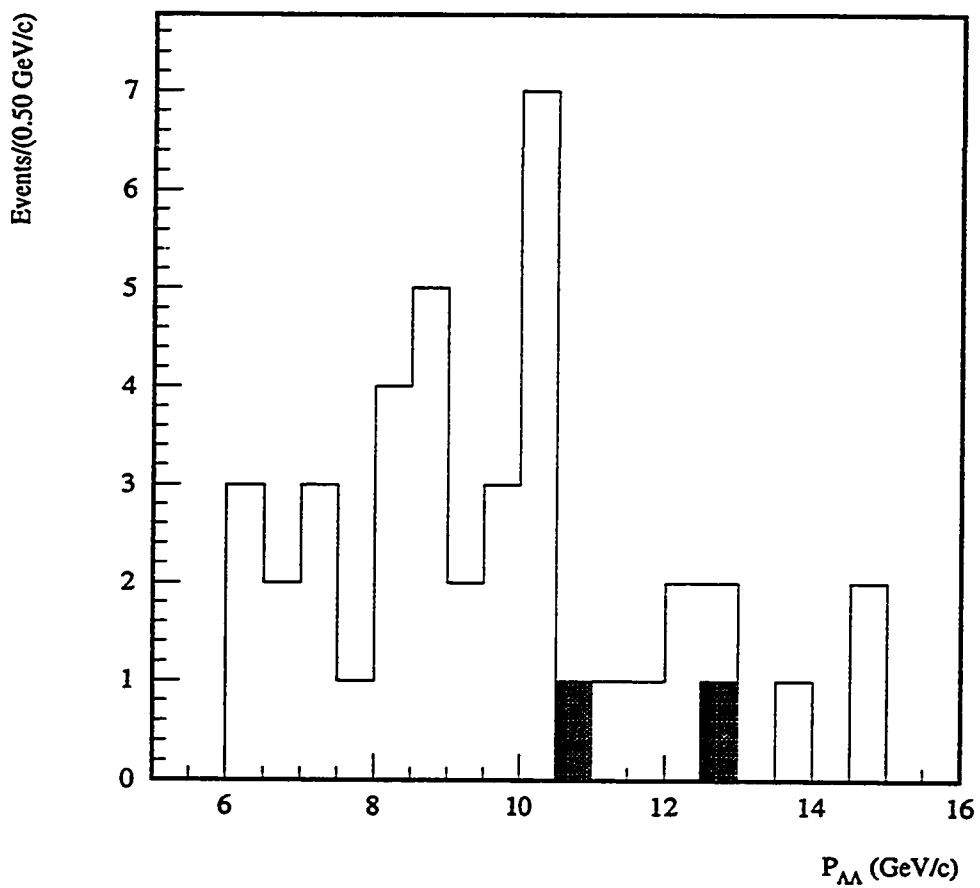


Figure 7.7:  $p_{\Lambda\Lambda}$  distribution. The solid boxes show the two empty veto events.

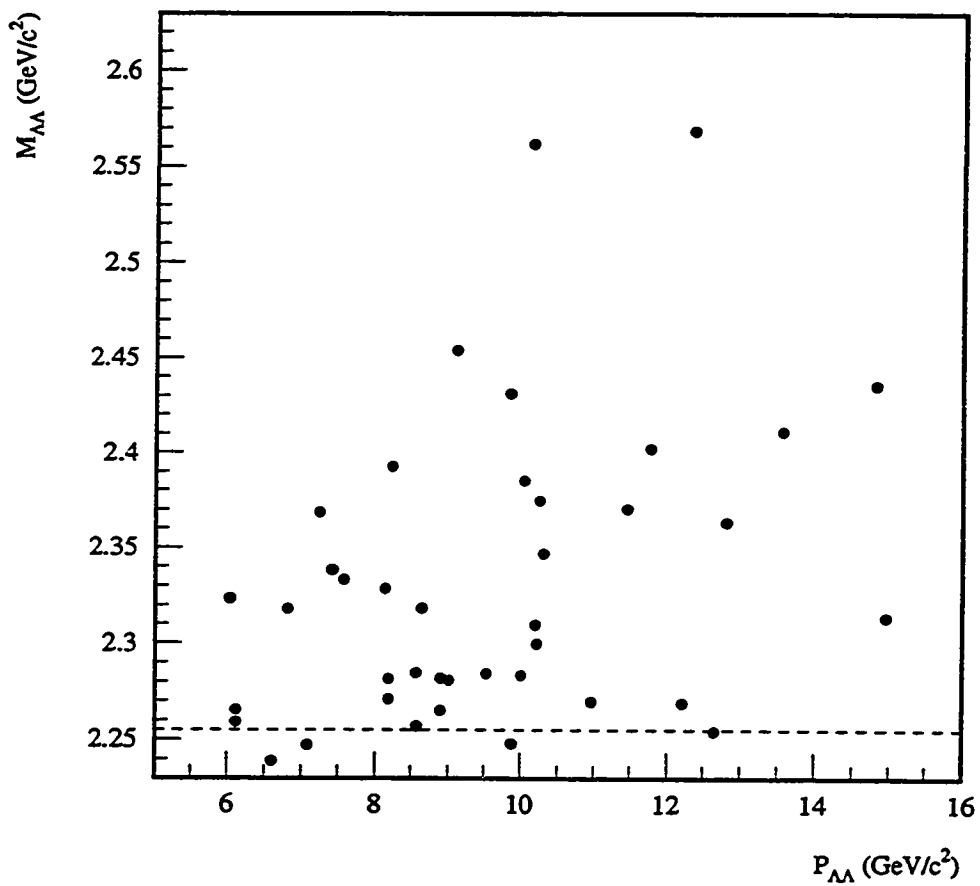


Figure 7.8: Scatter plot of  $M_{\Lambda\Lambda}$  vs  $p_{\Lambda\Lambda}$ . The dotted line shows the  $\Xi N$  threshold, below which only the  $\Lambda\Lambda$  channel is open for decay of the excited  $H^*$ .

Event	$M_{\Lambda\Lambda}$ GeV/c <sup>2</sup>	$p_{\Lambda\Lambda}$ GeV/c	$p_T^2$ (GeV/c) <sup>2</sup>	$K_{DSC}$ MeV
327	2.3630	12.78	0.235	20.21
1044	2.2681	10.97	0.501	2.23

Table 7.2: Kinematics of empty veto  $\Lambda\Lambda$  events. The  $\Lambda\Lambda$  invariant mass, momentum and transverse momentum are reconstructed using the spectrometer. The measured energy of the recoil,  $K_{DSC}$ , is the energy recorded in the dissociator.

parameter governs dissociation of a new type of hadron, it is reasonable to expect  $b$  to be the same as measured for the  $\Lambda K_S^0$  events. As noted earlier, the slope parameter is, to a very good approximation, independent of the type of hadron dissociating, being mainly a function of the size of the target particle. Figure 7.9 shows the distribution of  $p_T^2$  for the  $\Lambda\Lambda$  events. The distribution is not consistent with the small values of  $p_T^2$  expected in a diffractive process, and the two empty veto events are found at  $p_T^2 = 0.235$  and  $0.501$  (GeV/c)<sup>2</sup>, quite far out on an exponential distribution with slope  $b \sim 10$  GeV<sup>-2</sup>. The requirement  $p_T^2 < 0.330$  (GeV/c)<sup>2</sup> is 95% efficient for a signal with slope  $b = 9$  GeV<sup>-2</sup>. Only one empty veto event passes this  $p_T^2$  cut. This event is marginally consistent with coming from  $H$  dissociation. Both empty veto events are consistent with coming from the same process as the other 38 events, that is to say neutron interactions.

### 7.2.2 Empty Veto $\Lambda\Lambda$ Events: A Closer Look

Both empty veto events were observed with the dissociator in the downstream position. The measured kinematic quantities of the two empty veto  $\Lambda\Lambda$  events are listed in Table 7.2. Figure 7.10 is an event plot showing the vertex and dissociator information for one of the two events. Tracks are shown as solid lines, and a  $3\sigma$  error ellipse is shown at  $V^0$  vertex locations. (In the figure only one  $V^0$  vertex is visible; the second  $V^0$  decays outside the frame of the picture.) Dotted lines project  $V^0$  trajectories back to the  $VV$  vertex inside the DSC, where an error ellipse shows the position of the  $VV$ . On the left of the event display, bar graphs show pulse height and time of any

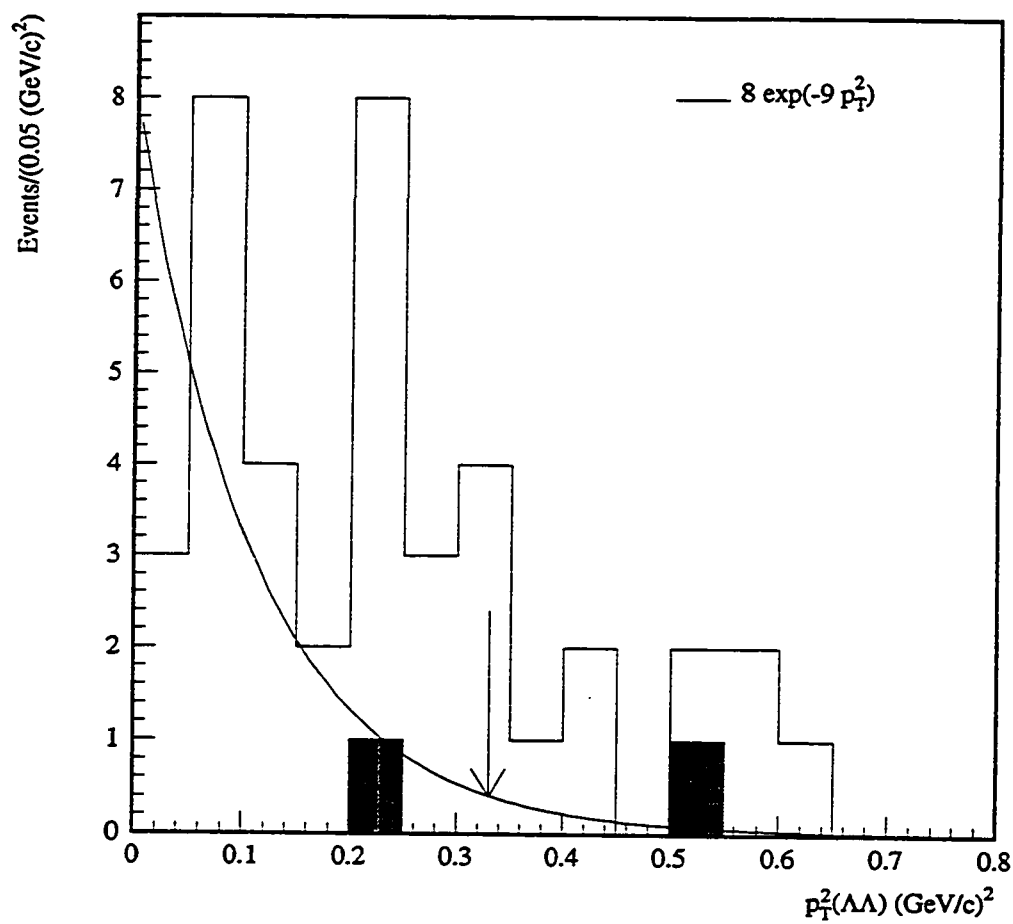


Figure 7.9: Distribution of  $p_T^2$  for  $\Lambda\Lambda$  events. Solid boxes show the two empty veto events. The superimposed curve shows the distribution expected for diffraction from nucleons, with the cut at  $p_T^2 = 0.330 \text{ GeV}^2$  shown by an arrow.

hit dissociator segments, which are numbered from 1–10 in the  $z$ -direction.<sup>1</sup> The VV vertex for event 327 is located in the sixth counter of the DSC, and the event has two hit DSC counters (number 5 and 6) with a small in-time energy deposit. Figures 7.11 ( $x, z$ ) and 7.12 ( $y, z$ ) plot the four tracks in the spectrometer, showing on the right a view of the entire spectrometer, and on the left a close up view of the tracks and associated hits in the drift chamber modules. Two close up views are plotted for each of the five chamber  $z$ -positions. For DC4 and DC5, the left and right modules are shown separately. For the front three chambers (DC1–DC3), the two views center on different tracks, occasionally showing the same hits and tracks when they are all close together. The wire hits in the drift chambers are plotted as circles showing the drift distance.<sup>2</sup> Small diamonds indicate the position on the drift circles used in the track fit. The trajectory plotted is the best fit track swum from the upstream chambers; multiple scattering can cause the ideal track fit to miss the actual hit positions in the final chambers.

Both events have the expected topology of  $H$  dissociation events: a VV reconstructed inside the dissociator, a small energy deposit in a few counters of the DSC and no veto signal. However the measured energy in the dissociator is too small in both events to be consistent with a proton recoil from dissociation. (Recall  $K = -t/(2m_p) \approx p_t^2/(2m_p)$ .) A coherent diffraction from carbon is also ruled out because there should be no measurable energy in the DSC. It is possible that these events come from an incoherent dissociation from a nucleon inside the carbon nucleus, which recoils and results in the measured energy, but the observed transverse momentum makes this unlikely. The  $p_T^2$  of event 1044 is too large to be consistent with  $H$  diffraction dissociation, and event 327 has a  $p_T^2$  only marginally consistent with expectations, lying on the tail of our measured  $\Lambda K_S^0 p_T^2$  distribution. We must conclude neither of these events comes from  $H$  dissociation, but they most likely

---

<sup>1</sup>DSC counters 9 and 10 refer to the two phototubes of the veto counter.

<sup>2</sup>Out of time hits are plotted as a square centered on the wire. Such early or late hits may be caused by tracks unassociated with the event, electronic cross talk or delta rays. It is not possible to convert these out of time hits to a physically consistent drift distance. In addition, some late hits are converted to the maximum drift distance. Examples of both types of out of time hits may be seen in the close up view of chamber 2u in Figure 7.11.

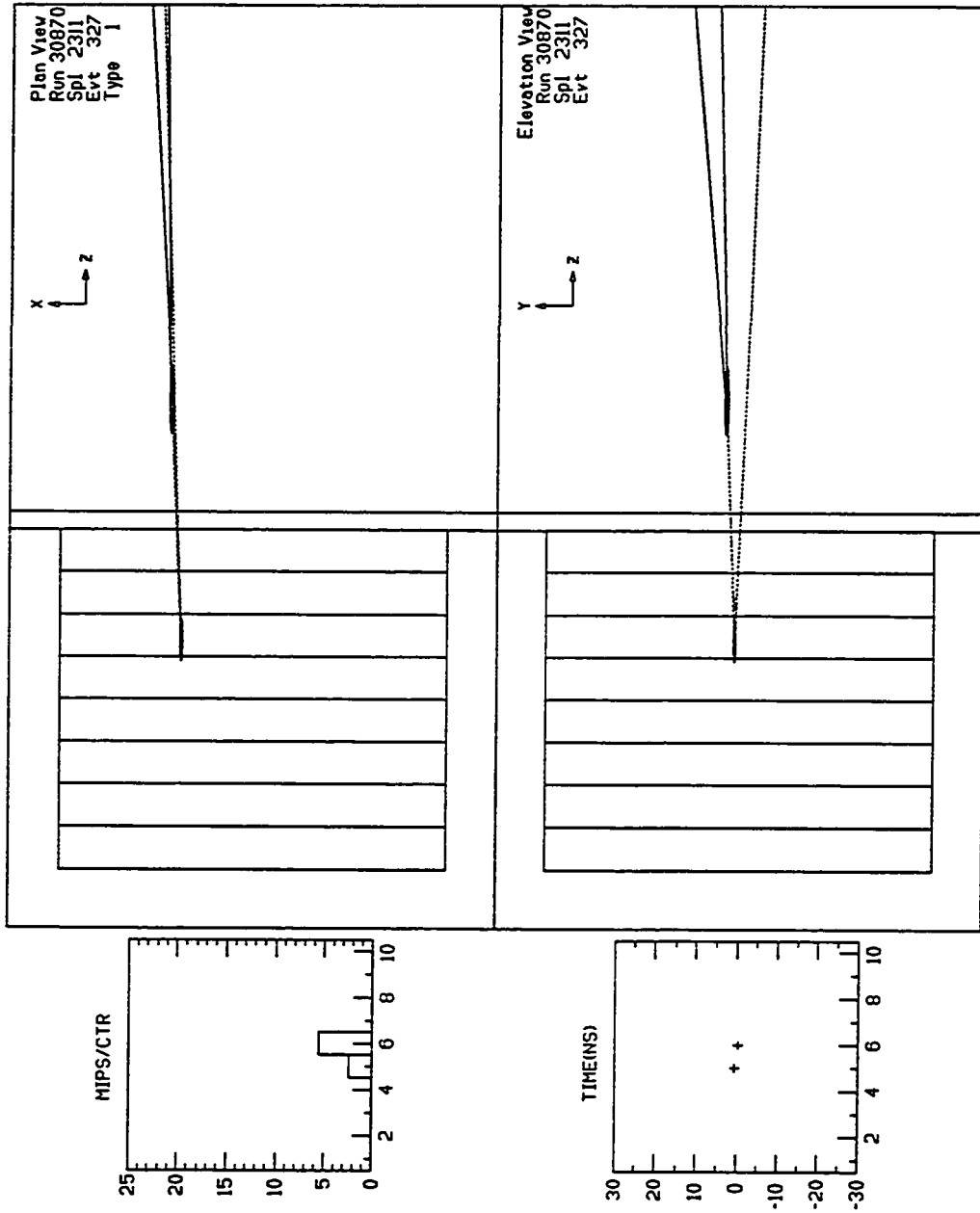


Figure 7.10: DSC Event Plot for Empty Veto AA Event.



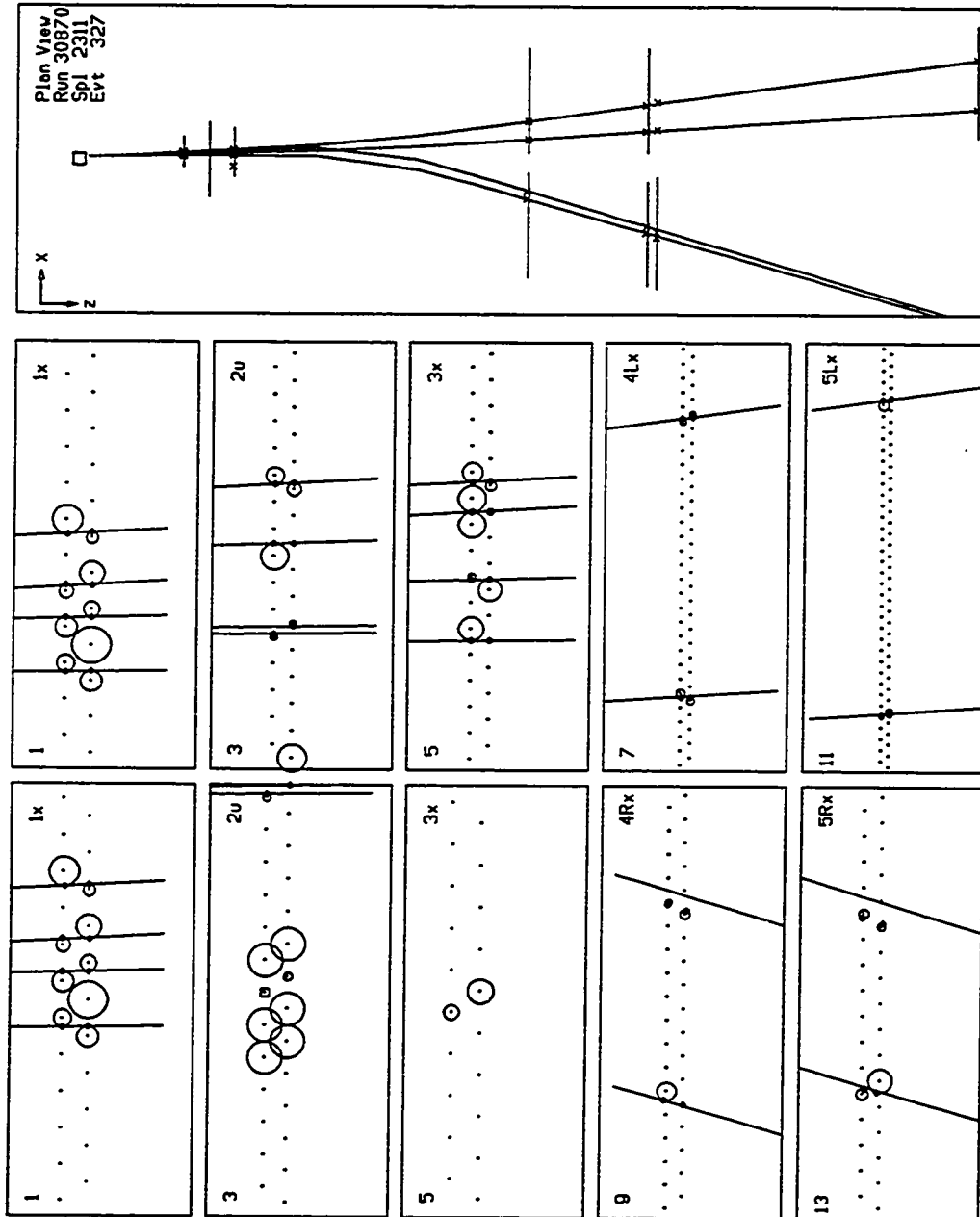


Figure 7.11: Event Plot ( $x, z$ ) for Empty Veto AA Event.

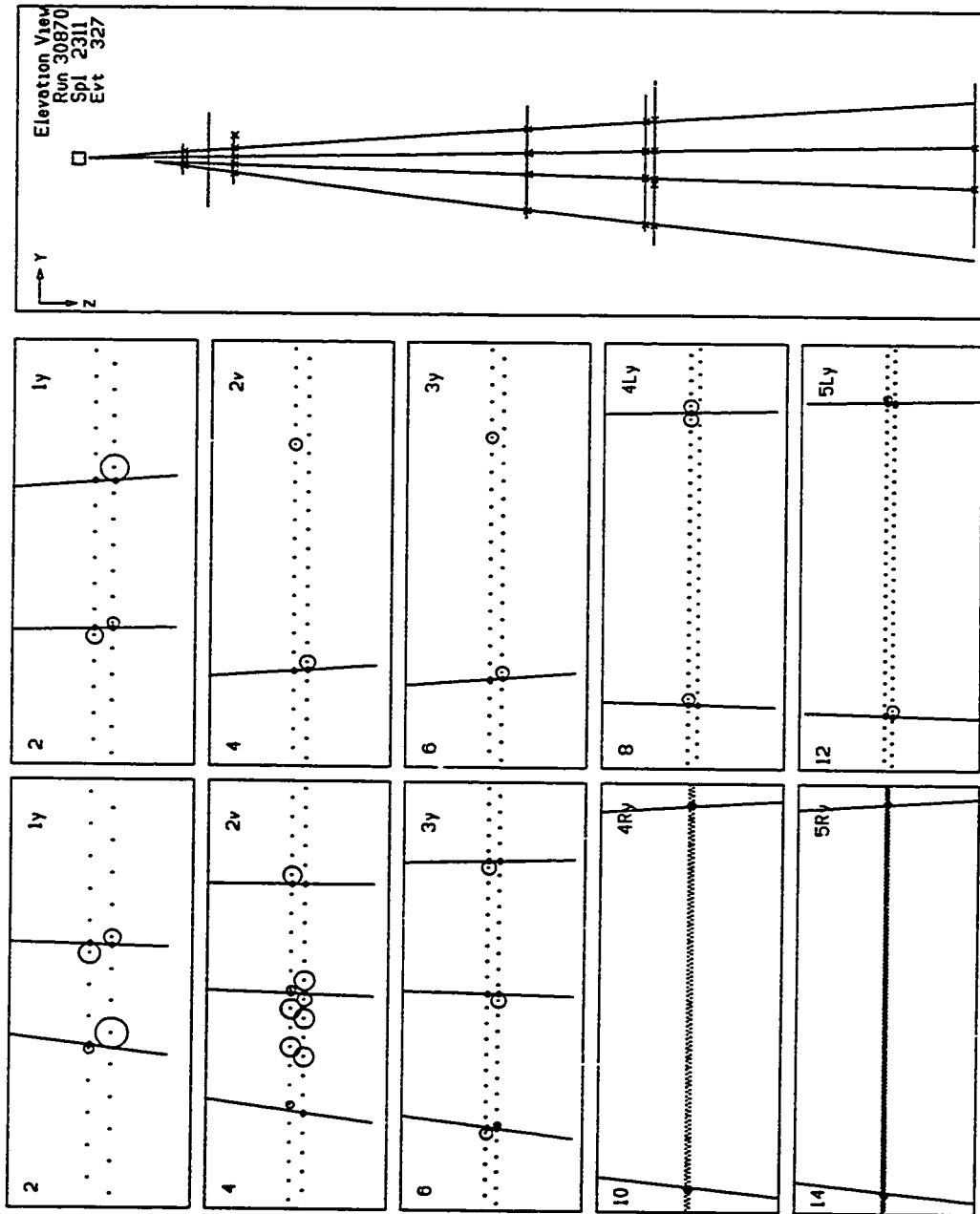


Figure 7.12: Event Plot ( $y, z$ ) for Empty Veto  $\Lambda\Lambda$  Event.

result from neutron interactions such as  $n + p \rightarrow \Lambda K^0 \Lambda K^0 + X$ , where  $X$  is some charged particle recoiling in the dissociator. The two  $K^0$ 's are not observed in the detector (quite likely if they are  $K_L^0$ 's) and result in the large measured  $p_T^2$ .

### 7.3 Setting a Limit on $H$ Production

Having observed only a single event consistent with  $H$  dissociation but also consistent with background, we now may set a limit on the cross section for production of  $H$  dibaryons in  $p$ -Pt collisions. We set a limit by normalizing to neutron production, where the neutron is observed by the coherent diffraction dissociation process  $n + C \rightarrow \Lambda K_S^0 + C$ .

#### 7.3.1 Method

The differential cross section for  $H$  production in  $p$ -Pt collisions at 24.1 GeV/ $c$  is given in terms of the cross section for neutron production as

$$\left. \frac{d\sigma_H}{d\Omega} \right|_{65 \text{ mrad}} = \left( \frac{N_{\Lambda\Lambda}^H A_{\Lambda K_S^0} \sigma_{\Lambda K_S^0}^C}{N_{\Lambda K_S^0} A_{\Lambda\Lambda} \sigma_{\Lambda\Lambda}} \right) \left. \frac{d\sigma_n}{d\Omega} \right|_{65 \text{ mrad}}. \quad (7.14)$$

Here we have normalized to the number of coherent  $\Lambda K_S^0$  events produced from carbon,  $N_{\Lambda K_S^0}$ , which we obtain from the fit to the  $t'$  distribution. The cross section for coherent diffraction dissociation of neutrons from carbon nuclei is  $\sigma_{\Lambda K_S^0}^C$ , and the cross section for  $H$  diffraction dissociation is  $\sigma_{\Lambda\Lambda}$ . Both of these cross sections must be calculated from phenomenological models, and as such they contribute significantly to the systematic error. The geometrical acceptance times efficiency of  $\Lambda K_S^0$  ( $\Lambda\Lambda$ ) event selection is given in the above by  $A_{\Lambda K_S^0}$  ( $A_{\Lambda\Lambda}$ ). Each of these terms is calculated using Monte Carlo simulation of  $H$  or  $n$  dissociation events. Because the limit is set on a ratio of cross sections, the systematic error involved in determining the efficiencies  $A_{\Lambda\Lambda}$  and  $A_{\Lambda K_S^0}$  is reduced; any common systematic error will cancel in the ratio of the two efficiencies, making the need for an absolute determination of the geometrical

acceptance and efficiency of the event selection unnecessary. The similarity of the coherent  $\Lambda K_S^0$  sample to the expected signal from  $H$  dissociation (four tracks, forward process) ensures that the ratio of efficiencies is likely to be free of error compared to the absolute efficiencies.

### $N_{\Lambda K_S^0}$

From a fit to the  $t'$  distribution, we find  $187 \pm 39$   $\Lambda K_S^0$  events attributable to coherent dissociation from carbon nuclei. These events break down into  $105 \pm 32$  events from the downstream dissociator position and  $81 \pm 18$  events from the upstream position.

### $A_{\Lambda K_S^0}$

The probability for a  $\Lambda K_S^0$  event produced coherently from carbon at the dissociator to be detected and identified in the analysis,  $A_{\Lambda K_S^0}$ , is calculated using Monte Carlo simulation. Monte Carlo events are generated using the neutron spectrum obtained from data (Figure 7.3), the simple four resonance model for  $M_{\Lambda K_S^0}$  (Equation 7.8), and an exponential  $t$  distribution with  $b = 68 \text{ GeV}^{-2}$ . A full detector simulation of the event in the Monte Carlo program is used to determine which events are geometrically accepted in the detector. The Monte Carlo program is integrated with the offline software programs so the simulated events may be analyzed by the same code as the actual events. The number of  $\Lambda K_S^0$  events identified by the analysis code is divided by the number of events generated to obtain the net efficiency.

Table 7.3 lists the result of this calculation for the two dissociator positions. The statistical uncertainty of the results is less than 2% of the determined efficiency. To assign a systematic uncertainty to these efficiencies, simulations were done using different neutron spectra and invariant mass spectra, both varied within acceptable limits determined by the observed events. The three neutron spectra in Figure 7.3 were used. In addition to the model for  $M_{\Lambda K_S^0}$  with four equally weighted Breit-Wigner resonances from Table 7.1 (Resonance 1), we consider a reweighted resonance model (Resonance 2), with the  $S_1(1775)$  and  $D_3(1950)$  resonances enhanced to 30% and 40% respectively, and a finite mass sum rule distribution (FMSR) weighted by

$n$ spectrum	$M_{\Lambda K_S^0}$ spectrum	$A_{\Lambda K_S^0}^u$	$A_{\Lambda K_S^0}^d$
Data	Resonance 1	$1.71 \cdot 10^{-3}$	$2.94 \cdot 10^{-3}$
Blobel	Resonance 1	$2.14 \cdot 10^{-3}$	$3.41 \cdot 10^{-3}$
Wang	Resonance 1	$2.06 \cdot 10^{-3}$	$3.37 \cdot 10^{-3}$
Data	Resonance 2	$1.58 \cdot 10^{-3}$	$2.73 \cdot 10^{-3}$
Data	FMSR	$1.25 \cdot 10^{-3}$	$2.35 \cdot 10^{-3}$

Table 7.3: Monte Carlo  $\Lambda K_S^0$  acceptance for different models. The models include three neutron spectra and three  $m(\Lambda K_S^0)$  distributions. Results for both DSC positions are denoted by the superscript  $u$  (upstream) and  $d$  (downstream).

phase space:

$$\frac{dN}{dM_{\Lambda K_S^0}} = \frac{1}{[M_{\Lambda K_S^0}^2 - M_n^2]} \frac{p^*}{M_{\Lambda K_S^0}}. \quad (7.15)$$

This distribution follows from the finite mass sum rule (See Section 4.2.1), which gives the average behavior of the differential cross section as  $dN/d\nu \sim 1/\nu$ , where  $\nu = M_{\Lambda K_S^0}^2 - M_n^2 - t$ . In Equation 7.15 we have ignored  $t$  compared to  $\Delta(M^2)$  and changed variable from  $\nu$  to  $M_{\Lambda K_S^0}$ . The results for these modified models are also given in the table. From the variation, an overall systematic error of 20% (15%) is assigned to the upstream (downstream) efficiency determined using the Data spectrum and the Resonance 1 model for  $M_{\Lambda K_S^0}$ .

### $A_{\Lambda\Lambda}$

The efficiency for  $H$  dissociation  $\Lambda\Lambda$  events is also determined from Monte Carlo. Lacking any signal to guide the choice of kinematic distributions for generating events, we consider a number of models for the  $H$  momentum spectrum and the  $H^*$  ( $\Lambda\Lambda$ ) invariant mass spectrum. We use two momentum spectra calculated in the coalescence model of Cousins and Klein (see Sec. 4.1.1)<sup>3</sup>, as well as  $H$ 's of fixed momentum  $p_H = 7.03$  GeV/ $c$ , which is the lab momentum of an  $H$  produced at rest in the center

<sup>3</sup>The second coalescence spectrum comes from a preliminary version of their coalescence calculation, which used different  $\Lambda$  production data.

of mass. The later is appropriate if the  $H$  is centrally produced, and is chosen as a simple and very different model for the production of  $H$  dibaryons. The  $H^*$  mass distribution from dissociating  $H$ 's is taken from the finite mass sum rule prescription modified by two body phase space:

$$\frac{dN}{dM_{\Lambda\Lambda}} = \frac{1}{M_{\Lambda\Lambda}^2 - M_H^2} \frac{p^*}{M_{\Lambda\Lambda}}. \quad (7.16)$$

A second invariant mass spectrum is taken as a resonance at  $2.3 \text{ GeV}/c^2$  with a width  $\Gamma = 0.250 \text{ GeV}/c^2$ . There is a dependence on the dissociation target (free proton or carbon nucleus) because of the smaller momentum transfer for coherent diffraction from carbon. Because we would accept either source of  $\Lambda\Lambda$  as a signal, we calculate separate acceptances for the two processes. The  $t$  distribution has slope  $b = 9 \text{ GeV}^{-2}$  for nucleon targets and  $b = 68 \text{ GeV}^{-2}$  for carbon targets.

Table 7.4 lists the efficiencies for the models considered. For the purpose of setting a limit, we average all the models for a particular target and take the spread of values as indicative of an overall systematic uncertainty of 60% for carbon targets and 80% for proton or nucleon targets.

#### $\sigma_{\Lambda\Lambda}$

The cross section for diffraction dissociation of  $H$ 's to  $\Lambda\Lambda$  was discussed in detail in Section 4.2. In several different models values ranging from 0.1–1.0 mb were found, and we found the exact value in each model to depend on the  $H$  mass. Without any more definite knowledge about the  $H$ , we take a central value of  $\sigma_{\Lambda\Lambda} = 0.5 \text{ mb}$ .

#### $\sigma_{\Lambda K_S^0}^C$

The cross section for coherent diffraction dissociation of neutrons on carbon to  $\Lambda K^0$  has not been measured, but we estimate it using an optical model [90, 28] to scale from the cross section for dissociation from protons, which has been measured in several experiments. A similar optical model has been used successfully to predict the cross section for the coherent process  $n + C \rightarrow p\pi^- C$  in terms of the cross section for scattering from individual nucleons [91].

$p_H$ spectrum	$M_{\Lambda\Lambda}$ spectrum	Target	$A_{\Lambda\Lambda}^u$	$A_{\Lambda\Lambda}^d$
Coalescence 1	FMSR	C	$1.47 \cdot 10^{-3}$	$1.91 \cdot 10^{-3}$
Coalescence 1	Resonance	C	$2.30 \cdot 10^{-3}$	$2.83 \cdot 10^{-3}$
Coalescence 2	FMSR	C	$0.79 \cdot 10^{-3}$	$1.27 \cdot 10^{-3}$
Coalescence 2	Resonance	C	$1.14 \cdot 10^{-3}$	$1.71 \cdot 10^{-3}$
Fixed	FMSR	C	$0.25 \cdot 10^{-3}$	$0.53 \cdot 10^{-3}$
<b>Average</b>		C	$1.19 \cdot 10^{-3}$	$1.65 \cdot 10^{-3}$
Coalescence 1	FMSR	$p$	$0.78 \cdot 10^{-3}$	$0.93 \cdot 10^{-3}$
Coalescence 1	Resonance	$p$	$1.78 \cdot 10^{-3}$	$2.12 \cdot 10^{-3}$
Coalescence 2	FMSR	$p$	$0.35 \cdot 10^{-3}$	$0.55 \cdot 10^{-3}$
Coalescence 2	Resonance	$p$	$0.70 \cdot 10^{-3}$	$1.10 \cdot 10^{-3}$
Fixed	FMSR	$p$	$0.07 \cdot 10^{-3}$	$0.15 \cdot 10^{-3}$
<b>Average</b>		$p$	$0.74 \cdot 10^{-3}$	$0.97 \cdot 10^{-3}$

Table 7.4: Monte Carlo  $\Lambda\Lambda$  acceptance for different models considered. The statistical uncertainty is  $\sim 3\%$  for all the models. The superscript  $u$  ( $d$ ) denotes the upstream (downstream) DSC position.

In the optical model, the nucleus is considered as a collection of nucleons which act as individual scattering centers, with some density distribution inside the nucleus. The neutron wave scatters from each of the nucleons, adding coherently in the forward direction. However, because of nuclear shadowing, the probability to scatter from an individual nucleon decreases as the wave moves through the nucleus. The wave must scatter coherently from all of the nucleons to result in the coherent process; if it does not scatter coherently, then the nucleus may be dissociated or left in an excited state. The effect of the distribution of nucleons inside the nucleus is seen through a form factor  $f(\mathbf{q})$ , derived from the density distribution. With the differential cross section for scattering from an individual nucleon parameterized as  $d\sigma/dp_T^2 = C_0 \exp(-bp_T^2)$ , the optical model gives the differential cross section for coherent scattering in the forward direction as

$$\frac{d\sigma_{\Lambda K_S^0}^C}{dp_T^2}(p_T^2 = 0) = C_0 A^2 |f(0)|^2. \quad (7.17)$$

Our optical model accounts for the possible decay of the intermediate  $N^*$  while still in the nucleus, spoiling the coherence. We obtain a form factor  $|f(0)|^2 \approx 0.08$  using a

simple model of the nuclear density. Varying the density model does not change the value of  $f$  by more than 10%. Using the slope parameters measured from our data, the overall ratio of coherent dissociation to dissociation from free protons is

$$\sigma(n + C \rightarrow \Lambda K^0 + C) = (1.4 \pm 0.35) \sigma(n + p \rightarrow \Lambda K^0 + p), \quad (7.18)$$

where the uncertainty comes from adding the 10% uncertainty from the choice of nuclear density in quadrature with the uncertainties in the the determination of the slope parameters  $b_C$  and  $b_i$  from the  $t'$  fit.

Ansorge *et al.* measured the diffraction dissociation cross section  $\sigma(n+p \rightarrow \Lambda K^0 + p)$  using a bubble chamber and a neutron beam of momentum 10–24 GeV/c [92]. Using their value of  $(8.7 \pm 3.5) \mu\text{b}$ , divided by two to obtain  $\Lambda K_S^0$ , we find  $\sigma_{\Lambda K_S^0}^C = 5.9 \pm 1.8 \mu\text{b}$ . This compares well with the cross section for  $p+p \rightarrow \Lambda K^+ + p$  obtained by Cleland *et al.* [87] for 30 GeV/c protons. Dividing by two to account for double counting of protons and by another factor of two for  $K^0 \rightarrow K_S^0$ , their measured value of  $(16.6 \pm 3.3) \mu\text{b}$  implies  $\sigma_{\Lambda K_S^0}^C = (5.81 \pm 1.16) \mu\text{b}$ . Averaging these two values and including a systematic uncertainty of 25% for the optical model we have

$$\sigma_{\Lambda K_S^0}^C = (5.85 \pm 1.04 \pm 1.46) \mu\text{b}. \quad (7.19)$$

$\Sigma^0 K_S^0$  production will also result in  $\Lambda K_S^0$  events because the  $\Sigma^0$  decays to  $\Lambda \gamma$  immediately. Ansorge *et al.* measured  $\Sigma^0 K^0$  production to be comparable to  $\Lambda K^0$  production ( $\sigma_{\Sigma^0 K^0} = 6.7 \pm 3.4 \mu\text{b}$ ), so we should increase the cross section  $\sigma_{\Lambda K_S^0}^C$  by a factor of two. However, an identical factor of two arises for  $\sigma_{\Lambda\Lambda}$  due to the additional channel  $H + p \rightarrow \Sigma^0 \Sigma^0 + p$ . We assume these factors cancel in the ratio.

$N_{\Lambda\Lambda}$

Because we observe a single event consistent with background, we set a 90% confidence level upper limit on the cross section by assigning  $N_{\Lambda\Lambda}$  to be the probability to observe one or zero events. Because of the large uncertainty (80%) in the sensitivity, the usual Poisson probability of 3.89 events is multiplied by a scale factor  $F$ , according to the



prescription of Cousins and Highland [93]. This method incorporates the uncertainty in the determination of the sensitivity into the upper limit, increasing the it from 3.89 to 7.3 events.

### 7.3.2 Result

We combine results from the two positions of the dissociator into a single limit:

$$\frac{d\sigma}{d\Omega}\Big|_{65\text{mr}} < \left[ \frac{N_{\Lambda\Lambda}^u + N_{\Lambda\Lambda}^d}{\frac{N_{\Lambda K_S^0}^u}{A_{\Lambda\Lambda}^u} (1.4A_{\Lambda\Lambda}^{u,C} + 6.34A_{\Lambda\Lambda}^{u,N}) + \frac{N_{\Lambda K_S^0}^d}{A_{\Lambda\Lambda}^d} (1.4A_{\Lambda\Lambda}^{d,C} + 6.34A_{\Lambda\Lambda}^{d,N})} \right] \frac{\sigma_{\Lambda K_S^0}}{\sigma_{\Lambda\Lambda}} \frac{d\sigma_n}{d\Omega}\Big|_{65\text{mr}} \quad (7.20)$$

Here we account for  $H$  dissociation either from a carbon nucleus with cross section  $\sigma_{\Lambda\Lambda}^C = 1.4\sigma_{\Lambda\Lambda}$  or from a single nucleon in carbon (scaling  $\sigma_{\Lambda\Lambda}$  by  $A^{2/3}$  to account for shadowing) or from a free proton. The ratio of hydrogen to carbon in scintillator is 1.1, so the net number of nucleon targets is  $1.1 + 12^{2/3} = 6.34$ . Inserting the values found above for the acceptances and number of events we have

$$\frac{d\sigma}{d\Omega}\Big|_{65\text{mr}} < 1.4 \cdot 10^{-4} \frac{d\sigma_n}{d\Omega}\Big|_{65\text{mr}} \quad (7.21)$$

$$< 0.6 \text{ mb/sr.} \quad (7.22)$$

In the last equation we have substituted 4.26 barn/sr for the neutron differential cross section at 65 mrad, obtained by scaling Blobel *et al.*'s values measured in  $pp$  collisions by  $A^{2/3}$  [61]. The limit obtained here must be modified for  $H$ 's with lifetimes less than  $10^{-7}$  s to account for the probability of the  $H$  to survive the  $\sim 20$  m flight to the target. That probability is approximately 50% for a centrally produced  $H$  ( $p = 7$  GeV/ $c$ ) with  $\tau_H = 10^{-8}$  s.

## 7.4 Conclusion and Implications

The limit obtained in Equation 7.22 is not sufficient to rule out the existence of the  $H$ , but it does begin to approach an interesting level. For example, the coalescence model

(Section 4.1.1) predicts cross sections within an order of magnitude. Of the other experiments, the only one with sensitivity to a long-lived  $H$  is Gustafson *et al.* However their result is for masses above  $2.0 \text{ GeV}/c^2$ , and for lifetimes  $\tau > 10^{-7} \text{ s}$ , while this experiment is also sensitive to lighter  $H$ 's with lifetimes  $\gtrsim 10^{-8} \text{ s}$ . As such this experiment explored new territory in the parameter space available to the  $H$  dibaryon. In addition, the production of 40  $\Lambda\Lambda$  events through  $n$ - $A$  collisions in our dissociator, shows that the ingredients of the  $H$  are already produced at available energies. These events are particularly interesting because they are produced at low invariant mass and therefore also at the small relative momenta which makes their coalescence likely.

# Appendix A

## BNL E888 Collaboration

Brookhaven National Laboratory, *Upton, New York 11973*  
Morgan May, Sebastian N. White

University of California, *Irvine, California 92717*  
William R. Molzon

University of California, *Los Angeles, California 90024*  
Robert D. Cousins†

Princeton University, *Princeton, NJ 08544*  
Val L. Fitch, Joshua R. Klein\*, Alan J. Schwartz†

Stanford University, *Stanford, California 94305*  
Milind V. Diwan, Karl M. Ecklund\*, George M. Irwin, Stanley G. Wojcicki

Temple University, *Philadelphia, Pennsylvania 19122*  
John Belz, Steven H. Kettell, Virgil L. Highland, Aurel Trandafir

The University of Texas at Austin, *Austin, Texas 78712*  
Gerald W. Hoffman, Karol Lang, James McDonough, Peter J. Riley, Jack L. Ritchie,  
Brent Ware\*, Steve Worm

The College of William and Mary, *Williamsburg, Virginia 23187*

Morty Eckhause, A. Dayle Hancock, Chris Hoff, John R. Kane, Yunan Kuang, Robert Martin, Robert E. Welsh, Michael T. Witkowski

† co-spokesperson

\* thesis student

# Bibliography

- [1] R.L. Jaffe. Perhaps a stable dihyperon. *Phys. Rev. Lett.*, 38(5):195, January 1977. And Errata 38:617.
- [2] T. DeGrand, R.L. Jaffe, K. Johnson, and J. Kiskis. Masses and other parameters of the light hadrons. *Phys. Rev.*, D12(7):2060, October 1975.
- [3] Carleton E. DeTar and John F. Donoghue. Bag models of hadrons. *Ann. Rev. Nucl. Part. Sci.*, 33:235, 1983.
- [4] A.Th.M. Aerts, P.J.G. Mulders, and J.J. deSwart. Multibaryon states in the bag model. *Phys. Rev.*, D17(1):260, January 1978.
- [5] P. J. Mulders and Anthony W. Thomas. Pionic corrections and multi-quark bags. *J. Phys. G*, 9:1159, 1983.
- [6] K. F. Liu and C.W. Wong. MIT bag model with center-of-mass correction. *Phys. Lett.*, B113(1):1, June 1982.
- [7] K. Nishikawa, N. Aoki, and H. Hyuga. Hyperons and the H-particle in the color dielectric model. *Nucl. Phys.*, A534:573, 1991.
- [8] D. Pal and J. A. McGovern. Mass of the dihyperon in the colour-dielectric model. *J. Phys. G*, 18:593, 1992.
- [9] Eugene Golowich and Thomas Sotirelis.  $O(\alpha_s^2)$  mass contributions to the  $H$  dibaryon in a truncated bag model. *Phys. Rev.*, D46(1):354, July 1992.

- [10] Koichi Saito. Masses of the multiquark states in the MIT bag model with the pion-cloud. *Prog. Theor. Phys.*, 72(3):674, September 1984.
- [11] M. Oka, K. Shimizu, and K. Yazaki. The di-hyperon state in the quark cluster model. *Phys. Lett.*, B130(6):365, November 1983.
- [12] B. Silvestre-Brac, J. Carbonell, and C. Gignoux.  $H$ -particle stability in the nonrelativistic quark model. *Phys. Rev.*, D36(7):2083, October 1987.
- [13] Kiyotaka Shimizu. Study of baryon-baryon interactions and nuclear properties in the quark cluster model. *Rep. Prog. Phys.*, 52:1, 1989.
- [14] T. H. R. Skyrme. A non-linear field theory. *Proc. Roy. Soc. London*, A260:127, 1961.
- [15] A. P. Balachandran *et al.* Doubly strange dibaryon in the chiral model. *Phys. Rev. Lett.*, 52(11):887, March 1984.
- [16] A. P. Balachandran, F. Lizzi, V.G.J. Rodgers, and A. Stern. Dibaryons as chiral Skyrmions. *Nucl. Phys.*, B256:525, 1985.
- [17] E. Witten. Current algebra, baryons and quark confinement. *Nucl. Phys.*, B223:433, 1983.
- [18] R. L. Jaffe and C. L. Korpa. Semiclassical quantization of the dibaryon skyrmion. *Nucl. Phys.*, B258:468, 1985.
- [19] Scott A. Yost and Chiara R. Nappi. Mass of the  $H$  dibaryon in a chiral model. *Phys. Rev.*, D32(3):816, August 1985.
- [20] Gilberto L. Thomas, Norberto N. Scoccola, and Andreas Wirzba. Dibaryons as axially symmetric skyrmions. *Nucl. Phys.*, A575:623, 1994.
- [21] Igor R. Klebanov and Karl M. Westerberg. A simple description of strange dibaryons in the skyrme model. PUPT-1555 (hep-ph/9508279), August 1995.

- [22] F. Butler *et al.* Hadron mass predictions of the valence approximation to Lattice QCD. *Phys. Rev. Lett.*, 70(19):2849, May 1993.
- [23] S. Itoh, Y. Iwasaki, and T. Yoshié. Hadron masses in quenched QCD. *Phys. Lett.*, B193:351, January 1987.
- [24] Paul B. Mackenzie and H. B. Thacker. Evidence against a stable dibaryon from Lattice QCD. *Phys. Rev. Lett.*, 55(23):2539, December 1985.
- [25] Y. Iwasaki, T. Yoshié, and Y. Tsuboi. *H* dibaryon in Lattice QCD. *Phys. Rev. Lett.*, 60(14):1371, April 1988.
- [26] T. Yoshié, Y. Iwasaki, and S. Sakai. Hadron spectrum on a  $24^3 \times 60$  lattice. *Nucl. Phys.*, B (Proc. Suppl.)17:413, 1990. reported at Lattice 89.
- [27] Nobuaki Kodama, Makoto Oka, and Tetsuo Hatsuda. *H* dibaryon in the QCD sum rule. *Nucl. Phys.*, A580:445, 1994.
- [28] Joshua R. Klein. *A Strange Matter: Searching for the H Dibaryon*. Ph.D. Dissertation, Princeton University, June 1994.
- [29] John F. Donoghue, Eugene Golowich, and Barry R. Holstein. Weak decays of the *H* dibaryon. *Phys. Rev.*, D34(11):3434, December 1986.
- [30] H. Ejiri *et al.* Search for the *H* dihyperon by double weak decay of nuclei. *Phys. Lett.*, B228(1):24, September 1989.
- [31] H.R. Gustafson *et al.* Search for new massive long-lived neutral particles. *Phys. Rev. Lett.*, 37(8):474, August 1976.
- [32] A.S. Carroll *et al.* Search for six-quark states. *Phys. Rev. Lett.*, 41(12):777, September 1978.
- [33] A.M. Badalyan and Yu.A. Simonov. The hadronic shift and the probability of producing the dilambda state *H*. *Sov. J. Nucl. Phys.*, 36:860, 1982.

- [34] G.T. Condo *et al.* Multinucleon captures of slow antiprotons in complex nuclei and a search for the  $H$  dibaryon. *Phys. Lett.*, B144(1,2):27, August 1984.
- [35] V.V. Barmin *et al.* Search for the reaction  $\bar{p}Xe \rightarrow K^+K^+X$  and for  $H$  ( $S=-2$ ) dibaryon. In S. Oneda and D.C. Peaslee, editors, *Hadron '91*, page 748, River Edge, NJ, 1991. World Scientific.
- [36] S.Aoki *et al.* Search for the  $H$  Dibaryon in ( $K^-$ ,  $K^+$ ) reactions. *Phys. Rev. Lett.*, 65(14):1729, October 1990.
- [37] J.K. Ahn *et al.* Search for  $H$  dibaryon by scintillating-fiber track detector. *Il Nuovo Cimento*, 107A(11):2415, November 1994. Presented at Hadron '93.
- [38] A.T.M. Aerts and C.B. Dover. On the production of the six-quark  $H$  dibaryon in the ( $K^-$ ,  $K^+$ ) reaction. *Phys. Rev.*, D28(3):450, August 1983.
- [39] B.A. Shahbazian *et al.* An evidence for a possible stable dibaryon. *Z. Phys.*, C39:151, 1988.
- [40] B.A. Shahbazian *et al.* The observation of a stable dibaryon. *Phys. Lett.*, B235:208, January 1990.
- [41] B.A. Shahbazian *et al.* Evidences for light  $H^0$  and heavy  $H, H^+$  stable  $S = -2$  dibaryons. *Il Nuovo Cimento*, 107A(11):2459, November 1994. Presented at Hadron '93.
- [42] B.A. Shahbazian *et al.* An evidence for the excited state of the  $S = -2$  stable light dibaryon. JINR Rapid Communications No.1[69]-95, 1995.
- [43] B.A. Shahbazian *et al.* Evidences for  $S = -2$  neutral  $H$  and positively charged  $H^+$  heavy stable dibaryons. *Phys. Lett.*, B316:593, 1993.
- [44] A.N. Alekseev *et al.* Search for an  $H$  dibaryon. *Sov. J. Nucl. Phys.*, 52(6):1016, December 1990.
- [45] M.I. Krivoruchenko and M.G. Shchepkin. Dilambda decays. *Sov. J. Nucl. Phys.*, 36(5):769, November 1982.



- [46] M. Danysz *et al.* Observation of a double hyperfragment. *Phys. Rev. Lett.*, 11(1):29, July 1963.
- [47] M. Danysz *et al.* The identification of a double hyperfragment. *Nucl. Phys.*, 49:121, 1963.
- [48] D.J. Prowse.  $\Lambda\Lambda\text{He}^6$  double hyperfragment. *Phys. Rev. Lett.*, 17(14):782, October 1966.
- [49] S. Aoki *et al.* Direct observation of sequential weak decay of a double hypernucleus. *Prog. Theor. Phys.*, 85(6):1287, June 1991.
- [50] R.H. Dalitz *et al.* The identified  $\Lambda\Lambda$ -hypernuclei and the predicted H-particle. *Proc. R. Soc. Lond.*, A426:1, November 1989.
- [51] C.B. Dover *et al.* Interpretation of a double hypernucleus event. *Phys. Rev.*, C44(5):1905, November 1991.
- [52] Carlton Brent Ware. *All Strange and Terrible Events: A Search for the H Dibaryon*. Ph.D. dissertation, The University of Texas at Austin, December 1995.
- [53] A.B. Migdal. Meson production at energies close to threshold. *Soviet Physics-JETP*, 1:7, 1955.
- [54] A. Schwarzschild and Č. Zupančič. Production of tritons, deuterons, nucleons and mesons by 30-GeV protons on Al, Be, and Fe targets. *Phys. Rev.*, 129:854, 1963.
- [55] L.L. Nemenov. Atomic decays of  $K_L^0$  mesons. *Sov. J. Nucl. Phys.*, 16:67, 1973.
- [56] L.L. Nemenov. Elementary relativistic atoms. *Sov. J. Nucl. Phys.*, 41:629, 1985.
- [57] H. Albrecht *et al.* Study of antideuteron production in  $e^+e^-$  annihilation at 10 GeV centre-of-mass energy. *Phys. Lett.*, B236:102, 1990.

- [58] F.S. Rotondo. Coalescence estimate of  $H$  dibaryon production in high-energy  $p + A$  collisions. *Phys. Rev.*, D47:3871, 1993.
- [59] Robert D. Cousins and Joshua R. Klein. Estimate of  $H$  dibaryon production through  $\Lambda\Lambda$  coalescence in  $p + A$  collisions. *Phys. Rev.*, D submitted 1994, 1995.
- [60] M. May *et al.* AGS Proposal P888: Search for the  $H$  dibaryon. Submitted to BNL PAC Jan 16, 1992.
- [61] V. Blobel *et al.* Inclusive neutron and lambda production in proton-proton interactions at 12 and 24 GeV/c. *Nucl. Phys.*, B135:379, 1978.
- [62] Particle Data Group. Review of particle properties. *Phys. Rev.*, D50:1173, 1994.
- [63] P. Skubic *et al.* Neutral-strange-particle production by 300-GeV protons. *Phys. Rev.*, D18:3115, 1978.
- [64] B.A. Cole, M. Moulson, and W.A. Zajc. Coalescence production of  $H^0$ 's in p-A collisions. *Phys. Lett.*, B350:147, May 1995.
- [65] K. Goulianos. Diffractive interactions of hadrons at high energies. *Physics Reports*, 101(3):169-219, 1983.
- [66] R.L. Cool *et al.* Diffraction dissociation of  $\pi^\pm$ ,  $K^\pm$  and  $p^\pm$  at 100 and 200 GeV/c. *Phys. Rev. Lett.*, 47(10):701, 1981.
- [67] K.J. Anderson *et al.*  $\Lambda$ -proton elastic scattering from 1 to 17 GeV/c. *Phys. Rev.*, D11(3):473, February 1975.
- [68] R.J. Glauber. Cross sections in deuterium at high energies. *Phys. Rev.*, 100(1):242, 1955.
- [69] V. Franco and R.J. Glauber. High-energy deuteron cross sections. *Phys. Rev.*, 142(4):1195, 1966.
- [70] A.P. Heinson *et al.* Measurement of the branching ratio for the rare decay  $K_L^0 \rightarrow \mu^+\mu^-$ . *Phys. Rev.*, D51(3):985, February 1995.

- [71] K. Arisaka *et al.* Improved upper limit on the branching ratio  $B(K_L^0 \rightarrow \mu^\pm \mu^\mp)$ . *Phys. Rev. Lett.*, 70(8):1049, February 1993.
- [72] P. Buchholz and K. McFarlane.  $n/K$  ratio. KL-Memo 268, E791, November 1989.
- [73] Yunan Kuang. Summary of target studies in 1992 run. KL-Memo 397, E871, August 1992.
- [74] K.A. Biery *et al.* A fast integrating eight-bit bilinear ADC. *IEEE Trans. Nucl. Sci.*, 36:650, 1989.
- [75] A. Schwartz and D. A. Ouimette. Stanford TDCs. KL-Memo 243, E791, August 1989.
- [76] R.D. Cousins *et al.* 32-channel digital 6-bit TDC with 2.5 ns least count. *IEEE Trans. Nucl. Sci.*, 36:646, 1989.
- [77] Simon Black, Bob Cousins, and Katrin Schenk. E888 magnetic field measurements and BFIELD routine. KL-Memo 389, E888, September 1992.
- [78] Milind V. Diwan and Marize Pommot-Maia. Measurement of  $\pi$ -interactions. KL-Memo 399, E791, August 1992.
- [79] R.D. Cousins *et al.* Fast parallel pipelined readout architecture for a completely flash digitizing system with a multilevel trigger. *Nucl. Inst. and Meth.*, A277:517, 1989.
- [80] Kurt A. Biery. The data acquisition system for BNL AGS Experiment 791. In J. Lillberg and M. Oothoudt, editors, *AIP Conf. Proc.*, number 209, 1990.
- [81] P.F. Kunz *et al.* The 3081/E processor. SLAC-PUB 3332, SLAC, April 1984.
- [82] William H. Press *et al.* *Numerical Recipes in FORTRAN: the art of scientific computing*. Cambridge University Press, 2nd edition, 1992.
- [83] Philip Mélése. Status of event fitting. KL-Memo 145, E791, December 1987.

- [84] R.D. Cousins and T.M. Kaarsberg. 9/89 release of the FT track and event fitting package. KL-Memo 248, E791, September 1989.
- [85] Virgil Highland. Runge-Kutta magnetic field transport. KL-Memo 124, E791, July 1987.
- [86] C. Mathiazhagan. The status of the E791 magnetic field and some studies on the track  $\chi^2$  problem. KL-Memo 268, E791, July 1990.
- [87] W.E. Cleland *et al.* The reaction  $pp \rightarrow (\Lambda K^+)p$  at 50 and 30 GeV/c: Partial-wave analysis, Deck Model and double Regge exchange. *Nucl. Phys.*, B239:27, 1984.
- [88] C.L. Wang. Empirical formula for inclusive proton spectra between 10 and 300 GeV. *Phys. Rev.*, D16:2196, 1977. J.R. Sanford and C.L.Wang, BNL Report Nos. 11299 and 11479, 1967.
- [89] D.D. O'Brien *et al.* Diffraction dissociation and Coulomb dissociation of high-energy neutrons by nuclei. *Nucl. Phys.*, B77:1, 1974.
- [90] Val Fitch. Private communication.
- [91] P. Mühlemann *et al.* Diffractive production of  $p\pi^-$  systems on nuclei between 8 and 24 GeV/c. *Nucl. Phys.*, B133:189, 1978.
- [92] R.E. Ansorge *et al.* Strange particle production in neutron-proton interactions at 10–24 GeV/c. *Nucl. Phys.*, B103:509, 1976.
- [93] Robert D. Cousins and Virgil L. Highland. Incorporating systematic uncertainties into an upper limit. *Nucl. Inst. and Meth.*, A320:331, 1992.